Patience is like an egg,

from it groweth great birds.

African Tribal Proverb

THE VACUUM ULTRA VIOLET SPECTRUM OF LASER EXCITED BARIUM

A Thesis submitted by

LIONEL WILLIAM JOHN KENT

for the degree of

DOCTOR OF PHILOSOPHY

in the

UNIVERSITY OF LONDON

The Blackett Laboratory
Department of Physics
Imperial College of Science and Technology
South Kensington
London SW7

December 1985

To both my family and Rose

ABSTRACT

In this thesis, the Vacuum Ultra Violet 5p-absorption spectrum of laser-excited Barium between 480Å and 860Å will be presented; the lower level of the transitions is the 6s5d configuration rather than the $6s^2$ ground state. The experiment is a natural development of previous work by Connerade et al (1979) on the 5p absorption spectrum of unexcited neutral Barium, where the observed spectrum was explained in terms of transitions to upper levels belonging to the manifold

$$5p^5(6s^2x6s5dx5d^2)[^2P_{1/2,3/2}]\ ns,nd\quad J=1$$

for which Rose et al (1980) have calculated the mixing coefficients for different configurations belonging to the parent ion limits. Notable differences in the VUV spectrum should result from prior excitation of one of the 6s valence electrons since the transitions

$$5p^6 6s5d\ ^{3,1}D_2 \longrightarrow 5p^5(6s5dx5d^2)\ ns,nd\ J=1,2,3$$

involve different mixing coefficients.

In the present experiment one of the 6s electrons was excited with a pulsed laser tuned to the $6s^2\ ^1S_0$ - $6s5d\ ^1P_1$ resonance line at 5535Å. The resulting population inversion with respect to the

$6s5d\ ^1D_2$ and $^3D_2$ metastable levels resulted in Amplifed Spontaneous Emission rapidly populating these lower levels. The probe continuum was pulsed and was generated by a focussing a Q-switched Ruby laser onto a Samarium target. The resulting plasma emits a spectrally pure continuum between ~400Å and ~1000Å of ~ 25 [ns] duration. Absorption spectra were recorded on photographic film at different delays between the dye laser pulse and the continuum pulse, each spectrum taking ~160 shots.

Entirely new structure was observed, with no clearly resolved transitions from the $6s6p\ ^1P_1$ level initially populated by the pump laser in any of the spectra. The spectra are fairly simple above ~690Å with relatively few lines of which some are believed to be of Ba_2^* dimer origin. At lower wavelengths the spectrum is extremely complex with many closely spaced but weak lines. Comparison with the calculations of Mansfield (1985, Private Communication) using the Cowan Code on excitations to the upper levels built on the configurations $5p^5(5d6s^2 x 5d^2 6s x 5d^3)$, reveals a basic disagreement between the theoretical and experimental distribution of absorption lines above 690Å. By contrast this same code gave fair agreement between experimental and calculated transitions for the unexcited Ba 5p spectrum above 690Å.

This has been interpretated as evidence that the

5d wavefunction becomes level-dependent in the presence of a 5p hole and a 6s5d valence configuration. If this hypothesis is correct, then it has important consequences for the theory of such transitions. This is because the theory is based on ab inito calculations which at present employ average of manifold wavefunctions. Such approaches fail for a sufficiently sensitive one electron wavefunction, for example the 5d wavefunction for the core and valence excited Barium as hypothesised here.

CONTENTS

	page
QUOTATION	1
TITLE	3
DEDICATION	5
ABSTRACT	7
CONTENTS	11
ILLUSTRATIVE MATERIAL	15
LIST OF TABLES	19
ACKNOWLEDGEMENTS	21
CHAPTER 1: INTRODUCTION	23
1.1 The Interest in Atomic Shells	23
1.2 The Interest in Barium for Inner Shell Studies	26
1.3 Aims of the Present Research	38
1.4 1.4.1 Experimental Method	42
1.4.2 Laser Induced Ionisation of of Barium	44
CHAPTER 2: THEORY	47
2.1 The Radial Problem - Its importance to contemporary work on atomic structure	47
2.2 Discussion of the Anomalous Barium Photo-Double Ionisation Phenomena	63
2.3 2.3.1 Techniques of Analysis for the Barium 5p spectrum	74
2.3.2 Multi-Channel Quantum Defect Theory and the application of "Lu Fano Plots" to the ordering of a spectrum into Rydberg series	77
2.4 Mixing Processes in the Barium 5p spectrum	93
2.5 Summary	97
CHAPTER 3: EXPERIMENTAL APPARATUS	101
3.1 Introduction	101
3.2 Introduction to the Experimental apparatus	101

3.3	The Pulsed Vacuum Ultra Violet Continuum Source	109
	3.3.1 Continuum sources in the vacuum ultra violet	110
	3.3.1.1 The Hopfield Continua	111
	3.3.1.2 The Synchrotron	112
	3.3.1.3 The BRV Source	113
	3.3.1.4 The Laser Produced Plasma: a review	115
	3.3.2 Properties of the Experimental Continuum	120
	3.3.2.1 Ruby Laser	120
	3.3.2.2 Target purity	121
	3.3.2.3 Source size	121
	3.3.2.4 Target orientation	121
	3.3.2.5 Target debris	122
	3.3.2.6 Temporal characteristics	122
	3.3.2.7 Source brightness	124
3.4	The Dye Laser System	129
	3.4.1 Introduction	129
	3.4.2 Reasons for using this type of laser	134
	3.4.3 The Broad Band Pump Co-Axial Dye Laser	138
	3.4.4 The Tuned Oscillator	142
	3.4.5 Oscillator alignment procedure	145
	3.4.6 The Passive Amplifier	147
	3.4.7 The overall performance of the tuned dye laser system	148
	3.4.8 Injection into the furnace	151
3.5	The Vacuum Ultra Violet Optical Arrangement	152
	3.5.1 Factors involved in the Optical Design	152
	3.5.2 Description of the Optical Arrangement	158
3.6	The Vacuum System	162
	3.6.1 Description of the Vacuum System	162
	3.6.2 Rapid build up of nitrogen and oxygen when pumping is stopped	165
3.7	The Furnace	167
CHAPTER 4:	EXPERIMENTAL PROCEDURE	176
4.1	Introduction	176
4.2	4.2.1 Synchronisation of the Dye laser and the Continuum Source	176

4.2.2 Description of the elements of of figure 4D1 178

4.3 Experimental Operation 180

4.4 Preparation of line list 187

CHAPTER 5: RESULTS AND DISCUSSION 193

5.1 Introduction 193

5.2 Results 194

5.2.1 Atlas of the "Resolved" Absorption Lines of Barium vapour lying between 830Å and 550Å after optical excitation by a high power dye laser tuned to the resonance line at 5535.48Å. 194

5.2.2 Commentary on the Photographic Spectra and Microdensitometer Traces 246

5.2.3 The Line List 250

5.3 Discussion 251

5.3.1 Barium level populations following laser excitation on the resonance line at 5535.48Å 251

5.3.2 Comparison of experimental spectra with theoretical calculations 261

5.3.3 Possible molecular features in the excited state spectrum at wavelengths above 690Å 278

CHAPTER 6: CONCLUSIONS AND SUGGESTIONS FOR FURTHER WORK 285

6.1 Conclusions 285

6.2 Further work 288

APPENDIX 1 List of Possible Transition Manifolds of the upper states corresponding to the 5p absorption spectra from the metastable $6s5d\ ^{3,1}D_{1,2,3}$ levels 297

APPENDIX 2 The Optimum Optical Arrangement for the Osmium Coated Condenser Mirror 300

APPENDIX 3 Summary of Pipe Conductances in the Molecular Regieme 316

APPENDIX 4 Preparation of a line list from optical comparitor measurements 317

APPENDIX 5 Derivation of the time t_o taken for the stimulated rate to equal the spontaneous rate for the transitions $6s6p\ ^1P_1 - 6s5d\ ^3D_2$ and $^1D_2$ 321

APPENDIX 6 Identification of the main limitations of the apparatus and suggested improvements 324

APPENDIX 7 Novel focussing arrangement for improving the "useful" power output of the plasma continuum source 330

REFERENCES 333

ILLUSTRATIVE MATERIAL

Photographs

	page
FIGURE 1P1: BARIUM 5P ABSORPTION SPECTRUM SHOWING ITS ORDERING INTO RYDBERG SERIES	33
FIGURE 3P1: THE EXPERIMENTAL APPARATUS (PLAN VIEW)	105
FIGURE 3P2: THE EXPERIMENTAL APPARATUS (SIDE VIEW)	107
FIGURE 3P3: THE SAMARIUM TARGET IN ITS HOLDER	123
FIGURE 3P4: THE EMISSION SPECTRUM OF THE SAMARIUM LASER GENERATED PLASMA	127
FIGURE 3P5: THE TUNED OSCILLATOR (PLAN VIEW)	131
FIGURE 3P6: THE DYE LASER SYSTEM	135
FIGURE 3P7: OSCILLOSCOPE TRACE OF CO-AXIAL DYE LASER PULSE	143
FIGURE 3P8: A TYPICAL FABRY PEROT INTERFEROGRAM OF THE TUNED DYE LASER SYSTEM OUTPUT	150
FIGURE 3P9: THE FURNACE	169
FIGURE 4P1(i) & (ii): OSCILLOSCOPE TRACES SHOWING THE DELAY BETWEEN THE RISING EDGE OF THE DYE LASER PULSE AND THE PEAK OF THE RUBY LASER PULSE FOR (i) 60 [NS] DELAY AND (ii) 250 [NS] DELAY	181
FIGURE 5P1: BARIUM 5P SPECTRA	195
FIGURE 5P2a: IMAGE ENHANCEMENT OF THE BARIUM 5P SPECTRA BETWEEN 503Å AND 643Å	199
FIGURE 5P2b: IMAGE ENHANCEMENT OF THE BARIUM 5P SPECTRA BETWEEN 562Å AND 698Å	201
FIGURE 5P2c: IMAGE ENHANCEMENT OF THE BARIUM 5P SPECTRA BETWEEN 668Å AND 793Å	203
FIGURE 5P2d: IMAGE ENHANCEMENT OF THE BARIUM 5P SPECTRA BETWEEN 726Å AND 850Å	205

Other figures

	page
FIGURE 1D1: BARIUM EFFECTIVE POTENTIAL FOR F ELECTRONS	27
FIGURE 1D2: HANSEN'S TWO STEP AUTOIONISATION MODEL FOR BARIUM	37
FIGURE 1D3: SIMPLIFIED TERM DIAGRAM OF BARIUM 1	41
FIGURE 2D1: BARIUM EFFECTIVE POTENTIAL FOR F ELECTRONS	54
FIGURE 2D2: ONE DIMENSIONAL SQUARE WELL POTENTIAL	56
FIGURE 2D3: "TUNNELLING" OF THE 4f ELECTRON IN BARIUM	59
FIGURE 2D4: BARIUM EFFECTIVE POTENTIAL FOR 5d ELECTRONS	60
FIGURE 2D5: HANSEN'S TWO STEP AUTOIONISATION MODEL FOR Ba	65
FIGURE 2D6: ENERGY LEVEL DIAGRAM FOR TWO NON-INTERACTING RYDBERG SERIES (AFTER WYNNE ET AL, 1979)	84
FIGURE 2D7: TYPICAL $-\nu_1$ (MODE 1) VRS ν_2 PLOT FOR A SPECTRUM CONTAINING TWO NON-INTERACTING RYDBERG SERIES	86
FIGURE 2D8: TYPICAL LU-FANO PLOT FOR A SPECTRUM CONTAINING TWO NON-INTERACTING RYDBERG SERIES	88
FIGURE 2D9: EFFECT ON A LU-FANO PLOT OF VARYING AMOUNTS OF INTERACTION BETWEEN IWO SERIES	88
FIGURE 2D10: REPRODUCTION OF THE LU-FANO PLOT FOR THE ARGON 3P ABSORPTION SPECTRUM (AFTER LU ET AL, 1970)	90
FIGURE 2D11a: LU-FANO PLOT FROM THE BARIUM 5P SPECTRUM, "d" SERIES VRS. "b" SERIES (AFTER CONNERADE ET AL, 1979a)	92
FIGURE 2D11b: LU-FANO PLOT FROM THE BARIUM 5P SPECTRUM, "k" SERIES VRS. POSSIBLE PERTURBERS (AFTER CONNERADE ET AL, 1979a)	92
FIGURE 3D1: THE OVERALL EXPERIMENTAL LAYOUT	103
FIGURE 3D2: SAMARIUM TARGET ORIENTATION W.R.T. RUBY LASER AND FURNACE AXES	123

FIGURE 3D3: MICRODENSITOMETER TRACE OF SAMARIUM CONTINUUM EMISSION BETWEEN 489.3Å AND 878.3Å 126

FIGURE 3D4: SCHEMATIC DIAGRAM OF THE DYE LASER SYSTEM 133

FIGURE 3D5: THE CO-AXIAL DYE LASER ELECTRICAL CIRCUIT 141

FIGURE 3D6: THE TUNED OSCILLATOR CAVITY 143

FIGURE 3D7: SCHEMATIC LAYOUT OF THE VUV CONTINUUM OPTICS 159

FIGURE 3D8(i) & (ii): SCHEMATIC DIAGRAMS OF TWO CONFIGURATIONS FOR FOCUSSING THE SOURCE ONTO THE SPECTROGRAPH SLIT VIA THE FURNACE 301

FIGURE 3D9: IMAGE ABBERATIONS AT THE SPECTROGRAPH SLIT DUE TO THE CONDENSER MIRROR 312

FIGURE 3D10: IMAGE ABBERATIONS AT THE SPECTROGRAPH FILM PLANE (600Å) DUE TO THE GRATING ONLY 314

FIGURE 3D11: IMAGE ABBERATIONS AT THE SPECTROGRAPH FILM PLANE (600A) DUE TO BOTH THE CONDENSER MIRROR AND THE GRATING 315

FIGURE 3D12: THE VACUUM SYSTEM LAYOUT 163

FIGURE 3D13: SCHEMATIC DIAGRAM OF FURNACE SECTIONED ALONG ITS OPTICAL AXIS IN THE HORIZONTAL PLANE 171

FIGURE 3D14: THE DYNAMIC CONTAINMENT SYSTEM 173

FIGURE 4D1: SYNCHRONISATION CIRCUIT FOR CONTROLLING THE RELATIVE DELAY BETWEEN THE RUBY LASER AND THE DYE LASER 177

FIGURE 4D2: TIME HISTORY DIAGRAM OF THE EVENTS LEADING TO THE FIRING OF THE TWO LASER SYSTEMS 179

FIGURE 5D1a: MICRODENSITOMETER TRACE OF THE 5P ABSORPTION SPECTRUM BETWEEN 497Å AND 859Å OF UNEXCITED BARIUM 208

FIGURE 5D1b: MICRODENSITOMETER TRACE OF THE 5P ABSORPTION SPECTRUM BETWEEN 497Å AND 859Å OF THE 6s5d $^{3,1}D_2$ EXCITED LEVELS OF BARIUM 209

FIGURES 5D2a(i) to (xiii): A set of overlapping microdensitometer traces of the 5p absorption spectrum of unexcited Barium, each covering a 40Å wavelength range as indicated below: -

FIGURE 5D2a(i) : Spectrum from 497Å to 537Å 210
FIGURE 5D2a(ii) : Spectrum from 520Å to 560Å 212
FIGURE 5D2a(iii) : Spectrum from 548Å to 588Å 214
FIGURE 5D2a(iv) : Spectrum from 576Å to 616Å 216
FIGURE 5D2a(v) : Spectrum from 604Å to 644Å 218
FIGURE 5D2a(vi) : Spectrum from 632Å to 672Å 220
FIGURE 5D2a(vii) : Spectrum from 660Å to 700Å 222
FIGURE 5D2a(viii): Spectrum from 688Å to 728Å 224
FIGURE 5D2a(ix) : Spectrum from 716Å to 756Å 226
FIGURE 5D2a(x) : Spectrum from 744Å to 784Å 228
FIGURE 5D2a(xi) : Spectrum from 772Å to 812Å 230
FIGURE 5D2a(xii) : Spectrum from 800Å to 840Å 232
FIGURE 5D2a(xiii): Spectrum from 819Å to 859Å 234

FIGURES 5D2b(i) to (xiii): A set of overlapping microdensitometer traces of the 5p absorption spectrum of Barium in the $6s5d\ ^{3,1}D_2$ excited levels, each covering a 40Å wavelength range as indicated below: -

FIGURE 5D2b(i) : Spectrum from 497Å to 537Å 211
FIGURE 5D2b(ii) : Spectrum from 520Å to 560Å 213
FIGURE 5D2b(iii) : Spectrum from 548Å to 588Å 215
FIGURE 5D2b(iv) : Spectrum from 576Å to 616Å 217
FIGURE 5D2b(v) : Spectrum from 604Å to 644Å 219
FIGURE 5D2b(vi) : Spectrum from 632Å to 672Å 221
FIGURE 5D2b(vii) : Spectrum from 660Å to 700Å 223
FIGURE 5D2b(viii): Spectrum from 688Å to 728Å 225
FIGURE 5D2b(ix) : Spectrum from 716Å to 756Å 227
FIGURE 5D2b(x) : Spectrum from 744Å to 784Å 229
FIGURE 5D2b(xi) : Spectrum from 772Å to 812Å 231
FIGURE 5D2b(xii) : Spectrum from 800Å to 840Å 233
FIGURE 5D2b(xiii): Spectrum from 819Å to 859Å 235

FIGURE 5D3: STICK DIAGRAM REPRESENTING THE CALCULATED (COWAN CODE) PHOTO-ABSORPTION LINES CORRESPONDING TO THE EXCITATION SCHEME $6s5d\ ^3D_2 \longrightarrow 5p^5(5d6s^2 x 5d^2 6s x 5d^3)$ 266

FIGURE 5D4: STICK DIAGRAM REPRESENTING THE CALCULATED (COWAN CODE) PHOTO-ABSORPTION LINES CORRESPONDING TO THE EXCITATION SCHEME $6s5d\ ^1D_2 \longrightarrow 5p^5(5d6s^2 x 5d^2 6s x 5d^3)$ 267

FIGURE 6D1: SCHEMATIC ARRANGEMENT FOR LENGTHENING A LINEARLY POLARISED LASER PULSE 291

FIGURE 6D2: SIMPLIFIED PARTIAL TERM DIAGRAM FOR YTTERBIUM I 295

LIST OF TABLES

page

TABLE 1: Average radius <r> of 6s and 5d wavefunctions for the configurations $5p^6 6s^2$, $5p^6 6s5d$, $5p^5 6s^2$ and $5p^5 6s5d$ of Ba and Ba^+ 62

TABLE 2: Line list of resolved VUV features between 844.6Å and 549.9Å of laser excited Barium corresponding to excitations from the levels $6s5d\ ^1D_2$, $^3D_2$ and $6s^2\ ^1S_0$ 236

TABLE 3: Theoretical (Cowan Code) 5p transitions above 680Å from the $6s^2\ ^1S_0$ level of Barium to levels built on the mixed manifold $5p^5(5d6s^2 x 5d^2 6s x 5d^3)$ compared with observation 268

TABLE 4: Theoretical (Cowan Code) 5p transitions above 690Å from the $6s5d\ ^3D_2$ level of Barium to levels built on the mixed manifold $5p^5(5d6s^2 x 5d^2 6s x 5d^3)$ 271

TABLE 5: Theoretical (Cowan Code) 5p transitions above 690Å from the $6s5d\ ^1D_2$ level of Barium to levels built on the mixed manifold $5p^5(5d6s^2 x 5d^2 6s x 5d^3)$ 272

ACKNOWLEDGEMENTS

I would like to thank my supervisor , Dr Anne Thorne for her assistance over the period of this work. I would especially like to thank her for obtaining a SERC grant extension to replace time lost through illness, and for her constant support and encouragement during the writing of this thesis.

I am greatly indebted to Dr Jean Connerade for many invaluable discussions on the theoretical aspects of the work. I am also especially grateful to Dr Connerade for bringing to my attention the "Dynamic Containment System" described in this thesis, without which no results could have been achieved.

I would also like to recognise the valuable contribution by Mrs Gillian Nave who traced my spectra on a digital microdensitometer, and for putting at my disposal the computer codes with which I generated the microdensitometer traces given in this thesis.

Special thanks are due to the members of the spectroscopy group's technical staff and in particular, Peter Ruthven who in the last weeks of the experimental work constructed many small items for my apparatus. Credit must also go to Morris Pym of the student workshop for his guidance during the

months that I was fabricating components for my apparatus.

For reasons of space it is not possible to mention by name all the other numerous people who assisted me, but I would still like to mention Dr Michael Crisp for providing me with a ray tracing programme, David Yarwood (now deceased) for his glass blowing, Miss Judith Preston for typing my manuscript and finally Dr Keith Burnett (my present employer) for his understanding during the writing of this thesis.

CHAPTER 1 THE INTRODUCTION

1.1. The Interest in Atomic Inner Shells

A good starting point for understanding the spectra of complex atoms is provided by the Independent Particle Model. This model replaces the pairwise electrostatic interactions between different electrons by an effective field $V(\underline{r})$. Such a field is of course an approximation but it greatly simplifies the analysis of complex atoms, since each electron is now viewed as moving in this field independently of the others. Both the "Hartree Fock" and the relativistically correct and therefore more exact "Dirac Fock" Models are good examples of the Independent Particle Model. The effective field in these models contain contributions from both the coulombic field of the nucleus and the field due to the average charge density of the electrons, the latter being deduced self-consistently. These models are useful since to a good approximation the excitation of one electron may be considered as being independent of the others. The other electrons act as spectators to the excitation and their eigenstates are relatively unchanged by it. Of course there will be changes in the $V(\underline{r})$ observed by these spectators but the model will remain valid provided the resulting perturbation to their eigenstate is small. This is indeed the case for both the excitation of valence electrons and X-ray

excitation of electrons from very low lying shells. In the valence electron case the model is valid because their wavefunctions are located predominantly outside the electron core. They therefore contribute little to the $V(\underline{r})$ observed by the spectator electrons, and the perturbation to this field when the valence electrons are excited to higher levels will be small. The validity of the Independent Particle Model for X-ray excitation is accounted for by the nuclear component. The subshells involved in X-ray excitations lie very close to the nucleus and so screen it very effectively. The effect of exciting one of these electrons is to increase the nuclear charge perceived by higher lying electrons. This results in changing the scaling but not the overall form of spectator electron's effective field. In the case of intermediate inner shells there is some doubt regarding the validity of the Independent Particle Model because the changes in the effective field are neither small nor dominated by the nuclear component.

The interest in inner shell spectra of atoms lies therefore in the importance of many body effects in their interpretation. Many Body Theory attempts to account for these effects by providing a better description of electron correlation effects than is achieved by the ultimately crude effective field approximation. For example this approximation

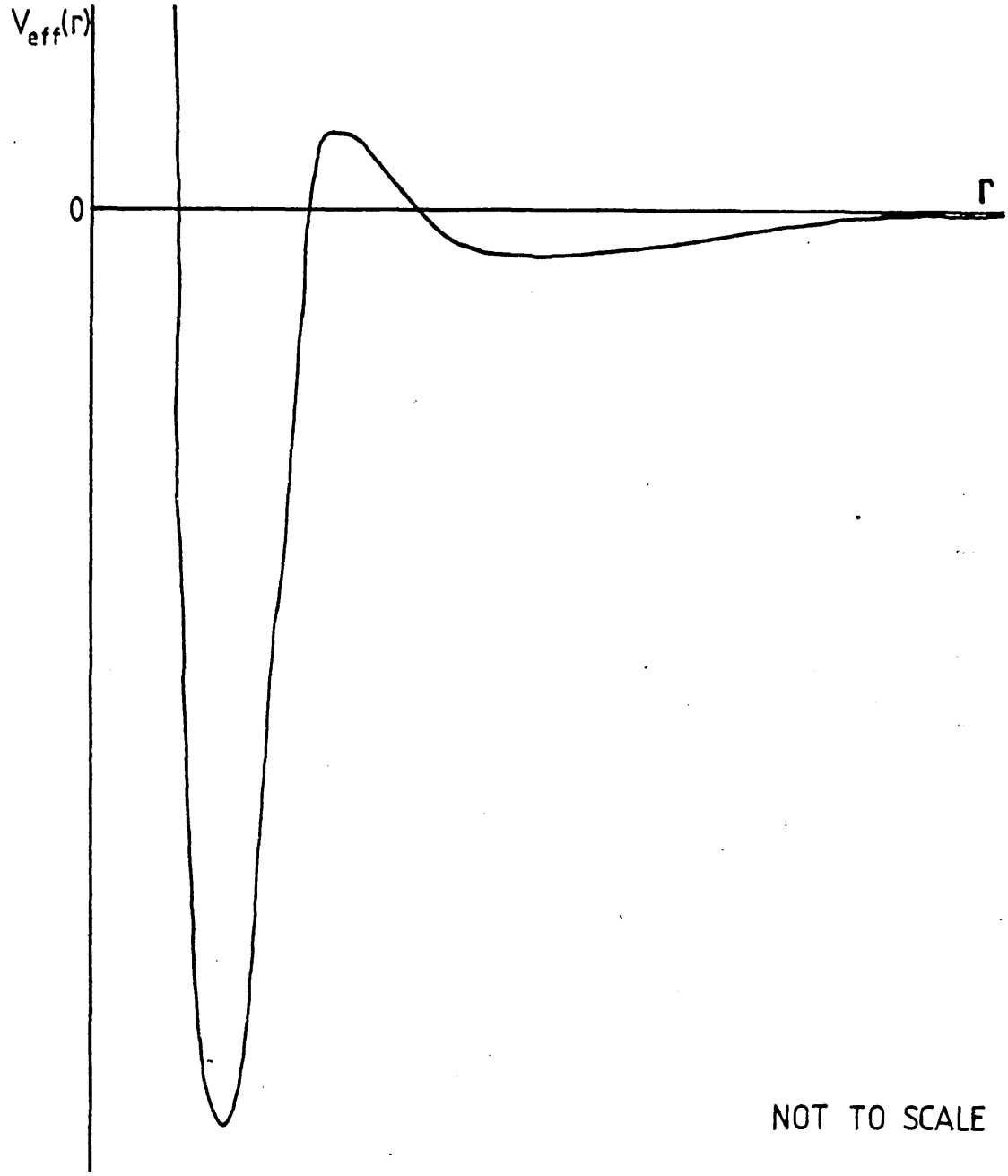
takes no account of the effect that an electron will polarize the region around it. This polarization is represented by a decrease in the charge density probability in its immediate vicinity, as represented by the eigenstates describing all the other electrons. Of the several possible approaches to Many Body Theory, the most complete according to Connerade (Review Article 1978) with regard to photoionization cross sections has been the M.B.P.T. (Many Body Perturbation Theory) of Kelly (1975), and the R.P.A.E. (Random Phase Approximation with Exchange) method of Amusia (1974). The MBPT and RPAE methods may essentially be considered as different forms of Diagramatic Perturbation Theory (i.e. using Feynmann Diagrams) applied to the calculation of higher order "polarization" terms than are included in the Hartree Fock model. Both approaches use Hartree Fock solutions as the initial zero order basis states. Diagramatic Perturbation Theory is discussed by Kelly (1975) and the difference between MBPT and RPAE can be summarized as follows: MBPT sums all possible perturbation diagrams up to a given order of approximation. RPAE by comparison takes into account certain classes of diagram representing the polarization of the electron medium and sums them to infinity. The argument for the RPAE approach is that certain classes of perturbation give rise to strong couplings and should be summed to infinity (Wendin 1974). In the words of Connerade both of these

approaches are incomplete, but each one represents a significant improvement over the "independent Particle Model" (That is they take into account effects not described by the IPM). These theories are extremely complex and the key question which arises is whether such theories are necessary for the interpretation of inner shell spectra.

1.2 The Interest of Barium for Inner Shell Studies

The effective potentials observed by f electrons are interesting because of their double well character, see Figure 1D1 below. One characteristic of such a potential is the tendency for the f eigenstate to be localized in one of the two valleys. Small changes in the potential barrier separating the two valleys leads to the possibility of an abrupt transfer of the f eigenstate from one valley to the other. Barium occupies a crucial position in the periodic table with regard to the phenomena. The 4f eigenstate of the 6s4f excited state of Barium (z=56) is localized in the outer valley. The 4f eigenstate of the 6s5d 4f excited state of Lanthanum (z=57) by comparison lies in the inner valley (Connerade Review Article 1978a), and is said to have exhibited "wavefunction collapse". Consequently the 4f eigenstate in Barium will be very sensitive to small changes in the potential barrier described above. For example with the 4d absorption spectrum of Barium, the 4f (and higher

FIGURE 1D1: BARIUM EFFECTIVE POTENTIAL FOR F ELECTRONS



nf states) eigenstate is unbound in the presence of the 4d core vacancy, and the spectrum has no sharp features due to direct photoionization into the εf continuum by the 4d electrons. However, the situation for this particular case is more complicated since the inner valley of the Barium f electron effective potential is capable of supporting one quasi-bound state. This state however lies above the f threshold and can tunnel into the outer valley where it then photoionizes. So this upper quasi-bound state gives rise to a very broad intense resonance which derives its breadth from its short lifetime and is known as "Giant Resonance". The origin for the double valley potential responsible for this "Giant Resonance" is discussed in terms of the Independent Particle Model in Chapter 2.

Calculations of the 4d-εf photoionization cross section of neutral Barium using RPAE predicted a collective oscillation of the entire 4d subshell (Wendin 1973). The physical manifestation of this oscillation, which was rather analagous to an atomic plasmon, was predicted to be a broad ($\sim$51 eV) resonance which was labeled a Giant Resonance and its existence was later confirmed experimentally by Connerade et al (1974). It should be clear from the above text of this subsection that multibody effects are occuring in the 4d absorption spectrum of neutral Barium. However it is important to note

that a qualitative description of the observed spectrum can be generated by more refined independent particle models which are capable of accurately modelling changes in the effective potentials caused by the excitation of the 4d electron.

Wendin's (1973) paper also predicted the presence of a "Giant Resonance" in the 5p absorption spectrum of neutral barium of width ~ 2.4 [eV]. Its origins were according to Wendin (1974) due to couplings between the $(5p;5d)^1P_1$ and the $(6s;np)\ ^1P_1$ excitation channels resulting in a "huge autoionizing resonance which decays into a continuum of excitations from the $6s^2$ subshell". The first experimental results on this spectrum were simultaneously reported by Connerade et al and Ederer et al in 1974.* Ederer et al's spectrum was more limited in scope and extended from only 520Å to 640Å whereas that of Connerade et al covered the entire spectrum from 502Å to 784Å. The spectrum was very complicated in structure and was not dominated by a single Giant Resonance of the type predicted by Wendin. This was very surprising in view of the

*The 5p spectrum of Barium had previously been observed prior to this work by Newsom at Imperial College using a BRV Source in 1970. However the spectrum was never published and these two groups recorded it later using a synchrotron as a background source.

success of Wendin's RPAE calculations on the 4d spectrum of Barium, where the discussion at the beginning of this subsection indicated that the results would be particularly dependent on the theoretical approximations employed. Reasons for the failure of RPAE in this particular case will be returned to later.

The 5p absorption spectrum was also much more complicated than would have been expected from the one electron scheme given below: -

$$5p^6 6s^2 ({}^1S_0) + h\nu_{VUV} \longrightarrow \{5p^5 6s^2 ({}^2P_{1/2,3/2})\}\ ns,nd({}^1P_1) \quad 1$$

This scheme would have been correct if the Spectator Electron Approximation* was valid for the 5p spectrum of Barium and would have led to only five series converging to two core limits. The observed complexity was attributed by Ederer et al to the presence of "many more series involving two electron excitation converging to excited states of BaII".

*The basic Independent Particle Model assumes that the occupancy of subshells by an atoms electrons will remain unchanged except for the electron under excitation. The Spectator Electron Approximation in addition requires that the relative orientations of the electron angular momenta that make up the total angular momentum should be unchanged except for the electron participating in the excitation. This approximation has proved very useful in accounting for the relatively simple 3d spectra of Manganese $3d^5 4s^2\ {}^6S_{5/2}$ (Baig et al 1979) and Chromium $3d^5 4s\ {}^7S_3$ (Connerade et al 1981) despite the partial filling of the 3d subshell. Many more core limits would have occurred if the relative orientations of the unexcited momenta had been scrambled by the excitation of a single 3d electron.

Connerade et al by comparison asserted that the observed spectrum showed "complex structures due to (5dx6s) mixing".

Here (5dx6s) means that the upper states occurring in the 5p spectrum are not due to a pure core configuration of $5p^5 6s^2 [^2P_{1/2,3/2}]$, but are instead composites arising from the mixing between the one electron core configurations $5p^5 6s^2$, $5p^5 6s5d$ and $5p^5 5d^2$ with $[^2P_{1/2,3/2}]$ character. Such mixing is a good example of Configuration Interaction and the 5p spectrum according to Connerade et al is better represented by the notation: –

$$5p^5 6s^2 (^1S_0) + h\nu_{VUV} \longrightarrow \{5p^5 (6s^2 x 6s5d x 5d^2)(^2P_{1/2,3/2})\} ns,nd(^1P_1) \quad 2$$

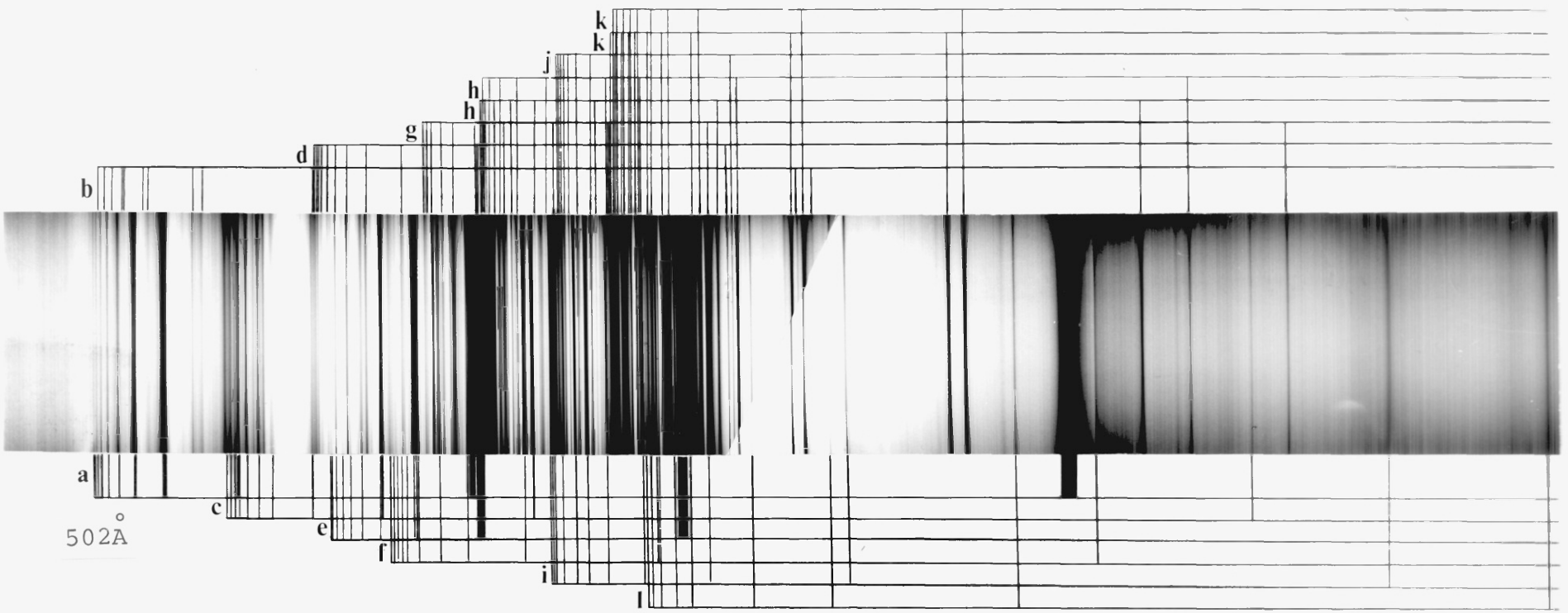
where the manifold $[6s^2 x 6s5d x 5d^2]$ represents the strongly mixed group of upper states described earlier.

This spectrum was later analysed by Connerade et al in 1979a using semi-empirical techniques which will be discussed in Chapter 2. Their analysis identified 14 series converging to 12 limits and a photograph of this spectrum showing this ordering is given in figure 1P1. Subsequent Multi-configurational Dirac Fock calculations by Rose, Grant and Connerade (1980) also predicted the presence of 12 series limits. Their calculations evaluated the mixing coefficients of the manifold

[$6s^2x6s5dx5d^2$] that made up those limits and 6 of the experimentally observed levels were explicitly identified. Later even higher resolution work by Baig et al in 1984 led to the identification of a further 2 series limits not previously observed by Connerade et al (1979a). These authors remarked that the original calculations by Rose et al (1980) did not suggest the presence of the two additional series limits at the observed energies, indicating a "need for an even more complete theoretical approach than the MCDF calculations performed to date".

It is quite clear from figure 1P1 that the barium 5p spectrum in <u>not</u> dominated by a single "Giant Resonance" of the type predicted by Wendin (1973,1974). The same result is also true of Lanthanum (z=57), but not for the other lanthanides (Tracy, 1977). Samarium in particular has an extremely strong resonance of a type reminiscent of Wendin's "Giant Resonance". The absence of the feature in Barium and Lanthanum was attributed by them to the presence of 6s-5d mixing which fragments the $(5p;5d)^1P_1$ Giant Resonance and spreads its character amongst many transitions containing significant 5d character. However if this was the case, then the similarity of the 5p spectra of both Barium (z=56) and Cesium (z=55) is remarkable. This is because the photo double ionization threshold by a single photon lies <u>above</u> the 5p spectrum for Cesium whereas for Barium it lies <u>well below</u>. So

FIGURE 1P1: BARIUM 5P ABSORPTION SPECTRUM SHOWING ITS ORDERING INTO RYDBERG SERIES
(After Connerade et al, 1979a)



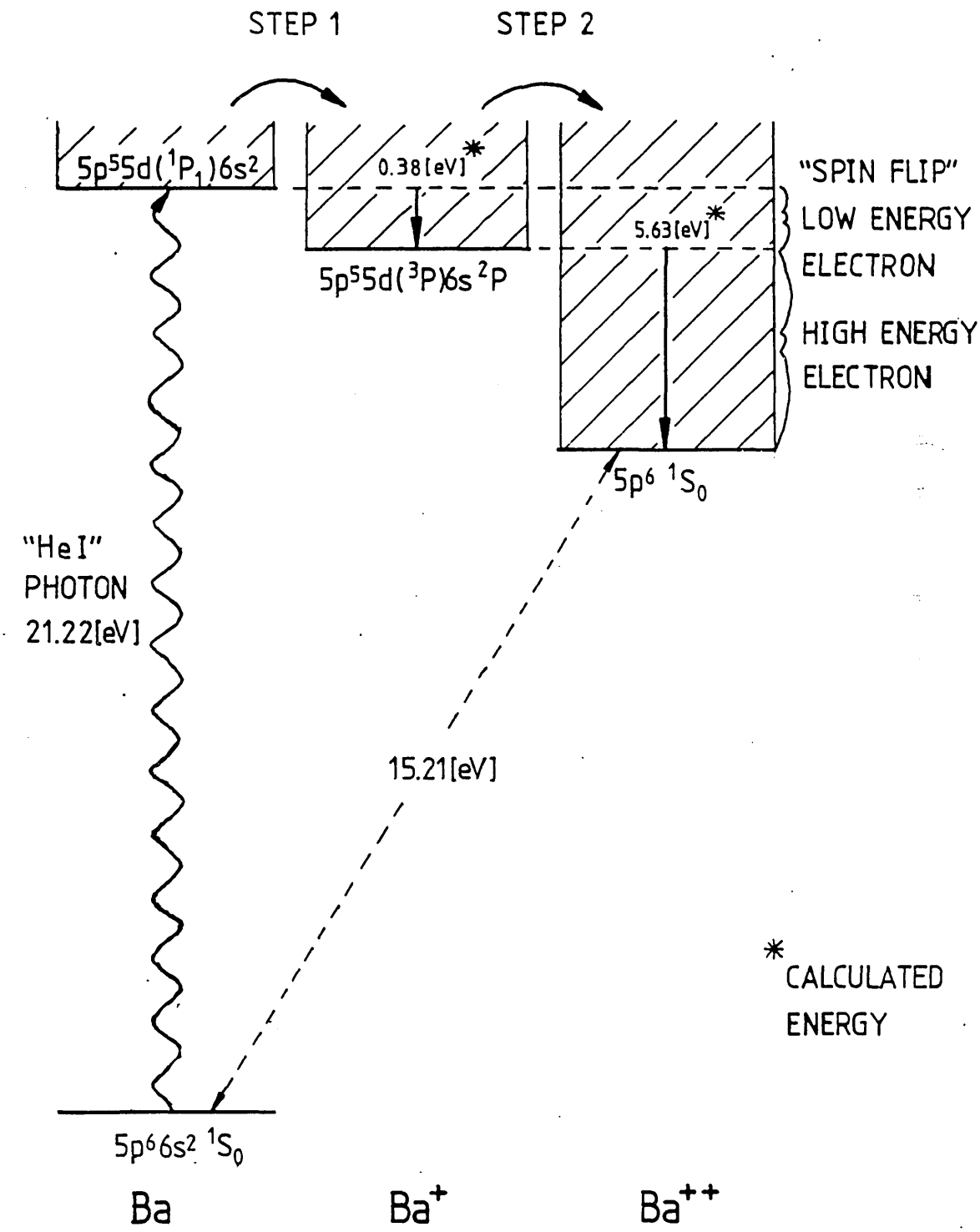
the coupling between the $(5p,nd)^1P_1$ and $(6s,np)^1P_1$ channels discussed by Wendin should have been very different resulting in very different spectra (Connerade (1979b)).

Further interest in the Barium 5p spectrum has been greatly stimulated by the discovery of a double photo-ionization anomaly. Barium was an ideal atom for studying the properties of photo-double ionization since it has the lowest known double ionization limit at 15.215 [eV] (Moore 1958). Hence the resonance lines emitted by both Helium and Neon discharge lamps could be used for this work. In 1974 the relative rates for double and single photoionization in Barium were measured by Brehm and Bucher using both the Helium line at 21.22 [eV] and the Neon lines at 16.67 [eV] and 16.85 [eV]. A Ba^{++}/Ba^{+} ratio of 0.25 was measured with the Neon lines and this was regarded as not unusual. However, they discovered that this ratio suddenly jumped to 2.4 at the 21.22 [eV] Helium line. This result was felt to be very surprising since the Double to Single ionization ratios measured for rare gas atoms using x-ray sources were much smaller. Typically only 17% at most of the atoms were doubly so (Brehm and Hofler, 1975). It should be pointed out that the cross section for simultaneously ejecting two s electrons into the photo-double ionisation continuum must be much smaller than for the ejection of just one s electron into the single photoionization

continuum (Connerade 1985 Private Communication) if the independent particle approximation is to have any validity at all. Brehm and Bucher suggested that the most likely explanation for their results was the ionization of a 5p electron followed by a subsequent Auger Process to yield Ba^{++}.

This totally unexpected Ba^{++}/Ba^{+} ratio for the 21.22 [eV] Helium line attracted the immediate interest of theoreticians in the field. Wendin (1978) interpreted the result as the manifestation of a many body process where two electrons were ejected simultaneously via intermediate non-energy conserving states. This very radical interpretation followed on from an argument by Fano who suggested that a resonance in the 5p shell polarization could lie in this energy region. The correlation effects between electrons in the 5p and 6s subshell could result in the "shattering of the $6s^2$ subshell", i.e. the ejection of two s electrons simultaneously. Such a mechanism would have been characterized by a <u>continuum</u> of energies in the ejected photo-electrons. In fact this result was not subsequently observed. A more convensional one electron scheme was proposed by Hansen in 1975 and is best described by the title, "Two Step Auto-ionization". His model which is represented diagrammatically in figure 1D2 below envisaged the following two step approach.

FIGURE 1D2: HANSEN'S TWO STEP AUTOIONISATION MODEL FOR Ba



Step 1 - Auto-ionization driven by Spin Flip of the core electrons.

$$5p^6 6s^2 ({}^1S_0) + h\nu_{21.22(eV)} \longrightarrow \{5p^5 5d({}^1P_1)\} 6s^2 ({}^1P_1)$$

$$\longrightarrow \{5p^5 5d({}^3P)\} 6s\ ({}^2P) + e^-$$

Step 2 - Auto-ionization driven by an Auger process filling 5p core vacancy.

$$\{5p^5 5d({}^3P)\} 6s({}^2P) \longrightarrow 5p^6 ({}^1S_0) + e^-$$

Such a two step mechanism would be characterized by the ejected photo-electrons having discrete energies and this has subsequently been demonstrated experimentally. Nevertheless the problem as will be seen in Chapter 2 has many facets and its study has given rise to the discovery of new developments.

1.3 Aims of the Present Research

It appears from the work of Connerade et al (1979a) and Rose et al (1980) that the 5p spectrum of Barium can be understood in terms of a multi-configurational model with a finite number of interacting configurations. The observed complexity is understood in terms of 6s-5d mixing and the general form of the structure acounted for using Multi-configurational Dirac Fock Calculations. Many body processes involving more complex diagrams such as those briefly sketched in section 1.2 do not

appear to be important in the case of the Barium 5p spectrum. More recent high resolution work by Baig et al (1984) on the Barium 5p spectrum has revealed two more series which cannot be accounted for by MCDF calculations. Hence the story is by no means closed.

Enough has been said about the spectrum of Barium excited from the ground state to indicate how complex the problems are and how desirable it is to provide independent data, preferably involving different excitation channels terminating on related configurations for a more detailed test of the theory. Probing the 5p spectrum of excited states of Barium would allow MCDF calculations of other levels to be compared with experiment. A level diagram showing the excited states of interest is given in figure 1D3.

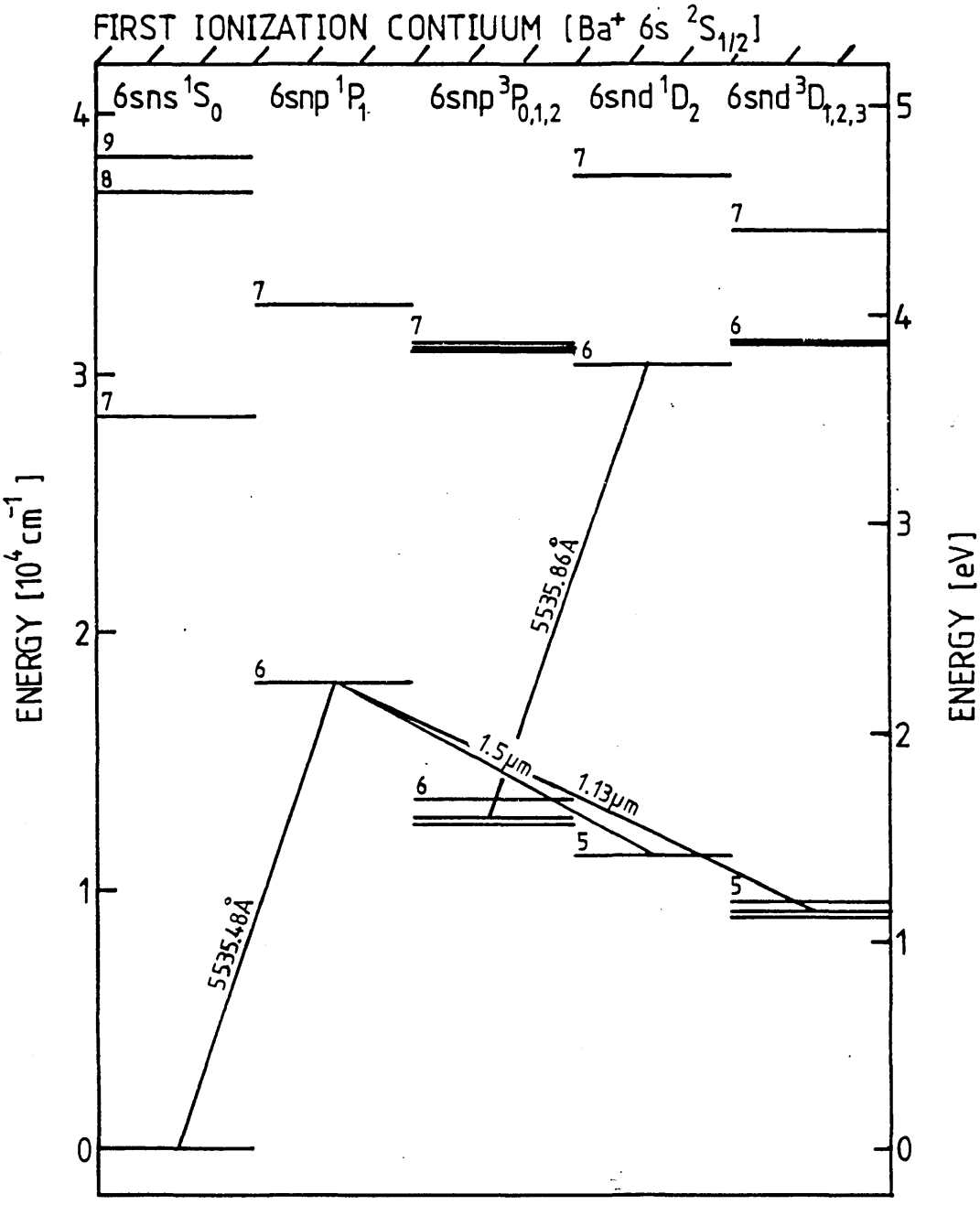
The aim of the present research was to record the respective 5p spectra of the Barium excited states $6s6p\,^1P_1$ and $6s5d\,^{3,1}D_{1,2,3}$. The $6s6p\,^1P_1$ state was to be populated using a dye laser tuned to the $6s^2\,^1S_0$-$6s6p\,^1P_1$ resonance transition at 5535Å. This excited state, if the spectator electron model was valid, would give rise to the following 5p excitation scheme.

$$5p^6 6s6p\ ^1P_1 + h\nu_{VUV} \longrightarrow (5p^5 6s6p)ns,nd \quad J=0,1,2 \qquad 3$$

However, the 5p excitation scheme would probably be more complex due to the presence of 6s-5d mixing and the upper states accessed would probably be better described by the manifold $5p^5[6s6px6p5d]ns,nd$. This spectrum would have been particularly interesting to study since it involves states of opposite parity to those seen in the 5p spectrum of unexcited Barium. An important consequence of this is that the 6s-5d mixing would be totally modified and would be seen with different mixing coefficients in the presence of the 6p electron. Unfortunately it proved impossible to measure this spectrum for reasons which are discussed in Chapter 5.

The $5p^6\ 6s5d\ ^{3,1}D_2$ metastable levels would be populated by radiative decay from the laser populated $6s6p\ ^1P_1$ level described earlier. The most recent calculations of the strength of the $6s6p\ ^1P_1$-$6s5d\ ^3D_2$ spin forbidden transition imply that it is stronger than the $6s6p\ ^1P_1$ - $6s5d\ ^1D_2$ allowed transition (Hafner and Schwartz, 1978). However the experimental evidence for this conclusion is contradictory with different workers reporting different results with regard to which transition is strongest (references given by Bowen and Thorne, 1985). Consequently 5p transitions can be expected from the two $6s5d\ ^{3,1}D_2$ metastable states to upper levels with J = 1, 2 and 3. In addition transitions to upper levels with J = 0 and 4 should also in principle be observable because of

FIGURE 1D3: SIMPLIFIED TERM DIAGRAM OF BARIUM 1



collisional population of the 6s5d $^3D_{1,3}$ metastable states. It is therefore reasonable to expect that the 5p spectrum from $^{3,1}D_{1,2,3}$ metastable states will be extremely complex with many series being observed converging to the core configurations below: —

$5p^5(6s5dx6s^2x5d^2)$ $[^2P_{1/2,3/2}]$
$5p^5(6s5dx5d^2)$ $[^2D_{3/2,5/2}]$
$5p^5(6s5dx5d^2)$ $[^2F_{5/2,7/2}]$
$5p^5(6s5dx5d^2)$ $[^4P_{1/2,3/2,5/2}]$
$5p^5(6s5dx5d^2)$ $[^4D_{1/2,3/2,5/2,7/2}]$
$5p^5(6s5dx5d^2)$ $[^4F_{3/2,5/2,7/2,9/2}]$

The above core configurations anticipate the presence of 6s5d mixing (where allowed) but the mixing coefficients will be different from those observed in the $6s^2\ ^1S_0$ spectrum.

1.4.1 Experimental Method

It is necessary for reasons explained in Chapter 3 that a pulsed high power dye laser should be used to populate the desired excited states. This method however has risks in that high degrees of laser induced ionization can be observed when optically pumping high vapour pressures of Alkali and Alkaline Earths on their resonance line with a high power laser (>1MW/cm^2). This was first discovered by Lucatorto and McIlrath (1976) when they observed almost complete ionization in sodium. Skinner (1980) observed up to 56% ionization in the alkaline

earths at densities above 10^{20} [m^{-3}] and this phenomenum has also been studied in Barium by Bachor et al (1981), Kunnemeyer et al (1983) and Jahreiss et al (1983). The mechanism for this ionization process and the reasons why it was not expected to be important in this experiment will be discussed in the next subsection.

A pulsed VUV continuum source emitting over the spectral range $\sim$ 500Å-800Å is required for this experiment because of the transient lifetimes of the excited states being probed in this experiment. The 6s6p $^1P_1$ level decays to the ground state by spontaneous emission with a lifetime of $\sim$ 8.4 [ns] and is therefore essentially only populated during the pump laser pulse ($\sim$100 [ns] FWHM). The 6s5d $^{3,1}D_{1,2,3}$ metastable states are much longer lived and decay to the ground state by collisional de-excitation. Their lifetime is therefore determined by the Barium number density in the absence of buffer gas (assuming no free electrons) and the lifetime for example of the 6s5d $^1D_2$ level at a number density of 10^{21} [m^{-3}] will be of the order of 370 [ns] (based on the quenching cross section data of Bowen and Thorne 1985). The study of the 6s6p $^1P_1$ spectrum therefore required a bright VUV continuum source which could be synchronized within the pump laser's temporal envelope. The best source for this role as will be seen in Chapter 3 was the laser generated plasma formed by focussing

the output of a Q switched laser onto a metal target (samarium). The 5p absorption spectrum was recorded photographically using a 1 metre spectrograph.

1.4.2. Laser Induced Ionization of Barium

It is necessary to understand the ionization mechanism's for Alkali Earth metal vapours by high power dye lasers in order to appreciate why ionization was not expected to occur in this experiment. The first ionization limit of Barium lies 5.210[eV] above the ground state (Lee et al 1977) and therefore the energy of at least three laser photons tuned to the $6s^2\ {}^1S_0$ - $6s6p\ {}^1P_1$ resonance transition (2.2[eV]) are required for ionization. The dominant mechanism for ionization at laser powers of $\sim$ 1 [MW/cm^2] and number densities of the order of 10^{19} - 10^{21} [m^{-3}] is generally believed to be the super elastic electron model proposed by Measures (1977). An electron colliding with an excited $6s6p\ {}^1P_1$ Barium atom may de-excite it and so emerge with a kinetic energy 2.2 [eV] in excess of its thermal energy. This energetic electron can then excite a second $6s6p\ {}^1P_1$ atom to higher energy level from which it can be ionized by either a second electron collision or by photo-ionization by the laser. A basic requirement for this model to be valid is the formation of seed electrons by some other process such as two-photon ionization from the resonance or metastable states. Bachor and Kock (1981) have

argued that resonant two photon ionization from the Barium 6s6p $^3P_1$ level, which is collisionally populated from the 6s6p $^1P_1$ level is possible, and may be more important in the formation of such seed electrons than say collisional processes involving two excited Barium atoms. This is because the intermediate 6s6p ^3P - 6s6d ^3P transition is only $\sim$ 0.4Å from resonance with the pump laser wavelength and a moderate bandwidth laser could therefore efficiently drive this process. In any event, all experiments which have achieved high degrees of ionization have used laser pulses of at least 100 ns duration. Bowen and Thorne (1985) observed less than 5% ionization in Barium at high number densities, 10^{19} - 10^{20} [m^{-3}], and high buffer gas pressures, $\sim$ 100 torr of He, using a laser very similar to that used in this experiment. The lack of ionization was attributed to the short duration of their laser pulse $\sim$50 [ns], and its narrow band width $\sim$ 0.025Å. A narrow bandwidth prevents the formation of seed electrons by the mechanism postulated by Bachor and Kock (1981). The short pulse length avoids the superelastic process from having time to build up. Another contributary factor to the lack of ionization may have been the high buffer gas pressure of Bowen et al experiments. Experimental evidence by Stacewicz and Krasinski (1981) indicates that laser induced ionization is attenuated by high buffer gas pressures due to the quenching of the 6s6p $^3P_1$ metastable state by the

buffer gas. However this mechanism was probably unimportant in Bowen et al's work because of the narrow bandwidth of their laser.

So in conclusion it was not anticipated that significant laser induced ionization would occur because of the narrow bandwidth and short duration of the pump dye laser which was similar to that of Bowen et al (1985). This seems to have been the actual case judging from the results of Lucatorto and McIlrath (1980) on the Ba^+ 5p absorption spectrum. None of the lines observed by Lucatorto et al that lay in the spectral range of interest to this experiment were in fact observed.

CHAPTER 2 THEORY

2.1 The Radial Problem - Its importance to contemporary work on atomic structure

Exact solutions to the energy eigenvalue equation describing a multi-electron atom cannot be achieved because of the non-central forces arising from the coulombic interaction between different electrons. The problem is made tractable by the Central Field Approximation where a spherically symmetric mean charge distribution is assumed. Such an approximation is justified on the basis that the static field arising from a spherically symmetric mean charge distribution would be less than any other distribution. In the Central Field Approximation the bulk of the electron-electron repulsion is represented by a central potential $S(\underline{r}_i)$ for each electron i centred at the nucleus. So the effective central potential $U(r_i)$ observed by electron i consists of the sum of the attractive coulombic potential of the nucleus and $S(\underline{r}_i)$. Hence the Hamiltonian for a N-electron atom can be approximated to zero order by: -

$$\hat{H} = -\frac{\hbar^2}{2m}\sum_{i=1}^{N}\nabla_i^2 + \sum_{i=1}^{N}U(r_i) \qquad 1$$

It should be noted that this equation does not include magnetic terms such as the spin orbit effect nor residual electrostatic terms due to the non

central component of the electron-electron electrostatic interaction. Although these terms vary in magnitude they are in most cases small compared to the terms given in equation 1 above and can usually be accounted for using perturbation theory. The energy eigenvalue equation using the Hamiltonian in equation 1 will yield N second order differential equations, one for each electron, which are coupled together via the effective central potential $U(r_i)$. These equations cannot be solved exactly because of this coupling, and Ab-Intio techniques such as the Hartree Fock method must be resorted to. Nevertheless it is still possible to make some general points on the possible solutions $|\Psi\rangle_i$ to the equation $\hat{H}|\Psi\rangle_i = E_i|\Psi\rangle_i$. As in the case of the hydrogen atom the eigenvalue equation is separable into radial and angular components and so consequently the spatial character of $|\Psi\rangle_i$ neglecting spin will be of the form: -

$$|\Psi(n,l,m_l)\rangle_i = {}^iR_{nl}(r)\,{}^iY_l^{m_l}(\Theta,\Phi) \qquad 2$$

The Spherical Harmonics ${}^iY_l^{m_l}(\Theta,\Phi)$ occur because the atomic potential is <u>radial</u> in character. A collorary of this result is that a closed subshell with $\Sigma l=0$ will have a spherically symmetric charge distribution which is consistent with the original Central Field Approximation. The most significant aspect of the spherical harmonics is that they can be <u>solved once and for all</u> and the solution is the

same for all central field atoms. The Radial Functions $^{i}R_{nl}(r)$ are by comparison unique to a given atom and must be solved on an atom by atom basis using numerical codes such as the Hartree Fock Code. This is necessary because the Radial part of the eigenvalue equation is explicitly dependent on the effective central potential $U(r_i)$.

Early work on the structure of atomic systems concentrated on achieving a good understanding of the possible angular momentum states of an atomic system and thus of the number of energy levels which could be expected. It should be remembered that the next step after solving the central field is to consider the e^{-}-e^{-} interactions when there is more than one valence electron and that this (electrostatic) interaction energy depends on the relative l, m_l, m_s of the two (or more) electrons and can be expressed by coupling the corresponding angular momenta. Early texts on the subject such as Condon and Shortley's classic of 1935, "The Theory of Atomic Structure", and even for that matter more modern texts, are characterized by a tendency to concentrate on the angular problem. This tendency is perhaps understandable bearing in mind that the angular problem is analytically solvable, easier to present in an elegant self-consistent manner and good for deriving the general properties of groups of atoms. Even so the radial problem was realised to be important at an early stage; for example in

explaining configuration interaction. (This phenomenon was for example briefly discussed by Condon and Shortley's text of 1935). Configuration interaction which was mentioned in Chapter 1, refers to the situation where terms of the same parity but of different electronic configuration are sufficiently close in energy that they mix. For example in Nickel (z=28) the separation of the $3d^8 4s^2\ ^3F$ (the ground state configuration given in the periodic table) and the $3d^9 4s\ ^3D$ terms is much smaller than their individual splittings arising from the spin orbit effect (Woodgate, 1980). So as a result it is no longer reasonable to say that nickel has such and such a ground state configuration implying it is pure. Even the ground state configuration of the Alkaline Earth Barium (z=56), which is normally said to be [Xe core] $6s^2\ ^1S_0$, exhibits configuration interaction. Calculations by Rose, Pyper and Grant (1978) using a Multi-Configurational Dirac Fock code show that the Barium configuration is not pure but is instead a mixture of [Xe core] $6s^2\ ^1S_0$ (92.2%), [Xe core $6p^2\ ^1S_0$] (6.4%), [Xe core] $5d^2\ ^1S_0$ (1.3%) plus much smaller contributions from two $^3P_0$ states. The mixing in the case of Nickel was due to the proximity of the binding energies of the 3d and 4s electrons and these can only be quantified if the radial dependence is known. One effect which can be attributed to configuration interaction in the ground state is the occurrence of multiple

excitations in the absorption spectrum of the system concerned. Consider for example the case of excitation from the ground state of Barium to the excited 6p5d $^1P_1$ state. This is formally a double excitation and its strength should therefore be extremely weak if the Independent Particle Model is valid. However the presence of $6p^2\ ^1S_0$ and $5d^2\ ^1S_0$ contributions in the Barium ground state $|\Psi,Ba_g\rangle$ mean that the process can be driven by mixing as illustrated below.

$$|\Psi,Ba_g\rangle = 0.96|6s^2\ ^1S_0\rangle + 0.253|6p^2\ ^1S_0\rangle + 0.114|5d^2\ ^1S_0\rangle \quad 3$$

Dipole Matrix element $\langle 6p5d\ ^1P_1|e\underline{r}|\Psi,Ba_g\rangle \simeq$

$0.96e\langle 6p5d\ ^1P_1|\underline{r}|6s^2\ ^1S_0\rangle + 0.253e\langle 6p5d\ ^1P_1|\underline{r}|6p^2\ ^1S_0\rangle$

$\simeq$ zero — non zero

$+ 0.114e\langle 6p5d\ ^1P_1|\underline{r}|5d^2\ ^1S_0\rangle \quad 4$

non zero

Configuration Interaction in excited atomic states can likewise give rise to many strong transitions which would formally be described as double excitations. The eventual interpretation of the Barium 5p spectrum was based on these ideas as will be seen later in this chapter.

The lack of fast computers until the 1960's made the radial problem very difficult to work on since real progress could only be made by iterative numerical solutions to the differential equations describing it. Doing this on mechanical desk

calculators proved a good disincentive to such work for most physicists and discouraged the use of complex theories such as the Hartree Fock description of the atom and the development of even more complex theories. The advent of such fast computers combined with improvements to the theory have provided new stimulus to the work. More recent work on the inner shell spectra of some elements has brought to light many interesting and novel effects of which two good examples are "Giant Resonances" and the closely related phenomenon of "Wavefunction Collapse", both of which were briefly mentioned in Chapter 1. Both of these phenomena are explicable in terms of radial wavefunctions and their origin and character will now be described in some detail since they are very relevant to the present work.

The origin of a "Giant Resonance" in the 4d-Ɛf spectrum of Barium was attributed in Chapter 1 to the double well character of the f electrons effective potential. But how does such a double well potential arise in the first place? The answer to this question lies in the kinetic energy terms of the multi-electron atom, $-\frac{\hbar^2}{2m_e}\nabla_i^2$. This term in spherical polar co-ordinates has the form: -

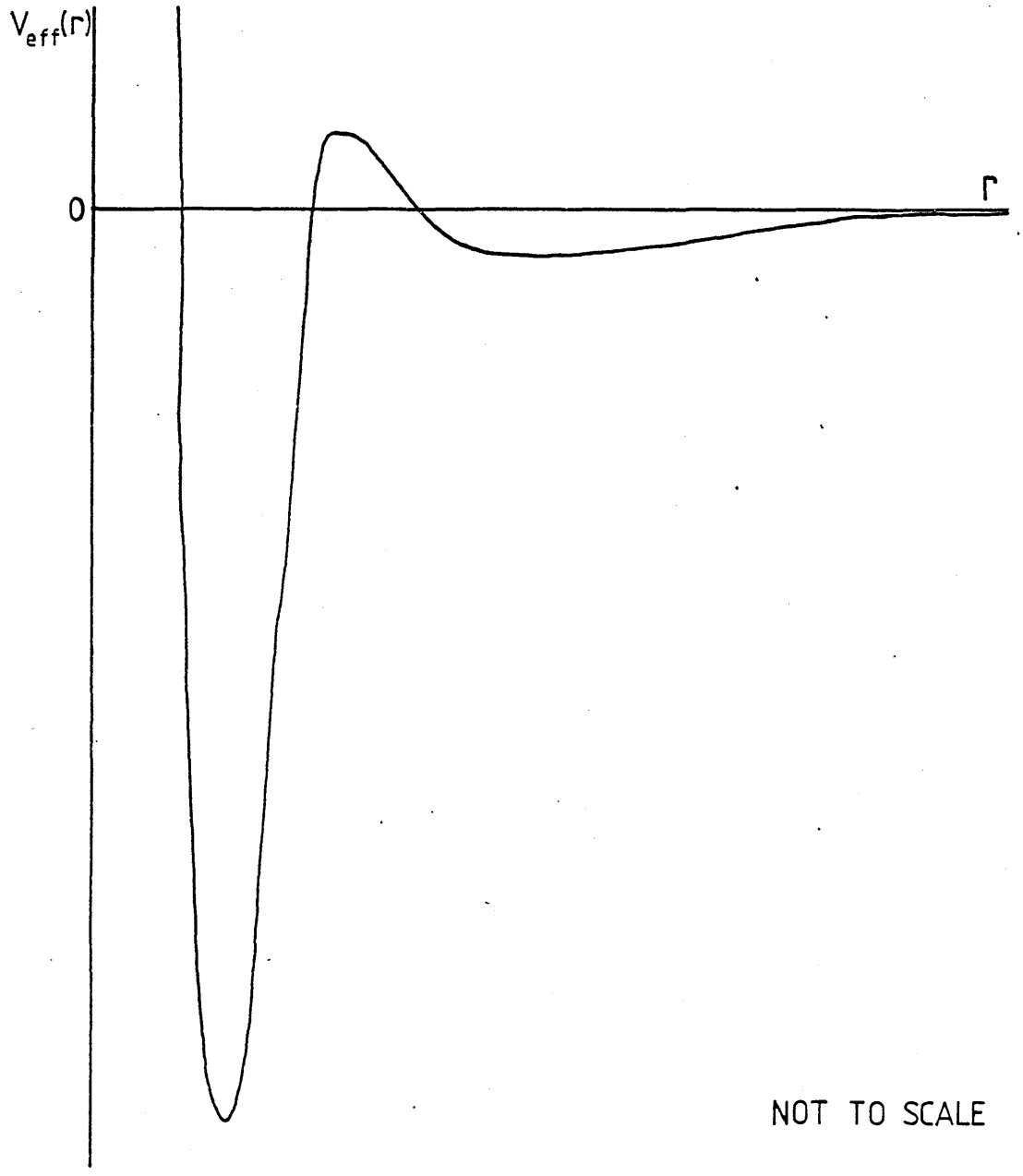
$$-\frac{\hbar^2}{2m_e}\nabla_i^2 = -\frac{\hbar^2}{2m_e}\frac{1}{r_i^2}(\partial/\partial r_i(r_i^2\partial/\partial r_i) + \frac{1}{\sin^2\theta_i}\frac{\partial^2}{\partial\phi_i^2} + \frac{1}{\sin\theta_i}\frac{\partial}{\partial\theta_i}(\sin\theta_i\partial/\partial\theta_i) \quad 5$$

which becomes

$$-\frac{\hbar^2}{2m_e}\nabla_i^2 = -\frac{\hbar^2}{2m_e r_i^2}\left(\partial/\partial r_i\left(r_i^2\partial/\partial r_i\right) - \hat{L}_i^2\right) \qquad 6$$

since the angular terms in the brackets of equation 5 correspond to the total orbital angular momentum squared operator $\hat{L}^2$. It therefore follows that the multi-electron Hamiltonian contains a term of the form $+\frac{\hbar^2}{2m_e r_i^2} l_i(l_i+1)$ (Spherical Harmonics describing one electron orbitals are eigenstates of $\hat{L}^2$). This term is called the centrifugal barrier term since it is the analogue of the centrifugal potential in classical mechanics (Connerade, 1978a). The ocurrence of a double valley effective potential for the f electrons can now be understood in terms of the following model. An f electron at very large r will observe a nucleus heavily screened by the other electrons of the atom. The attractive coulombic potential ($\propto 1/r$) will dominate the repulsive centrifugal potential ($\propto 1/r^2$) at large r and so the f electron will observe a net attractive potential, see figure 2D1. As the electron closes with the nucleus the centrifugal repulsion term will gradually take over giving rise to the potential barrier separating the outer valley from the inner valley. The inner valley occurs because the screening of the nucleus drops sharply as the electron penetrates the atom exposing the electron to a much stronger nuclear field. The final potential barrier close to the nucleus occurs

FIGURE 2D1: BARIUM EFFECTIVE POTENTIAL FOR F ELECTRONS

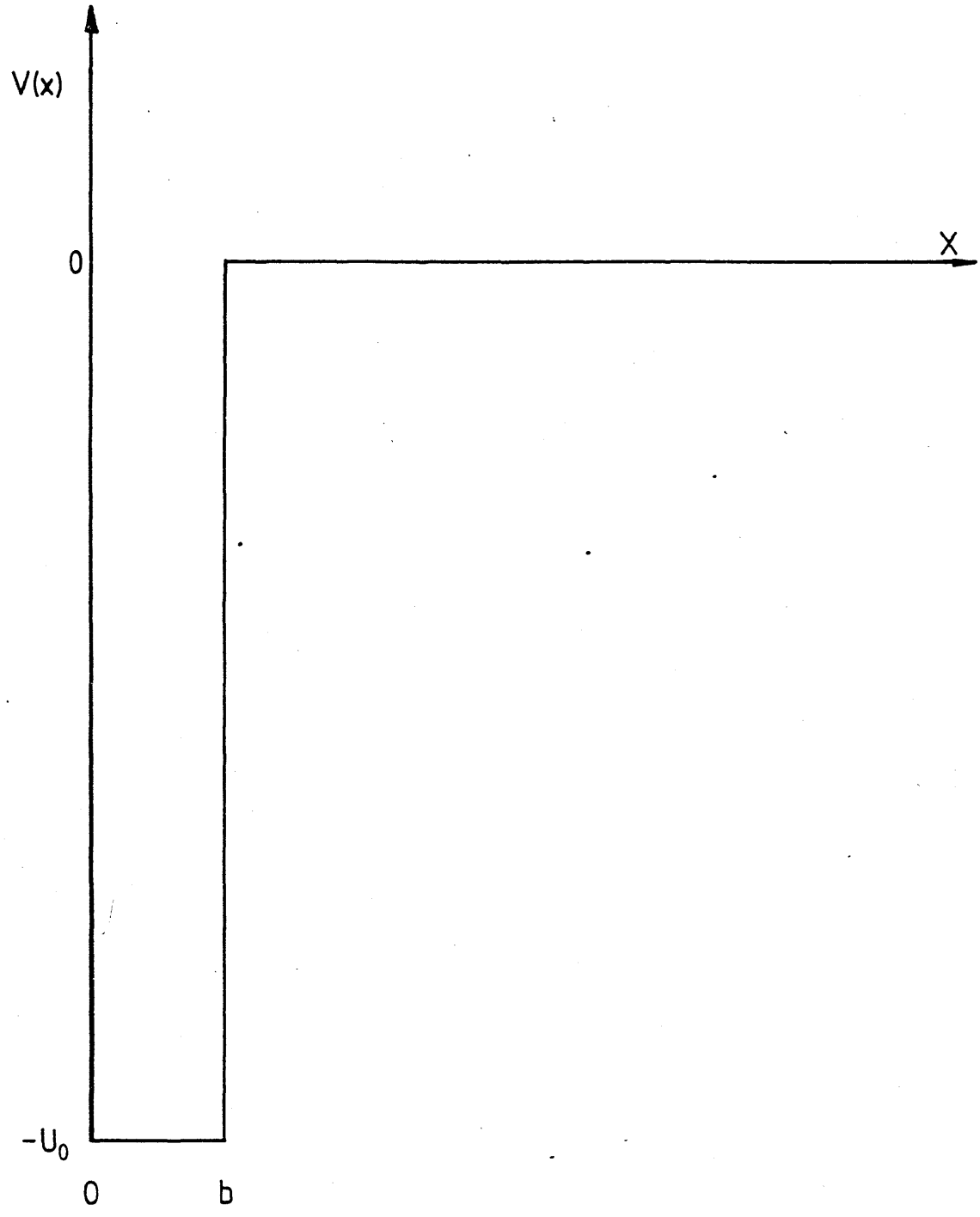


because of the fast increase of the $1/r^2$ term in the centrifugal potential at small r.

The inner well of the double valley potential described above holds the key to understanding the 4d spectra of specific atomic systems. Unlike the coulombic potential the well is short ranged and therefore does not have an infinite number of eigenstates. In fact it is possible for a sufficiently narrow or shallow well to contain just one or even no bound states. This result can be easily demonstrated by considering the possible bound states of the closely analogous one dimensional square well potential with just one infinite and one finite barrier as shown in figure 2D2. This potential well, of width b and depth U_o, is discussed by Kompaneyets (1961) who demonstrates that it has a finite number of eigenstates and that the condition for at least one bound state is that b^2U_o should be greater than $\frac{\pi^2\hbar^2}{8m_e}$.

In chapter 1 it was pointed out that the 4f effective potential of Barium was a border-line case where small changes in the potential barrier separating the two valleys, could result in the collapse of the 4f wavefunction from the outer to the inner valley. The "Wavefunction Collapse" of just the 4f eigenstate in an atomic system results in the 4d-nf excitation channel being dominated by the 4d-4f transition. This occurs because the 4d

FIGURE 2D2: ONE DIMENSIONAL SQUARE WELL POTENTIAL



eigenstate lies close to the nucleus resulting in a large overlap between the 4d wavefunction and the collapsed 4f wavefunction which is not matched by other 4d-nf overlaps. The resulting intense transition is labeled a "Giant Resonance".

It was pointed out in Chapter 1 that the Barium effective potential for f electrons contained no bound states in the outer well in the presence of a 4d core vacancy. Nevertheless there was an intense "Giant Resonance" of extraordinary width observed experimentally, and in terms of the independent particle model this was attributed to the existence of a bound state in the inner well which lies above the 4d-nf ionization energy threshold. Consequently the electron of the inner well is quasi-bound since it can tunnel into the outer well, see figure 2D3, resulting in photoionisation. Note that this ionization process is <u>not</u> the same as autoionisation where a bound state ionises due to interactive couplings with continuum states lying at the same energy since only one state is involved. The upper state responsible for the "Giant Resonance" in Barium is a hybrid in the sense that it has the character of a bound 4f electron in the inner well (implying a large overlap with the 4d eigenstate) and a continuum character in the outer well. This hybrid character is indicated by the notation used by Connerade to describe this transition $4d \longrightarrow \overline{4,\varepsilon}f$. The enormous width of the Barium

Giant Resonance" is attributed to the short lifetime of the quasi-bound state of the inner well due to rapid tunnelling of the electron into the outer well. This explanation implies that the width of the resonance will rapidly decrease as the binding energy of the inner well's bound state drops towards the ε_f threshold, an effect which is indeed seen (Connerade, 1984). This is because the probability of an electron tunnelling into the outer well diminishes with increasing binding energy.

It was stated in Chapter 1 that the complexity of the spectrum of neutral Barium arising from excitation of a 5p electron could be understood in terms of strong 6s-5d mixing in the excited levels. Such pronounced mixing was not observed in the ground state of Barium, and it is now possible as the result of the above discussion to appreciate why mixing might occur only in the presence of a 5p core vacancy. The effective potential of 5d electrons in Barium does <u>not</u> exhibit the double valley structure observed for the 4f electrons since the Centrifugal Barrier term which is proportional to $l_i(l_i+1)$ is now smaller. Nevertheless the Barium 5d effective potential does exhibit an inflection in its shape, see figure 2D4. It consists of a deep valley close to the nucleus which rises to to a shallow plateau at larger r before finally tending to zero at infinity (Connerade, 1983, Private Communication). The potential is therefore

FIGURE 2D3:"TUNNELLING" OF THE 4F ELECTRON IN BARIUM

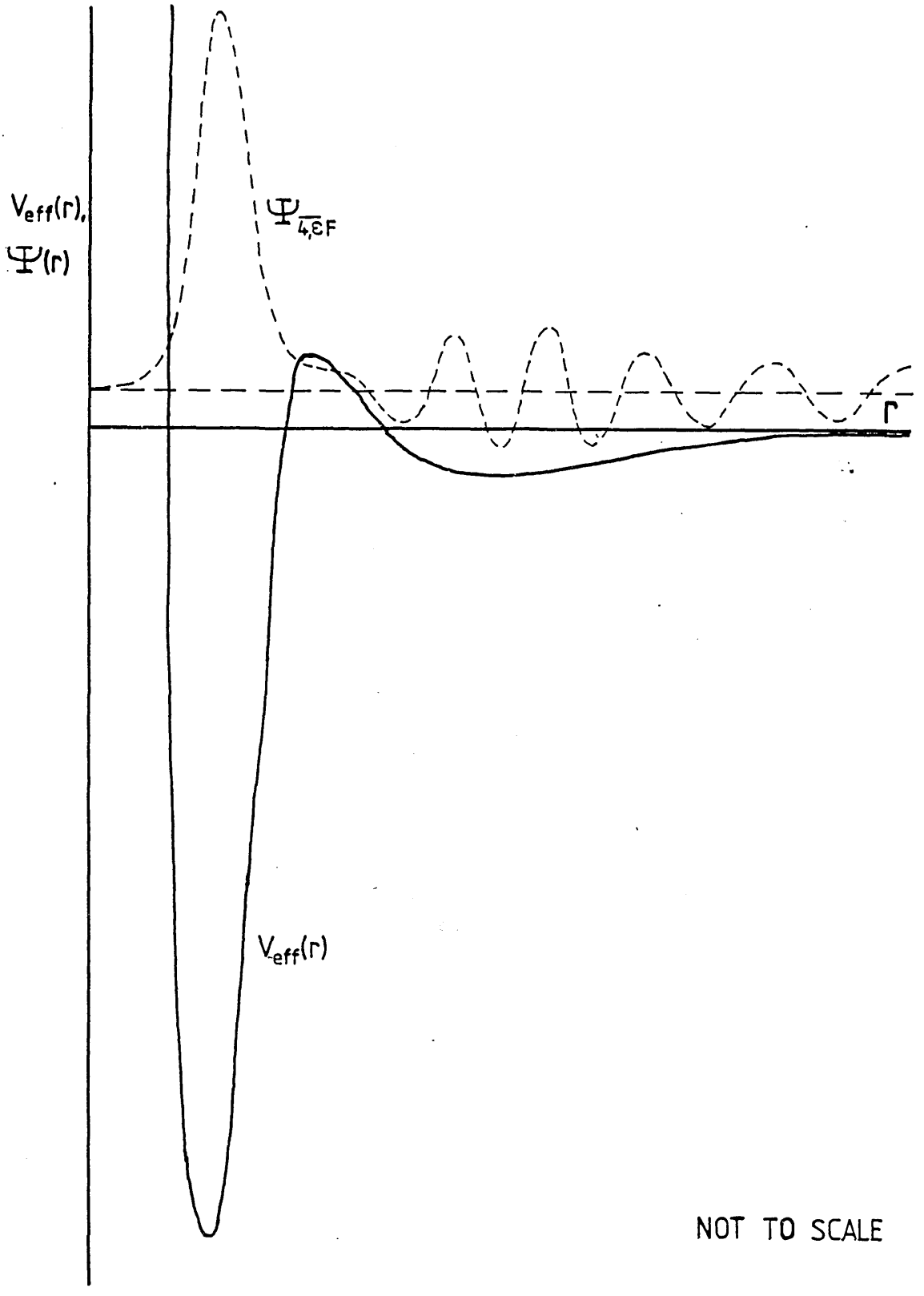
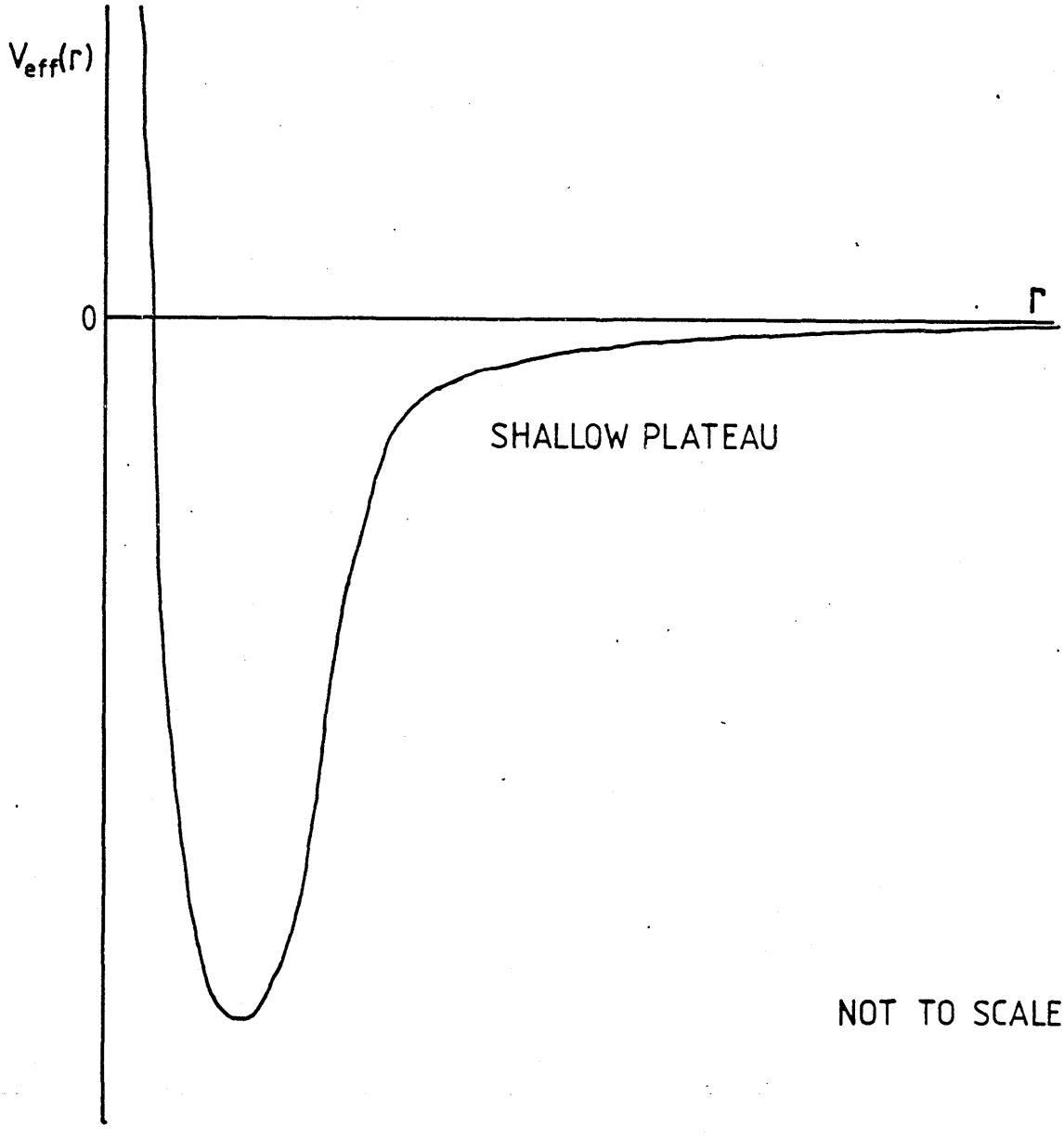


FIGURE 2D4: BARIUM EFFECTIVE POTENTIAL FOR 5d ELECTRONS



"soft" in that small changes in the depth of the deep valley or its width can result in the 5d wavefunction collapsing into or expanding out onto the plateau. Such "softness" is not mirrored by the effective potential of Barium 6s electrons where the centrifugal barrier absent (l_i=0). It therefore does not have the "double valley" or even the "deep valley plus extended plateau" character necessary for instabilities in the wavefunction. Dirac Fock calculations by Rose et al (1978) and (1985, Private Communication) on the mean radius of the 6s and 5d wavefunctions in the presence (and absence) of a single vacancy in the 5p shell provide supporting evidence for the above assertions on the relative sensitivities of the 6s and 5d wavefunctions. The results of these calculations based on the electronic configurations $5p^6\ 6s^2$, $5p^6\ 6s5d$, $5p^5\ 6s^2$ and $5p^5\ 6s5d$ are listed in Table 1. The picture for the origin of 6s-5d mixing in Barium which emerges is that of a pronounced contraction of the 5d wavefunction in the presence of a 5p core vacancy, while that of the 6s electron is relatively unaffected. This results in an increase of the binding energy of the 5d electron to a value similar to that of the 6s electron.

Another consequence of "softness" in an electrons effective potential is that relativistic corrections become important since small changes in the potential give rise to large changes in the

TABLE 1: Average radius $\langle r \rangle$ of 6s and 5d wavefunctions for the configurations $5p^6 6s^2$, $5p^6 6s5d$, $5p^5 6s^2$ and $5p^5 6s5d$ of Ba and Ba^+

Configuration	Average Radius (atomic units)		$\langle r \rangle_{6s} / \langle r \rangle_{5d}$
	$\langle r \rangle_{6s}$	$\langle r \rangle_{5d}$	
$5p^6 6s^2$ *	5.083	---	---
$5p^6 6s5d$ **	5.247	3.921	1.338
$5p^5 6s^2$ *	4.222	---	---
$5p^5 6s5d$ *	4.384	2.945	1.488

1 a.u. = 5.292×10^{-11} [m]

Data Source

* Rose, S.J.; (1985) Private Communication

** Rose et al (1978)

Data were based on single manifold O.L. (Optimal Level) M.C.D.F. calculations.

The larger contraction of the 5d wavefunction compared with the 6s wavefunction after the removal of a 5p electron is demonstrated by the increase in $\langle r \rangle_{6s} / \langle r \rangle_{5d}$.

resulting wavefunction. Consequently non-relativistic calculations based on the Schrodinger Equation such as the Hartree Fock (HF) method cannot be expected to be accurate. Good accuracy can only be achieved if calculations based on the relativistically correct Dirac Equation are used such as the Dirac Fock (DF) method.

Enough has been said about the aspects of the Radial Problem to emphasis its importance in understanding the present work. It should be quite clear that the angular aspect of the Atomic Problem is now well understood and that future progress will come out of the work on the Radial Problem.

2.2 Discussion of the Anomalous Barium Photo Double Ionisation Phenomena

Much of the interest in the Barium 5p absorption spectrum has been stimulated by the anomalous photo-double ionisation rate of Barium described in Chapter 1. The two problems are interconnected and important questions regarding the nature of the anomaly have been posed. Opinion amongst the theorists (see Chapter 1) has been divided along the lines of those who support a multi-body picture and those who support an independent particle model based on the Two Step Autoionisation process of Hansen (1975). Hansen's model was critically dependent on the availability of an energetically

viable intermediate state and he advanced the $\{5p^5\ 5d\ [^3P]\}\ 6s^2\ ^2P$ state of the Barium ion as a possible candidate. The anomaly therefore stimulated interest in the work on identifying the Rydberg series deduced by Connerade et al (1979a); Since this intermediate state would have to have corresponded to one of the observed series limits. The relationship between the present work and the work into the double ionization anomaly is as follows. The present 5p absorption work investigates the absorption of a photon and the resulting excited states, whereas photoionisation studies look at how these states subsequently decay. A factor they have in common is the significance of 6s-5d mixing in their interpretation. Future work on the anomaly might involve studies of the photodouble and single ionization rates of laser excited states of Barium as a function of V.U.V. probe wavelength. Such work would however require a knowledge of the excited states 5p absorption spectrum so that wavelength dependent features in the ionisation studies might be correlated to features in the absorption spectrum.

The Two Step Autoionisation model of Hansen given in Chapter 1 which is summarized in figure 2D5 was based on the results of both his own Hartree Fock calculations and on the experimental data of Brehm and Hofler (1974) and Hotop and Mahr (1975). These experimental workers had studied the

FIGURE 2D5: HANSEN'S TWO STEP AUTOIONISATION MODEL FOR Ba

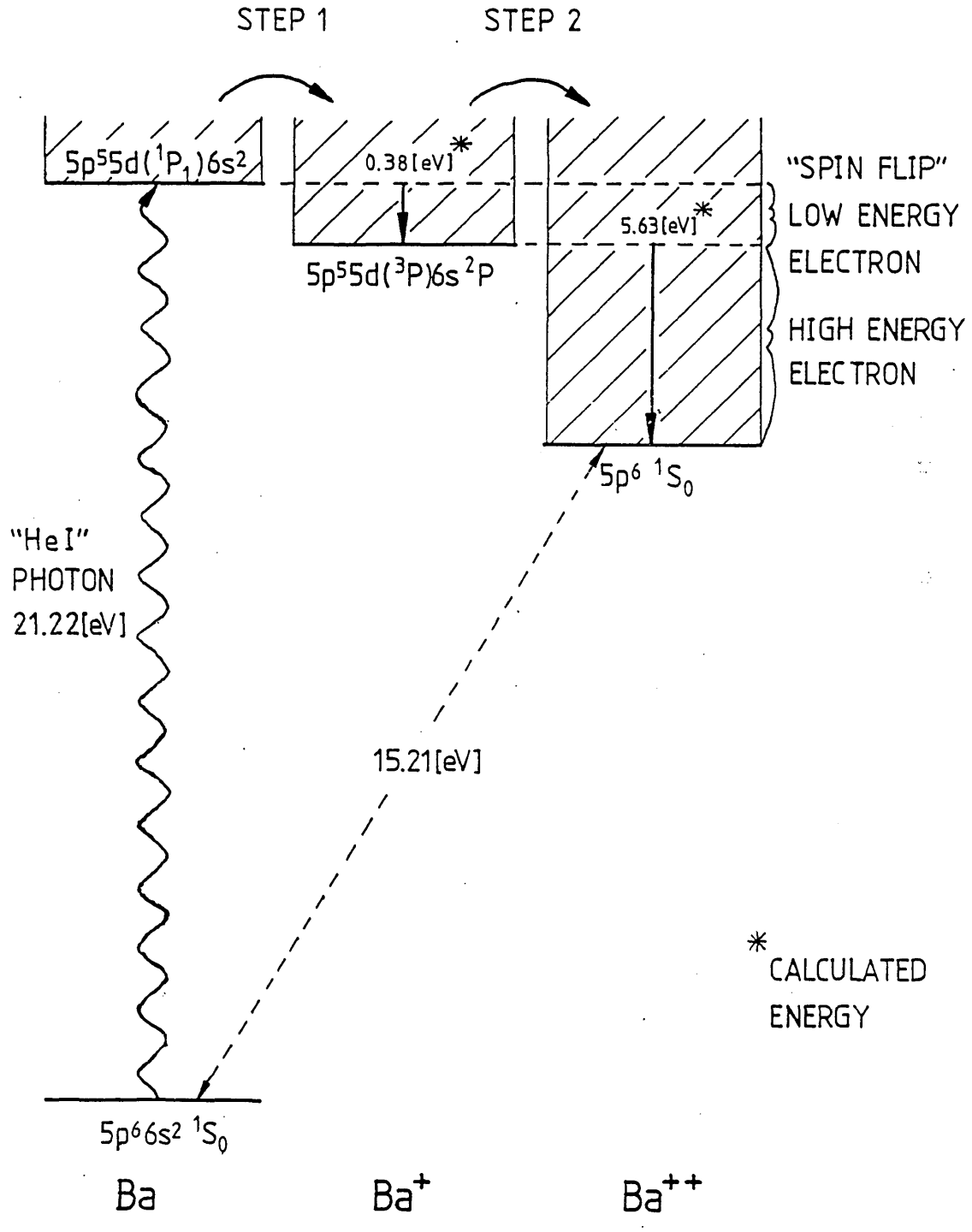


photo-electron spectrum resulting from irradiating Barium vapour with the Helium 21.22 [eV] line. Both sets of data were in broad agreement although the higher resolution of Hotop et al's experiment permitted the observation of features not resolved by Brehm et al. Essentially Hotop et al resolved two groups of three peaks in their photo-electron spectrum: a high energy group at 5.935 [eV] 5.852 [eV] and 5.798 [eV] and a low energy group at 0.067 [eV], 0.150 [eV] and 0.204 [eV]. This indicated that a single photon was in an indirect way removing two electrons from the atom since the energy difference between the Helium photons and the Barium second ionisation limit was 6.005 [eV]. Hansen pointed out that the Helium line at 21.22 [eV] lay very close in energy to that of the $\{5p^5\ 5d\ [^1P]\}\ 6s^2\ ^1P$ term which he calculated to be at 20.5 [eV] $\pm$ 1 [eV] above the Barium ground state. This state could then autoionize to states <u>above</u> or below the Barium double ionization limit leading to a second autoionization in the case of the former. Further calculations by Hansen indicated that the $\{5p^5\ 5d\ [^3P]\}\ 6s\ ^2P$ term of Ba^+ lay $\sim$ 0.38 [eV] below the proposed $\{5p^5\ 5d\ [^1P]\}\ 6s^2\ ^1P$ Ba initial state indicating that Two Step Autoionisation was energetically viable, the process being driven by a "spin-flip" of the $5p^5\ 5d$ core. This is the process which was represented in figure 2D5 and would be characterized by the emission of a high and a very low (less than 1 [eV]) energy electron, which indeed

corresponds to the observed spectrum. The intermediate level described above was cited as an example and he pointed out that other states built on the configurations $5p^5\ 5d\ 6s$, $5p^5\ 5d^2$ might also be possible intermediate states. The chief problem with Hansen's analysis, as he himself pointed out, was that Multi-Configurational Hartree Fock Calculations are not sufficiently accurate (i.e. not better than 1 [eV]) to be able to say with confidence that the intermediate state was indeed energetically viable. The absence of a high Ba^{++}/Ba^{+} ratio when probed with the Neon lines at 16.67 and 16.85 [eV] could in his model be attributed to the absence of any intermediate states embedded in the Ba^{++} continuum.

Hansen's Two Step Autoionisation Model described above would imply that a high Ba^{++}/Ba^{+} ratio should be expected at higher excited levels in the 5p spectrum. Hence it is clear that the experiments of Hotop and Mahr, and Brehm and Bucher needed to be repeated using a tunable V.U.V. source to test this prediction. A number of years were to pass before this was eventually done. In the meanwhile Connerade (1977) and Connerade, Rose and Grant (1978) advanced suggestions on the mechanism of high double ionization rates. The mechanism suggested in the earlier paper is not relevant to Barium, but the second paper (Connerade et al (1978)) looked specifically at the question of whether the

intermediate levels required by Hansen's Two Step Autoionisation model for Barium did indeed exist. They pointed out that the series analysis of the Barium 5p spectrum by Connerade et al (1979) did indeed suggest (i), that the Helium 21.22 [eV] line excited a state with significant $5p^5\ 6s^2\ 5d\ ^1P_1$ character (as required by Hansen's model) and (ii), that this upper state lay in the continuum associated with the four 5p thresholds, labelled i,j,k and l in that paper, belonging to the Ba^+ manifold of $5p^5\ (6s^2x6s5dx5d^2)$. This suggested that Hansen's basic model was correct provided one (or more) of these thresholds contained a significant admixture of $5p^5\ 5d\ [^3P]\ 6s$. However it would be more accurate to say that the two step autoionisation process was driven by $6s^2x6s5d$ mixing rather than by a "spin-flip" of the core. The results of Multi-Configurational Dirac Fock (MCDF) calculations by Rose et al (1980) indicated that three of these thresholds did indeed contain such an admixture, even though a quartet rather than Hansen's doublet state was involved. Furthermore two of these experimental thresholds corresponded in energy to those observed by Hotop and Mahr's (1975) data, thus confirming Hansen's basic picture of the process.

Further experimental evidence of the two step autoionisation process was provided by the data of Rosenberg, Lee and Shirley (1980). Their experiment

investigated the ejected electron energy spectrum of Barium and Ytterbium under excitation by electron impact. The results implied that the excited atoms decayed preferentially by two step autoionisation once the 5p electrons were excited to states above the 5p thresholds. The evidence for this conclusion in the case of Barium lay in the low intensity of the ejected electron energy spectrum above 15.8 [eV] which corresponded to the energy of the lowest autoionisation resonances observed by Peart and Dolder (1968) for Ba^{+}. More highly excited Barium states had to decay in a two step process since a discrete rather than continuous structure was observed. They suggested on the basis of this hypothesis that some of the stronger BaI autoionising resonances above the first 5p ionisation threshold should yield even larger ratios of Ba^{++} to Ba^{+} than that observed by Brehm and Bucher using Helium 1 radiation. (This resonance is relatively weak in the absorption spectrum.) However this hypothesis could only be unambigously tested by using variable energy impact electrons (the electrons energies in this work were continuous) or photons.

The first such data was provided by Holland and Codling (1980) who used monochromated (bandwidth 2Å) synchrotron radiation. They found that their mass spectrometer measurements of the Ba^{++}/Ba^{+} ratio did <u>not</u> correlate in energy to the photo-absorption

structures observed by Connerade et al (1979a). Their data instead seemed to imply a correlation between increases in the Ba^{++}/Ba^{+} ratio and some of the 5p ionisation thresholds observed by Connerade et al (1979). This result seemed to imply a many body non-resonant origin to the anomalous Ba^{++}/Ba^{+} rates. They noted that their results posed the following four important points regarding the Two Step Autoionisation model of Ba^{++} formation. One, why did the Ba^{++} crossection remain low in the range 602-590Å where there were 5p ionisation thresholds associated with limits k and l (Connerade et al's 1979a, series identifications) and excited states associated with series i and j? Second, their Ba^{++}/Ba^{+} ratio results seemed to suggest an asymmetric resonance at $\sim$580Å which they suggested might be related to Wendin's Giant Resonance which they said should lie at this wavelength. Thirdly, if the $5p^5(6s^2x6s5dx5d^2)11s$ resonance is required to explain the Ba^{++}/Ba^{+} ratio observed by Brehm and Bucher (1974) (coincident with the He 1 line), then why didn't higher members of the series also show large ratio's for Ba^{++}/Ba^{+}? In fact Holland et al observed a minimum in the ratio at around 573Å where these members lay. Lastly, if the weak 584Å resonance is responsible for the large observed Ba^{++}/Ba^{+} ratio, why doesn't a much stronger resonance at 576.11Å show an even larger ratio? They claimed in conclusion that their results indicated that the process of excitation and

subsequent decay of the excited neutral states must be separated, since their data did not suggest a correlation between a high absorption crossection and a high Two Step Autoionisation rate.

A mechanism for reconciling the contradictory conclusions drawn by Holland et al (1980) and Hotop et al (1975), arising from their respective experiments, was very soon advanced by Connerade and Martin (1980). They suggested that there were two contributary factors to a high Ba^{++}/Ba^{+} ratio at different wavelengths. First, a "general many body" background that increases slowly with energy and exhibits steps at each 5p ionisation threshold, and secondly a contribution that was resonant in energy (Two Step Autoionisation) utilising initial upper states with significant admixtures of $5p^5 6s^2 5d\ ^1P_1$ (Hansen's upper state). It was further suggested that since these processes are distinct, that they could interfere with one another. (Two different routes to the same final state). The results of such interference is an asymmetric "Fano Profile" which manifests itself as a asymmetric resonance like profile in the Ba^{++}/Ba^{+} ratio as was observed by Holland and Codling (1980). It was a novel and appealing idea that direct photodouble ionisation should be enhanced by such coupling to discrete resonances located above the 5p ionisation thresholds. There was however a flaw in its applicability to the data of Holland et al in that

other asymmetric resonances in the Ba^{++}/Ba^{+} ratio should have been observed with other levels containing appreciable $5p^5\ 6s^2\ 5d\ ^1P_1$ character. Such resonances were not clearly observed.

Shortly afterwards, very high resolution work on the Ba^{++}/Ba^{+} ratio as a function of photon wavelength, some of it to 0.15Å precision, was published by Lewandowski, Granz, Hotop and Ruf (1981). They found that the gross features of their results were in reasonable agreement with the data of Holland et al. However the fine features now showed a clear correlation between the Ba^{++} production rate and the photoabsorption crossection for wavelengths below 590Å. On the other hand they found that the Ba^{++}/Ba^{+} ratio did not faithfully replicate the Ba^{++} production rate. This implied that regions of strong photoabsorption below 590Å feed both the Ba^{++} and Ba^{+} channels, but with varying branching ratios. In particular they found that the series "e" (identified by Connerade et al (1979a)), except for the first member, led to peaks in both the Ba^{++} and Ba^{+} channels. However no such clear structure was observed in the Ba^{++}/Ba^{+} ratio. Lastly they found that the Ba^{++} production rate went practically to zero above 590Å which happens to correspond to the lowest $5p^5$ nl n'l' state measured by electron spectroscopy. So it is quite clear that the Ba^{++} ion production is driven by a Two Step Autoionisation process. The formation of Ba^{++} ions

in the case of the series "e" was summarized by Connerade and Martin (1983) to be as follows: -

Step 1

$$5p^6\ 6s^2\ {}^1S_0 \rightarrow 5p^5 \left\{ 6s^2 x 6s5d(\text{level "e"}) \right\} nd \quad n \geqslant 6\ J=1.$$

followed by autoionisation thus: -

$$5p^5 \left\{ 6s^2 x 6s5d(\text{level "e"}) \right\} nd \longrightarrow 5p^5\ 6s5d\ {}^4P + e^- d\ J=1.$$

leaving the Ba^+ ion in one of three $^4P_{1/2,3/2,5/2}$ states and yielding a photoelectron spectrum containing three peaks as observed by Hotop and Mahr (1975)

Step 2

$$5p^5\ 6s5d\ {}^4P_{1/2,3/2,5/2} \longrightarrow 5p^6\ [{}^1S_0] + e^-\ l$$

This "autoionisation" of the Ba^+ excited state (Auger decay would perhaps be a more accurate description) would give a further three peaks in the photoelectron spectrum which were the mirror image of those produced in Step 1.

2.3.1 Techniques of Analysis for the Barium 5p Spectrum

An understanding of the techniques used by Connerade et al (1979a) is useful in order to appreciate how the spectrum produced in this work might eventually be analysed. These workers used three distinct approaches for their analysis that resulted in the identification of 14 series converging to 12 limits, some of the identifications being very tentative.

Approach 1 - Ordering the observed lines by inspection into plausible series which converged to Ba^+ levels previously observed by Roig (1976). The authenticity of these line assignments to given series were then checked using the graphical technique of "Lu Fano plots". This is a graphical technique for studying perturbations between series and is based on Multi Channel Quantum Defect Theory (M.Q.D.T.). This approach in conjunction with the second approach below enabled the Barium ground state spectrum to be reduced semi-empirically to 14 series converging to 12 limits. The qualitative details of the link between M.Q.D.T. and Lu Fano plots, their construction and interpretation will be left to the next subsection (2.3.2) since the topic is very large.

Approach 2 - Comparisons with the 5p spectrum of the Lanthanides (Tracy 1977). Connerade et al (1979a) remarked that 6s-5d mixing becomes progressively less important along the periodic table from Barium to Ytterbium. The energy dependence of several features in the spectrum can be followed back from Ytterbium (Z=70) to Dysprosium (z=66) with confidence and, for the "giant resonance" from Ytterbium to Samarium (z=62). The energy dependence is nearly linear and extrapolating the position of the giant resonance back to Barium would place it at 581Å which is close to a particularly intense group of broad lines actually observed. It can be argued that the Ytterbium 5p spectrum is the hypothetical spectrum of Barium in the absence of 6s-5d mixing because of the effective screening of its nucleus by its closed 4f subshell. Unfortunately there is no data on 5p absorption spectra of the Lanthanides in the presence of an excited valence electron, so this approach has no practical value with respect to the analysis of the 5p absorption spectra of laser excited Barium.

Approach 3 - The use of Ab-Initio calculations to identify features in the spectrum. Such calculations are necessary for two main reasons. Firstly, many of the Ba^+ 5p absorption lines observed by Roig (1976) remain unassigned and so series running to the corresponding levels have not been identified. Secondly, the assignment of lines

to the lower members of a given series cannot be confirmed with any confidence using Lu Fano plots, for reasons which will be elucidated in the discussion of M.Q.D.T. The identification of such members in a complex spectrum can only be confirmed by Ab-Initio calculations which because of the importance of relativistic effects in Barium should be based on the Dirac equation. Such calculations should also take account of the possibility of configuration interaction by constructing eigenstates which are linear combinations of various pure electron configurations, and also various L-S states of fixed J if L-S coupling is being used to describe a state exhibiting intermediate coupling. The combination which gives the lowest energy will by the variational theorem be the best approximation to the true eigenstate. The approach is rather reminiscent of a function being approximated by a series of Fourier components. The chief problem with the technique is that the configurations must be chosen "by hand" and including more and more configurations results in larger demands on computer time. Rose et al (1980) using multi-configuational Dirac Fock (MCDF) calculations have tentatively identified the series a,b,c,d,e,f and h. Their calculations for example indicated that the core configuration corresponding to the series a and b limit was: -

$$|\Psi_{a,b}\ \text{core}\rangle = -0.8902|5p^5 6s^2\ {}^2P_{1/2}\rangle$$

$$-0.0015|5p^5 5d6s[{}^1P]\ {}^2P_{1/2}\rangle$$

$$+0.1007|5p^5 5d6s[{}^3P]\ {}^2P_{1/2}\rangle$$

$$-0.0076|5p^5 5d6s\ {}^4P_{1/2}\rangle$$

$$-0.0201|5p^5 5d6s\ {}^4D_{1/2}\rangle$$

$$+0.0159|5p^5 5d^2[{}^3P]\ {}^2S_{1/2}\rangle$$

$$-0.0874|5p^5 5d^2[{}^1S]\ {}^2P_{1/2}\rangle$$

$$+0.2345|5p^5 5d^2[{}^1D]\ {}^2P_{1/2}\rangle$$

$$+0.3329|5p^5 5d^2[{}^3P]\ {}^2P_{1/2}\rangle$$

$$-0.0197|5p^5 5d^2[{}^3P]\ {}^4P_{1/2}\rangle$$

$$-0.1439|5p^5 5d^2[{}^3P]\ {}^4D_{1/2}\rangle$$

$$+0.0460|5p^5 5d^2[{}^3F]\ {}^4D_{1/2}\rangle$$

2.3.2 Multi-Channel Quantum Defect Theory and the application of "Lu Fano Plots" to the ordering of a spectrum into Rydberg Series

Multi-Channel Quantum Defect Theory (M.Q.D.T.) was first formulated by Seaton in 1966 and its significance to the present work lies in the subsequent derivation of the important graphical technique of "Lu Fano Plots". Hence this subsection will begin with a qualitative discusion of the physical concepts which underline M.Q.D.T., before describing the construction and interpretation of Lu

Fano Plots.

Rydberg series in atomic spectra are associated with the excitation of a single electron from one level of an atom to a "channel" of levels corresponding to fixed l but increasing Principle Quantum Number n. Their energies are given by the simple formula first proposed by Rydberg: -

$$E_i(n,l) = I_i - \frac{R}{[n - \mu(E_i,l)]^2} \qquad 7$$

where I_i is the ionisation limit of the ith channel, R is the Rydberg constant $\frac{2\pi^2 m_e e^4}{(4\pi\varepsilon_o)^2 h^2} = 2.179\times10^{-19}$ [J] and $\mu(E_i,l)$ is the Quantum Defect of the atom for excited electrons of angular momentum l. An important property of the Quantum Defect is the approximate independence of its value upon the electron energy $E_i(n,l)$. Its value is determined principally by the angular momentum l of the running electron. Sometimes this approximation breaks down because of mutual perturbations between different Rydberg Channels and a theoretical treatment of these channels is then dependent on MQDT. Since the quantum defect is zero for hydrogen, it quantifies in some way the departure of the atoms central field potential from a coulombic potential.

Beyond a certain radius r_o, the excited electron will lie outside the electron core and in this

region will perceive a coulomb potential. Hence the radial part of the electrons wavefunction in this region will consist of a superposition of regular and irregular coulomb functions f(E,l,r) and g(E,l,r). Such a superposition is necessary in order that the wavefunction and its first derivative should be continuous at the boundary E-V(r)=0 (non-hydrogenic energy levels) and that the wavefunction should go to zero as r goes to infinity. The radial dependence of the wavefunction U(E,r) representing the excited Rydberg electron in the region $r>r_0$ is therefore of the form:-

$$U(E,r) = N_E[f(E,l,r)\cos\pi\beta - g(E,l,r)\sin\pi\beta] \qquad 8$$

where N_E is a normalization constant and β is some constant which is determined by making the wavefunction continuous at the boundary $r=r_0$. Consideration of the asymtopic forms of f(E,l,r) and g(E,l,r) at infinity requires that β be equal to the quantum defect $\mu(E,l)$(Fano,1970 or Starace, 1976). The approximate independence of the Quantum Defect with energy is due to the kinetic energy of the electron [E-V(r)] being much larger than E in the core region (where E is defined with respect to the ionisation limit). For this electron, the number of oscillations of its wavefunction in the core region will not appreciably change for states of sufficiently large n and therefore kinetic energy.

The assignment of spectral lines to a Rydberg series may be confirmed by a plot of the deduced values of $\mu(E)$ as ordinate (using equation 7) against E as abcissa. Such a plot should yield a line of points which converge asympotically with increasing n onto a horizontal line which should cross $\mu(E)$ axis at the asympotic value of the quantum defect. Any point which lies off the asymptotic line would either be an incorrectly assigned line, or a perturbed line due to its interaction with some other line(s) nearby in energy. The identification of such perturbed lines required an extension to the above single channel discussion to encompass the interactions with other channels, hence MQDT.

It was stated in Chapter 1 that the analysis of the Barium 5p absorption spectrum from the ground state by Connerade et al (1979a) indicated the presence of 14 series running to 12 limits. Each series limit corresponds to a given core state of the atom which in the limit of the Rydberg electron being ionised would correspond to a level in Ba^+. Connerade et al's (1979a) analysis indicates that lines belonging to different series (or channels) can strongly interact. The physical result of such an interaction is the mixing of the responsible Rydberg members resulting in an energy shift from their expected positions, which also manifests

itself as a sudden fluctuation in the quantum defect as deduced from equation 7. The energy range over which two lines might interact will scale with the strength of the interaction between the respective channels

But why should such states interact in the first place? The usual approach to understanding the "perturbations" between the different states is based on a state by state analysis using Ab-initio calculations. These generate a wavefunction consisting of an array of one electron wavefunctions for each state and will reflect the importance of the "electrostatic" and "spin orbit" interactions. The non central component of the "electrostatic" interaction is responsible for the LS coupling scheme for angular momenta while the "spin orbit" interaction give rise to j-j coupling. In practice, both interactions are important and the true angular momenta coupling scheme will lie intermediate between the two cases. Atomic states are frequently expressed in terms of a mixture of LS basis states. Two "interacting" Rydberg states will contain LS coupling components in common, and the two states are said to "mix" and "interact". The problem with this approach to identifying states associated with a complex spectrum is that it proceeds on a state by state basis and does <u>not highlight underlying patterns</u> to the apparently "irregular" behaviour of a given Rydberg series. Some members of a Rydberg

series will be found to be highly mixed with states belonging to other series, yet others will not and there will be no apparent regularities to such behaviour in a given series. There may also be problems with the above state by state approach near an ionization limit where many states at once may be needed in the multi-configuration calculations.

The MQDT is an alternative approach which treats entire Rydberg channels in a unified way. The conceptual picture which emerges is of Rydberg electrons that spend most of their time outside the electron core where the potential is coulombic in form. On entering the core, electron electron interactions become important and result in the possibility of the electron being scattered into the Rydberg state of another channel lying close by in energy. Hence the true eigenstates of the system must be a mixture of the above two (or more) channels such that the interaction responsible for the scattering by the core is diagonalised. The theory therefore proposes that one basis set for the problem will consist of a set of "collision channels or "i" channels" (Wynne et al, 1979) and these correspond to the Rydberg channels described above. The channel therefore describes a set of states which have an outer electron of a given energy, a core in a definite energy level, a specific angular momentum for both the core and the Rydberg electron and their coupling. An example of an LS coupled i

channel would be the set of discrete states $Ba\{5p^5 6s^2[^2P_{1/2}]\}ns\ ^1P_1$ and the $Ba\{5p^5 6s^2[^2P_{1/2}]\}\varepsilon s\ ^1P_1$ continuum. The Rydberg Channels of a spectrum may sometimes be represented approximately by a set of pure LS coupled channels which might be valid for the Rydberg electron in the absence of the core interaction. Often these channels are not eigenstates of the core interaction and thus two states of the same parity and angular momentum lying close by in energy can strongly perturb one another and mix. The presence of such mixing may be identified in the case of two interacting channels, using the graphical technique of "Lu Fano Plots" developed by Lu and Fano (1970).

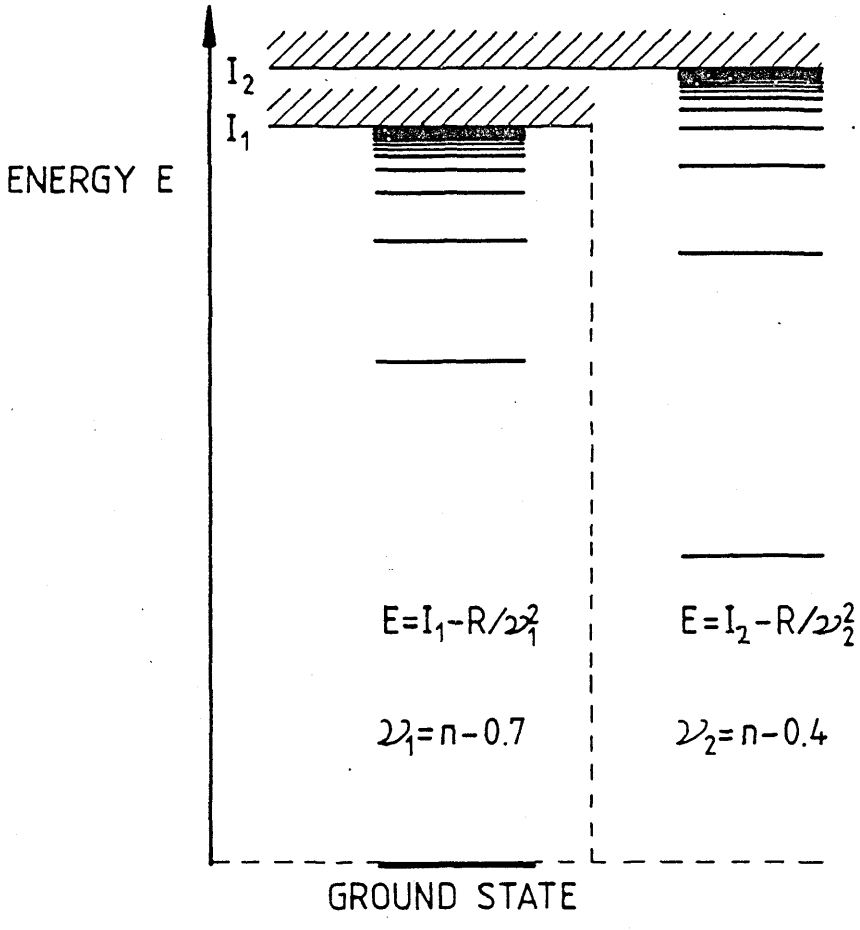
It is useful when introducing the Lu Fano plot technique to consider a schematic spectrum with two Rydberg series running to two different ionisation limits I_i, see figure 2D6. Each of these limits will correspond to different states of the atomic core and the resulting energy level distribution may be summarized by the following pair of Rydberg formulae: -

$$E = I_1 - \frac{R}{\nu_1^2} \qquad 11a$$

$$E = I_2 - \frac{R}{\nu_2^2} \qquad 11b$$

where $\nu_1 = n_1 - \mu(n_1)$ and $\nu_2 = n_2 - \mu_2(n_2)$ and n_i are integers. It is possible by considering E as a continuously varible parameter that values for

FIGURE 2D6: ENERGY-LEVEL DIAGRAM FOR TWO NONINTERACTING RYDBERG SERIES (AFTER WYNNE ET AL,1979)



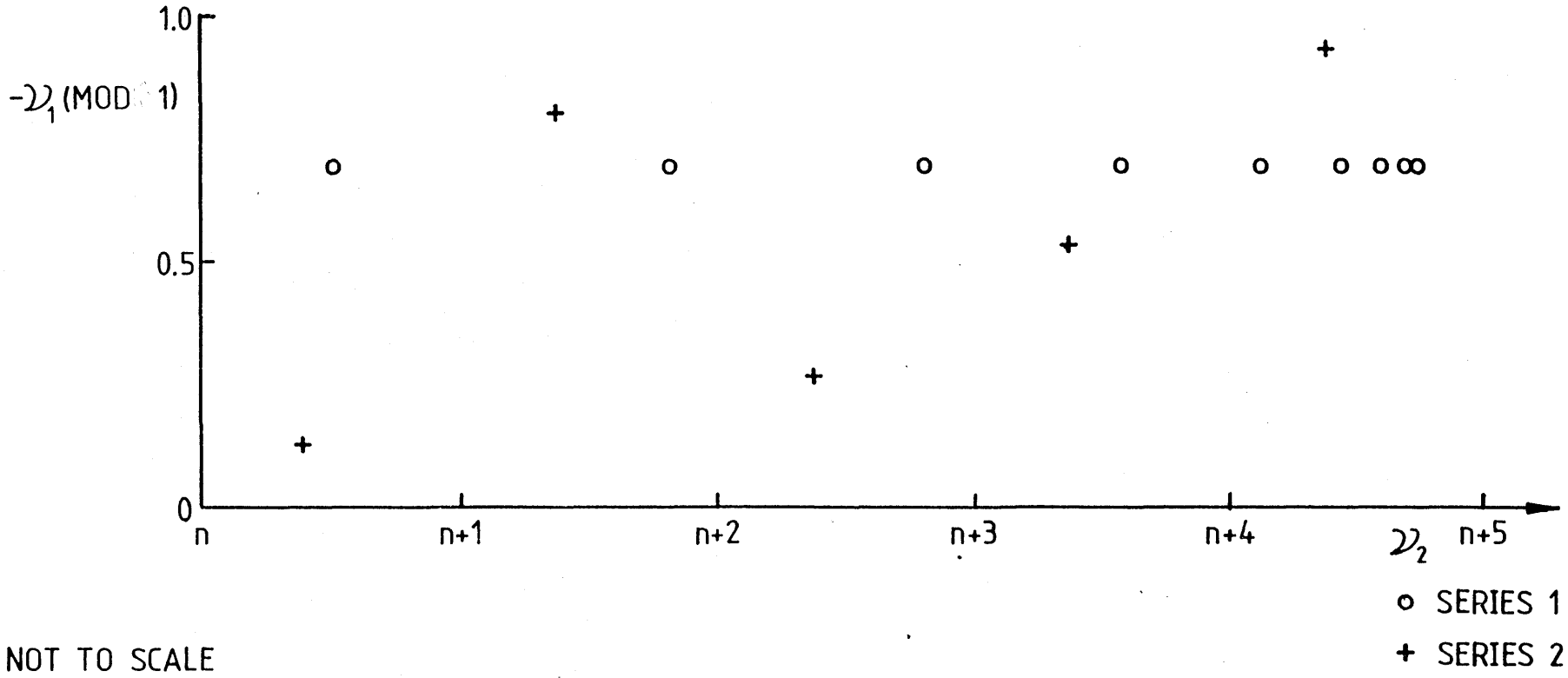
ν_1 and ν_2 may be deduced from equations 11 for each observed line in the "discrete part" of the spectrum. These values would be related by the equation: -

$$\nu_1 = \left(\frac{1}{\nu_1^2} - \frac{I_1 - I_2}{R}\right)^{-1/2} \qquad 12$$

But what meaning can be attributed to these deduced values for the parameters ν_1 and ν_2? For series 1 the values of ν_2 are essentially an energy index for each level. The corresponding values of ν_1 on the other hand identify the level and gives its quantum defect since $-\nu_1 (\text{mod } 1) = \mu_1$. For series 2 the value of ν_2 identifies the line and the corresponding ν_1 is now an energy index. Consequently the character of a plot of $-\nu_1 (\text{mod } 1)$ versus ν_2 for the members of both series in the absence of any mutual perturbations will be as follows. The plotted members of series 1 will form an approximately horizontal line which will be equivalent to a quantum defect versus energy plot. On the other hand, the deduced values of $-\nu_1 (\text{mod } 1)$ $[=\mu_1]$ for the members of series 2 will <u>not</u> be constant, but they will be distributed along the axis at integer values reflecting the essential periodicity of the Rydberg series, see figure 2D7. However the values of ν_2 deduced for series 2 using 11b also fulfil the role of an energy index.

If the resulting plot is then folded along the

FIGURE 2D7: TYPICAL $-\nu_1$(MOD 1) VRS. ν_2 PLOT FOR A SPECTRUM CONTAINING TWO NONINTERACTING RYDBERG SERIES



NOT TO SCALE

ν_2 axis onto a unit square by plotting $-\nu_1$(mod 1) versus $-\nu_2$(mode 1), a graph called a "Lu Fano Plot" similar to that in figure 2D8 will be generated. The intersection of the horizontal line with the $-\nu_1$(mod 1), axis yields the quantum defect of series 1 while the intersection of the vertical line with the $-\nu_2$(mod 1) axis yields the quantum defect of the second series.

The significance of the intersection of the horizontal and vertical lines is that any plotted member near this intersection will lie close in energy to a member(s) of the other series. "Switching on" the interactions between the two series for these members will lead to perturbations in their energy level position, and hence their quantum defect. The Lu Fano Plot would register this intersection by an up-down displacement of the members of series 1 ($-\nu_1$(mod 1) = μ_1) and a left-right displacement of the members of series 2 ($-\nu_2$(mod 1) = μ_2). The sense of the displacement would depend on whether the series 1 (or 2) member was higher in energy than the series 2 (or 1) member(s), its magnitude would depend on the proximity of the given member to the intersection on the Lu Fano Plot. Figure 2D9 shows the effect of increasing the intensity of the mutual interaction between two series on the resulting Lu Fano plot. It can be seen from the diagram that the effect of "turning on" the interaction is to generate an

FIGURE 2D8: TYPICAL LU-FANO PLOT FOR A SPECTRUM CONTAINING TWO NONINTERACTING RYDBERG SERIES

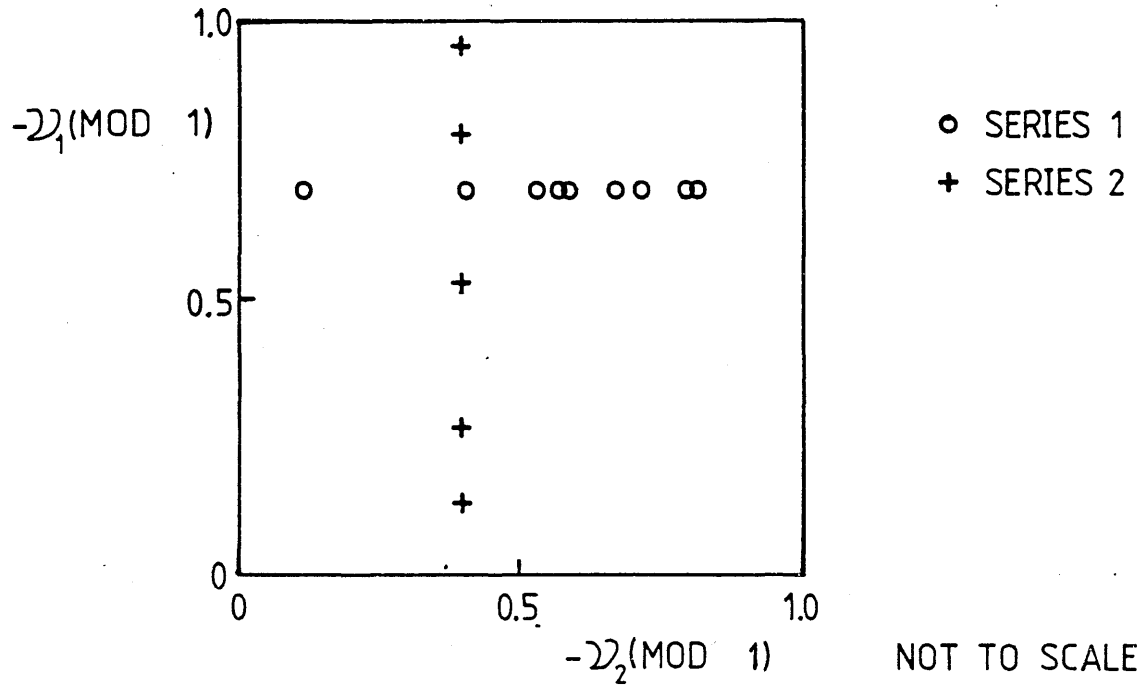
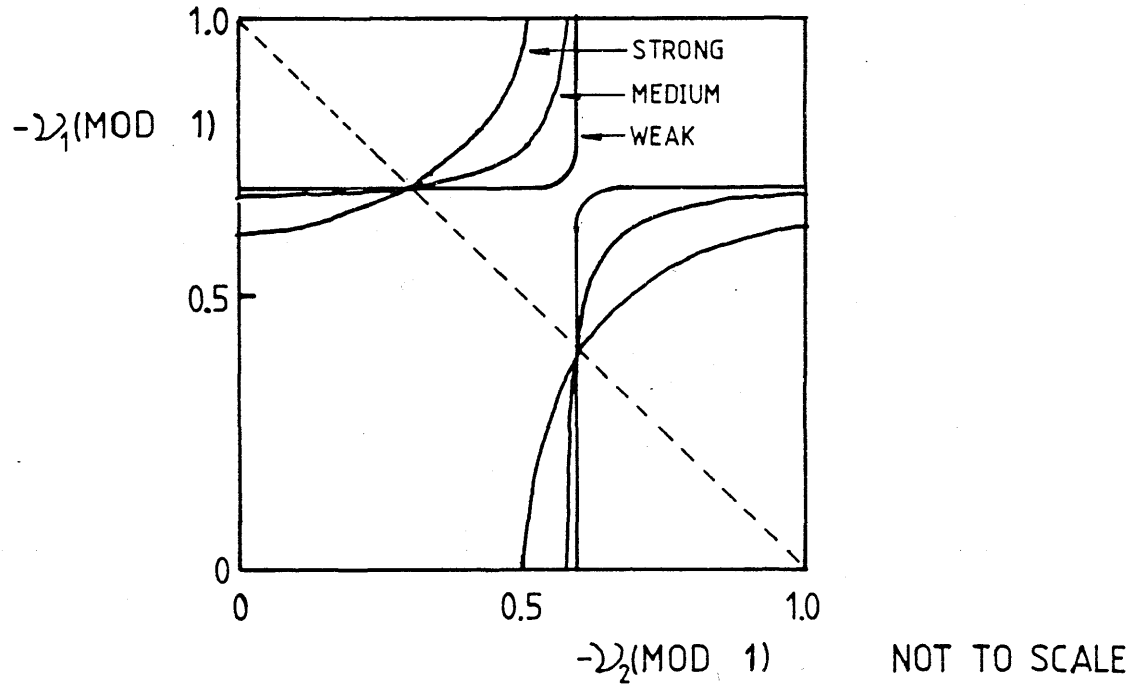


FIGURE 2D9: EFFECT ON A LU-FANO PLOT OF VARYING AMOUNTS OF INTERACTION BETWEEN TWO SERIES

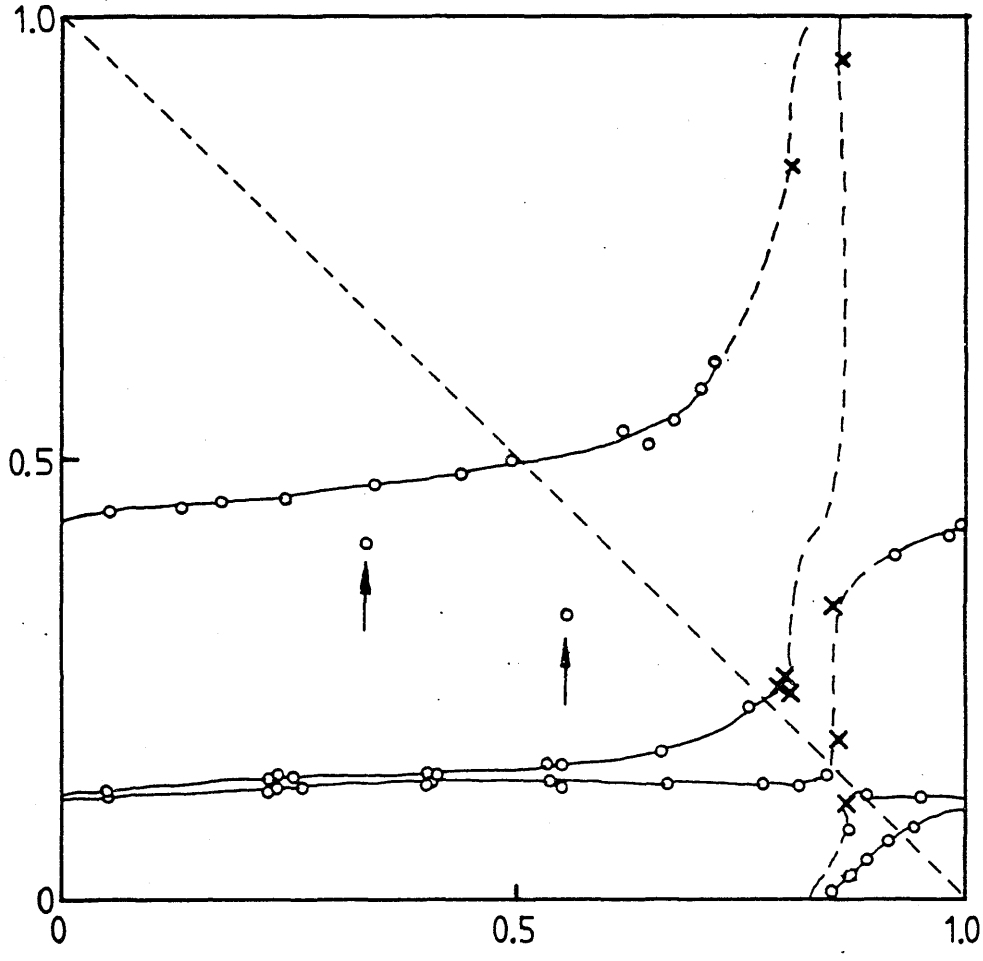


avoided crossing. The Lu Fano plot therefore provides an excellent visual aid to the identification of the strength of the interaction since the stronger the interaction the larger the separation of the two curves.

Lu and Fano in 1970 described the application of this diagramatic technique on 3p spectra of Argon (amongst other rare gases). This spectrum is more complex than the above model example in that it contained 5 Rydberg series, of which 3 converged to $3p^5\ ^2P_{3/2}$ limit and 2 to the $3p^5\ ^2P_{1/2}$ limit. Figure 2D10 is a reproduction of Lu and Fano's Argon graph which serves to emphasise one very important property of the Lu Fano Plot: the curves are continuous in the sense that a line which exits one side of the plot re-enters the plot from the opposite side with the same gradient. The Argon plot also illustrates another important property of a Lu Fano Plot in that any arbitary vertical line cuts the curve 3 times (3 series running to I_1), any arbitary horizontal line cuts the curve twice (2 series running to I_2) and that the leading diagonal from top left to bottom right cuts the curve 5 times (total of 5 series in spectrum). Lastly the degree of mixing between two channels for a given line may be deduced from the gradient of the curve in the Lu Fano Plot at the observed lines plotted position.

There are difficulties in constructing Lu Fano

FIGURE 2D10: REPRODUCTION OF THE LU-FANO PLOT FOR THE ARGON 3P ABSORPTION SPECTRUM (AFTER LU ET AL, 1970)



o MEMBERS OF SERIES RUNNING TO $3p^5(^2P_{3/2})$ CORE LIMIT

× MEMBERS OF SERIES RUNNING TO $3p^5(^2P_{1/2})$ CORE LIMIT

↑ MEMBERS ($\nu < 4$) SHOWING DEPARTURE FROM INTERPOLATED CURVE

plots for spectra which contain more than 2 series limits. This is because an N dimensional diagram in ν space is required to represent the mixing between N(N>2) core level channels (Armstrong et al 1977). However Connerade et al (1979a) found that it was possible to construct meaningful two dimensional Lu Fano plots for the Barium 5p spectrum despite the presence of 12 identified core limits. Such two dimensional plots of $-\nu_1 (\text{mod } 1)$ versus $-\nu_2 (\text{mod } 1)$ remain useful provided the perturbations to a given series are predominantly due to series running to just one other limit. Figures 2D11a and 2D11b are typical plots deduced by Connerade et al (1979a) for the Barium 5p spectrum. The plot in figure 2D11a represents the interactions between series "d" and "b" (their notation). Figure 2D11b represents the interactions between the series "k" and possible perturbers. Such plots are useful, especially for an extensively perturbed channel like series "k", for substantiating the original series assignments picked by eye.

Locating the ionisation limits I_i of a complex spectrum containing many interacting channels is a major difficulty when seeking to apply the Lu Fano technique. The series in the ideal world should be clearly observable up to their ionisation limits but in practice this is rarely the case. Hence the technique cannot be applied unless for each series a sufficient number of unperturbed lines is observed.

FIGURE 2D11a: LU-FANO PLOT FROM THE BARIUM 5P SPECTRUM, "d" SERIES VRS. "b" SERIES (AFTER CONNERADE ET AL 1979a)

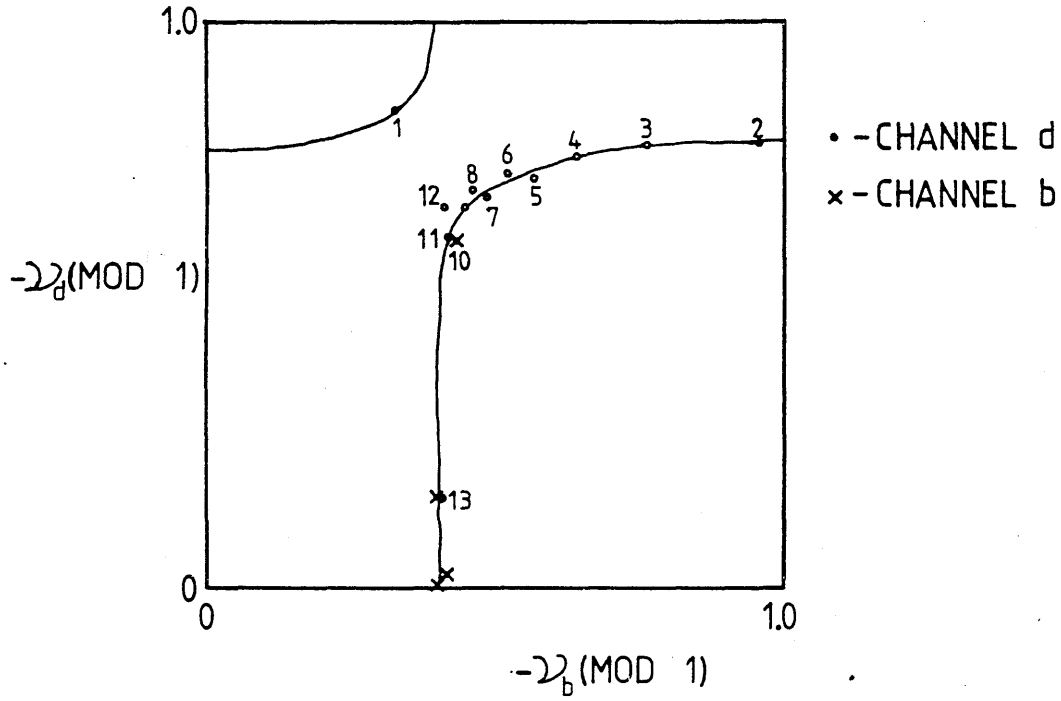
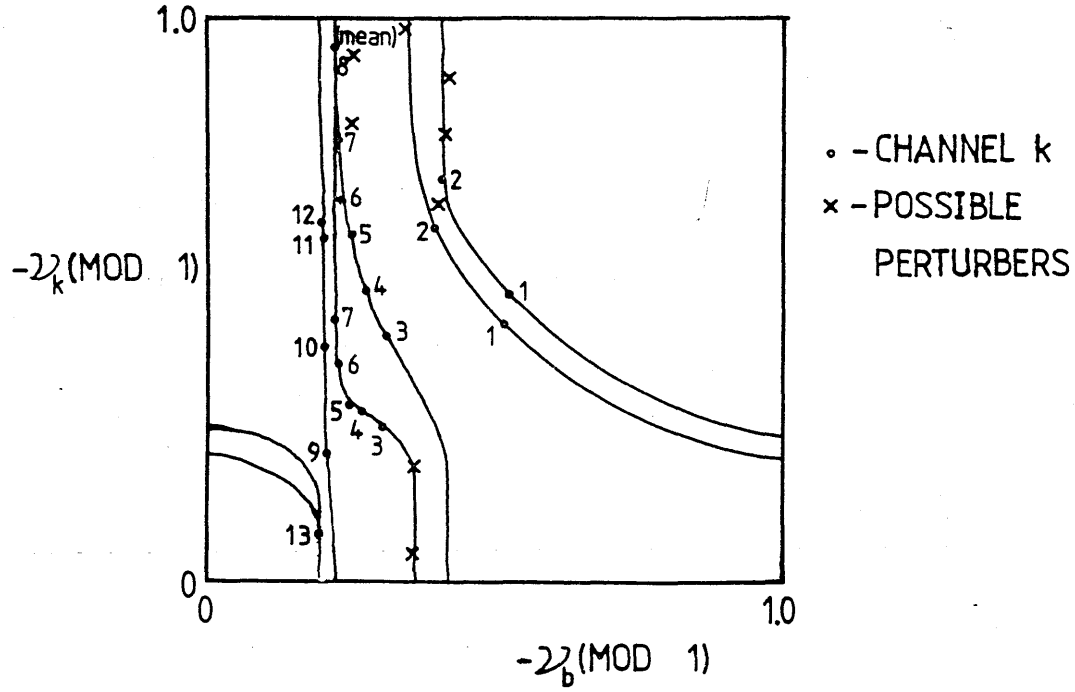


FIGURE 2D11b: LU-FANO PLOT FROM THE BARIUM 5P SPECTRUM, "k" SERIES VRS. POSSIBLE PERTURBERS (AFTER CONNERADE ET AL 1979a)



In the latter case the values of I_i, which should correspond to levels of the ion, may be deduced from interpolations of the Rydberg formula.

2.4 Mixing Processes in the Barium 5p spectrum

The presence of so many limits in the 5p absorption spectrum of unexcited Barium indicates that the excitation of the 5p electron drastically "rattles" the electron core resulting in a large number of core states being populated. The large number of such core states was attributed by Connerade et al (1979a) to mixing between the configurations $5p^5 6s^2$, $5p^5 6s 5d$, $5p^5 5d^2$ of the atomic core. This type of mixing was known as "Parent Ion Mixing" since the mixing between different configurations of the same parity is confined to the electron core and does not involve the running electron. As a result long series converging to supernumary limits are observed since the mixing is present for all values of n of the running electron. Support for this view of the mixing process is provided by the calculations of Rose et al (1980) on the above configurations. It is however possible to conceive of mixing processes which occur after the running electron has been coupled to the core. This type of mixing does not give rise to long series since the couplings between the core and the running electron diminish with increasingly higher states of excitation. The process however does permit core

states of the opposite parity to the $5p^5 6s^2$ configuration such as $5p^5 6s6p$ to mix together, but such transitions are often weak and can be considered separately from the main spectrum (Connerade et al, 1979a). Very weak transitions corresponding to core states containing significant $5p^5 6s6p$ character are nevertheless observed in the 5p absorption spectrum of unexcited Barium at wavelengths below 500Å (Connerade et al (1985) Private Communication).

Returning to parent ion mixing, it should be noted that this approximation breaks down for the lowest members of the resulting series. Basically, this is because there is no distinction between the running electron and the core for these low lying states. The core mixing coefficients for these states will be very different from high lying states and so it is rather meaningless to assign the resulting lines to a given series.

A 5p absorption spectrum starting from the Barium $5p^5 6s6p\ {}^1P_1$ state would in principle provide a very useful test of the concept of parent ion mixing in the Barium atom. The upper states accessed would exhibit 6s-5d mixing and if the Parent Ion approximation was valid would be described by the manifold $5p^5(6s6p x 6p5d)$ ns,nd J=0,1,2 which would have opposite parity to the manifold of states observed in the Barium ground state spectrum. The

mixing coefficients for the different configurations would be different and states built on $5p^5(6s5d)$ are inaccessible by excitation from $5p^6 6s6p\ ^1P_1$ through parent ion mixing, since the states of the parent ion have different parity, and do not mix. They can however be reached through mixing processes which occur after the Rydberg electron has been coupled to the core as mentioned earlier, so their absence from the experimental photo-absorption spectrum would confirm the parent ion mixing mechanism while their presence would reveal a different, more complex, mixing process.

It is interesting to recall that Connerade and Tracy (1977) attributed the absence of Wendin's 1974 $(5p;5d)^1P$ Giant Resonance in the Barium 5p spectrum to 6s5d mixing breaking it up and spreading its strength amongst levels containing 6s5d character. This leads to the speculation that perhaps the Barium $5p^6 6s6p\ ^1P_1$ 5p absorption spectrum might reveal the Giant Resonance if the mixing coefficients in the presence of the 6p electron happen to be smaller. Unfortunately it proved impossible to measure this spectrum for the reasons given in chapter 5.

It was however possible to measure the 5p spectrum starting from the $5p^6 6s5d\ ^{3,1}D$ metastable states of Barium. Again 6s5d mixing was expected, and many series converging to the core

configurations below were anticipated in the event of the parent ion mixing approximation being still valid.

$5p^5(6s5dx6s^2x5d^2)$ $[^2P_{1/2,3/2}]$

$5p^5(6s5dx5d^2)$ $[^2D_{3/2,5/2}]$

$5p^5(6s5dx5d^2)$ $[^2F_{5/2,7/2}]$

$5p^5(6s5dx5d^2)$ $[^4P_{1/2,3/2,5/2}]$

$5p^5(6s5dx5d^2)$ $[^4D_{1/2,3/2,5/2,7/2}]$

$5p^5(6s5dx5d^2)$ $[^4F_{3/2,5/2,7/2,9/2}]$

The mixing coefficients would be different from those of the ground state except for states with total J=1 built on the manifold $5p^5(6s5dx6s^2x5d^2)$ $[^2P_{1/2,3/2}]$ which would correspond to the same states as those accessed in the Barium ground state spectrum. Consequently one might expect to observe superimposed on the complex structure due to all the other manifolds and upper states, the entire Barium ground state spectrum shifted to the red by the energy separation of the 6s5d metastable states above the ground state (1.12 [eV], 1.14 [eV], 1.19 [eV], and 1.41 [eV] respectively). For example the intense line at 692.2Å* attributed to the transition

*The wavelength of this transition according to Connerade et al (1979a) is 693.66Å. This line is however extremely broad (≳4Å) and asymmetric and Connerade et al's value for the wavelength is probably based on an optical comparitor measurement. If the "crosshair" of the instruments microscope was set on the centre of the line as preceived through its eyepiece, the asymmetry of the line profile might well yield their wavelength value. This may be confirmed by reference to the microdensitometer trace of figure 5D2a (vii) of chapter 5 and the wavelength given in the text corresponds to the peak of the line profile as measured in this experiment.

$5p^6 6s^2\ ^1S_0 \longrightarrow 5p^5 6s^2 5d\ ^3P_1$ should be seen again at 738.4Å, 739.4Å, 741.5Å and 751.5Å if all the metastable $6s5d\ ^{3,1}D_{1,2,3}$ levels had been populated. In practice these shifted lines were not observed (see Chapter 5). A list of all the possible transition manifolds in the event of the parent ion approximation being valid is given in Appendix 1. Bearing in mind that the complex Barium ground state spectrum arose from just the excitation scheme: -

$$5p^6 6s^2\ ^1S_0 \longrightarrow \{5p^5 (6s^2 x 5d x 5d^2)\ [^2P_{1/2,3/2}]\} ns,nd\ J=1$$

the spectrum resulting from the metastable 6s5d D states can be expected to be incredibly complex with many more lines being present than was observed in the Barium ground state spectra. Consequently at the resolution used in this work, it could be expected that only the strongest transitions would be observed and the presence of the rest might well be indicated by a quasi-continuum. Such a background absorption was indeed observed as will be seen in Chapter 5.

2.5 Summary

In section 2.1 the importance of the radial problem to future work in atomic structure was examined, and was illustrated by a study of the physical origin of Giant Resonances in terms of the Independent Particle Model. Out of this discussion

emerged the concept of "soft" effective potentials for electrons where small changes in the central field due to the excitation of an electron can yield pronounced changes in another wavefunction, the 5d wavefunction of Barium being cited as an example. In the case of Barium, the presence of a 5p core vacancy leads to a depression of the binding energy of the 5d electron with respect to the 6s electron resulting in the mixing of the three configurations $5p^5 6s^2$, $5p^5 6s5d$ and $5p^5 5d^2$ as proposed by Connerade et al (1979a).

Section 2.2 was devoted to the photodouble ionisation anomaly of Barium when 5p electrons are excited by VUV radiation. Its link with the present work arises from its study of the subsequent decay mechanism of the excited states responsible for the 5p absorption spectrum, and the importance of 6s-5d mixing in driving it. An ionisation mechanism based on an independent particle model, such as the proposed Two Step Autoionisation Model, would be consistent with the analysis of both Connerade et al (1979a) and Rose et al (1980), whose ab initio calculations assume the validity of the independent particle model. If it had transpired that the anomalies interpretation had required a many body based model, then this would have cast doubt on the fundamental adequacy of the MCDF calculations performed by Rose et al (1980). It is worth recalling in this context that Baig et al (1984) in

their high resolution studies of the Barium 5p absorption spectrum had discovered a further two series which they could not plausibly link with any of limits calculated by Rose et al (1980) (Chapter 1).

Section 2.3 discussed the methods by which a complex spectrum can be analysed. This is done primarily by semi-empirical techniques which can be checked for authenticity by using Lu Fano Plots. M.Q.D.T. was discussed qualitatively in some detail in order to link the graphical technique of Lu Fano plots with their theoretical origin. Ab intio calculations must be resorted to in order to identify the core states responsible for the observed series and are used primarily to search for the corresponding ionisation limit energies. They are also used to identify the low lying Rydberg members which cannot be identified using Lu Fano plots. Another use for Lu Fano plots described in Section 2.3 was for identifying the members of a Rydberg channel which can perturb a given line of another channel. This is especially useful if the unperturbed channels are known since the principle configurations required for a MCDF calculation of the energy level can then be deduced. This is significant bearing in mind that the interacting configurations used in MCDF and MCHF calculations must be chosen by hand. It is not practical in computer time to include all possible

configurations in such calculations.

In section 2.4 the 6s-5d mixing of Barium in the presence of a 5p core vacancy was attributed to the concept of parent ion mixing where the running electron is not involved in the mixing process. Other forms of mixing which involve the running electron are possible but do not lead to long series running to supernumery limits. The interest in observing the 5p spectrum of the excited states of Barium lies in the provision of further data on 6s-5d mixing which can then be compared with MCDF calculations. Finally it was predicted that the 5p spectrum from the Barium 6s5d $^{3,1}D_{1,2,3}$ metastable states would be exceedingly complex due to the possibility of many more mixing manifolds. A list of possible transitions is given in Appendix 1.

CHAPTER 3: EXPERIMENTAL APPARATUS

3.1 Introduction

In this chapter the experimental apparatus is discussed in detail with particular attention to the reasons for the configuration and the methods adopted. Section 3.2 begins by describing the overall layout of the apparatus to put the experiment into perspective. Sections 3.3 and 3.4 then discuss the requirements for the VUV continuum source and the tunable dye laser respectively and describe the construction and the performance of these two essential components. Section 3.5 discusses the specification and design of an optical system to achieve maximum light throughput. The vacuum system and the furnace are then described in Sections 3.6 and 3.7 respectively.

3.2 Introduction to the Experimental Apparatus

This section will describe the overall layout of the apparatus. As shown in figure 3D1, the VUV absorption spectrum of barium contained in the furnace (F) was photographed with a 1 [m] Yves Jobin spectrograph (S) using as a background continuum source the plasma produced by a Ruby Laser (R) focussed onto a samarium metal target (T). The Barium vapour was optically pumped by a tunable dye laser (D), injected through a small hole in the coating of the

mirror (O) used to focus the continuum source on to the spectrograph slit.

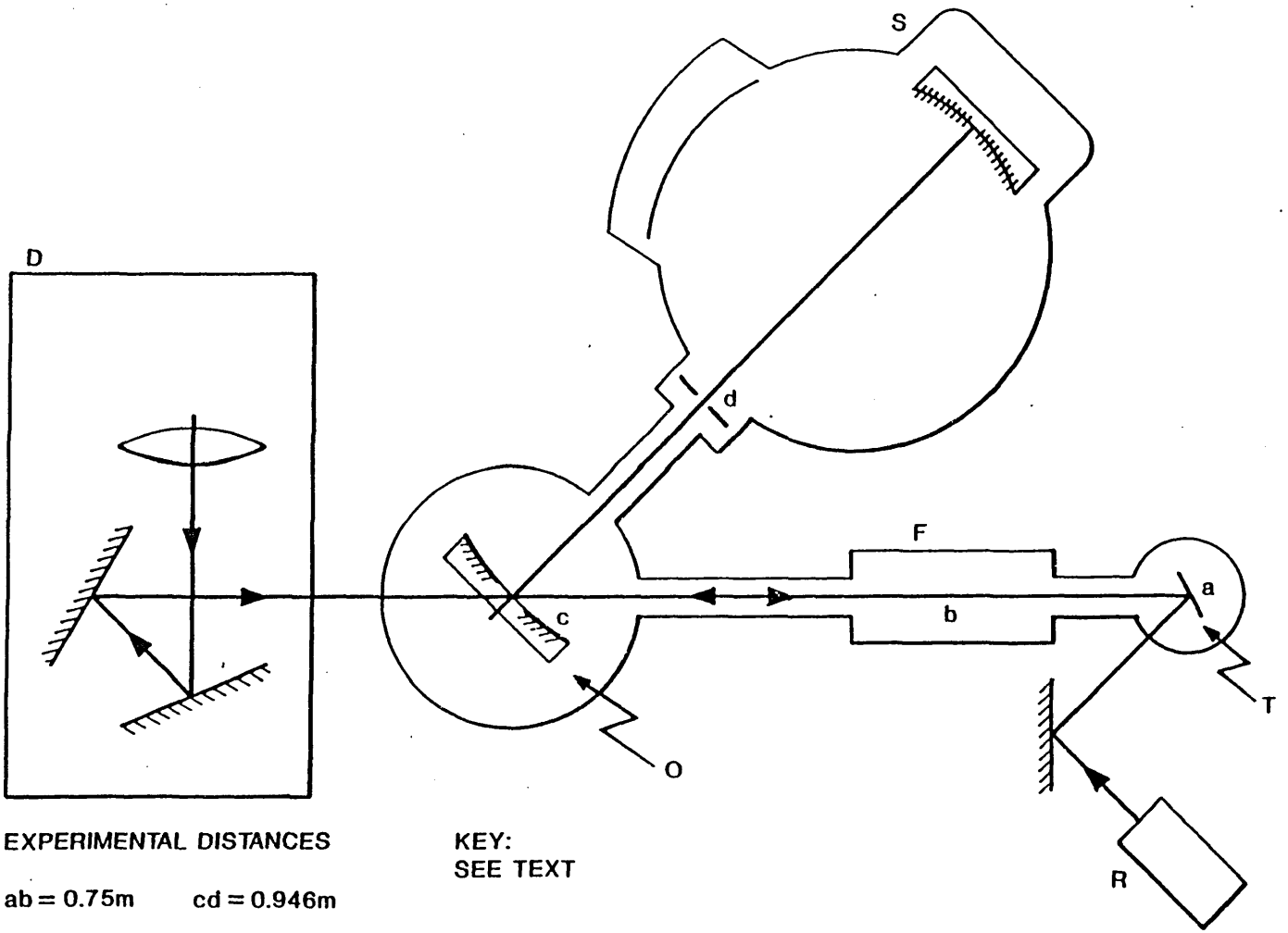
The apparatus for the purposes of this discussion could be divided up into the four main elements, the pulsed VUV continuum source, the pumping dye laser, the optical arrangement for collecting and analysing the VUV spectrum and finally the furnace. The basic experimental requirements for these elements were as listed below:

1. A bright continuum source was required to minimize the number of shots required for a good spectrum. In addition, it was desirable that the pulse length of the source be shorter than that of the dye laser envelope. This placed a further requirement that the source be both short, < 50 ns, and reproducible, < 50 ns.

2. The pumping dye laser had to be capable of saturating a column density of barium, $>10^{15}$ [cm^{-2}] over a cross-section of $\geqslant 2$ [mm]. This required a pump beam with a power density of the order of 0.4 [MW cm^{-2}].

3. An optical arrangement to focus the light source on to the slit of the vacuum spectrograph. The spectrograph would then record the absorption spectrum on photographic film.

FIG 3D1 – OVERALL LAYOUT OF EXPERIMENTAL APPARATUS



EXPERIMENTAL DISTANCES

ab = 0.75m cd = 0.946m

ac=3.041m

KEY:
SEE TEXT

4. The furnace had to contain a high column density of barium, $\gtrsim 10^{15}$ [cm^{-2}] (Ederer et al, 1974), to observe a clear 5p absorption spectrum.

The dye laser when tuned to the $6s^2\ {}^1S_0 \rightarrow 6s6p\ {}^1P_1$ resonance line at 5535Å rapidly populated the metastable 6s5d levels via the higher 6s6p level. This column of excited barium vapour was then probed by the VUV continuum at a chosen delay after the rising edge of the dye laser. The light was then collected by an osmium coated mirror located beyond the furnace and focussed on to the spectrograph slit. The spectrum was recorded on a 35 mm Kodak 101 emulsion film from Kodak Eastman Ltd. Figures 3P1 and 3P2 are photographs of the apparatus described above.

Figure 3P1 - Explanation

This photograph shows the relative locations of its six major elements. These were: -

1. The Ruby Laser - Bottom lefthand corner of picture.

2. The VUV Source Chamber - The small aluminium drum to the right of the ruby laser.

FIGURE 3P1: THE EXPERIMENTAL APPARATUS (PLAN VIEW)

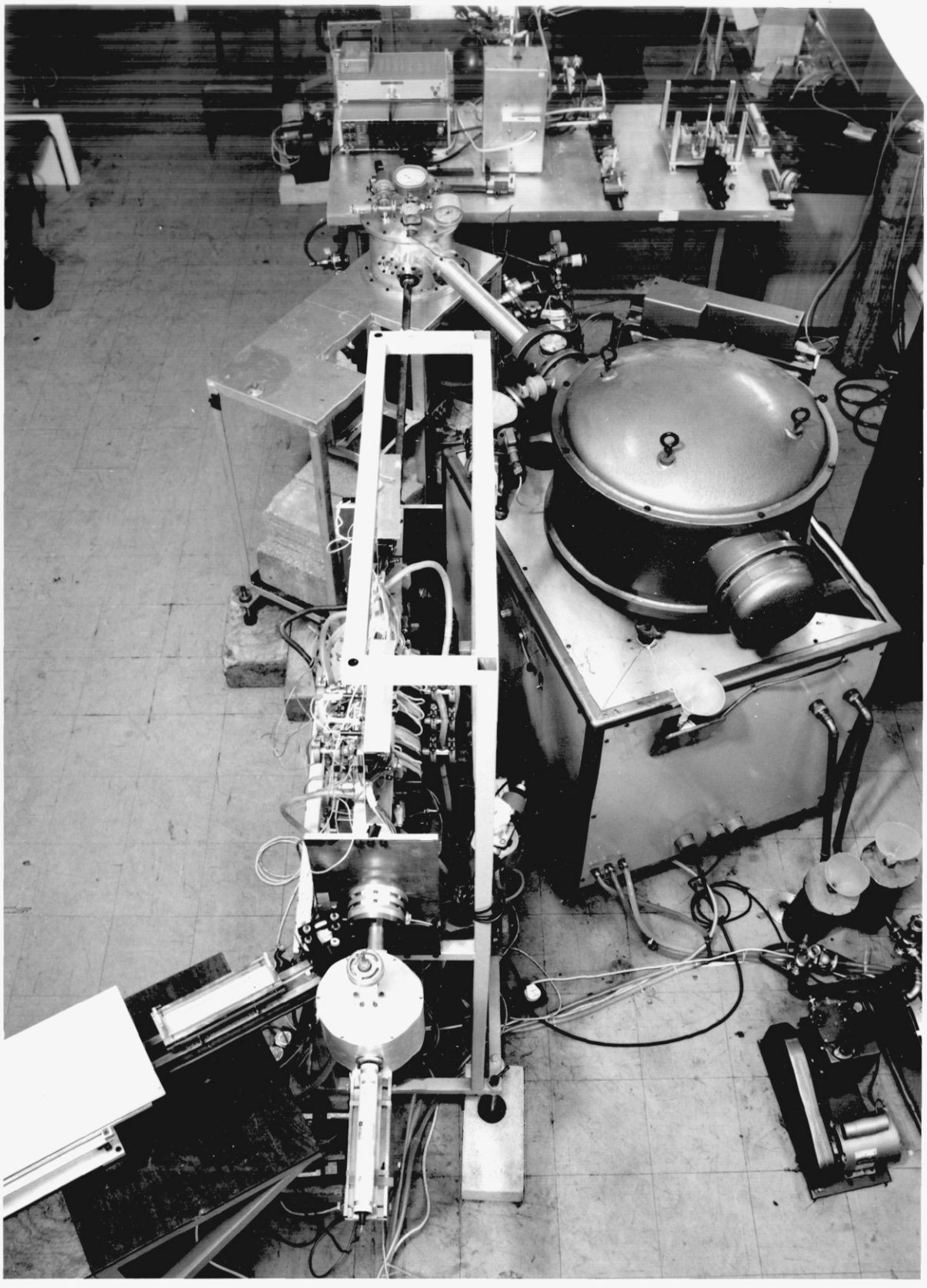
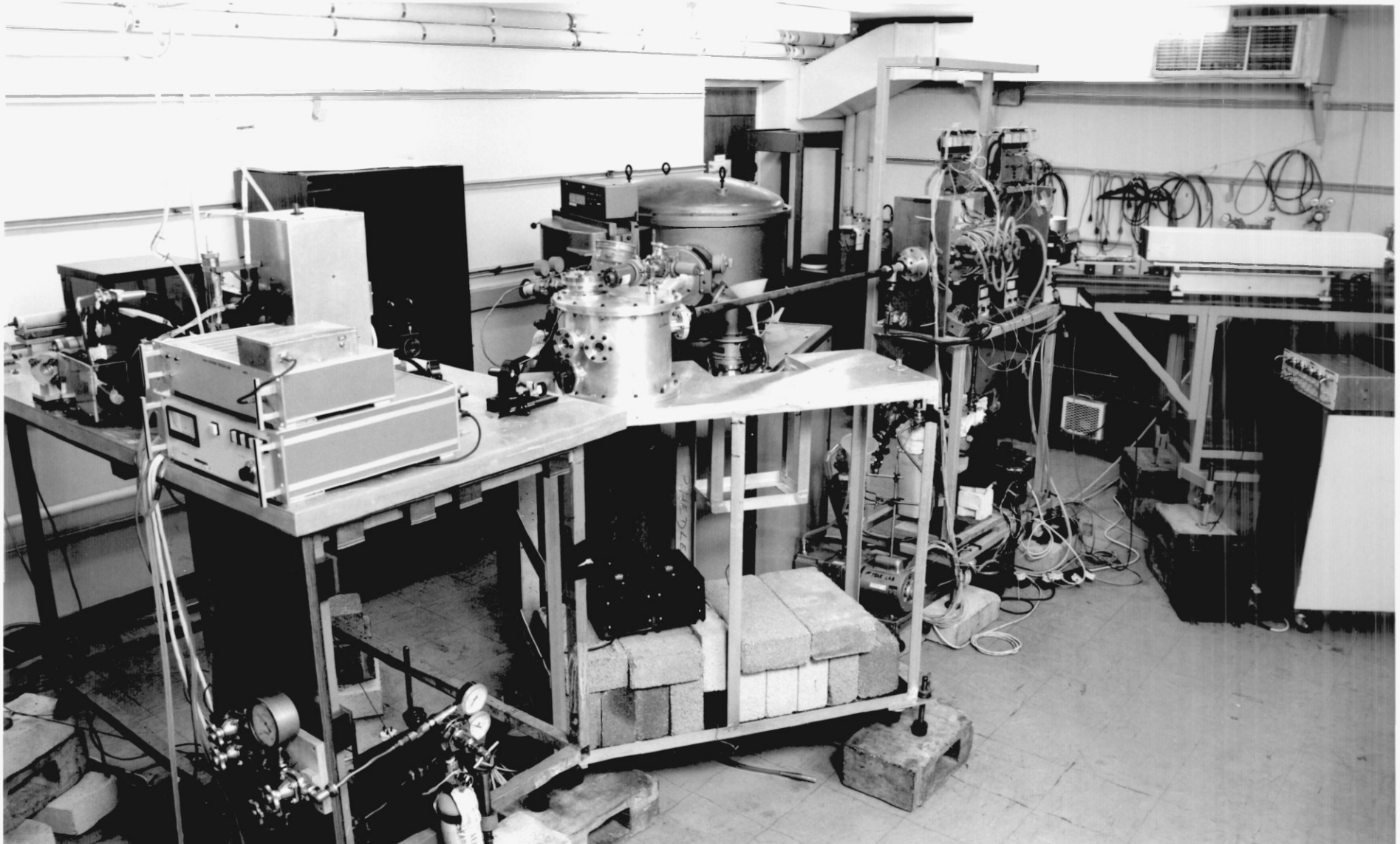


FIGURE 3P2: THE EXPERIMENTAL APPARATUS (SIDE VIEW)



3. The Furnace - This is located within the metal girder frame in the centre of the picture.

4. The Mirror Chamber - The large aluminium drum in the centre top quarter with the capsule dial gauges on its lid.

5. The Vacuum Spectrograph - Centre right of the picture.

6. The Dye Laser System - This was mounted on the large aluminium table in the top centre of the picture.

3.3 The Pulsed Vacuum Ultra Violet Continuum Source

The pulsed continuum required for this project was emitted by a laser produced plasma. This plasma was generated by focussing the output of a Q switched Ruby laser on to a samarium target. However, before discussing this source in detail it is constructive to consider the merits of the main alternatives. This study should help clarify the reasons for choosing this source and how it was superior to the alternatives discussed.

3.3.1 Continuum sources in the vacuum ultra violet

A bright and "clean" pulsed continuum between 500Å and 800Å was required for this experiment. This was because all the absorption lines arising from the excitation of the barium 5p electron lie within this wavelength range. However in this spectral range spectroscopists have always faced the problem of finding a suitable clean continuum. The common problem of most sources in this region is the presence of all manner of known or unknown impurities. These can give rise to many strong emission or absorption lines. Such lines are obviously undesirable since it is necessary to identify which lines are due to the source and which are "real" and because they may mask weak features present in the absorbing medium. Another factor to consider when choosing a source is its temporal characteristics. Its pulse length and synchronisation jitter are of particular interest. At the beginning of this work it was not apparent that the $6s6p\ ^1P_1$ state that was populated by the tuned dye laser would rapidly depopulate into the $6s\ 5d\ ^{3,1}D_2$ metastable states. It was therefore believed that the continuum pulse should be shorter than that of the dye laser. This would have ensured that the absorption of the continuum was measured only in the presence of the excited state whose natural lifetime was only 8.4 [ns].

The four main continua that have seen the most use in the VUV for absorption spectroscopy have been the Hopfield Continua (Samson, 1967), Synchrotron Radiation (Codling, 1973), the BRV source (Fox et al, 1973) and finally the Laser Produced Plasma (Carrol et al,1980). The criteria with which an order of merit could be assigned to the above sources were {a} pulse length, {b} reproducibility of pulse synchronisation, {c} brightness between 500Å and 800Å, {d} continuum quality between 500Å and 800Å and {e} source repetition rate.

3.3.1.1 The Hopfield Continua

This continuum arises from the decay of an excited inert gas molecule to a low lying state before dissociating. These excited molecules are generated by a spark discharge in a pure inert gas. The continuum pulse commences approximately 0.14 [μs] after the termination of the current discharge (implying awful pulse sychronisation problems {b}) and has a duration of 16 [μs] (which is far to long {a}). The shortest wavelengths are produced by the He Continuum, which has a useful range of 580Å to 1100Å (so it doesn't go down to 500Å {d}). The brightness of the source is extreamely weak compared with the BRV {c}. So in conclusion this source was most unsuitable for this experiment despite the excellence of the continuum between 580Å and 1100Å.

3.3.3.2 The Synchrotron

A synchrotron is an electron accelerator which has the property of circulating electrons within a closed orbit at relativistic velocities. These electrons radiate energy as predicted by the classical theory of electromagnetism. This radiation will be polarized and extends in wavelength from down in the X-ray to beyond the infra red (Codling, 1973). The radiation is also concentrated into a very narrow cone whose axis forms a tangent to the electron orbit. For example, the divergence of the French 540 [MeV] "ACO" machine is only 10^{-5} [srad] at 500Å (Kunz, 1974). The intensity of the continuum as a function of wavelength can be theoretically calculated and is very smooth. There is no line structure and so the source is unrivalled with regard to its spectral quality. However its temporal characteristics are not suitable for this experiment. The output is quasi cw with very short intence bursts of radiation (0.1-1 [ns] (Kunz, 1974)) with a frequency of between 1 [MHz] and 500 [MHz] (machine dependent). The intensity of the continuum pulses is of course dependent on the accelerator energy of the machine. However, the flux of the synchrotron pulses for small solid angles ($\sim 10^{-5}$ [srad]) is in general comparible to those of a laser generated plasma.

In conclusion, the synchrotron has many admirable properties compared with other continuum sources. However, its quasi cw nature made it most unsuitable for this project and it was in any case unavailable.

3.3.1.3 The BRV Source

The BRV source is a three electrode device developed by Ballafat et al in 1961 for producing intense continua in the VUV. This continuum is emitted by a plasma produced by a vacuum spark discharge between two electrodes of extremely low inductance. The anode of the device is usually made of Uranium both for its refractory properties and its high Z value. The electrical discharge is triggered by a "sliding spark" which propagates along the surface of an insulator from the third electrode. When the device is triggered the main vacuum spark produces a Uranium plasma at the anode with a diameter of 1.5 [mm] and an electron temperature of the order of 2.5×10^{5} [K] (Kuhne et al, 1977). The plasma continuum is very bright (10^{12} [ph/Å/srad/pulse] at 340Å (Kuhne et al, 1977) but is overlaid by a fair number of weak emission lines. The origin of the continuum has been attributed to Bremsstrahlung on account of the intensity dependence on the inverse square of the wavelength (Kuhne et al, 1977). The temporal

characteristics of the BRV have greatly improved over the years. These days the pulse length (at 640Å) and reproducibility of the pulse synchronisation are about 60 [ns] and 50 [ns] respectively. However, the pulse length of the source is wavelength dependent and increases with wavelength (400Å, 40 [ns]; 640Å, 60 [ns]; 900Å, 90 [ns] (Kuhne et al, 1982)). The reproducibility of the continuum intensity from shot to shot is quite poor at 20%, but this was unimportant in this experiment. The maximum repetition rate of device is $\sim$ 0.1 [Hz] which was much faster than the experimental dye laser. The BRV source is intolerant of high ambient gas pressures. The gas between the gap tends to electrically breakdown above $\sim 10^{-3}$ [torr], often resulting in damage to the surface of the devices sliding spark gap. Obviously this is a serious limitation if the device is placed at the end of a furnace containing a buffer gas. The chief disadvantage of the BRV is the need to periodically replace the uranium anode pin after a few thousand shots. This is necessary because of a pit which is gradually eroded into the tip of anode. Anode replacement is an involved operation and the subsequent realignment of the experimental condensing mirror would have been difficult due to the pulsed nature of the source and shot to shot variations in the position of the plasma.

In conclusion, it must be said that the BRV source could have been used for this experiment. However, the laser produced plasma is far superior on the counts of brightness (4 times better in ph/Å/srad/mm^2/pulse), pulse length (2 times better), pulse synchronisation jitter (10 times better), pulse reproducibility (4 times better), ambient gas pressures (far superior) and maintenance (much better).

3.3.1.4 The Laser Produced Plasma: a review

This plasma is produced by focussing any highpower Q switched laser such as Ruby or Neodymium onto the surface of a solid, usually a metal. The energy of the laser is normally between 1 and 10 Joules and the pulse length between 10 to 30 [ns]. The mechanism of the plasma formation has been discussed in the literature (Ehler, 1966) but essentially the arguments run as follows. The intense electric field of the focussed laser beam causes surface ionisation on the target. These ionised electrons are then rapidly heated by the laser field to a high electron temperature ($\sim$55 [eV]). Further ionisation of the target surface occurs because of these hot electrons and the electron density rapidly increases until the electron plasma frequency is equal to the laser frequency. This density varies with the laser wavelength but for ruby radiation equals 2×10^{21} [cm^{-3}]. At this density incoming

radiation is reflected and further absorption only takes place in order to maintain this density in the expanding plasma (Carroll et al, 1983). Meanwhile the target surface is heated by these electrons and "boils off" forming a hot expanding plasma. Ion stages up to and including 16 are produced in the plasma. The radiation emitted by the plasma consists of two types - line emission characteristic of the ion stages present due to bound-bound transitions, and continuum radiation due to free-bound and free-free transition. The continuum has been attributed to mainly free-bound emission (O'Sullivan, 1983) with bremsstrahlung accounting for only 10% of the total intensity and being more important at longer wavelengths. When the possibilities of this plasma as a UV continuum source were realised a hunt for the best targets was begun. It was found that low z targets (e.g. aluminium) tended to emit strong lines which dominated the weak continuum emission. The reverse tended to be true for high z targets like tungsten. The tungsten continuum was useful but was still overlaid by some line features.

In 1978, Carroll et al reported on the continua emitted by rare earth targets. The rare earths from Samarium (z=62) through to Ytterbium (z=70) were all found to emit strong and remarkably line free continua. Samarium was particularly good with a smooth continuum extending from 35Å up to 2000Å.

The few emission lines present were weak and mostly at longer wavelength. Ytterbium by comparison emitted a more uniform continuum between 35Å and 600Å. At longer wavelengths prominent emission lines were superimposed on the still strong continuum. Another paper in 1980 by Carroll et al gave further details on their work with rare earth targets. Essentially they reported a progressive decrease in the regions of line free continua when going from elements z=62 (Samarium) through to z=70 (Ytterbium). However, Mahajan et al (1979) has reported that no lines were observed above 600Å for Ytterbium when the plasma core was focussed onto the spectrograph slits. So it appears that the lines reported by Carroll et al are probably due to less highly ionised atoms occurring in the cooler periphery of the plasma. The peak emission of these plasmas was measured photographically and found to lie in the region of 100Å to 120Å.

The improved continua of some of the rare earth elements compared to other high z atoms is a very interesting phenomenon which has been attributed to the partial filling of the 4f subshell of these elements and of all ion stages which are generated in the plasma (O'Sullivan, 1983). This partial filling even with high degrees of ionisation has been ascribed to the collapse of the 4f wavefunction with higher ion stages. Such a collapse results in the binding energy of the 4f subshell growing more

rapidly than either the 5s or 5p subshells of the xenon core with increasing ion stages. Consequently the 4f subshell is more tightly bound than either the 5s or 5p subshells for sufficient degrees of ionisation. So as a result the ground states of all ion stages in the plasma contain 4f electrons. Consider for example the case of Samarium IX. The electronic configuration of the ground state of neutral Samarium is [xenon core] $6s^2\ 4f^6$. It might reasonably be expected that the ground state configuration of Samarium IX in the absence of any 4f wavefunction collapse would be xenon-like. In fact the ground state configuration according to the Hartree Fock Calculation of O'Sullivan (1983) is [Kr core] $5s^2\ 4d^{10}\ 5p^2\ 4f^4$. A partially filled 4f subshell leads to an enormous number of energy levels. There are for example 83024 allowed lines predicted for the $4d^{10}4f^6 - 4d^9 4f^7$ transition and for the $4d^{10}\ 4f^3 - 4d^9\ 4f^4$ transition there are 4574 (Carroll et al, 1983) The oscillator strengths of transitions involving configurations with partially filled 4f shells will be extremely small simply because of the vast number of allowed lines. As the result any emission lines associated with such transitions will be extremely weak and will be swamped by the plasmas free-free and free-bound continuum emission. In cases where the 4f shell is either nearly empty/full this is no longer true.

The number of allowed lines are now far fewer and the oscillator strength therefore stronger. For

example there are in principle 3 allowed lines for the $4d^{10}4f^{13} - 4d^{9}4f^{14}$ transition and 3 emission lines might reasonably be expected. This argument is supported by the observation that line emission seen in the Ytterbium plasma appeared to be due to low ion stages where the 4f subshell would be full or nearly full.

The spatial size of this source is very small compared with the others described earlier. The exact size is of course dependent on the diameter of the focussed laser spot. Values quoted in the literature vary between 120 [μm] and 800 [μm] (Ehler, 1966;Kuhne, 1982). The temporal characteristics of this source are well suited to the present experiment. In general the plasma emission closely follows that of the laser. The risetime is faster than that of the laser while the decay time is slower (Carroll et al, 1980). The absolute brightness of a Ytterbium plasma has been measured by Carroll et al (1983). At 1200Å they measured a value of 4.4×10^{10} [ph/srad/Å/pulse] using a 2.2 [J] and 30 [ns] ruby laser pulse. The corresponding value at 80Å was 1.5×10^{11} [ph/srad/Å/pulse] using this time only a 1 [J] pulse. In this connection it should be noted that the intensity of the continuum is relatively insensitive to increasing laser energies above 1 [J] (O'Sullivan, 1982).

3.3.2 Properties of the Experimental Continuum

The general properties of this type of source have been discussed in the proceeding subsection. In this subsection, the measured characteristics of the continuum used in this experiment will be listed under appropriate headings.

3.3.2.1 Ruby Laser

A commercial system from J.K. Lasers Ltd (U.K.) was used for this experiment. The system consisted of a ruby oscillator with a planer output coupler and a 5 [m] radius of curvature rear mirror. The systems rated maximum output energy was 1.5 [J] with a repetition rate of 1 [Hz] and pulse length of 25 [ns] F.W.H.M. The beam quality of the system was very poor and gave very uneven oblong burn patterns on exposed polaroid. The poor spatial quality of the output was primarily due to uneven pumping of the system's ruby rod by its two linear flashlamps. Most good ruby systems have four linear flashlamps in the pumping chamber to avoid this effect. The beam divergence of the system was ~ 8 [mrad]. In practice the laser was operated at a maximum energy and repetition rate of 1.25 [J] and 10 shots/minute respectively. This measure was designed to extend the lifetime of the systems pockel cell whose A.R. coating had repeatedly been burnt by previous users. The author using the above conditions never

encountered any problems with the systems pockel cell.

3.3.2.2 Target purity

The target used for this work was Samarium metal foil of 0.25[mm] thickness from Koch Light Ltd (U.K.). The quoted purity was 99.9% and a company representative stated that the bulk of the impurities were other lathanides. The largest non lanthanide impurity was calcium with a concentration of 10 p.p.m.

3.3.2.3 Source size

The source size was estimated by measuring the output from the spectrograph's zero order vacuum photodiode for different slit widths. From these results the source's half width was estimated to be 300 [μm]. The size of the focussed ruby spot was estimated from the size of the craters produced in the target to be 900 [μm] wide and 400 [μm] high. Intensity variations across the oblong focus were probably responible for the large discrepency between source and crater sizes.

3.3.2.4 Target orientation

The target orientation with respect to the incoming ruby laser and the direction of observation is shown in figure 3D2. The angle between the furnace and the ruby axes was 60^{o} and was the smallest which could practically be achieved. A

smaller angle would have required the target to be placed further from the furnace. A small angle minimises occlusion of the plasma by the side of crater. Figure 3P3 shows a typical target foil in its holder after use. Each crater is made by 160 shots and is of size 0.9 [mm] by 0.4 [mm].

3.3.2.5 Target debris

Debris from the target formed an opaque yellowish (due to oxidation) coating on part of the interior of the source chamber. Judging by the thickness of the coating most of the debris was blasted into a cone with a 30^{o} interior angle back towards the incoming laser beam. Little debris was blasted in the direction of the osmium mirror.

3.3.2.6 Temporal characteristics

In agreement with Carroll et al (1980) the rise time of the continuum pulse was faster than the decay time and the pulse length was about 30 [ns]. The synchronisation reproducibility was determined by that of the ruby laser which was 5 [ns]. The shot to shot signal reproducibility was monitored by the spectrographs zero'th order vacuum photodiode and was found to be better than 10%. It was discovered that a surface oxide layer on the target reduced the continuum output by 28%. The output improved progressively as this layer was blasted off

FIGURE 3D2: SAMARIUM TARGET ORIENTATION W.R.T. RUBY LASER / FURNACE AXES

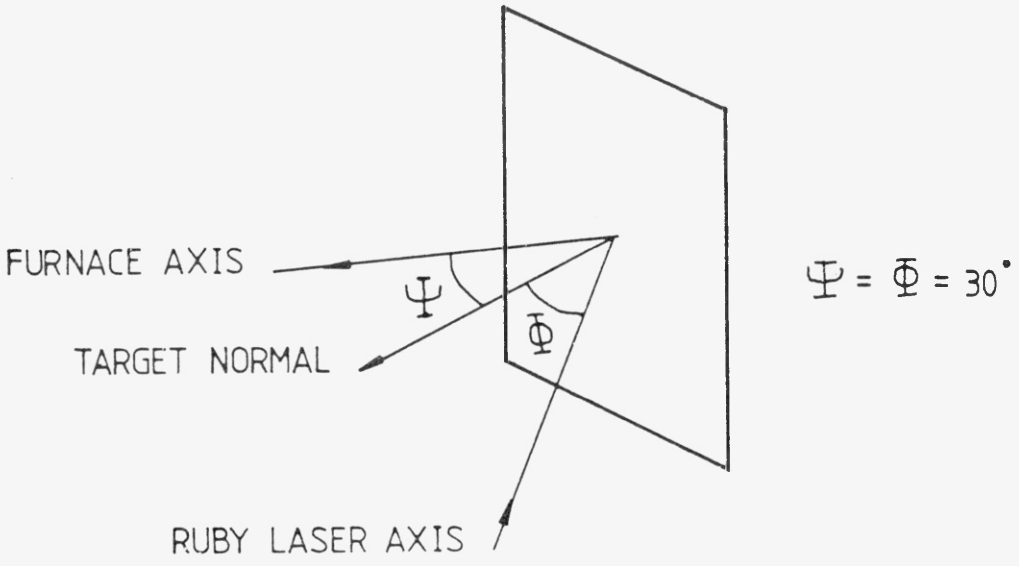
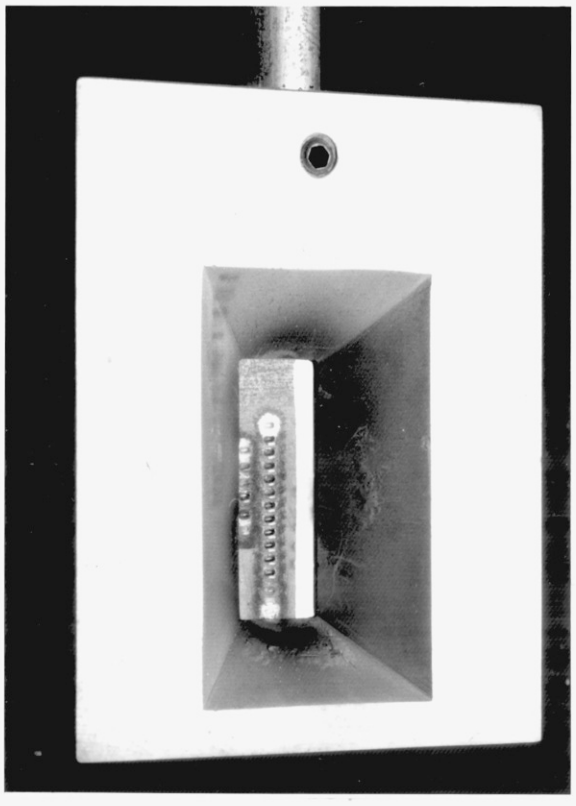


FIGURE 3P3: THE SAMARIUM TARGET IN ITS HOLDER



by the laser and the output saturated after about 20 shots.

3.3.2.7 Source brightness

An estimate of the source brightness was made using two methods. The first involved measuring the output from the vacuum photodiode due to flux reflected into zero order by the spectrograph's grating when the slit was wide open. The second approach was based on the density of exposed grains in the photographic film on which the continuum spectrum was recorded. In both cases the calculation required estimates of the osmium coated mirrors reflectivity, 30% (Cox et al, 1973), and the collected solid angle of continuum emission, 2×10^{-5} [srad]. For the photodiode method, estimates of the photodiode quantum efficiency, 10%, the efficiency of the grating into zero order, 10% (Learner, 1985, Private Communication) and the spectral range of the detected photons, 400Å were also required. This range was estimated from the spectral plate and was centred at 600Å. The long wave limit was due to the copper workfunction and the short wavelimit arose from the fall off in the grating efficiency. Combining all these factors plus the charge actually collected by the photodiode, 3×10^{-10} [C], lead to a brightness of 7×10^{11} [ph/Å/srad/pulse] which falls between the values measured by Carroll et al (1983) at 1200Å and 80Å respectively.

In the photographic calculation it was necessary to have in addition values for the following quantities: -

{i} The energy density of incident photons required to blacken the photographic film at 600Å to the observed density of~2D^{+}, 10^{-3} [Joules/m^{2}] (Burton et al (1973)) {ii} The height of the spectrum at 600Å, 2.6 [mm] {iii} The dispersion of the grating, 3.95 [Å/mm], {iv} The efficiency of the grating into 1st order, 10% (Learner, 1985, Private Communication), {v} The photon energy at 600Å, 3.3×10^{-18} [J] {vi} The number of shots in a spectrum, 160 {vii} The slit width of the spectrograph, 25 [μm] {viii} The dimensions of the source, ~ 300 [μm] diameter. Combining all of the above yielded a source brightness of 9×10^{12} [photons/Å/Steradian/pulse] at 600Å.

The factor of ~10 disagreement between the above two figures for the source brightness is primarily due to the spectrum being at its most intense at ~600Å, see figure 3D3. The average density of the spectrum between 400Å and 800Å is ~1D which from the data of Burton et al (1973) on Kodak 101-01 film would yield an average brightness of 9×10^{11} [photons/Å/Steradian/pulse] over the range 400-800Å.

$^{+}D = - \log_{10}$ (transmission)

FIGURE 3D3: MICRODENSITOMETER TRACE OF THE SAMARIUM CONTINUUM EMISSION BETWEEN 489.3Å AND 878.3Å

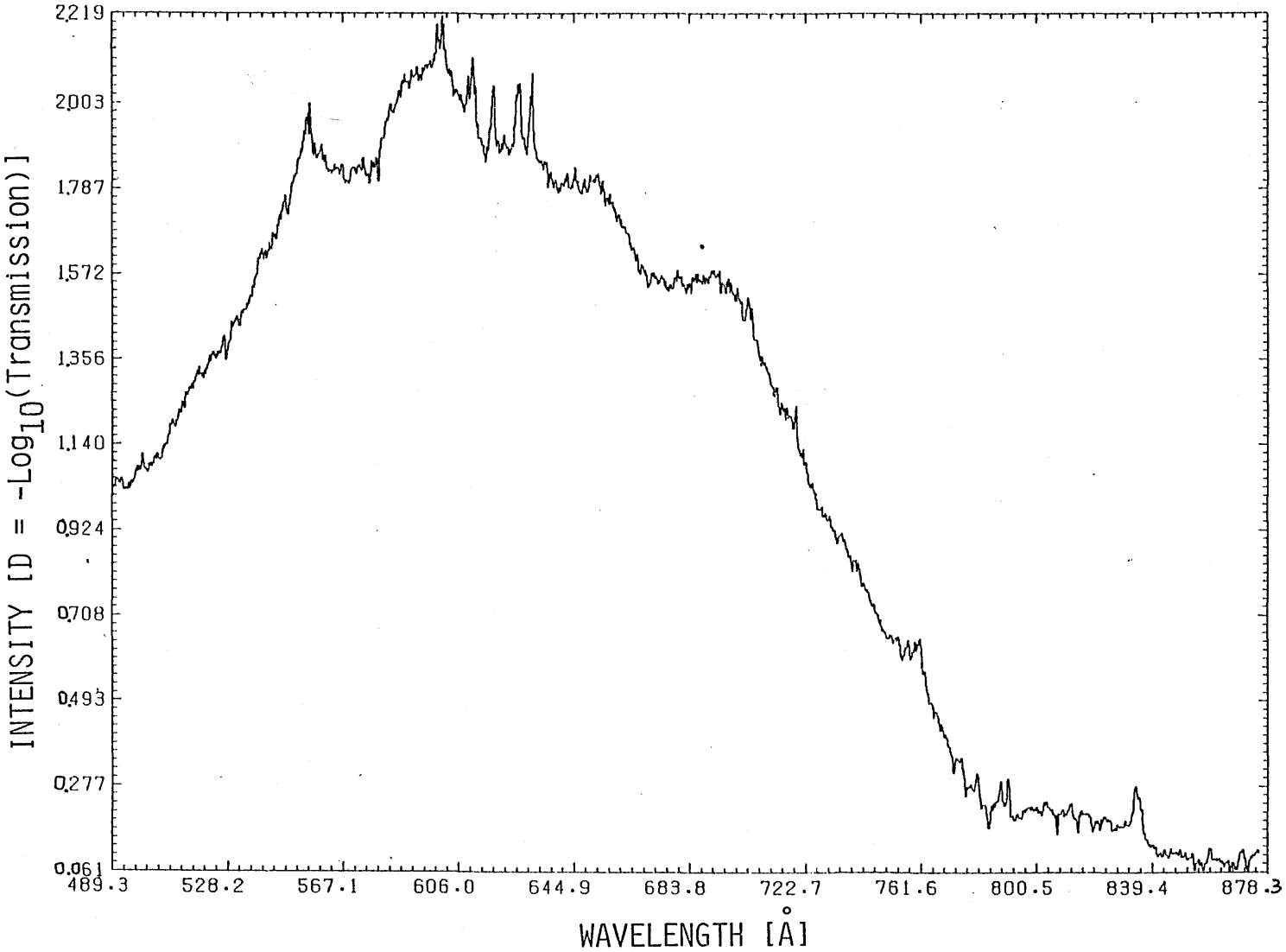


FIGURE 3P4: THE EMISSION SPECTRUM OF THE SAMARIUM LASER PRODUCED PLASMA



A - The emission spectrum

B - Illustrative absorption spectrum showing the Helium Principle Series

These results are in good agreement with those recorded by A. Pantinakis at this laboratory who obtained a figure of 10^{12} [ph/A/srad/pulse] with the same laser using a tungsten target. However, the Samarium continuum is much cleaner than tungsten with few emission lines being present. In any case, these are very weak as can be seen in the two spectra of the Samarium continuum in figure 3P4. The microdensitometer trace of the Samarium emission spectrum clearly shows the high quality of the Samarium continuum and its suitability for absorption work, figure 3D3.

3.4 The Dye Laser System

3.4.1 Introduction

The objective of the dye laser system was to saturate the $6s^2\ ^1S_0 - 6s6p\ ^1P_1$ transition at 5535Å for a column density of $\gtrsim 10^{15}$ [cm^{-2}] (section 3.2), and for as large a column area as possible. There were four essential requirements for the dye laser system which were: -

(i) A power density of $\gtrsim 0.4$ [MW cm^{-2}] was needed to saturate the above column density which was estimated by considering the spontaneous emission losses from a column of barium vapour of column density $\sim 10^{15}$ [cm^{-2}].

(ii) The spectral bandwidth needed to be of the order of the Doppler width of the Barium resonance line $\sim 10^9$ [Hz] (10 [mÅ]).

(iii) The pulse length should be larger than that of the background continuum ($\sim$25 [ns]) but less than $\sim$200 [ns] in order to reduce the risk of ionisation observed by other workers (chapter 1, section 1.3).

(iv) The geometry of the overall arrangement in which the dye laser radiation passes through a small hole (2 [mm]) in the focussing mirror M as shown in figure 3D1, demands that the laser beam have both a small cross section (less than a couple of mm in diameter) and a low divergence (a couple of mrad).

The laser configuration used consisted of a "littman" type oscillator (Littman et al, 1976), see figure 3P5 followed by a passive amplifier. Both the dye cell in the littman cavity and the amplifier dye cell were optically pumped by a broadband co-axial flashlamp laser. Figure 3D4 shows a diagram of the overall system and figure 3P6 is a photograph of the same. This pumping approach was used by the authors predecessor Julian Bowen (1985), who conducted a series of successful experiments on the fluorescence of barium vapour when pumping on its resonance transition. Bowen also used the laser

FIGURE 3P5: THE TUNED OSCILLATOR (PLAN VIEW)

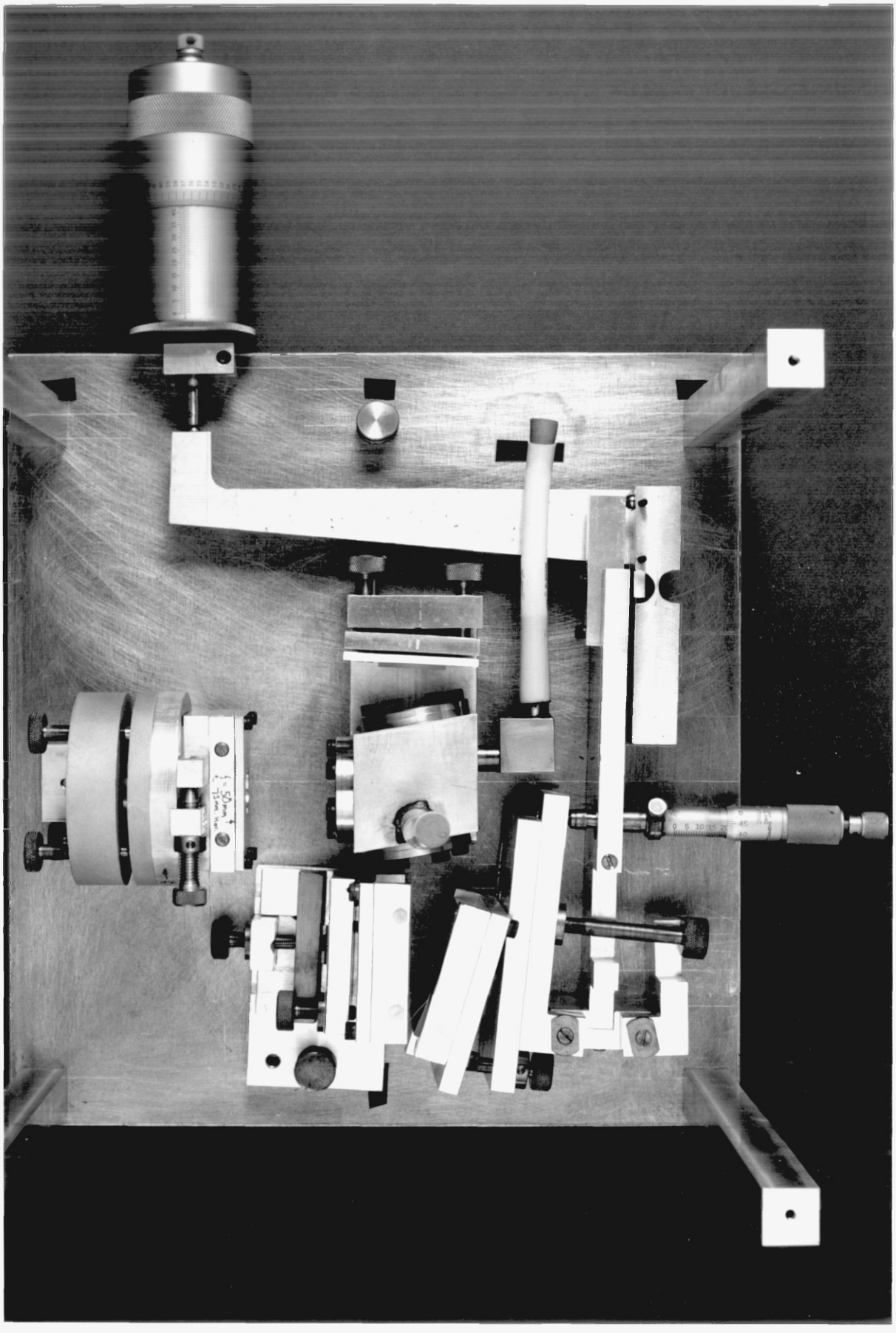
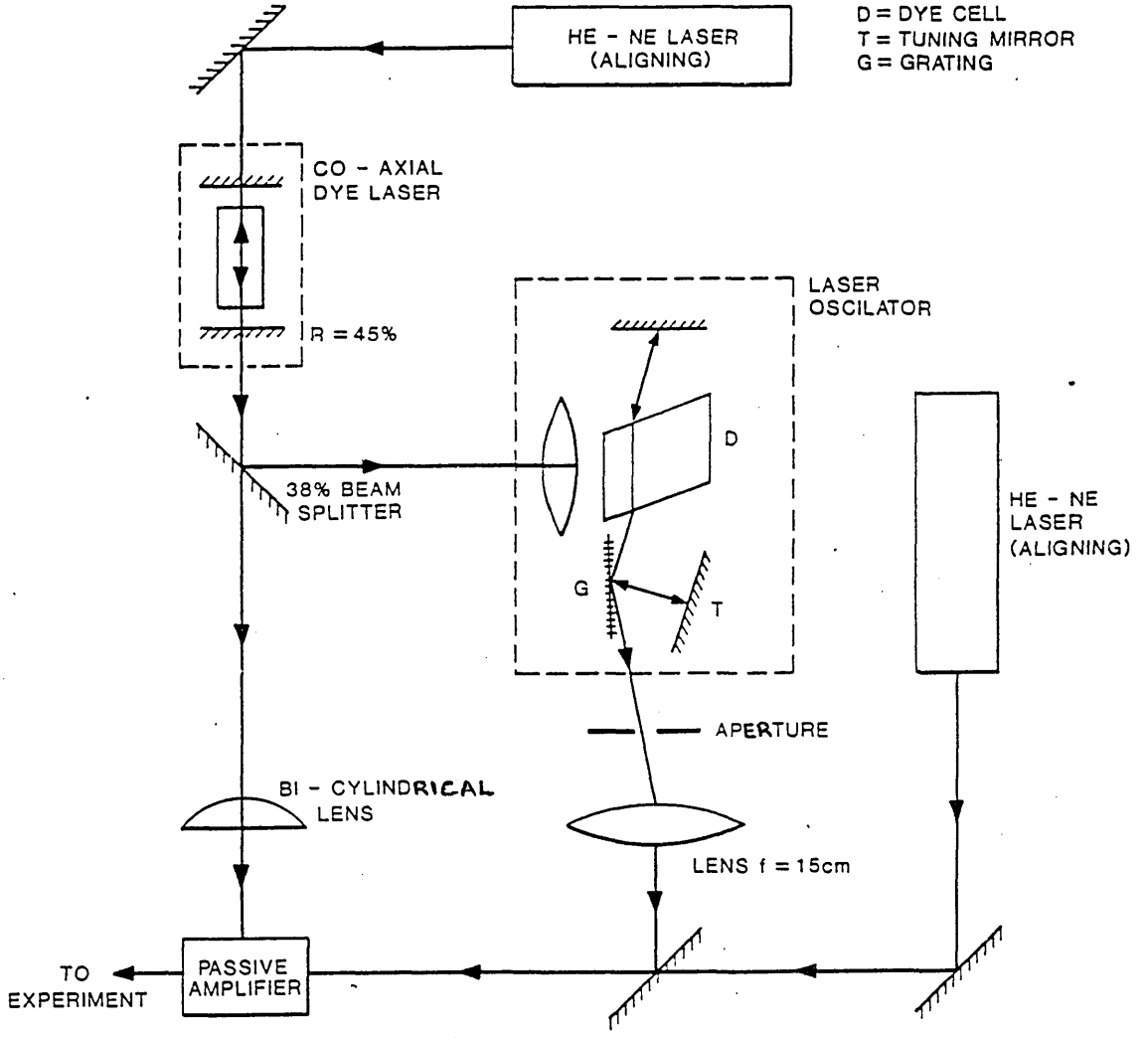


FIG 3D4 - THE DYE LASER SYSTEM



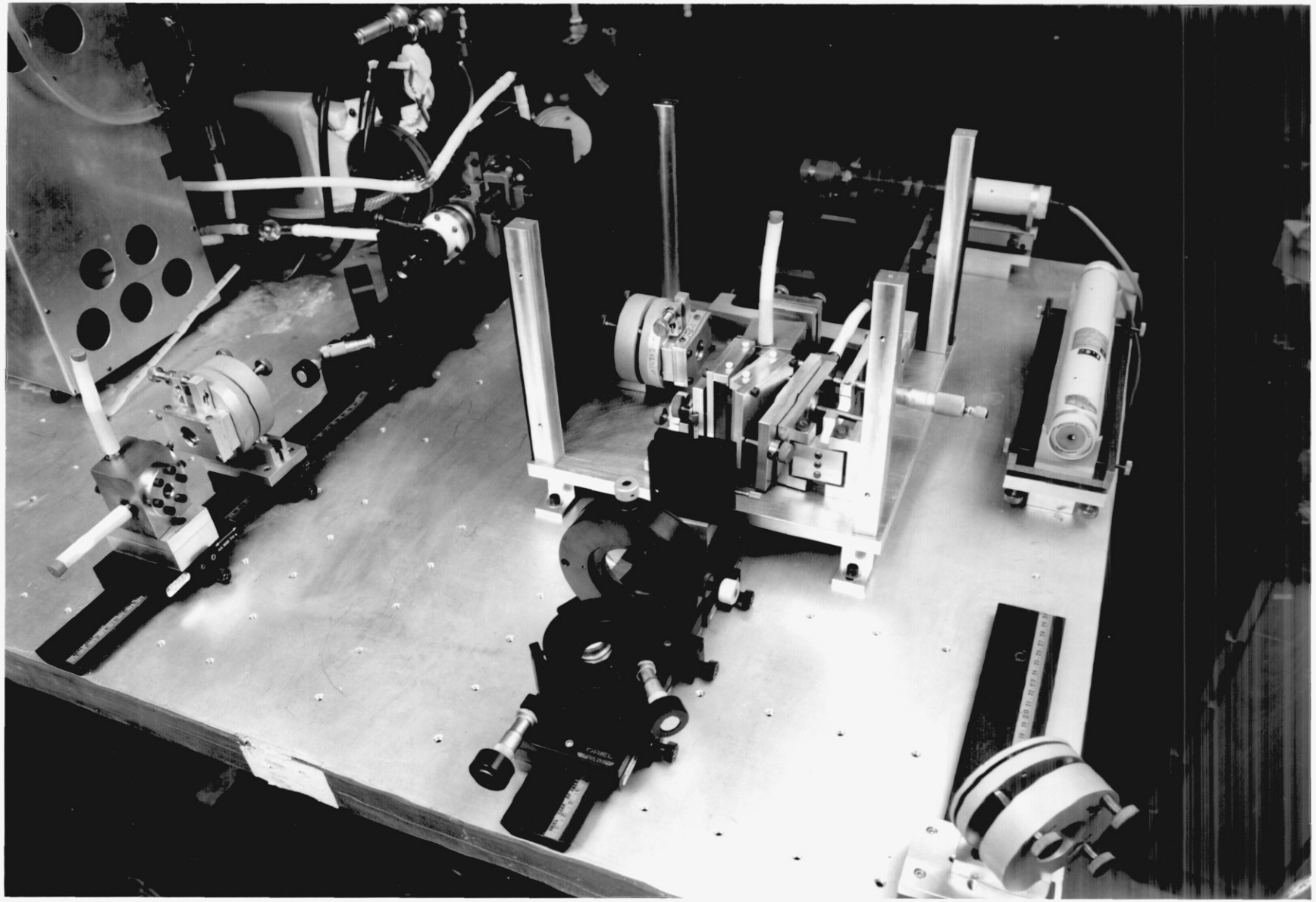
to investigate the populations of some of the metastable levels lying below the barium 6s6p $^1P_1$ level. However for the present work the oscillator was completely rebuilt by the author and an amplifier stage was constructed to increase the power output.

3.4.2 Reasons for using this type of laser

According to requirement (iii) given in 3.4.1 a dye laser with a pulse length longer than 25 [ns] was required. This requirement could not be satisfied by either a nitrogen or a doubled ruby pumped laser system and a co-axial flashlamp laser based system was needed. Tuned output from such a system could be achieved by inserting intercavity etalons within the cavity of the co-axial laser. Alternatively the laser could be run broadband and the output used to optically pump a second tuned cavity. The reasons for choosing the second alternative will now be examined.

An etalon tuned co-axial laser is not appropriate for this experiment given the injection geometry outlined in section 3.5. The problem is fundamental to the systems characteristics. In a co-axial laser the dye solution is flowed down a long quartz tube curvette located within a mirror cavity. The laser bandwidth can increasingly be reduced by inserting more and more etalons of

FIGURE 3P6: THE DYE LASER SYSTEM



decreasing free spectral range inside the cavity. Unfortunately the efficiency of the cavity is grossly reduced by these etalons and normally a second flashlamp pumped amplifier is located outside the cavity. The beam divergence of this system is quite good at 2 [mrad] but the beam diameter is quite large at 8.5 [mm] for the co-axial flashlamp heads available to the author. It is difficult to estimate the power output to be expected from such a system since this is dependent on many factors. Factors such as the electrical inductance of the flashlamp circuit, the energy discharged through the flashlamps, the dye used are but a few examples. Nevertheless an estimate of an upper limit for this output can be made from the results of Salter who used a system of this type. Salter (1979) achieved a 0.4 [MW] output within a 0.3Å bandwidth at 5896Å using the dye Rhodamine 6G. By comparison the output at 5535Å for the same bandwidth using the dye Coumarin 540A, (Exciton Chemical Corporation Inc (USA)) the most efficient dye at this wavelength, would have been much less (by a factor of at least 2). This is because co-axial lasers are much less efficient with coumarin dyes (Exciton Chemical Corporation Inc.(USA)). By contrast the littman oscillator amplifier used for this experiment gave a ~70 [kW] maximum output with a beam diameter of less than one [mm] emerging from the amplifier and a beam divergence of only 0.5 [mrad]. So the etalon tuned co-axial system was capable of yielding in principle

up to 2.9 times as much tuned power as the littman system. However, requirements (i) and (ii) of subsection 3.4.1 need a higher power density than that used by Salter, within a narrower spectral band width. This could not be achieved simply by focussing the laser into the centre of the furnace because of the geometrical constraints of (iv), which requires the beam to have a diameter of about 2 [mm] where it enters the system and a comparable diameter (energy dependent) in the centre of the furnace, 2.3 [m] away. The combination of small cross-section and low divergence could not be achieved with a co-axial system. The littman system on the other hand, was capable of giving 0.7 [MW cm^{-2}] over a diameter of 3.6 [mm] in the furnace after passing through the 2 [mm] mirror aperture.

3.4.3 The Broad Band Pump Co-Axial Dye Laser

A broadband co-axial dye laser was used to optically pump both the littman oscillator and its amplifier. This type of laser has been described in great detail by both Skinner (1974) and Salter (1979) and was similar to the one operated by the authors predecessor, Julian Bowen (1982). The laser's active medium consists of a dye solution which was flowed down a long cylindrical quartz cuvette and was optically pumped by a linear co-axial xenon flashlamp. This flashlamp emits an intense continuum when ever a high energy electrical

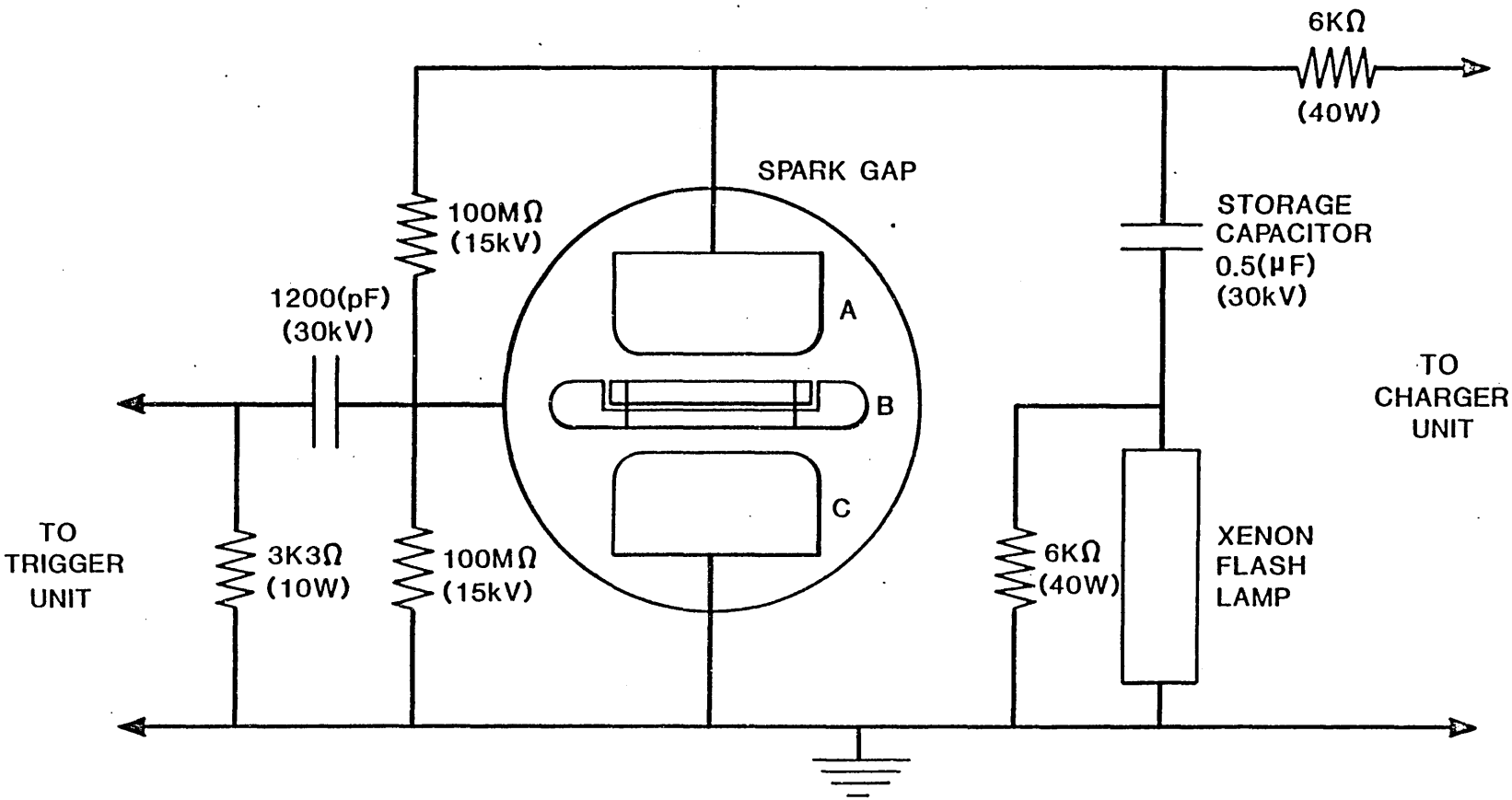
discharge is passed through it.

The laser cavity is produced by placing a dielectrically coated broad band mirror at each end of the dye cuvette. The reflectivities of the two mirrors were respectively ~100% and 45% at 4800Å and were aligned using a He Ne laser beam which ran colinear with the flashlamp axis. The dye cuvette formed part of a closed loop through which a total of 1.5 litres of dye solution was circulated. This solution was sucked out of a glass reservoir by a micropump (run off the mains), then pushed through a filter unit followed by a heat exchanger, before entering the dye cuvette after which it was returned to the reservoir to be recycled. The filter was a Balston unit fitted with a 5 [μm] pore size filter. The heat exchanger was simply a glass spiral submerged in a water tank through which cold tap water was flowed. As a result the dye temperature was a function of the season and varied between ~13°C in winter to ~21°C in summer. The heat exchanger was necessary to prevent the dye being heated up to ~31°C by the micropump. The dye solution consisted of Coumarin 480 Exciton Chemical Corporation Inc (USA) dissolved in methanol at 30 [mg/litre] (1.2×10^{-4} [molar]) concentration.

About 90 [J] of stored electrical energy was discharged through the co-axial flashlamp per laser shot. Storage and discharge of the energy was

controlled by the circuit in figure 3D5. Energy was stored on a 0.5 [μF] high voltage capacitor that was charged up to 19 [kV] through a pair of 6 [kΩ] resistors by a Hartley Measurements Ltd (U.K.) capacitor charger unit. A three electrode spark gap pressurized with nitrogen gas to just below its breakdown threshold at 19 [kV] prevented the capacitor from automatically discharging. The 6 [kΩ] resistor connected to the "live" line of the charger unit protected the unit from high voltage spikes of opposite polarity that might have resulted from ringing in the discharge circuit. The other 6 [kΩ] resistor across the flashlamp ensured that the voltage across the spark gap remained constant. The discharge of the capacitor through the flashlamps was controlled by the spark gap. This was fired by applying to its trigger pin a 10 [kV] pulse from a Chelsea Instruments Ltd (U.K.) W8 HV unit. This pulse caused the nitrogen gas between the gap to breakdown forming a good conductor. The energy output from the laser varied but was typically 500-600 [mJ] with fresh dye and the corresponding pulse length was ∿540 [ns] F.W.H.M., see figure 3P7. However this energy was dependent on the age of the flashlamps with respect to the number of firings. This occured because the quartz tubes, especially the outer tube, became gradually opaque due to increasing surface deposits of unknown origin. The far greater opaqueness of the inner surface of the outer tube

Fig 3D5 COAXIAL DYE LASER SPARK GAP CIRCUIT



A = LIVE ELECTRODE
B = "SPLIT PIN" TRIGGER PIN
C = EARTH ELECTRODE

would tie in with the minimization of the lamps inductance if the discharge occurred near this surface. This is because the earth return loop is formed by a co-axial brass tube outside the flashlamp. Increasing opaqueness of the outer tube reduced the amount of light reflected by the aluminium reflector wrapped round this quartz tube, and thus the dye pumping. Restoration of the laser's performance was achieved periodically (every few thousand shots) by cleaning the quartz tubes in dilute hydroflouric acid. A single fill of dye solution was adequate for a single experimental run of 160 shots. However the tuned output from the littman oscillator plus amplifier declined by typically 30% because of dye degradation in the co-axial laser arising from photodecomposition. By contrast the co-axial laser used by Bowen needed fresh dye after only 30 shots despite using a much lower flashlamp energy of ~56 [J] (15 [kV]). It is not clear to the author why Bowen's dye solution was so short lived.

3.4.4 The Tuned Oscillator

The tuned cavity consisted of a pair of 100% mirrors and a diffraction grating in the configuration shown in figure 3D6, an arrangement pioneered by Littman et al in 1976. Some of the fluorescence from the pumped region is reflected back by the rear mirror resulting in amplified

FIGURE 3P7: OSCILLOSCOPE TRACE OF CO-AXIAL DYE LASER PULSE

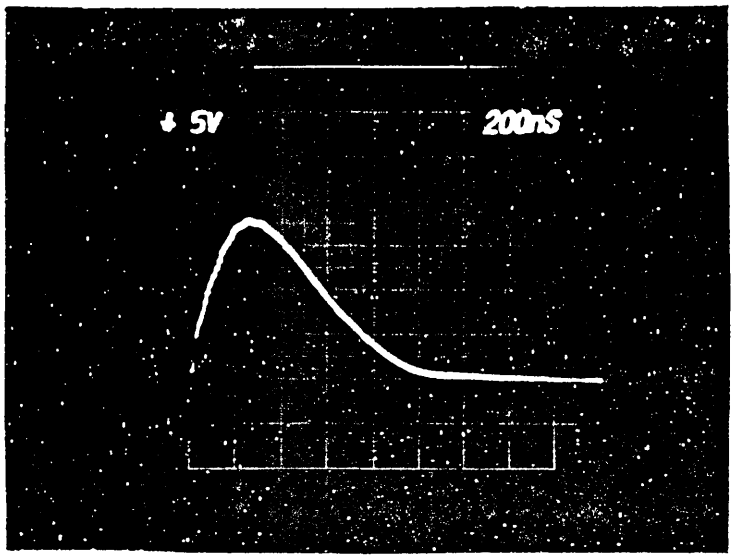
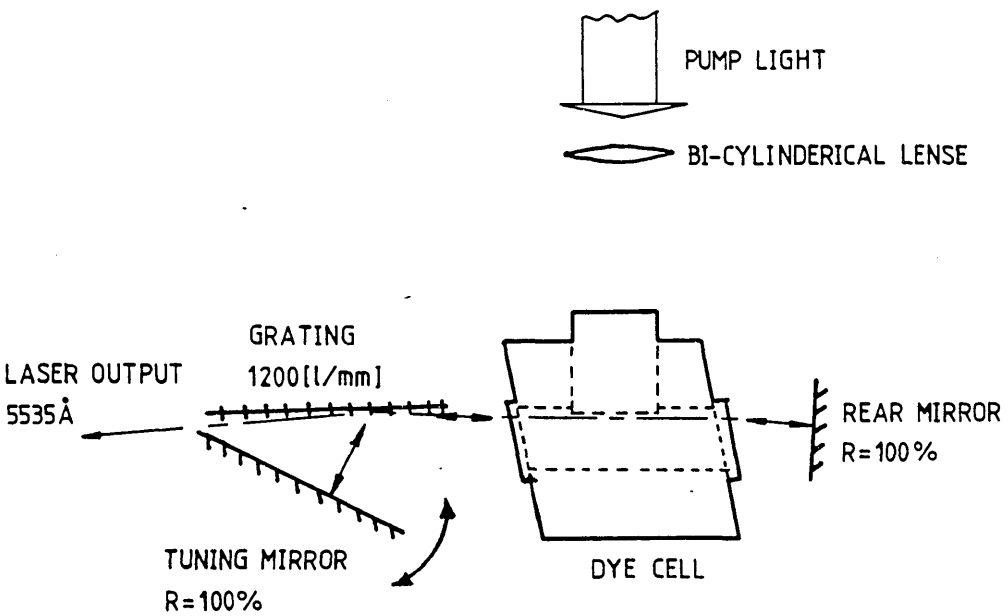


FIGURE 3D6: THE TUNED OSCILATOR CAVITY



spontaneous emission (A.S.E.) along the laser axis. This A.S.E. then hits the diffraction grating and a small amount of it (typically $\leqslant$ 5%) is diffracted into the 1st order. The tuning mirror then reflects this diffracted light back towards the grating and some of this is diffracted a second time back towards the dye cell. Any radiation which actually passes through the pumped region will undergo yet further amplification, thus selecting out a particular wavelength. Repetition of this process leads to a very narrow line width for the radiation that oscillates in the cavity, provided of course the gain in the dye is sufficiently large to overcome the basic inefficiency of the feedback. Tuned radiation couples out of the cavity very efficiently by zeroth order reflection off the grating which is very high ($\geqslant$95%) because of high angle of incidence.

Bowen's original oscillator was reconstructed by the author. The principle reason was the need to replace his dye cell which had glue sealed windows and was in a poor state by the end of his work. A new dye cell, with O-ring sealed demountable windows was constructed as a replacement. O-ring seals are preferable to glue which is susceptible to solvent attack. For example, other colleagues in the author's laboratory found that their dye solvent attacked the glue seal to the extent that their cells' windows actually fell off! The new dye cell was large with 45 [mm] separating the two quartz

windows. These windows were parallel but were inclined at an angle of 10^{o} to the inner surface of the pumping window to prevent parasitic laser action between them (no clear line of sight between them). Bowen's 1200 [lines/mm] grating was retained but a dielectric mirror was used in place of his aluminium coated tuning mirror. The cavity length was also reduced from the 180 mm's of Bowen's cavity to the 130 mm's of the authors oscillator. Reducing the cavity length increases the wavelength separation of the longitudinal modes and drives some of them outside the laser gain profile.

3.4.5 Oscillator alignment procedure

The oscillator was initially aligned using a nitrogen laser since its repetition rate when pumped with the co-axial laser was so slow (due to thermal turbulence). Firstly, the nitrogen laser beam was tightly focussed using a quartz bicylindrical lens to a line focus just inside the dye solution adjacent to the pumping window. The horizontal and vertical focal length of the lens in the visible were respectively 75 [mm] and 50 [mm]. A slightly brighter patch of light compared to the fluorescence background could be observed at a short distance from the dye cell (a few hundred mm) when the nitrogen beam was tightly focussed. This brighter patch was due to Amplified Spontaneous Emission (ASE) along the line focus. The axis of the line

focus was then adjusted to make it horizontal by rotating the bicylindrical lens. This was achieved by monitoring the location of the patch described above. The rear 100% mirror was then adjusted to reflect this A.S.E. back into the pumped region of the dye cell to produce a fairly bright and small spot at a distance. Further adjustments were made to the bicylindrical lens to optimise the brightness of the spot. After this the grating was then moved into the path of the A.S.E. beam and rotated about its vertical axis until a green line was seen along its length. It was important to remember that the grating was blazed and care had to be taken to ensure that it was correctly orientated to maximise the light diffracted into first order. A very marked visible difference was observed for the light diffracted by the grating between the two possible grating orientations. This left only the tuning mirror to be aligned before lasing action could be achieved. Prior to the entire lining up proceedure described above, the tuning mirror was roughly orientated about the vertical axis to reflect 5535Å light from 1st order back down its original path. Rotation of the tuning mirror about its horizontal axis eventually leads to lasing action. This was indicated by a huge increase in the brightness of the green streak along the grating and the output (of course), the presence of speckle in the output beam and the appearance of a bright spot on the rear mirror. The oscillator was then replaced on a

kinematic mount on the laser systems aluminium table. A beam splitter was used to slit off 38% of the co-axial lasers output which was used to drive the oscillator. It was found that the bicylindrical lens needed to be refocussed because of chromatic abberation and some fine adjustments were found to be needed for the two mirrors and grating.

The laser was then roughly tuned using a Rank-Hilger (UK) 1 [m] Monospek monochromator fitted with a photographic attachment. A barium hollow cathode lamp from Cathodeon (U.K.) was used as a reference source. Fine tuning was then achieved by maximising the fluorescence off the barium vapour column in the furnace described in section 3.7 as observed through a side port.

3.4.6 The Passive Amplifier

Unlike Bowen's original system a passive amplifier was fitted onto the laser in order to amplify the oscillators tuned output. This amplifier consisted of a dye cell identical to the one in the reconstructed oscillator (subsection 3.5.4) and was optically pumped using the remaining 62% of the co-axial laser's output. A bicylindrical lens, identical to the one used in the oscillator, was used to focus the pump radiation into a line focus. The output beam of the oscillator was focussed into this excited dye column and thus amplified. Such a

passive amplifier is more efficient than the oscillator because there is no gain being depleted by a 100% mirror reflecting A.S.E back through the pumped region and thus competing with the tuned output. The beam waist in the amplifier cell was at least 3 times greater than the waist in the oscillator dye cell by virtue of the ~X3 magnification of the focussing lens which followed the spatial filter, see figure 3D4. Alignment of the amplifier was found to be very tricky because of the low repetition rate of the oscillator. The chief problem was the need to get the incoming oscillator beam to run parallel to the amplifier pump window. Otherwise the beam partially reflected off this window giving two outputs, or it partially missed the pumped region which was obscured by the pump window. The alignment approach chosen was to deliberately reflect part of the beam off the pump window yielding two spots, and then to adjust the input beam until the two spots just merged into one.

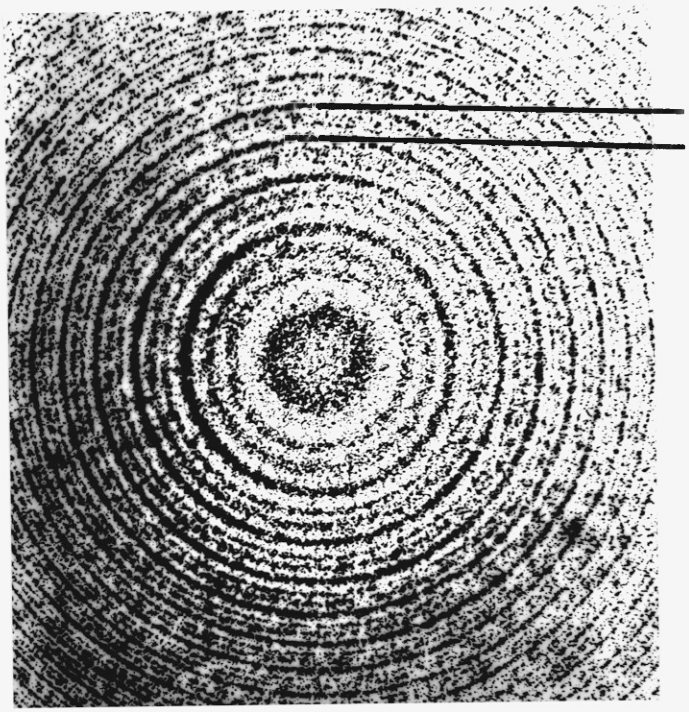
The signal gain of the amplifier was about 4 which taking into account the different input energies implied the amplifier was 2.5 times more efficient than the oscillator.

3.4.7 The overall performance of the tuned dye laser system

All of the experimental spectra of laser excited

barium were taken with the dye cells of the tuned system being filled with Coumarin 540A from Exciton (U.S.). This was found to be a suitable replacement for the Pilot 495 laser dye from New England Nuclear (U.S.A.) used by Bowen which was no longer available. The dye concentrations in both the oscillator and the amplifier were very high at 2 [g/litre] (6.5×10^{-3} [molar]) and 1.5 [g/litre] (4.9×10^{-3} [molar]) respectively using methanol or a solvent. Each dye cell was filled with only 5 cc's of dye solution which was not circulated. A practical circulation system would have been two expensive to run at these concentrations because of the volumes which would be involved. The maximum energy output of the oscillator amplifier was typically ~ 7 [mJ]. However, this was a function of the co-axial laser input and over an experiment of 160 shots would decline to 4.5 [mJ], but could be restored by replacing the pump laser's dye. The corresponding pulse length of the tuned output was typically 100 [ns] F.W.H.M. This is much shorter than the 540 [ns] F.W.H.M. pump laser pulse and the rapid termination was due to thermal turbulence destroying the optical quality of the dye solution in the dye cell. The two laser pulses rose together but the tuned output declined to zero before the peak of the pump pulse. The divergence of the output from the amplifier was extremely small at only ~ 0.5 [mrad]. Both the mode structure and the line width of the tuned output were measured using a

FIGURE 3P8: A TYPICAL FABRY PEROT INTERFEROGRAM OF THE TUNED DYE LASER SYSTEM OUTPUT



The three modes present in a single laser shot are clearly observable in this interferogram

3 [cm] thick solid quartz etalon. This etalon had a free spectral range of 35 [mÅ] (at 5535Å) and a finesse of 20. The laser output was found to contain 3 modes separated by 11 [mÅ] ± 1 [mÅ], the line width of each of these being less than the etalons instrumental width 1.75 [mÅ]. This mode structure corresponds to the longitudinal mode spacing of a cavity of optical path length 139 ± 14 [mm]. The measured optical pathlength of the cavity was in fact 143 ± 5 [mm]. Figure 3P8 shows a typical interferogram recorded using the above etalon. The laser output was horizontally polarized. This must have been due to the more efficient diffraction, at near grazing angles, of horizontally rather than vertically polarized light by the grating.

3.4.8 Injection into the furnace

The scheme chosen involved injecting the tuned laser beam into the furnace via a 2 [mm] diameter clear apperture in the osmium coated mirror. This was made especially difficult by the extremely slow repetition rate of laser which was only 1 shot every 20 seconds (max). The approach chosen was to shine a He Ne beam through the rear surface of the mirror used to direct the oscillator beam into the amplifier. By ensuring that the two beams were approximately co-linear, a cw aligning aid was created. It was then not difficult to ensure that the He Ne beam passed through the osmium coated

mirrors clear aperture and that part of it exited the furnace at the other end of the apparatus. An unexpected bonus was the circular diffraction pattern observed outside the mirror chamber due to He Ne light impinging on the osmium boundary of the clear aperture and being reflected out of the chamber via a side port. By ensuring that the rings were of even intensity, the tuned green beam could be guaranteed to run through the centre of the aperture. Thus the beam orientation could be altered with confidence without worrying about missing the aperture and burning the osmium coating off. About 56% of the incident energy was actually transmitted through the osmium coated mirror. The net flux at the centre of the furnace was ~ 0.4 [MW/cm^{-2}] maximum (beam diameter 3.6 [mm]).

3.5 The Vacuum Ultra-violet Optical Arrangement

3.5.1 Factors involved in the Optical Design

The 5p spectra of the 6s5d $^{3,1}D_2$ metastable states of Barium in this experiment were recorded on photographic film using a 1 meter normal incidence spectrograph. An alternative approach using photoelectric detection with a monochromator was never seriously considered because of the number of shots which would have been required. A spectrum at 0.1Å resolution using a monochromator with the same dispersion as the above spectrograph would have

required at least 4500 shots (for one shot at each 0.1Å interval) to cover the wavelength range 450Å to 900Å. This was clearly impractical in this work because of the low repetition rate and limited dye lifetime [~200 shots] of the dye laser. The primary aim when designing this optical system was to maximize the VUV flux density at the film for a given slit width, subject to the constraint that all of the VUV radiation should pass through the laser pumped barium column. Ease of alignment had also to be considered in practice.

Since the source was necessarily a long way from the slit, the flux density at the latter could be increased by using a condenser mirror despite the relatively low reflectivity of any coatings at normal incidence in the VUV. The best reflector in this region is osmium which has a peak reflectivity of 29% at 620Å. (Cox et al (1973)). This can be further increased to around 34% by using "semi-transparent films" of between 150 to 200Å thickness. The increase in reflectivity is attributed to interference effects in the bulk material (Cox et al (1973).

The small diameter of the optically pumped barium vapour column was the limiting aperture of the system. This diameter was only 3.6 [mm] as was explained in section 3.4. In principle the light flux could have been maximized by focussing the

source in the centre of the furnace and refocussing it onto the spectrograph slit. Such an arrangement with ideal mirrors would have increased the power incident per unit area at the slit by a factor of ~ 4 over a single mirror arrangement. However the gain in reality would have been virtually cancelled by the 30% reflectivity of the second mirror. The alternative of using grazing incidence mirrors (in the form of toroids to eliminate astigmatism) was rejected because they are difficult to align and very expensive. In any case, such a grazing incidence arrangement would have been extremely long to avoid the accretion of target material on the first toroid mirror. A minimum separation of 2.5 [m] between this mirror and the target would have been necessary for the mirror to have a useful lifetime of a few hundred thousand shots. This figure is based on the work of A. Pantinakis, who in the course of some preliminary work on laser generated plasmas in this laboratory found that debris "blown off" the target gradually coated his mirror. The reflectivity of his mirror's gold coating, which was located only 8 [cm] away from the target, seriously deteriorated after a few hundred shots (no exact figures are available).

Failing a two mirror system, the next best arrangement was a single mirror which projected an image of the source directly onto the slit. This mirror could have been used to produce either a

demagnified or magnified image of the source on the slit plane. In both cases the furnace would have been best located in the longer of the two optical arms where the solid angle of the cone of light is least. Of course the next question is which of these two arrangements was best for this work? This problem is looked at in some detail in appendix 2 and what follows is an outline of the problem and its solution. For the demagnifying case the total flux incident on the slit plane is <u>independent</u> of the demagnification M_T and is governed by the furnace aperture. However the flux <u>density</u> at the slit does scale as $1/M_T^2$. At the film plane the situation is different. Here it transpires that the flux density, and thus the number of shots necessary for a spectrum is fairly independent of M_T because of the spectrographs astigmatism. A high demagnification is however good since the height of the spectrum scales as $1/M_T$ (see appendix 2).

In the magnifying case the solid angle of light collected by the condenser mirror, and thus the total light falling on the slit plane varies with M_T for images smaller than the furnace aperture. For larger images the light actually falling on the slit plane is constant. The flux density at the slit is also constant for all M_T and it therefore comes as no great surprise that the flux density at the film is a weak function of M_T (the spectrograph's

astigmatism is negligible for this case, appendix 2). But it turns out that the height of the spectrum scales with M_T (larger length of slit illuminated) and so high magnification is advantageous.

With regard to practical arrangements, the largest sensible demagnification for a demagnifying arrangement would have been $\sim$x1/5. This figure corresponded to the situation where the solid angle subtended at the slit, just fills the grating. The largest sensible magnification for a magnifying arrangement would have been $\sim$x2. The origin of this figure is the need to keep the source mirror distance of the order of 2.5 [m]. Lack of laboratory space prevented the serious consideration of long optical arms of length greater than 5 [m]. In appendix 2 it is shown that the flux density at the film for a x1/5 demagnification arrangement is $\sim$1.12 times better than a x2 magnifying system. It is also shown in this appendix that the bulk of the astigmatism for the system is due to the spectrographs grating, and furthermore that the astigmatism of the focussing optics for sufficiently small angles of incidence has little effect on the final flux density. Consequently there was no great advantage in using torroidal mirror as regards astigmatism.

When designing the optical system, special

consideration had to be taken over how to inject the dye laser beam into the furnace. For example, it was preferable for the laser beam to propagate in an opposite direction to the continuum beam to reduce the possibility of laser light scattering into the spectrograph via the slit. The two basic alternatives were characterized by the descriptions "crossed axes" and "coincident axes" solutions, respectively. The axes of the continuum and dye laser beams for the first alternative were not parallel but were arranged to cross at the furnace core to produce the necessary overlap between the two beams. This approach was unavoidable with a conventional condenser mirror since there was no unobstructed line of sight along the continuum axis running through the furnace (bounded by mirror at one end and source (or slit) at the other). This method could have been achieved in practice by routing the laser beam so that it first missed the condenser mirror before entering the furnace core. However, it would be difficult to align over the long distances involved (section 3.5.2) because of the problem of accessing where the two beams actually crossed. In the second alternative, the laser beam was injected into the furnace via a small aperture in a near normal incidence mirror. This greatly eases the alignment since the two axes of the laser and the continuum are coincident along the entire optical arm that contains the furnace. Hence by ensuring that the dye laser hits the source

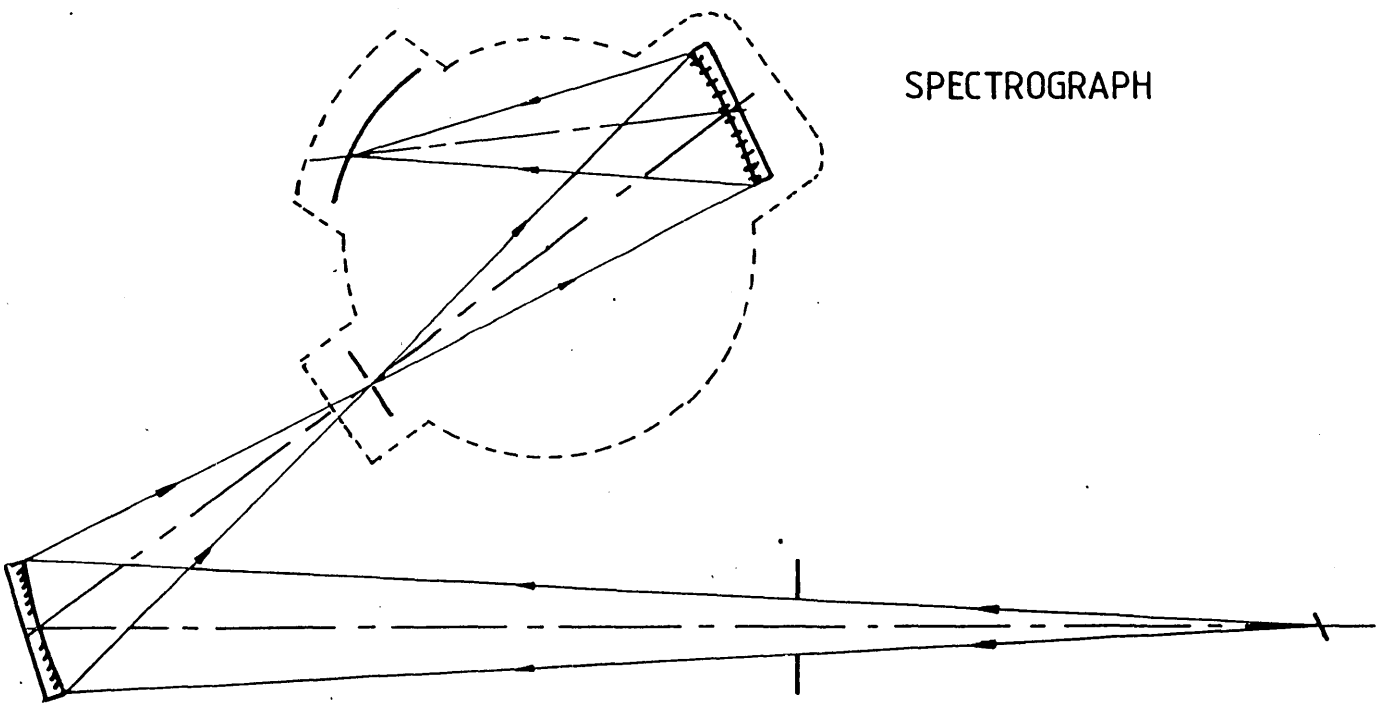
crater, overlap of the two beams in the furnace is guaranteed provided the dye laser beam has diverged sufficiently (easily checked). This novel approach would not have been practical with a torroidal mirror because of the expected distortion in the dye laser beam.

The experimental demagnification of x1/3.15 was less than the ideal x1/5 for other practical reasons. The separation between the source and the mirror needed to be kept as small as possible because of the finite divergence of the laser. This separation was in fact governed by (i) the physical size of the spectrograph body, (ii) the need to keep the angle of incidence of the condenser mirror sufficiently small so that its astigmatism was small compared with that due to the spectrograph grating, and lastly the availability of a standard mirror blank of suitable radius of curvature. The demagnification of x1/3.15 represented a compromise solution to the problem.

3.5.2 Description of the Optical Arrangement

A schematic layout of the continuum optical system is given in figure 3D7. The four main components were the VUV continuum source described in section 3.3, a circular aperture at the end of the furnace assembly, an osmium coated condensing mirror and finally a 1 meter normal incidence vacuum

FIGURE 3D7: SCHEMATIC LAYOUT OF THE V.U.V CONTINUUM OPTICS



spectrograph. The condensing mirror consisted of a $\lambda/20$ BK7 plane concave substrate which was osmium coated by Acton Research Corporation (US). It had a diameter of 25.4 [mm] and a radius of curvature 1.5 [m]. An area of diameter 2 [mm] at the centre of this mirror was left uncoated for injecting the dye laser into the furnace. A flatness of $\lambda/20$ represented the best surface finish available for a standard mirror substrate. Even so at VUV wavelengths it was effectively flat to only $\lambda/2$ but this is adequate for a condensing mirror. The mirror was mounted on a gimbol mount manufactured by Ardel Kinematic (US). Fine adjustments of the mirror alignment could be achieved in the vacuum using a pair of electrically powered micrometer screws called "motor mikes" which rotated the mount about its orthogonal axes. The angle 2i between the angles of incidence and reflectance of the condenser mirror was 30^{o}. The mirror was located 3.041 [m] away from the source and the separation between the mirror and the spectrograph slit was 0.964 [m]. So the source's image at the slit was demagnified by a factor of x0.317. The effect of astigmatism, the most important optical aberration for this system, was to stretch the "circular" image into a vertical elipse. The solid angle of the continuum emission collected by the osmium mirror was restricted by the aperture at the end of the furnace to just 2×10^{-5} steradians. The corresponding effective diameter and f/number of the mirror was therefore 16 [mm]

and 1/191 respectively. This aperture ensured that the observed absorption spectrum arose solely from optically excited barium vapour.

The vacuum spectrograph was manufactured by Jobin-Yvon (France). The instrument was fitted with a 2400 [lines/mm] grating blazed for 620Å. The grating was square with sides 25.4 [mm] and the angle of incidence of incoming VUV light was $\sim 12^{o}$. The reciprocal dispersion of the instrument was measured to be 3.95Å/mm and since a 25 [μm] slit width was used experimentally, the resolution of the instrument was slit limited to $\sim$0.1Å. A vacuum photodiode located in zero order monitored the light reflected by the grating and thus the alignment of the condenser mirror. The photodiode consisted of a copper photocathode, the photoelectrons from which were collected by a positively biased fine wire grid located in front of the cathode. The device's sensitivity is wavelength dependent as shown by the graph of the photoelectric yield of copper against wavelength given in Samsons (1967) Standard reference on page 228. The photoelectric yield climbs from the threshold at 1400Å to a maximum at $\sim$ 800Å. The yield then declines and reaches a quarter of its peak height at $\sim$200Å.

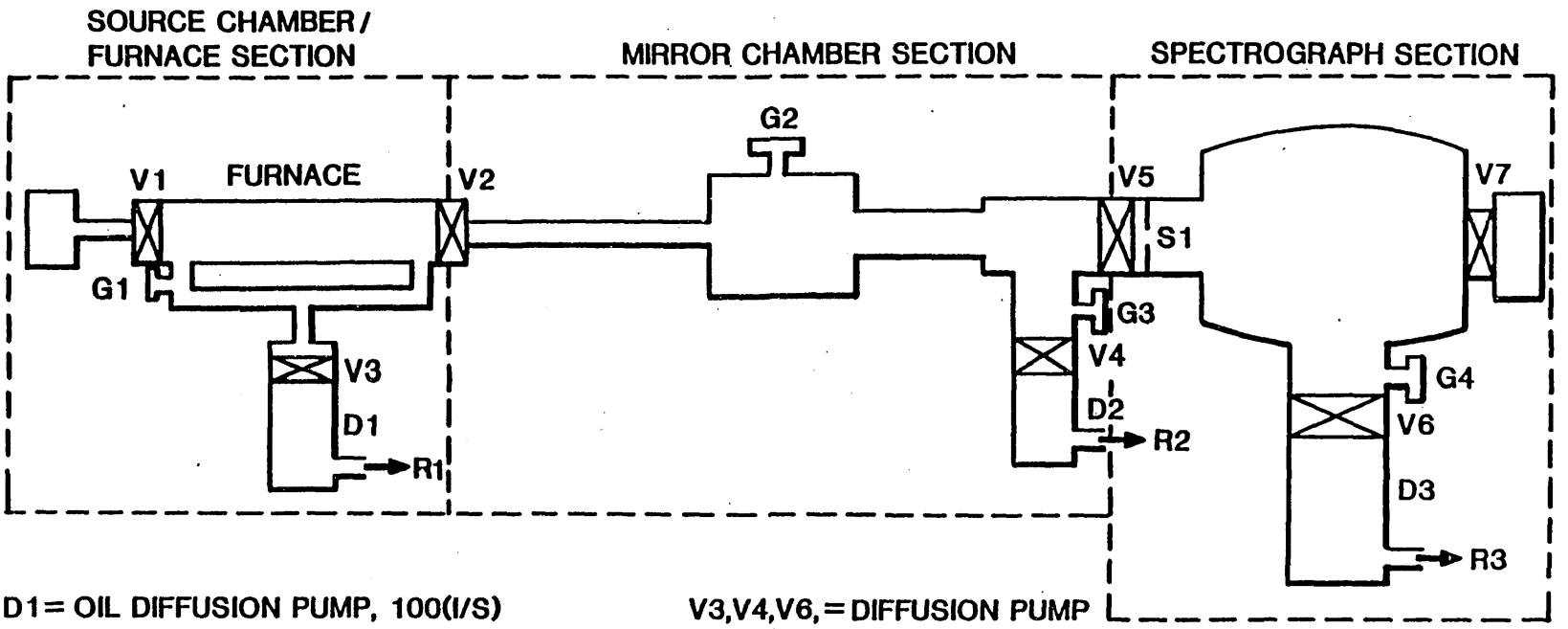
3.6 The Vacuum System

3.6.1 Description of the Vacuum System

The complete vacuum system consisted of three main sections each with its own pumping system, see figure 3D12. In this figure only the more important elements such as the Diffusion pump locations, etc, are shown. Details of, for example, the rotary pump roughing lines are omitted for reasons of clarity.

The volumes for each of these three sections were approximately; 290 litres for the spectrograph, 19 litres for the mirror chamber and 6.7 litres for the source chamber/Furnace Section (Diffusion pump volumes not included). The pump locations were completely a matter of expediency. That is the pumps D2 and D3 were an integral part of the commercial built spectrograph, likewise the pump D1 as built into the already existing Furnace. The gate valves V1 and V2 were fitted to maintain the vacuum in the rest of the system when furnace was let up to atmospheric pressure with argon for refilling. During an experiment the gate valve V2 was usually kept closed except when firing the lasers to expose the spectrograph film. This was done to prevent any barium escaping into the mirror chamber since the furnace was operated without any buffer gas. Gate Valve V7 allowed the film to be changed without requiring that the entire

FIG 3D12 – THE VACUUM SYSTEM LAYOUT



D1 = OIL DIFFUSION PUMP, 100(I/S)

D2 = OIL DIFFUSION PUMP, 55(I/S)

D3 = OIL DIFFUSION PUMP, 350(I/S)

R1,R2,R3 = FORE LINE TO ROTARY PUMPS

G1,G2 = PENNING GAUGES (EDWARDS)

G3,G4 = PENNING GAUGES

SI = SPECTROGRAPH SLIT

V1,V2 = GATE VALVE (IDENTICAL)

V3,V4,V6, = DIFFUSION PUMP FLAP VALVES

V5 = GATE VALVE (ISOLATING SPECTROGRAPH)

V7 = GATE VALVE (ISOLATING SPECTROGRAPH "PLATE CHAMBER")

NOTE:

(1) ROUGHING LINES ARE NOT SHOWN

(2) LOW VACUUM GAUGES, PIRANI'S ETC ARE NOT SHOWN

spectrograph be let up to atmosphere.

For reasons of safety the vacuum pumps were not operated overnight. The ultimate vacuums achieved after pumping for about 8 to 12 hours were $\lesssim 10^{-6}$ torr in the spectrograph, 2×10^{-5} [torr] in the mirror chamber and 3×10^{-5} [torr] in the furnace after baking it. The vacuums achieved in the furnace and the mirror chamber were not particularly impressive. However the effective pumping speeds in both cases were drastically reduced by the unavoidably long pipes. In the case of the mirror chamber, the ultimate pressure could have been greatly improved by siting a diffusion pump directly below the main aluminium chamber. Unfortunately there were no spare pumps conveniently available and these vacuum pressures were in any event adequate for the experiment. The effective pumping speeds for each chamber could be evaluated by application of the standard vacuum conductance formulae in appendix 3 to the pipe work. The pumping speed for the mirror chamber was 17 [litres/sec] and for the furnace a mere 7 [litres/sec]. From this information it was possible to estimate the leak rates in [torr litre/sec], since the gas throughputs (Gas pressure x pumping speed) for each section should equal their leak rates. This approach yielded values of 3.4×10^{-4} [torr litre/sec] and 2.1×10^{-4} [torr litre/sec] for the mirror chamber and the Furnace/source chamber respectively. These leak

rates are very high and were the principle reason why the furnace was run without a buffer gas as shown below.

3.6.2 Rapid build up of nitrogen and oxygen when pumping was stopped

Both nitrogen and oxygen strongly absorb in the vacuum ultra violet. The absorption coefficients of both nitrogen and oxygen have been measured by Huffman et al in 1963/64. In both cases their measurements extended from 1000Å-1060Å to 580Å (the useful range of their continuum source). For nitrogen the spectral region down to 724Å is dominated by very strong absorption bands. Below this limit the absorption is predominantly due to the ionisation threshold at 796Å. The strength of this continuum absorption goes from 0 [cm^{-1}] at 796Å to 400 [cm^{-1}] at 742Å to 980 [cm^{-1}] at 661Å. At lower wavelengths the strength of this continuum remains roughly constant at 980 [cm^{-1}]. The strength of the oxygen continuum lies in the range of 600 [cm^{-1}] to 1000 [cm^{-1}] for all wavelengths between 810Å and 580Å. The absorption coefficient k at N.T.P is related to the photo absorption cross section σ in cm^2 by the simple relationship, $k = n_o\sigma$, where n_o = Loschmitts number, 2.69×10^{19} [molecules/cm^3] at N.T.P. The attenuation experienced by the incident continuum radiation of intensity I_o after passing through a distance x

[cm^{-1}] of an absorbing medium is given by: -

$$I = I_o \exp(-n\sigma x)$$

where n = the number density [molecules/cm^3] of the gas and σ = the photo absorption cross section [cm^2] of each molecule. Thus the average number density of air molecules between the Samarium target and the spectrograph slit required to attenuate the continuum at 600Å to 1/e is 6.85×10^{13} [cm^{-3}] (taking $k = 980$ [cm^{-1}]). This corresponds to a pressure of only 1.9×10^{-3} [torr]. This pressure would be reached in about 90 seconds for the leak rates and volumes given above, i.e. within minutes, in the event of the pumps being isolated (neglecting losses into the spectrograph via its slit arrangement).

Such a rapid pressure build up on isolating the vacuum chambers from the pumps was indeed observed. Consequently the system had to be continuously pumped during an experimental run. In principle it should have been possible to use a buffer gas even while continuously pumping. However the Helium could not be pumped through the furnace without simultaneously sweeping the Barium vapour out of it. This problem was avoided in practice by isolating the furnace pumps from the furnace and by introducing the Helium buffer gas into the system via a needle valve located just beyond the furnace section near valve V2 (see figure 3D10). Helium was

then flowed down the long copper pipe connecting the furnace assembly to the aluminium mirror chamber, and was then predominantly pumped out via the "throttled down" diffusion pump D2 (see figure 3D12) and to a lesser extend by the spectrograph's diffusion pump D3 via the slit mechanism. This approach did not work however because of the build up of impurities in the furnace which was not effectively pumped through the small 6.5 [mm] diameter aperture connecting the furnace to the mirror chamber.

3.7 The Furnace

Figure 3P9 is a photograph of the experimental furnace complete with its asbestos insulated heating shell and figure 3D13 on the following page is a diagram of the same furnace sectioned along its optical axis in the horizontal plane. The furnace was originally constructed in 1977 by another worker and was designed with a view to running it without a buffer gas by means of copper baffles at each end which condensed out almost all escaping vapour. Unfortunately the design with regard to running it without a buffer gas was flawed. The chief problem lay with the location of all the stainless steel stops which were originally used for containing the barium in the heated region. These were located far too close to the edges of the heated region and were therefore relatively cold resulting in the Barium

vapour tending to condense out on them. The other difficulty with the design arose from the six side arms allowing observation of the hot region. The appertures in the stops located in each of the side arms increased the rate of vapour loss from the hot region. These two problems meant that it was not possible to maintain a sufficiently high vapour pressure of Barium throughout an experiment. This difficulty was only cured when the centre of the furnace was fitted with the "dynamic containment system" described later.

Temperatures along the furnace were measured using three Ni:Ni chrome thermocouples. These were located at positions 1,2 and 3 in figure 3D13 on the top surface of the stainless steel jacket. The furnace was heated by electrical resistance coils fabricated from commercial nichrome elements. The length of the heated section of the furnace was 31 [cm] which corresponded to the length of the nichrome elements. The furnace jacket and the resistance elements used to heat it were thermally insulated by a shell constructed out of asbestos sheets. The normal operating temperature of the furnace, 880^{o}C, was achieved with an electrical power input of about 2000 [W]. 880^{o}C corresponded to the temperature measured by the thermo couple located at position 2. The corresponding temperatures at position 1 and 3 were 850^{o}C. The number density of Barium at the centre of the

FIGURE 3P9: THE FURNACE

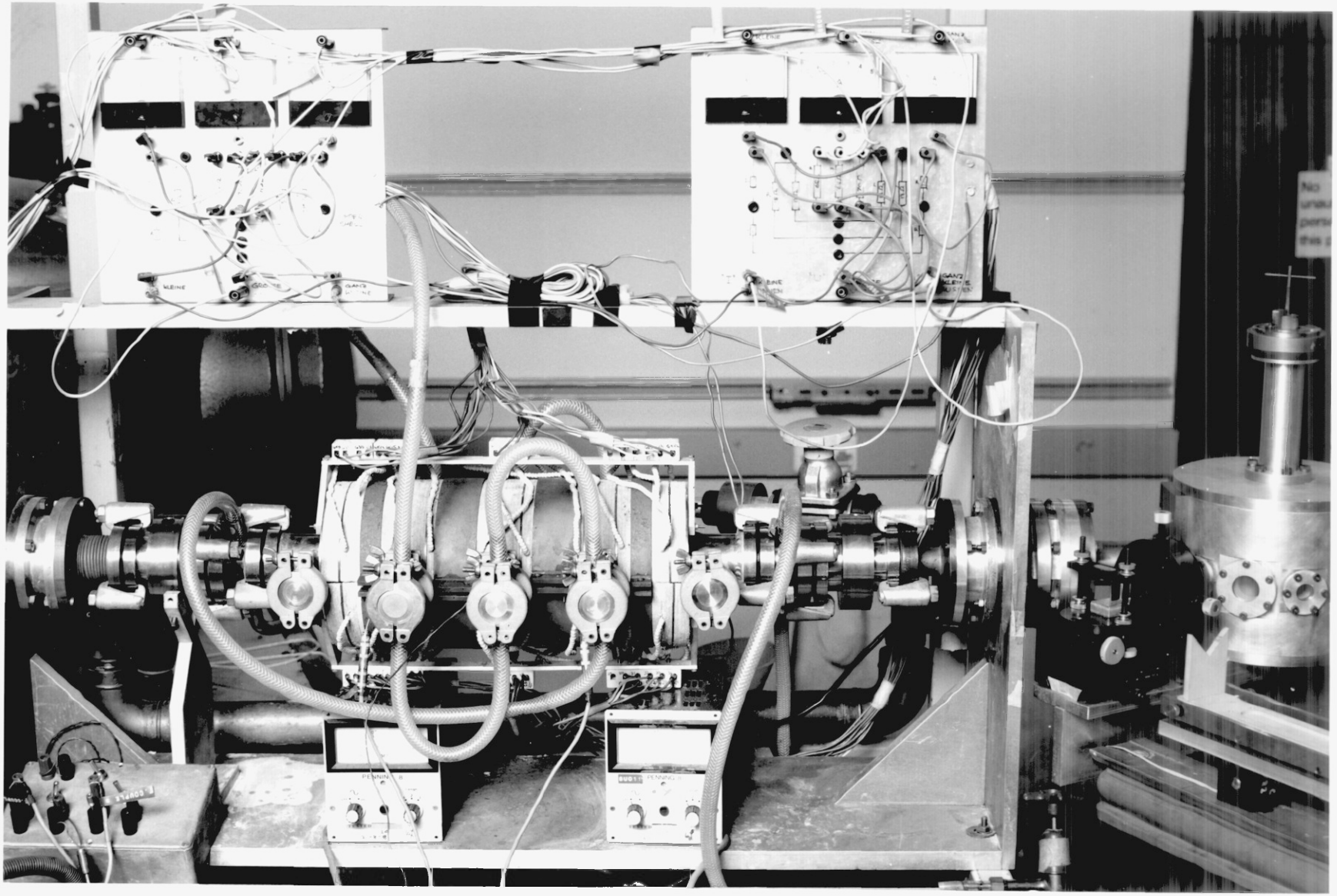
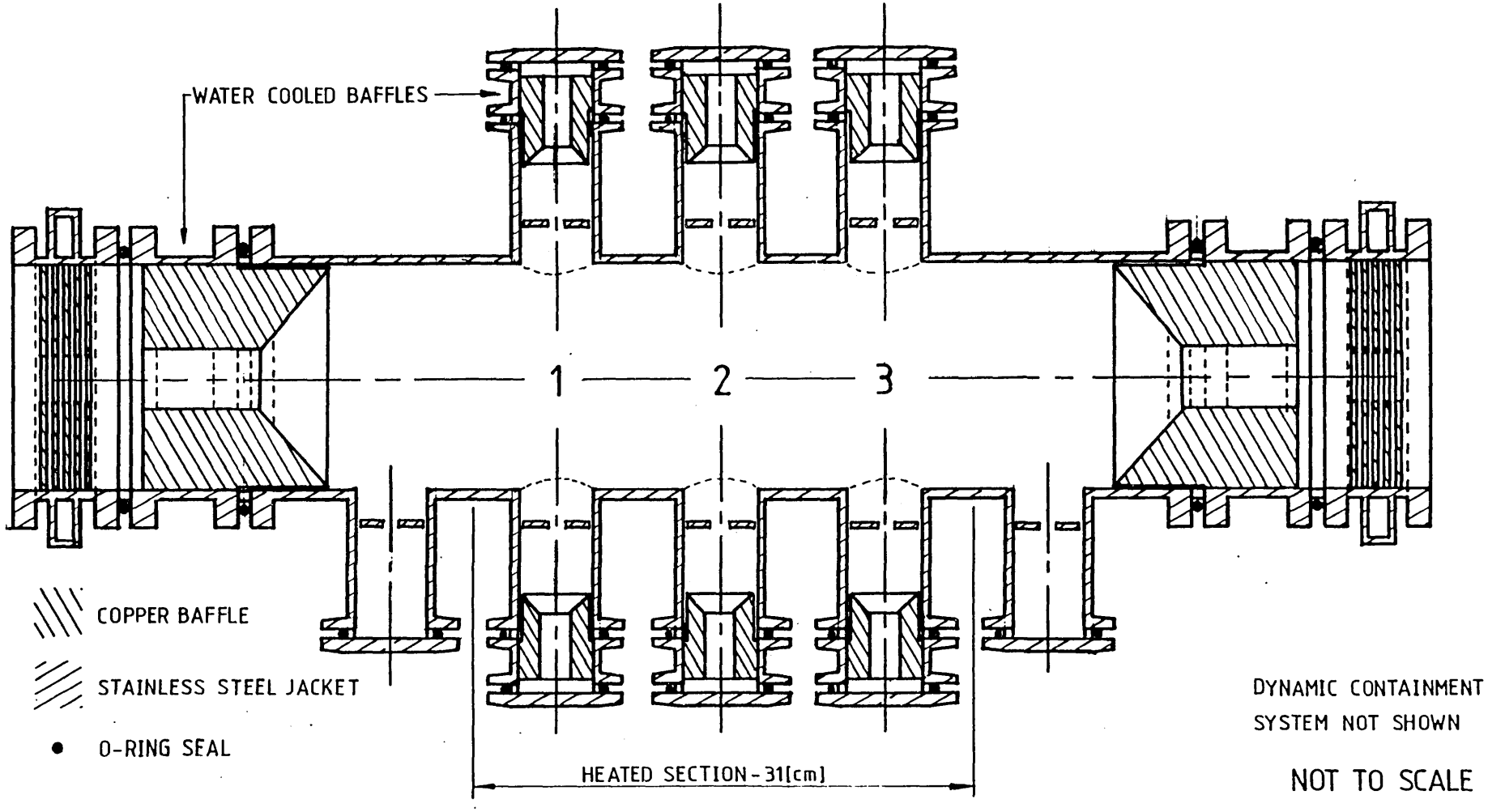


FIGURE 3D13: SCHEMATIC DIAGRAM OF FURNACE SECTIONED ALONG ITS OPTICAL AXIS IN THE HORIZONTAL PLANE

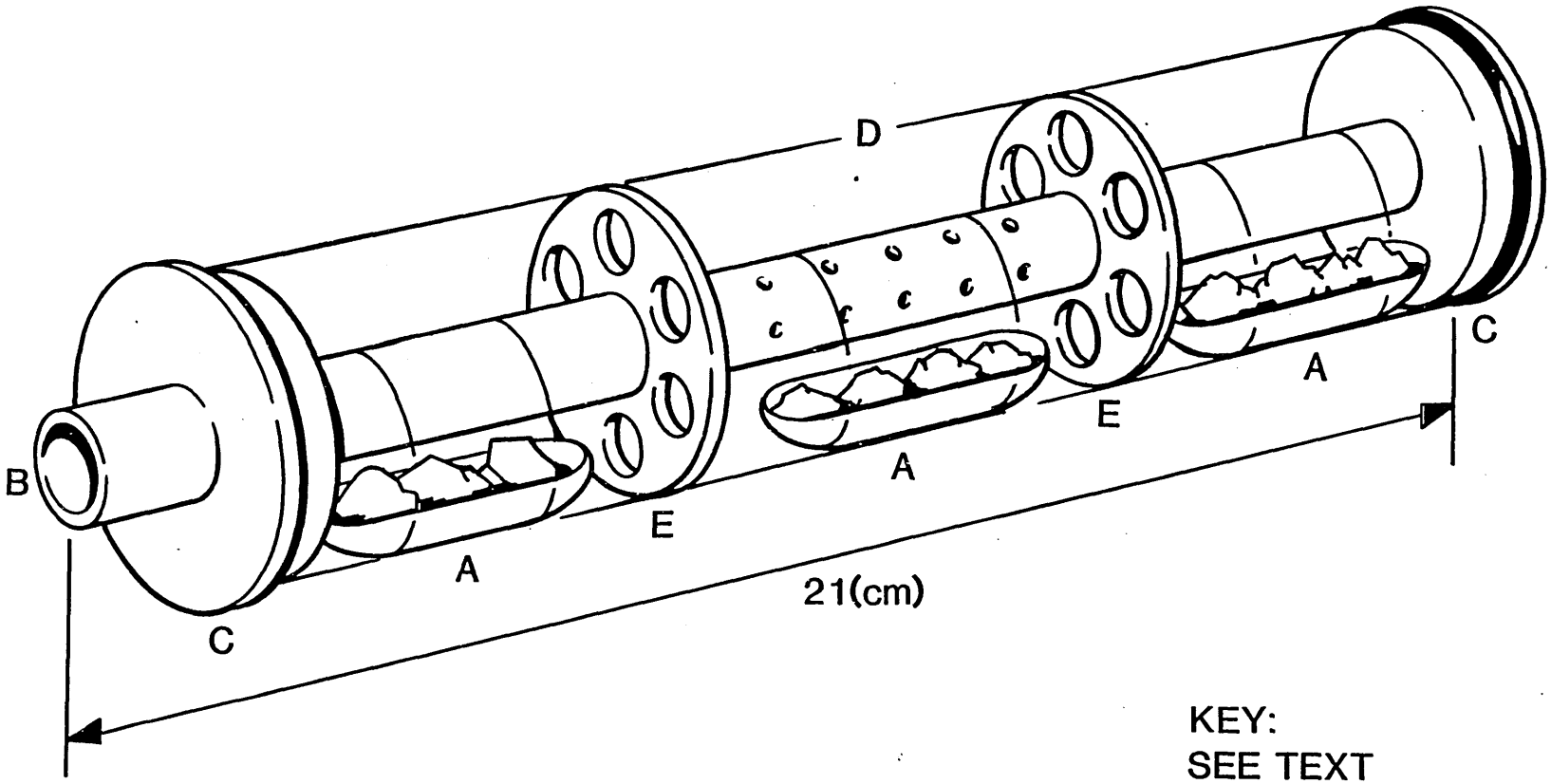


furnace was estimated using the temperature verses vapour pressure curve of Barium. A temperature of 880°C would yield a maximum number density of $3x10^{15}$ [cm^{-3}]. In practice the number density was believed to have been a good deal smaller by a factor of at least 15, see later for explanation.

The copper baffles at each end of the furnace prevented vapour from escaping out of the furnace system into the rest of the apparatus. Most of the escaping vapour condensed out on to the water cooled funnel shaped baffles. These baffles were also used to prevent the Oring seal at each end of the furnace pipe from overheating. This was achieved by the good thermal contact between the copper baffles and the oven pipe it fitted into.

The "dynamic containment system" was similar to the one discussed by Connerade (1978) and figure 3D14 shows the system as used in this experiment. Barium vapour from the three boats [A] passed through twenty small holes in the narrow bore tube [B] coaxial with the furnace. The tube was supported by two discs [C] of the diameter of the inside of the furnace. This assembly was surrounded by two sheets of stainless steel [D] in order to prevent the vapour from escaping into the side arms of the furnace. The two inner discs [E] supported these sheets, and the large holes in them ensured that the Barium vapour was distributed throughout

FIG 3D14 THE DYNAMIC CONTAINMENT SYSTEM



KEY:
SEE TEXT

the annular volume between the sheets and the inner tube. Seventy to ninety grams of Barium metal was loaded into the three boats [A]. The total area of the array of small holes was chosen to be about the same as the cross sectional area of the bore of the inner tube. This according to Connerade (Private Communication, 1984) gave the optimum performance regarding column density and vapour losses. The rate of vapour loss from the tube was minimised by the low conductance of its long narrow bore (210 [mm] long, 6 [mm] inner diameter). In practice the furnace with this dynamic containment system maintained an adequate vapour density at the normal operating temperature of 880^{o}C for six to eight hours, after which the absorption decreased and eventually (after eleven to fifteen hours) disappeared. The average mass loss, out of the system was estimated to be about 6 grams/hour on the basis of the above figures.

The furnace was heated up very gradually over at least four hours to about 770^{o}C to decrease such temperature differentials. However, the final temperature of 880^{o}C was then achieved in about one hour by winding the electrical input up in one jump. This last step aimed to reduce the much higher Barium losses that were expected at the higher temperatures.

Although vapour pressure data gives a Barium

number density of about 3 x 10^{15} [cm^{-3}] at 880°C, the actual number density was known to be lower for the following reason. There was evidence that the laser burned through the vapour column within <10 [ns] (laser pulse length attenuated by less than 10 [ns]). This set an upper limit of 2 x 10^{14} [cm^{-3}] to the number density from the considerations of section 3.4.1 with a laser power of 0.4 [MW cm^{-2}].

The absorption lines in the laser excited spectrum were much weaker than those in the unexcited spectrum. Higher number densities would have been desirable to bring up the weaker lines, but it was not possible to achieve this without a radical redesign of the furnace because of the finite containment time. This varies as the inverse square of the number density and hence pressure. This relation can be understood by recalling that the mass loss rate through a tube varies as the product of the pipes conductance and pressure gradient, and the pipe conductance at sufficiently high number density is in itself proportional to the average pressure (Turnbull et al 1962). In any event the present dye laser was not sufficiently powerful to saturate a column density higher than that actually used.

CHAPTER 4 EXPERIMENTAL PROCEDURE

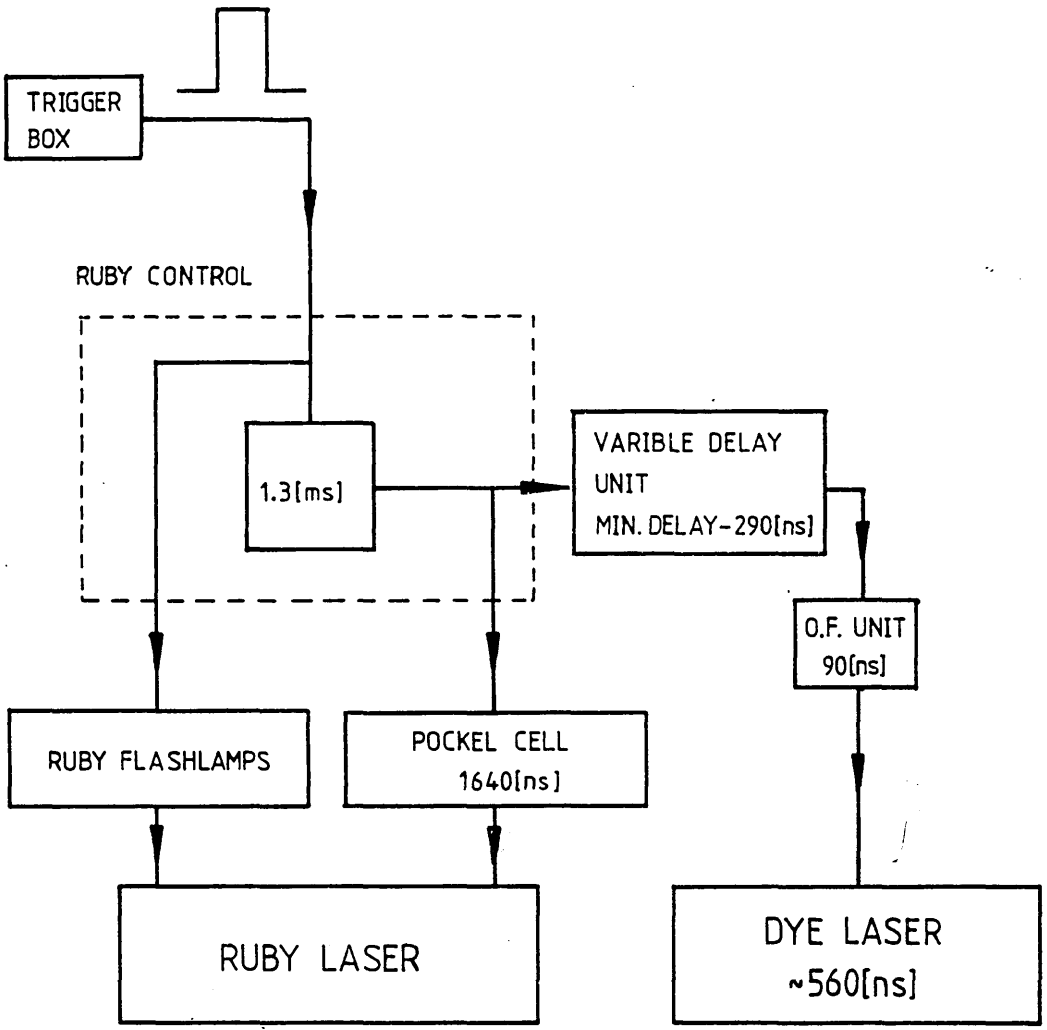
4.1 Introduction

This chapter will concentrate on the experimental procedure now that the individual components have been described in chapter 3. As such the chapter can be broken into two parts. Firstly, the recording of the 5p absorption spectrum, and secondly, the preparation of a line list from the recorded photographic spectrum. Accurate synchronization (section 3.2) between the ruby laser responsible for the continuum and the dye laser was important when recording a spectrum. The chapter will therefore start in section 4.2 with a description of the time synchronization system between the two lasers. This is followed in section 4.3 by a detailed account of a typical experimental run. Finally section 4.4 will concentrate on the preparation of a line list from the photographic spectrum.

4.2.1 Synchronisation of the Dye Laser and the Continuum Source

Figure 4D1 shows the arrangement used to control the delay between the Dye laser and the Ruby laser. The variable delay unit in this configuration enabled the Dye laser to fire between $\sim$700 [ns] before the Ruby laser and any time after it. Figure

FIGURE 4D1: SYNCHRONISATION CIRCUIT FOR CONTROLLING THE RELATIVE DELAY BETWEEN THE RUBY LASER AND THE DYE LASER



4D2 shows the time history of the events leading up to the firing of the two lasers.

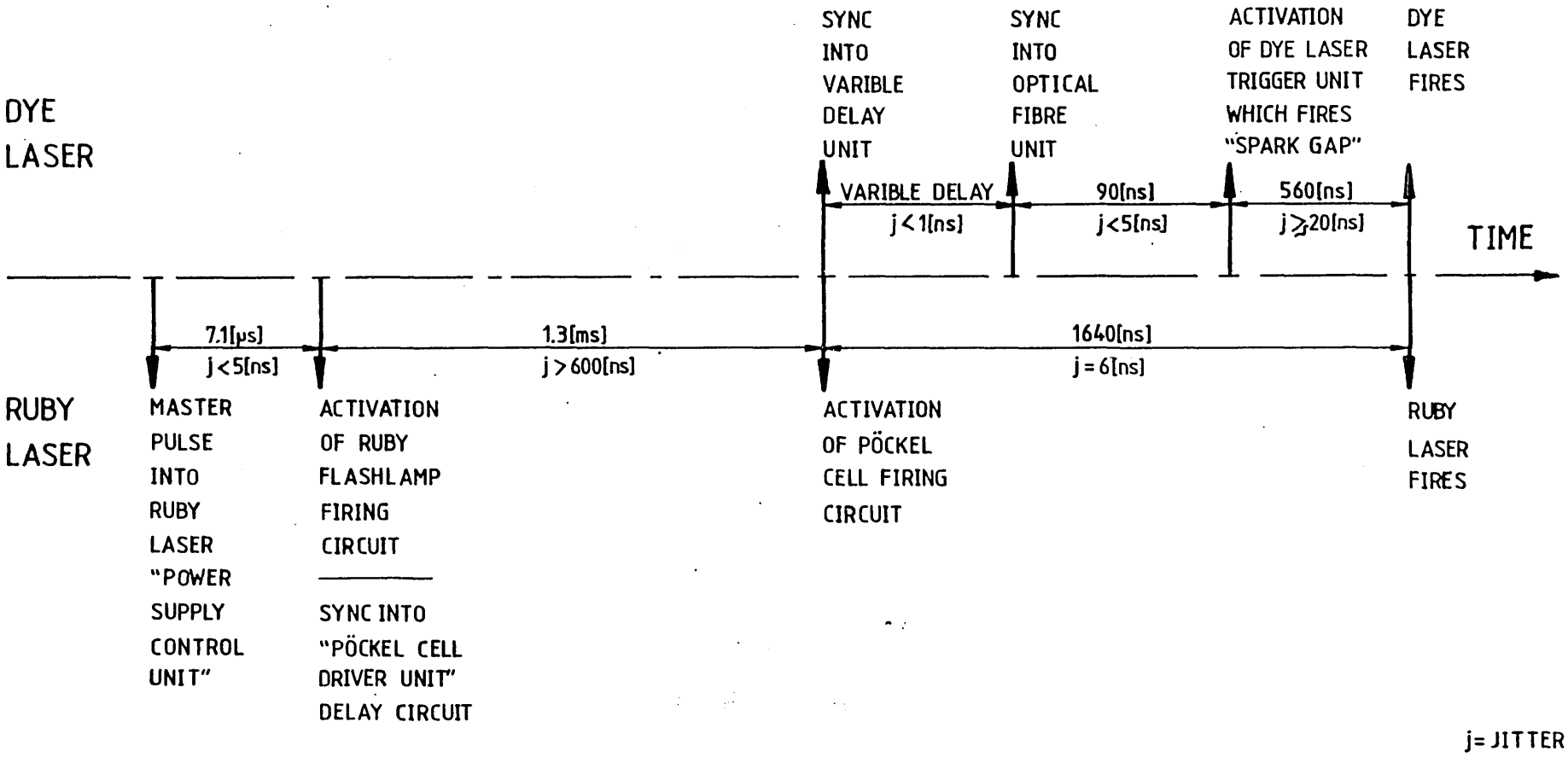
4.2.2 Description of the elements of Figure 4D1

Trigger Box - This generated the master pulse used to fire the two lasers via the circuitry shown in the figure.

Ruby Control - The Ruby laser used for generating the continuum source was manufactured by J.K. Lasers (UK) Ltd. The Ruby Control Box of the diagram represents the lasers two main control units: The "Power Supply Control Unit" and the "Pockel Cell Driver Unit". The "Power Supply Unit" controlled the charging voltage of the power supply and triggered the electrical discharge of the systems storage capacitor bank through the Xenon flashlamps used to optically pump the laser. The "Pockel Cell Driver Unit" controlled the delay between the firing of the flashlamps and the opening of the Pockel Cell which preceeded lasing. This unit emitted a sync pulse 1.64 [μs] before the opening of the Pockel Cell with a Jitter of 6 [ns] to one standard deviation.

Variable Delay Unit - The relative timing of the two lasers were controlled by a Chelsea Instruments (UK) multi-channel delay unit from Chelsea Instruments (UK). For the purpose of these experiments only a single channel of the unit was used. This was suitably altered to give delays

FIGURE 4D2: TIME HISTORY DIAGRAM OF THE EVENTS LEADING TO THE FIRING OF THE TWO LASER SYSTEMS



between 290 [ns] and 1300 [ns].

O.F. Unit - A Radio Spares (UK) optical fibre link was used to electrically isolate the two lasers.

4.2.3 Delay Monitoring

Two photodiodes were used to monitor the delay between the two lasers. One was positioned outside the source chamber and monitored the transmission of the pump dye laser past the samarium target strip. The other photodiode monitored the transmission through the rear mirror of the ruby laser. Both photodiodes (Centronics O.S.D. - 2 HSA) had a rise and fall time of 1.5 [ns]. A Tekronics 7623A storage scope was used to measure the delay between the rising edge of the Dye laser pulse and the peak of the Ruby laser pulse. The storage scope was triggered by the leading edge of the pulse emitted by the photodiode monitoring the dye laser, and was used to display the "subtracted" outputs from the two photodiodes. Figure 4Pl(i) & (ii) shows two polaroids of typical oscilloscope traces of the relative pulses. The top polaroid 4Pl(i) shows a relative delay of 60 [ns] between the rising edge of the Dye laser pulse and the peak of the Ruby laser pulse which was recorded during an experiment. The lower polaroid 4Pl(ii) corresponds to a relative delay of 250 [ns] between the rising edge of the Dye laser pulse and the peak of the Ruby pulse.

FIGURE 4P1(i) & (ii): OSCILLOSCOPE TRACES SHOWING THE DELAY BETWEEN THE RISING EDGE OF THE DYE LASER PULSE AND THE PEAK OF THE RUBY LASER PULSE FOR (i) 60 [NS] DELAY AND (ii) 250 [NS] DELAY

FIGURE 4P1(i): 60 [NS] DELAY

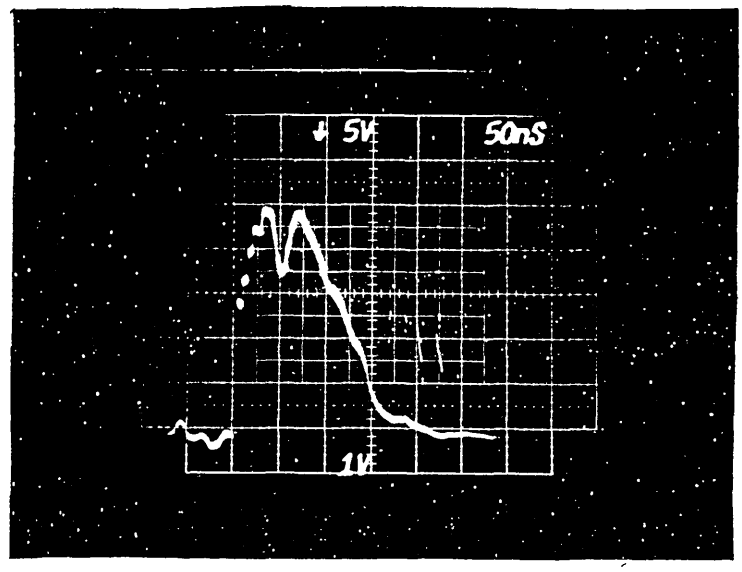
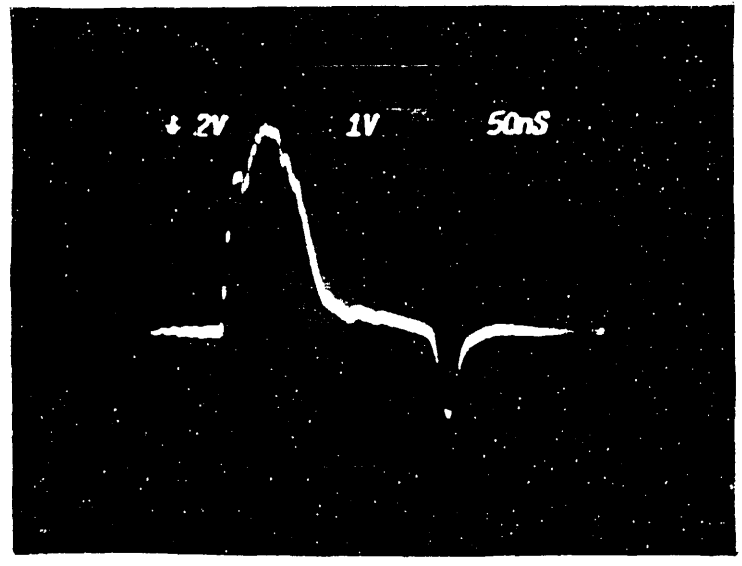


FIGURE 4P1(ii): 250 [NS] DELAY



The Jitter in the delay between the rising edge of the Dye Laser's pulse and the peak of the Ruby Laser's pulse could be got as low as ±10 [ns]. The chief limitation to achieving this degree of reproducibility lay with the spark gap of the Dye Laser. The performance of the spark gap tended to be erratic due to for example, electrical "tracking" along the insulator surfaces on which its three electrodes rested. During experimental runs some systematic drifts in the relative delay between the two lasers was observed over a period of many shots (typically 30-40). However, the Delay Monitoring System allowed these to be identified and compensated for during an actual experiment by making adjustments to the "varible delay unit".

4.3 Experimental Operation

At least three days before the planned experiment the furnace would be taken apart in order to reload the "Dynamic Containment System", located inside, with Barium metal. This core without exception was always soldered onto the furnace jacket by residual quantities of Barium. Consequently the furnace needed to be flushed through with water in order to weaken this joint and thus permit the core to be knocked out of the furnace jacket. Then the stainless steel sheets wrapped around the core, to form the containment system, were removed and the interior washed out to remove any Barium Hydroxide etc. A new

pair of sheets were then rolled on a rolling mill to a diameter slightly less than the core and then fitted onto it. After this the entire furnace system was dried and reassembled and pumped down during what remained of the day.

The assembled furnace would then be pumped throughout the next day in order to outgas any moisture absorbed by the surfaces of the furnace interior during the cleaning process. Therefore no Barium was loaded into the furnace at this stage, and the furnace was usually baked with its own heating system to assist the outgassing of the water vapour.

On the following day, about 100 grams of Barium rod from Kock Light Ltd (UK) would be cut up into short lengths using a guillotine and any surface oxide removed by a metal file. Further oxidation was prevented by using storage paraffin to exclude air from the clean surfaces during these operations. This storage paraffin was subsequently removed from the Barium surfaces, just prior to loading into the furnace, with petrol which had the advantage of being far more volatile and so much easier to pump away. The furnace was again let up to atmospheric pressure with argon gas and the core removed. A total of between 70 and 90 grams of Barium was then loaded into the three boats of the containment system which was then replaced in the furnace jacket

and the furnace reassembled. Care was taken to maintain the interior of the furnace and the containment system in an argon atmosphere at all times during these operations. The furnace was then pumped down and gently baked at about 450°C for the rest of the day. Unfortunately it was not possible for safety reasons to run the pumps overnight. Nevertheless the gentle baking was continued at this temperature overnight. Doing this had the advantage of reducing the time needed to reach the final operating temperature the next day.

Early the next morning the pumps were again switched on and the electrical heating input increased in three steps to achieve a temperature of about 770°C. This temperature lies above the melting point of Barium at 715°C and was usually achieved within four to five hours. Meanwhile the dye laser system was filled with new dye and its output energy measured. Accurate imaging of the source onto the slit was checked by firing the Ruby laser after achieving the "jump off" temperature of 770°C. The osmium mirror was then tweaked to maximise the continuum transmission through the 25 [μm] slit as monitored by the spectrographs vacuum photodiode. Fresh film was then loaded into the plate chamber of the spectrograph.

The final operating temperature of the furnace at 880 °C was then obtained by increasing the

the electrical power input up to the maximum 2000 [W] used. While the furnace was being heated up to the final temperature, the relative delay between the dye laser and the ruby laser was set utilising the monitoring system described in section 4.2.

The recording of the experimental spectra was usually started between one and two hours after the electrical power input was raised to its final level. Any delays normally occurred because of problems with the reproducibility of the dye laser's triggering. Without exception two unexcited Barium spectra were always taken, one before the excited state spectrum and one after it. These two spectra acted as checks on the column density of Barium throughout the experiment. They also served as a means to compare the strengths of the laser excited to the unexcited state absorption. All spectra were recorded with 160 shots of the VUV continuum.[+] The repetition rate for the unexcited spectrum was 10 shots/minute while for the laser excited spectrum it was between 0.5 and 1 shot/minute. This limit

[+]Occasionally during the recording of the excited state spectrum the pump dye laser would either not fire or would fire before the Ruby laser. Such shots would only contribute to the Barium ground state lines and so these shots were repeated. This ensured that the spectrum had 160 shots probing the laser excited states. The number of shots were not many, for example in the 60 [ns] and 250 [ns] spectra recorded in figure 5D1 there were 24 and 5 such events, respectively.

was self imposed in order to maximise the lifetime of the Ruby lasers pockel cell although the laser was rated for up to 60 shots/minute. This was because other workers had lost much time through the burning of the pockel cells antireflection coatings with this particular laser at high repetition rates. The second limit was placed by the relaxation time of the thermal turburlance in the uncirculated dye in both the oscillator and amplifier dye cells of the Dye laser system. This turbulence spoiled the optical quality of the dye medium and arose from the large amount of energy being dumped into the dye cells by the coaxial pump laser. During the actual recording of the excited state spectrum the relative delay between the two lasers for each shot was recorded using the monitoring system described in section 4.2. The gate valve V2 between the mirror chamber and the furnace was closed between each shot. This reduced the amount of Barium vapour escaping into the mirror chamber while the excited state spectrum was being recorded. The Samerium target was moved after the recording of each spectrum in order to prevent the target being burnt through which normally occurred after about two hundred shots. Surface impurities on the target were cleaned off each time it was moved by firing twenty shots of the Ruby laser with the gate valve V2 between the furnace and the mirror chamber closed. It usually took about four hours to record the three spectra onto the one strip of film.

The exposed film was then removed and developed in a solution of continuously agitated D19 for four minutes which had been diluted 1:1 with water, as recommended by the manufacturers of the film. The film was then washed, "fixed" in "Hypam" fixer (Ilford, UK) diluted 1:4 with water, washed again in water containing a small amount of detergent and then hung up to dry.

4.4 Preparation of the line list

The line list given in Chapter 5 was constructed from the data generated by a Joyce Lobel (UK) Digital Microdensitometer. The preparation of this line list involved three basic operations. First, the photographic film needed to be densitometered. Second, a dispersion curve had to be fitted to the excited state spectrum in order to convert the line positions into wavelengths. This curve as will be seen later was constructed from the ground state spectrum on the same plate and was then fitted to the excited state spectrum with the aid of some source absorption lines common to both. Thirdly, the positions of the Barium absorption lines were evaluated from the microdensitometer trace and their wavelength deduced from the above dispersion curve.

The photographic film used to record the spectrum was mounted on a glass plate, the film

being held flat with adhesive tape at its edges. The spectra on the film were densitometered with a "Joyce Lobel" (UK) Digital Microdensitometer belonging to the Plasma Group of this laboratory. A stepping motor was used to move the slide on which the spectra were mounted in 5[μm] steps (or integer multiples there of), and the instrument at each step took a reading of the spectrum's density D ($-\log_{10}$ [transmission]). These readings were stored on a "Tandy" (Japan) microprocessor to which the instrument was interfaced. The slit in front of the microdensitometers photomultiplier was set to sample a 25 [μm] wide rectangle of the spectrum which corresponded to the slit width of the spectrograph. A narrower sampling rectangle would have not increased the resolution of the spectral lines and would have merely increased the noise level (averaging over fewer grains). It was found that there was little improvement in the spectral resolution between 5 [μm] or 10 [μm] sampling steps and the densitometer traces in Chapter 5 were therefore taken at 10 [μm] sampling steps. This raw data giving the density of the spectra at 10 [μm] steps was then transferred from the "Tandy" microprocessor to the Imperial College Mainframe Network for analysis.

This analysis involved first, the production of a line list and secondly, the generation of the wavelength calibrated microdensitometer traces given

in Chapter 5. Fortunately, the computer codes necessary for achieving these two goals were already in existence, having been developed by Mrs G. Nave of the author's research group in connection with her own work.

The VUV continuum emitted by the laser generated Samerium plasma is nearly devoid of any strong absorption or emission lines with which to construct the dispersion curve for the excited state spectrum. The Barium excited state spectrum on the other hand does contain many observable ground state lines as may be seen in figure 5D1 of Chapter 5. However most of these lie at wavelengths below 628Å and there are relatively few at higher wavelengths. To avoid any inaccuracies at wavelengths above 628Å arising from chance coincidences between Barium ground state and excited state absorption lines, the dispersion curve was generated solely from the ground state spectrum on the same film. This curve was then transferred to the excited state spectrum using the two very sharp absorption lines in the continuum source at 555.9Å and 555.4Å as transfer standards. In Mrs G. Nave's computer codes, the origin of the dispersion curve was defined to be at the beginning of the data file giving the spectrums plate density D at 10 [μm] steps. Hence it was extremely easy to effect the transfer of the dispersion curve: it involved adding 179 (in this particular case) dummy points to the beginning of

the excited states data file. This brought the locations of the above samerium absorption lines on the data files for the excited and ground state spectra into coincidence. Confirmation of the accuracy of this fit (to 10 [μm] or 1 data point) was provided by checking that the peaks of some of the strong and sharp Barium ground state lines, seen in both spectra, were at the same position in their respective data files. The technique of course assumes that any irregularities along the film will be the same for both spectra.

The dispersion curve representing the functional relationship between line positions on the film and their corresponding wavelength was generated using a Chebyshev Polynomial fit routine. A Chebyshev Polynomial fit according to Connerade (Private Communication, 1984) is superior to a conventional polynomial expansion in powers of x due to its "greater stability" at the boundaries of the region for which calibration lines exist. This is because an approximation using Chebyshev Polynomials allows a larger average squared error but may keep the extreme errors down (Arken, 1970).

The positions of the calibration lines in the ground state spectrum were deduced with the aid of some computer software developed by Nave. This software displayed a chosen section of the microdensitometer trace giving the spectrum's

density D verses position [μm] on a Tekronics (US) graphics terminal. The position of each sharp line of known wavelength which could be confidently identified from the papers of either Connerade et al (1979a) or Baig et al (1984) was then registered manually with a curser on the screen and the corresponding wavelength then entered. A Chebyshev Polynomial fit routine then fitted a dispersion curve to this data. Any incorrectly identified lines are characterized by their property of lying far from the fitted curve. The routine automatically rejected these and then repeated the fitting procedure with the remaining calibation lines. All of these were found to fall within ± 0.08Å of the fitted curve.

Having generated the dispersion curve, the line list was then prepared. This involved deducing the positions of the lines in the excited state spectrum and then using the dispersion curve to evaluate their wavelength utilizing the software provided by Nave. An enlarged section of the microdensitometer trace was projected onto a Tekronics terminal screen, and the positions of the peaks in the trace corresponding to lines seen on the film were then registered using a curser. An enlarged photographic print of the three spectra recorded on a single film during an experimental run was used to assist in discriminating between spurious peaks due to say dust, or scratches and

legitimate peaks due to real lines.

The accuracy of the wavelengths given in the line list is better than ±0.1Å as may be confirmed by reference to strong Barium ground state lines seen in both excited and ground state spectra.

It should be pointed out that the line list given in Chapter 5 supersedes a previous list generated from line positions measured with a Carl Zeiss Jena (East Germany) Optical Comparator, which was prepared when the above Digital Densitometer and associated computer software was unavailable to the author. A problem encountered with the optical comparator was that some of the weaker lines were very difficult to see through the instrument's microscope. As a result it was not possible to accurately "set" on these lines and they were not included in the line list even though they could be seen on the enlarged photographic prints of the spectra. It was nevertheless encouraging to find that the two lists were generally in agreement even if they were produced in quite different ways. The preparation of the line list from the optical comparator measurements is sketched in Appendix 4.

CHAPTER 5 RESULTS AND DISCUSSION

5.1 Introduction

The results of the laser excited Barium absorption experiment will be presented in this chapter starting in Section 5.2 with an atlas of the "resolved" absorption lines measured between 845Å and 549Å. This subsection will contain both illustrative material in the form of photographic spectra and microdensitometer traces, as well as a line list of the resolved lines in table 2.

These results will then be discussed in subsection 5.3. The discussion will open with a study of which Barium levels were populated as a result of laser excitation and are thus responsible for the observed spectra, the discussion will then relate the impact of these results on the theoretical calculations by Mansfield (Private Communication, 1985) using the Cowan Code (subsection 5.3.2). Finally the chapter will close with a study on the origin of possible molecular profiles due to $Ba^*(6s5d)$-$Ba^*(6s5d)$ or $Ba^*(6s5d)$-$Ba(6s^2)$ dimers observed at wavelengths above 690Å.

5.2 Results

5.2.1 Atlas of the "Resolved" Absorption lines of Barium Vapour lying between 845Å and 549Å after optical excitation by a high power dye laser tuned to the resonance line at 5535Å

The experimental results will be presented in this section in the form of photographic spectra, microdensitometer traces and finally a line list table giving the wavelengths of the more prominent lines.

Figure 5P1 shows two sets of Barium photographic spectra. Each set corresponds to the three spectra recorded during an experimental run. The spectra marked "c" and "d" are "reference" spectra of unexcited Barium taken before (c) and after (d) the main laser experiment. These spectra provide confirmation that an adequate number density of Barium was maintained throughout the two experimental runs. Spectrum A corresponds to the 5p absorption spectrum of excited Barium recorded $\sim$ 60 [ns] after the rise of the Dye laser, and within the pulse envelope of the dye laser. Spectrum B corresponds to the 5p absorption spectrum of excited Barium recorded $\sim$ 250 [ns] after the rise of the Dye laser, and outside the pulse envelope of the dye laser. The short spontaneous lifetime of the 6s6p $^1P_1$ level ($\sim$8.4[ns]) means that spectrum B will

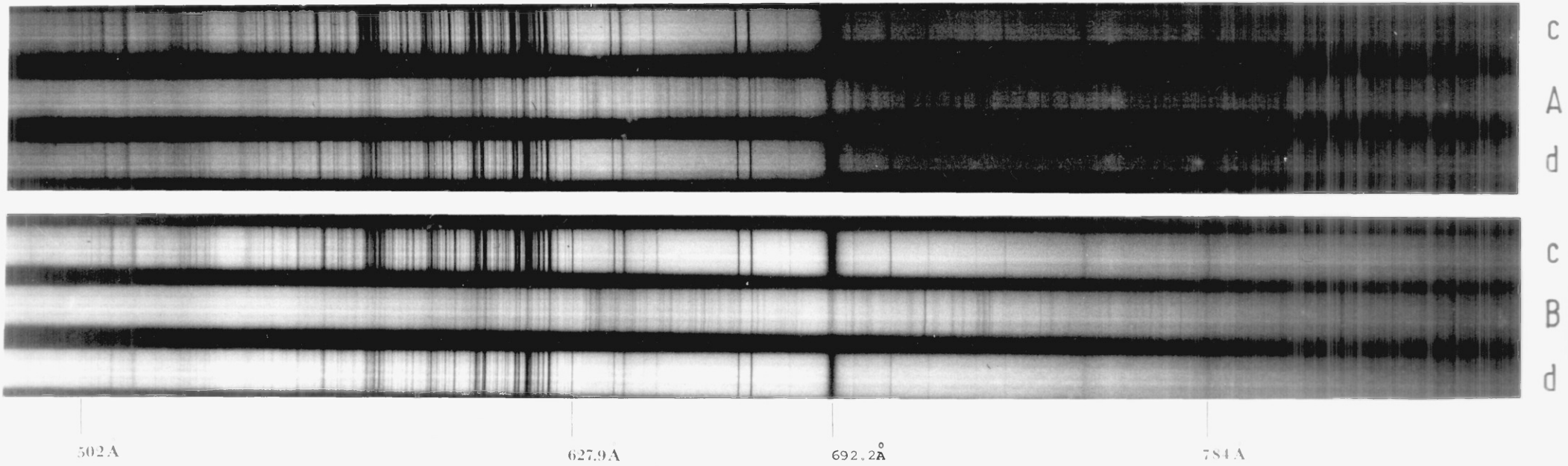
FIGURE 5P1: BARIUM 5P SPECTRA

A - Spectrum of Laser Excited Barium 60 [ns] after the rise of the Dye Laser and <u>inside</u> the laser pulse

B - Spectrum of Laser Excited Barium 250 [ns] after the rise of the Dye Laser but <u>outside</u> the laser pulse

c - Spectrum of Unexcited Barium taken <u>before</u> the Laser Experiment

d - Spectrum of Unexcited Barium taken <u>after</u> the Laser Experiment



contain no absorption lines arising from this level. Careful observation of spectra A and B shows them to be identical with no extra lines being perceptible in Spectrum A due to the 6s6p $^1P_1$ level. Reasons for this result will be examined in subsection 5.3.1.

It can be seen from figure 5P1 that the absorption lines of the excited state spectra are in general much weaker than those arising from the Barium ground state. These weak features may be photographically enhanced using the extremely high contrast film "Kodalith" (Kodak Eastman Ltd, US). The procedure involves making "positives" of the original film on Kodalith film from which the four photographic prints, figure 5P2a to 5P2d were produced. Each of these four prints correspond to overlapping sections of the Barium VUV absorption spectra, and together cover the wavelength range from 503Å to 850Å. The upper spectrum is the absorption spectrum of the Barium ground state while the lower one corresponds to spectrum B of figure 5P1. Although the resulting prints are extremely grainy, the image enhancement process does serve to bring out the complex new structure at wavelengths greater than 622Å in the laser excited Barium Spectrum.

The final collection of illustrative materials is a set of microdensitometer traces of the two spectra given in the preceeding photographic prints

(figures 5P2a to 5P2d). The spectra were densitometered on a Joyce Lobel (U.K.) digital microdensitometer, and the traces generated by computer codes provided by Mrs G. Nave of this laboratory. The two spectra are presented in parallel, the Barium ground state spectrum on the even pages, the Barium excited state spectrum on the odd pages. This presentation approach is used to aid easy comparison of the two spectra. Figures 5D1a and 5D1b are traces of the entire spectra between 497Å and 859Å of the ground and laser excited states respectively. Figures 5D2a(i) to (xiii) and figures 5D2b(i) to (xiii) break the same spectra up into 13 overlapping sections, each scanning a wavelength range of 40Å. The intensity scale on these traces corresponds to the measured plate density [D]. The noise level is approximately 0.03 [D] (peak to peak) and is comparible to that of the Samarium continuum. The wavelength scale was generated by a Chebyshev Polynomial fit routine. Its accuracy for the ground state spectrum was better than ±0.08Å over the wavelength range 502Å to 784Å. Outside this range it was not possible to quantify the accuracy of the scale due to the lack of any Barium absorption lines of known wavelength. The wavelength scale for the trace of the laser excited Barium spectrum was likewise expected to be good to ±0.08Å over the wavelength range ∿ 502Å to ∿ 784Å. This is because the scale was constructed with the same Chebyshev fit as was used to construct

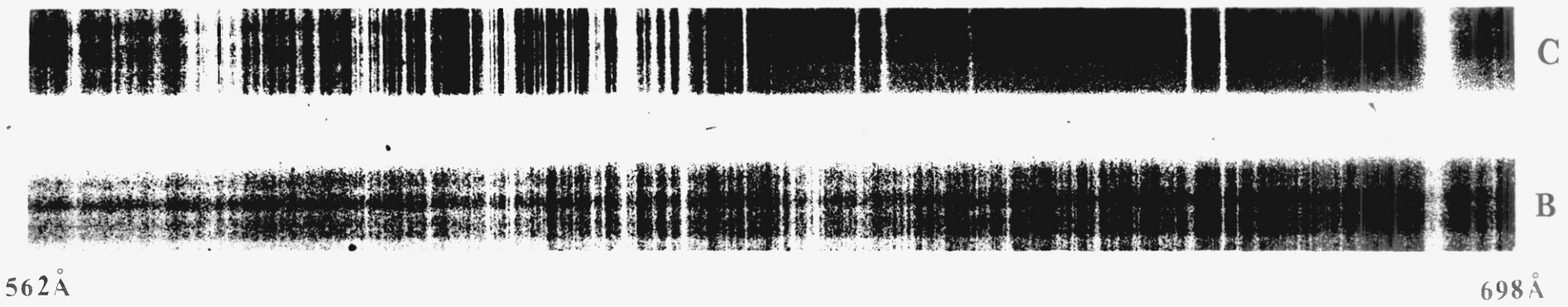
FIGURE 5P2a: IMAGE ENHANCEMENT OF THE BARIUM 5P SPECTRA BETWEEN 503Å AND 643Å



B - Spectrum of Laser Excited Barium 250 [ns] after the rise of the Dye Laser but outside the laser pulse

C - Spectrum of Unexcited Barium taken before the Laser Experiment

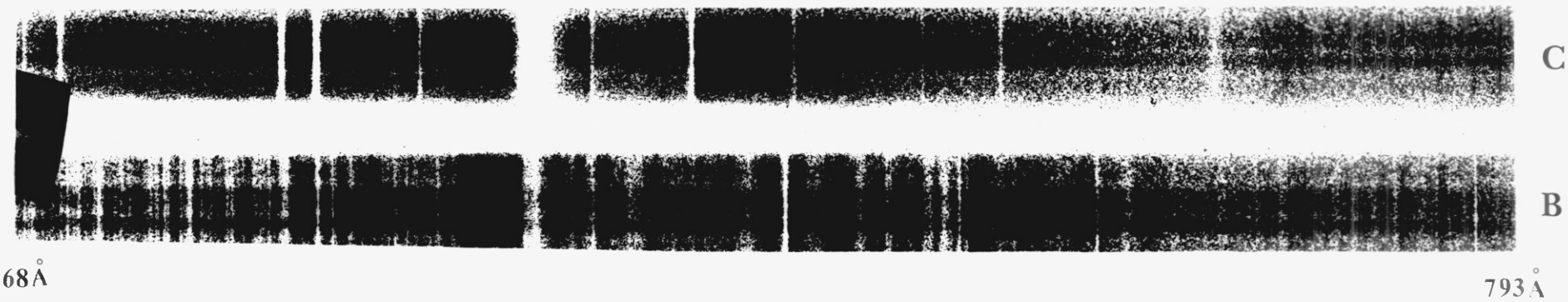
FIGURE 5P2b: IMAGE ENHANCEMENT OF THE BARIUM 5P SPECTRA BETWEEN 562Å AND 698Å



B - Spectrum of Laser Excited Barium 250 [ns] after the rise of the Dye Laser but outside the laser pulse

C - Spectrum of Unexcited Barium taken before the Laser Experiment

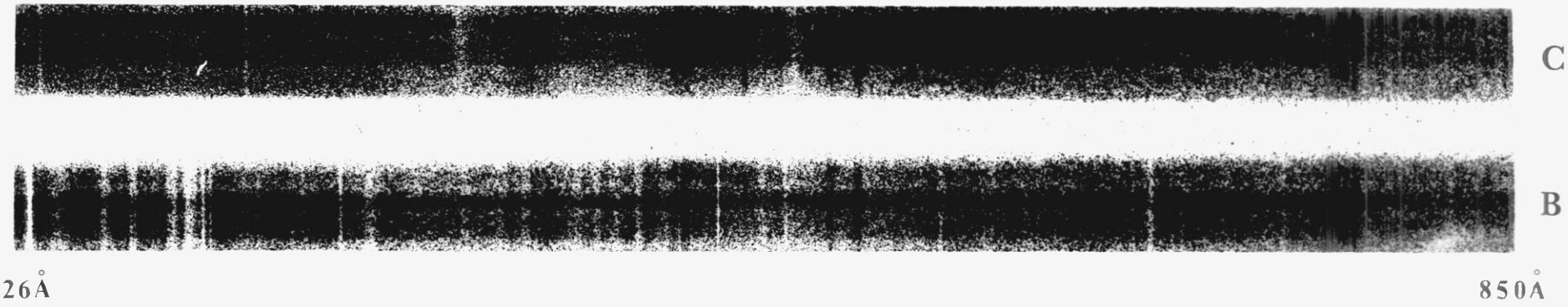
FIGURE 5P2c: IMAGE ENHANCEMENT OF THE BARIUM 5P SPECTRA BETWEEN 668Å AND 793Å



B - Spectrum of Laser Excited Barium 250 [ns] after the rise of the Dye Laser but outside the laser pulse

C - Spectrum of Unexcited Barium taken before the Laser Experiment

FIGURE 5P2d: IMAGE ENHANCEMENT OF THE BARIUM 5P SPECTRA BETWEEN 726Å AND 850Å



B - Spectrum of Laser Excited Barium 250 [ns] after the rise of the Dye Laser but outside the laser pulse

C - Spectrum of Unexcited Barium taken before the Laser Experiment

the scale of the ground state spectrum.

FIGURE 5D1a: PHOTO-ABSORPTION SPECTRUM OF UNEXCITED BARIUM BETWEEN 497Å AND 859Å

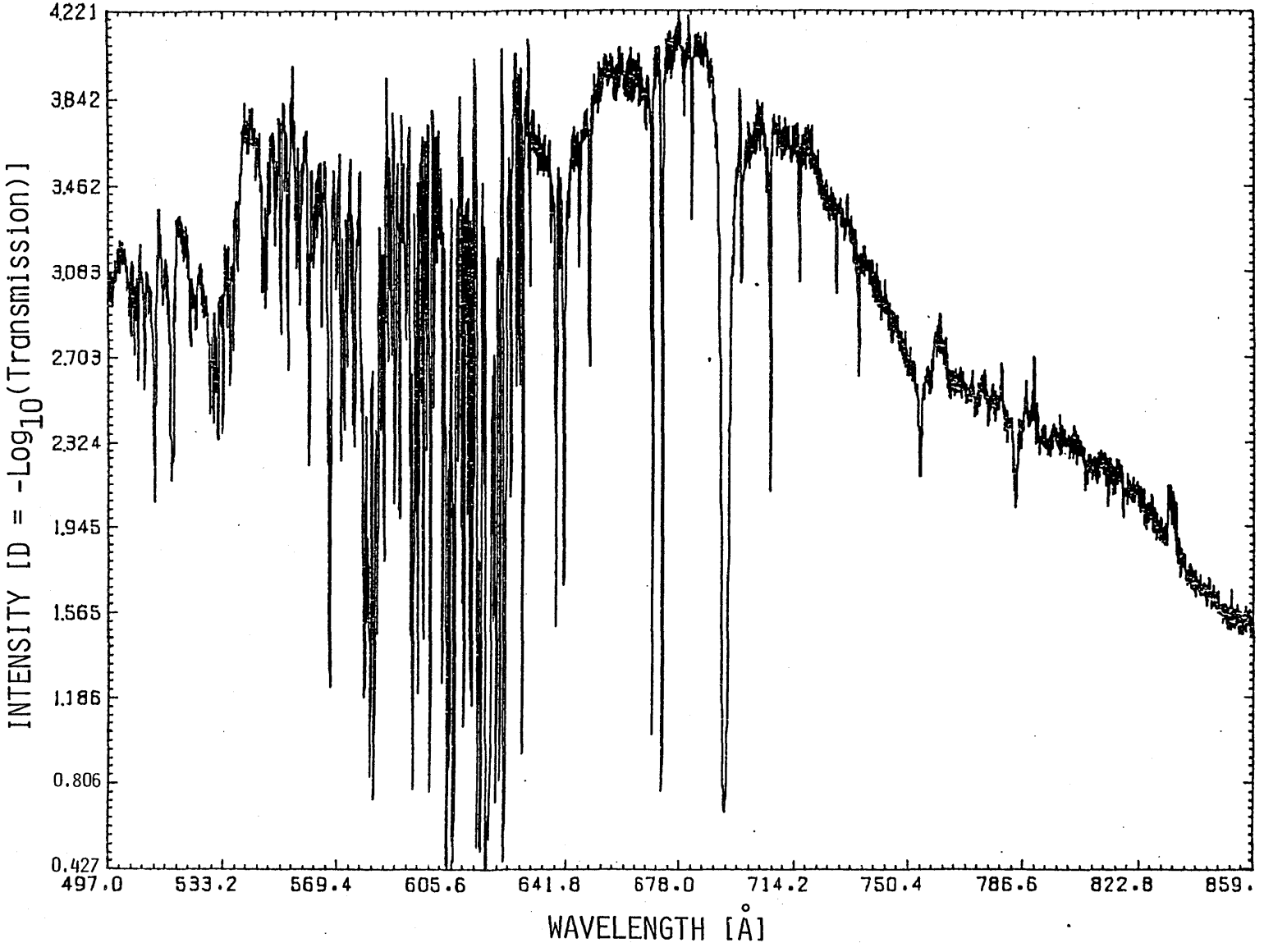


FIGURE 5D1b: PHOTO-ABSORPTION SPECTRUM OF LASER EXCITED BARIUM BETWEEN 497Å AND 859Å

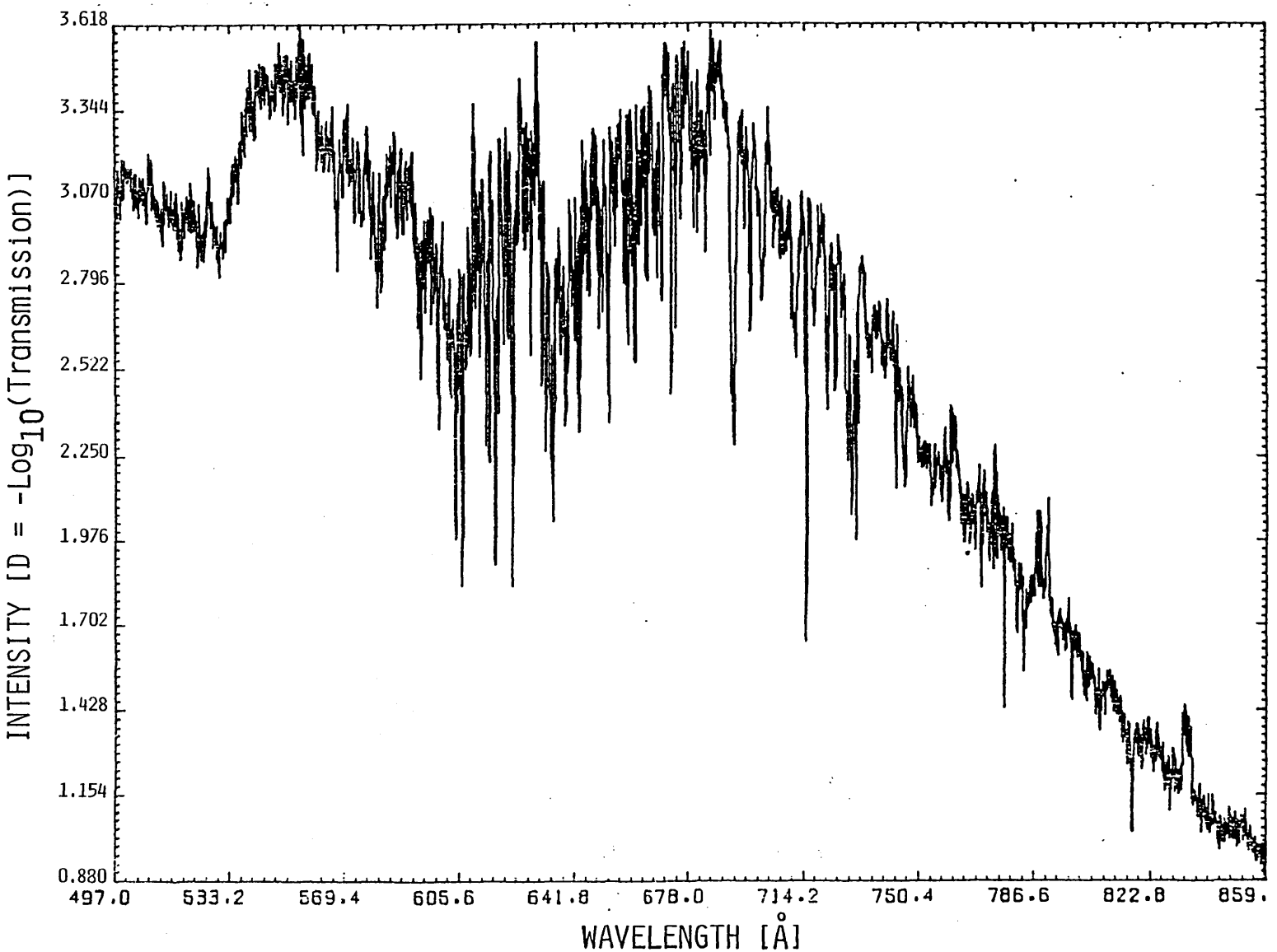


FIGURE 5D2a(i): PHOTO-ABSORPTION SPECTRUM OF UNEXCITED BARIUM BETWEEN 497Å AND 537Å

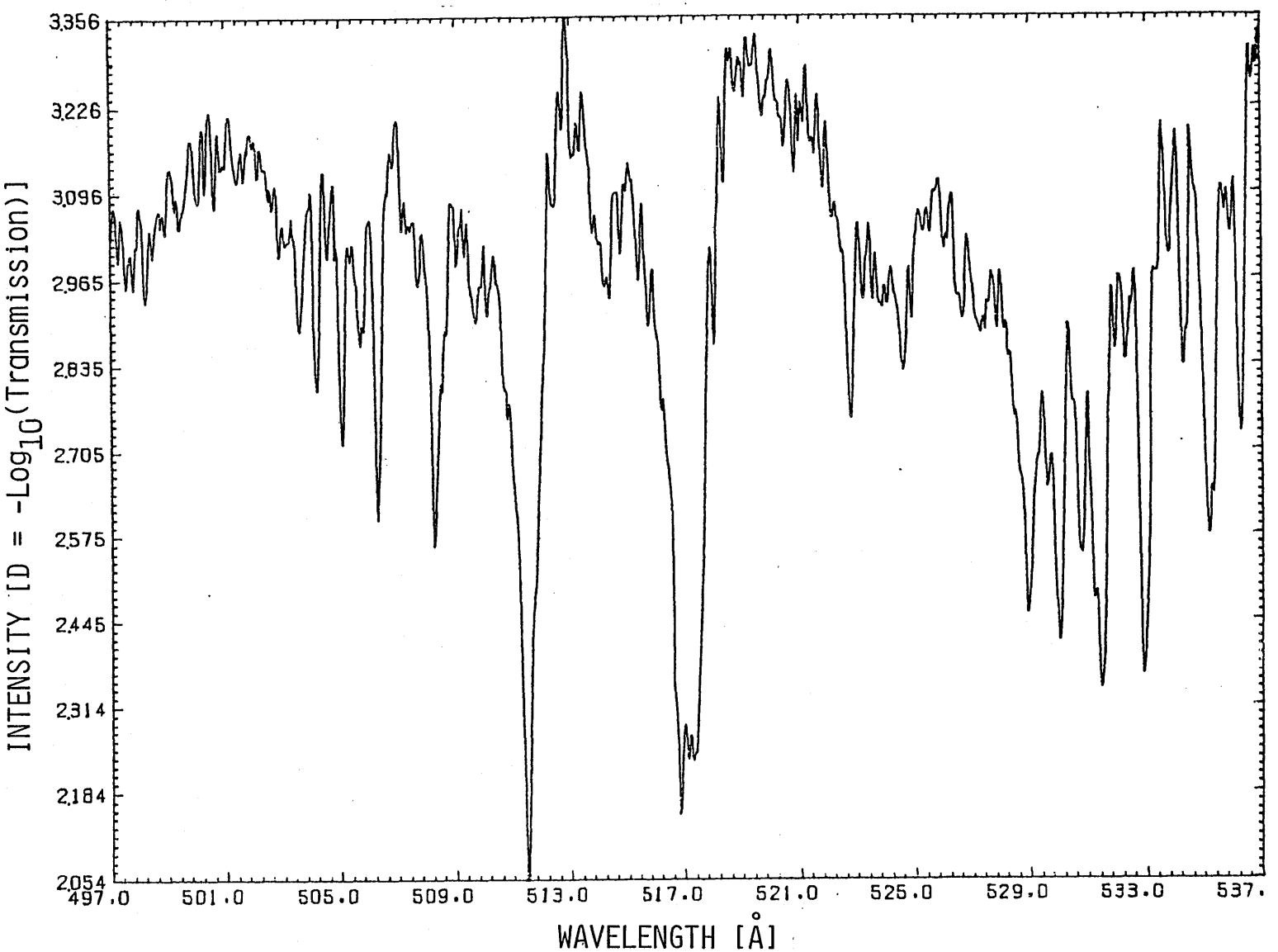


FIGURE 5D2b(i): PHOTO-ABSORPTION SPECTRUM OF LASER EXCITED BARIUM BETWEEN 497Å AND 537Å

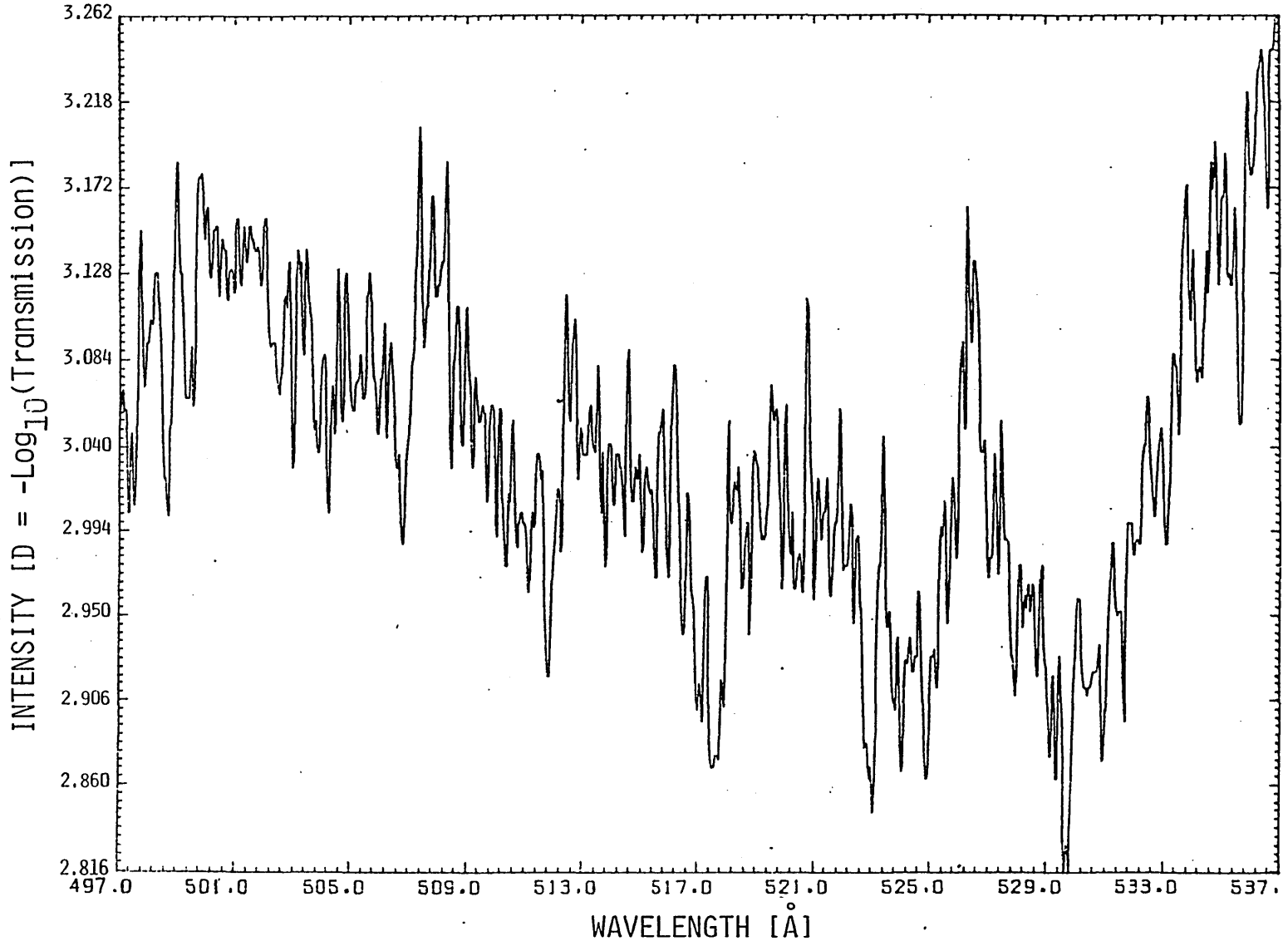


FIGURE 5D2a(11): PHOTO-ABSORPTION SPECTRUM OF UNEXCITED BARIUM BETWEEN 520Å AND 560Å

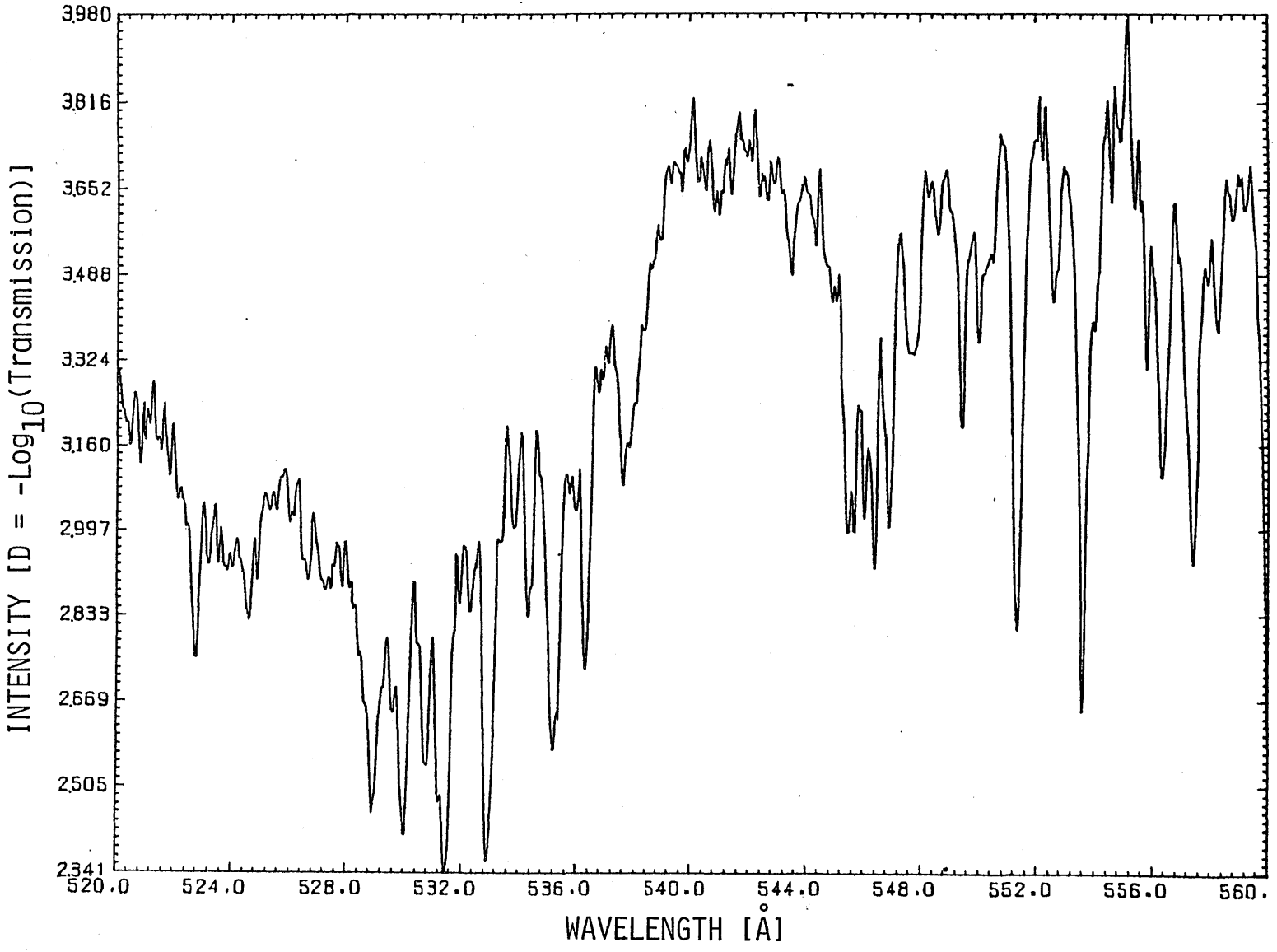


FIGURE 5D2b(ii): PHOTO-ABSORPTION SPECTRUM OF LASER EXCITED BARIUM BETWEEN 520Å AND 560Å

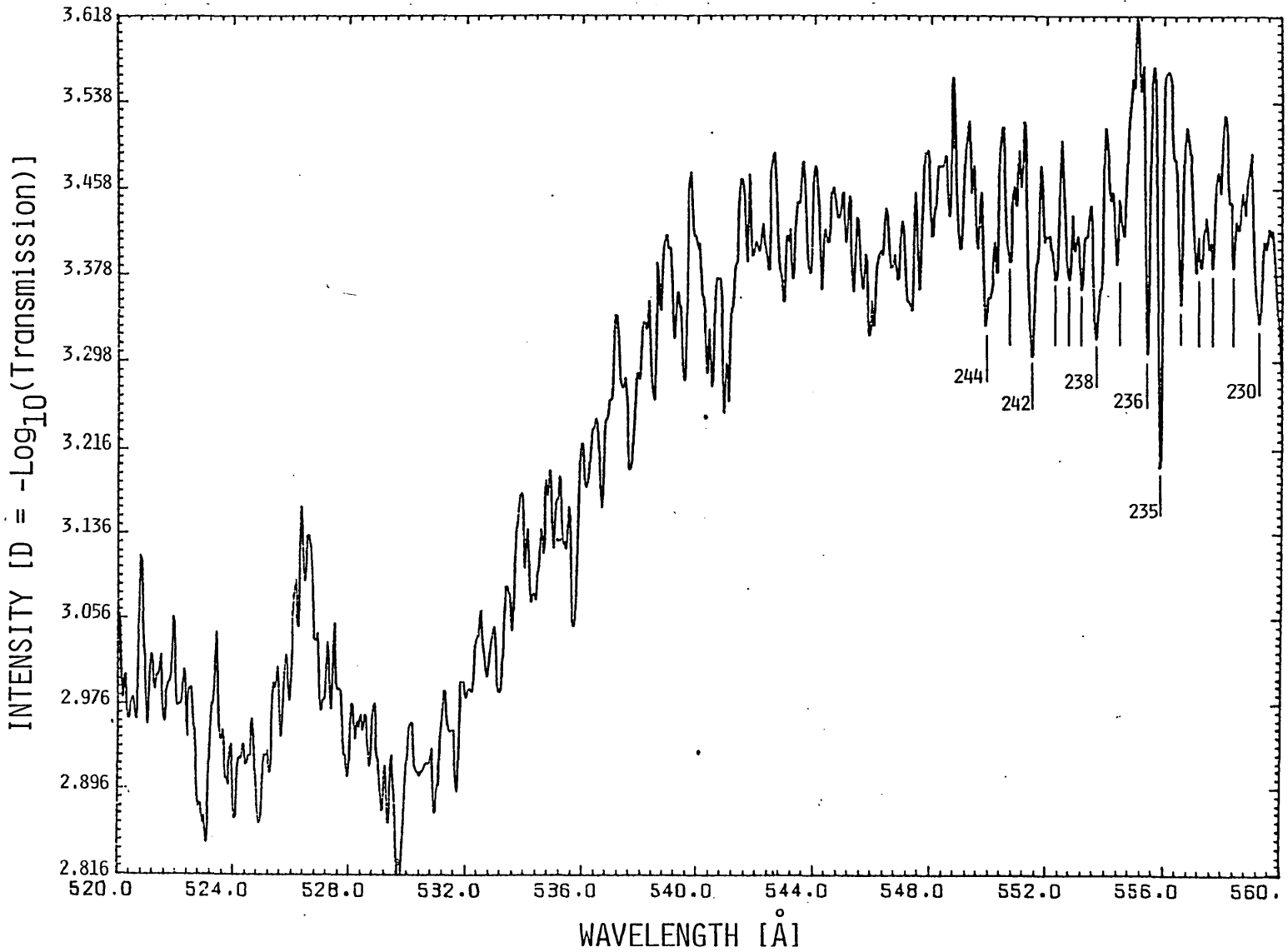


FIGURE 5D2a(iii): PHOTO-ABSORPTION SPECTRUM OF UNEXCITED BARIUM BETWEEN 548Å AND 588Å

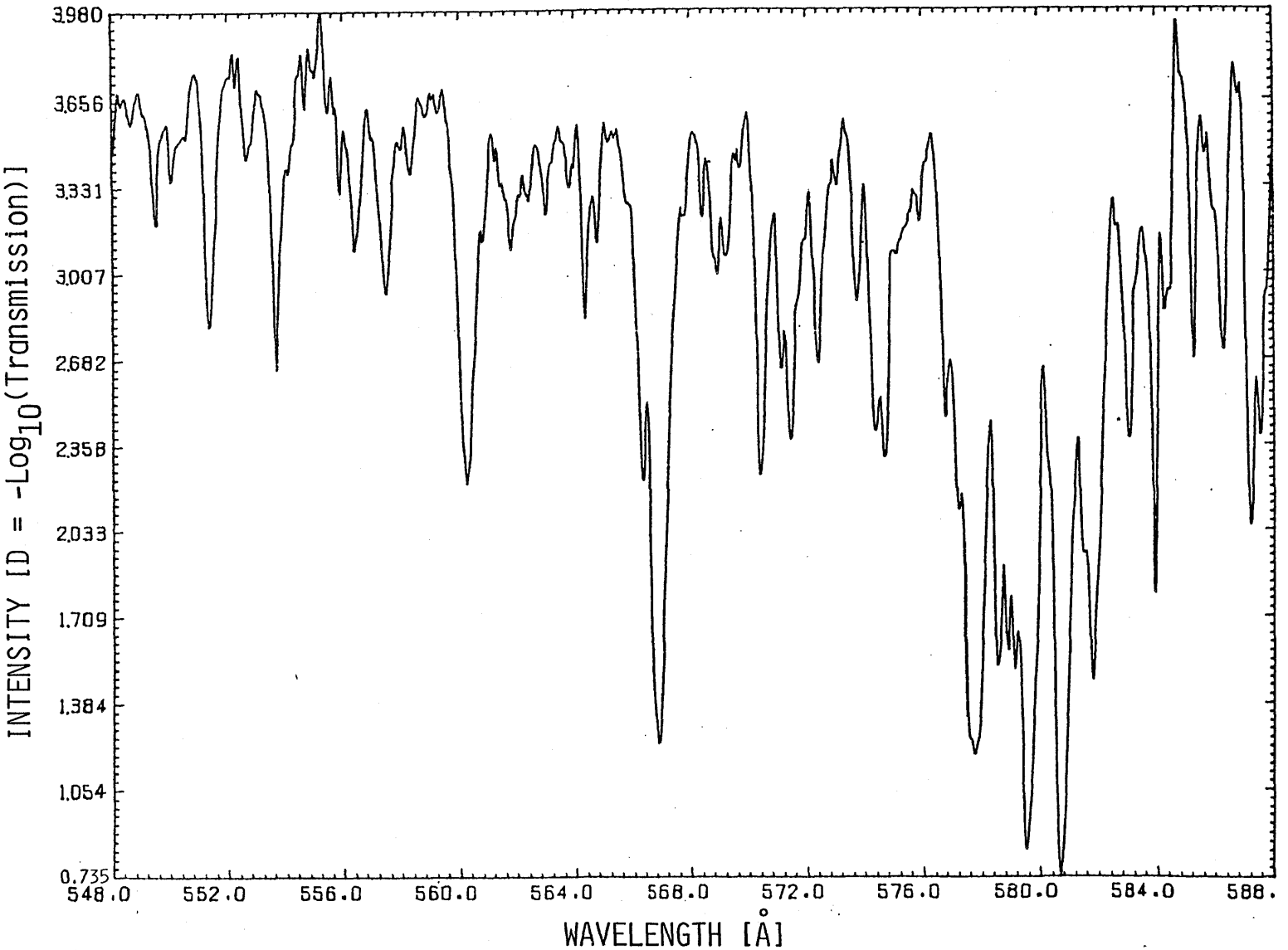


FIGURE 5D2b(iii): PHOTO-ABSORPTION SPECTRUM OF LASER EXCITED BARIUM BETWEEN 548Å AND 588Å

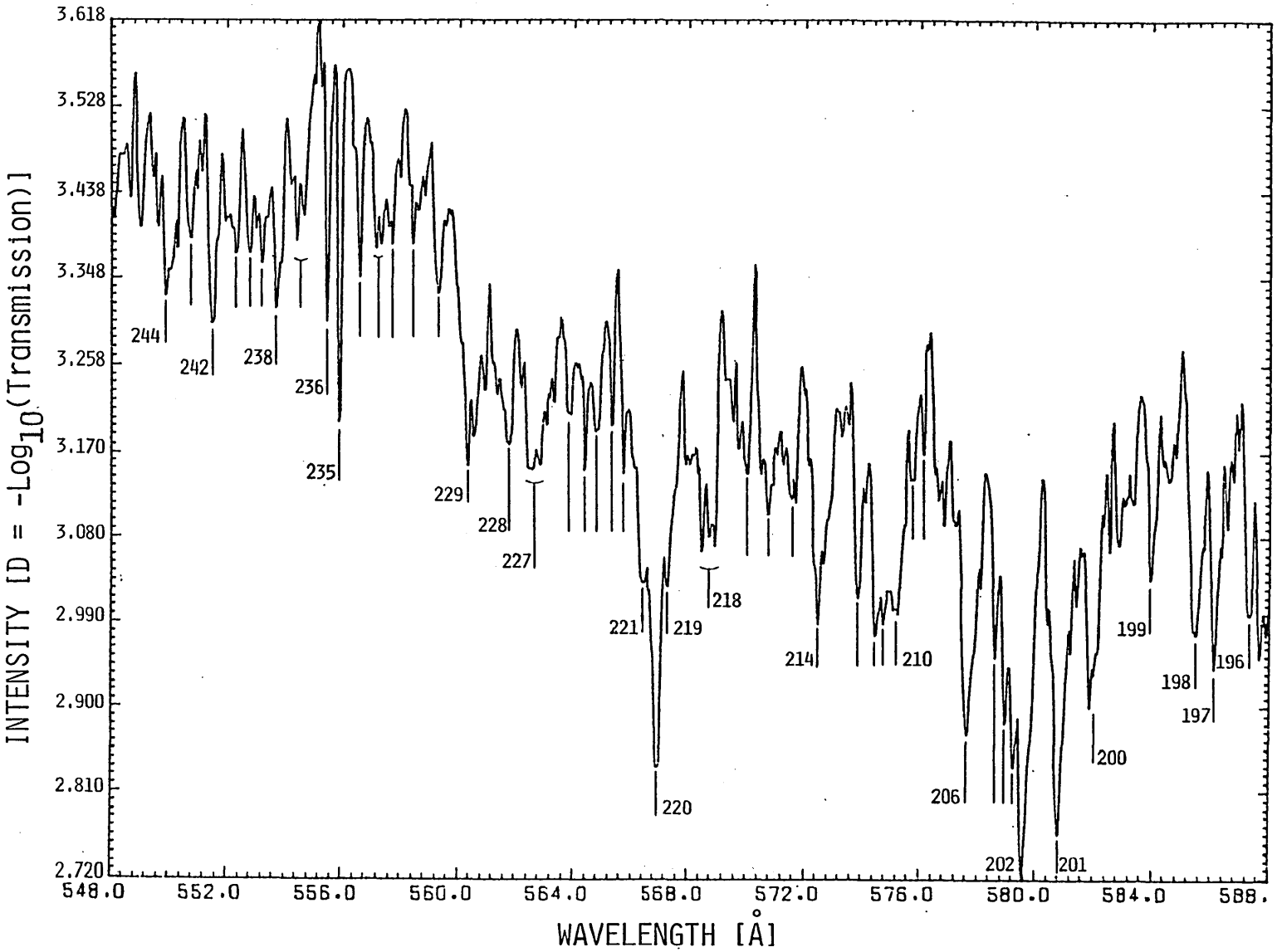


FIGURE 5D2a(iv): PHOTO-ABSORPTION SPECTRUM OF UNEXCITED BARIUM BETWEEN 576Å AND 616Å

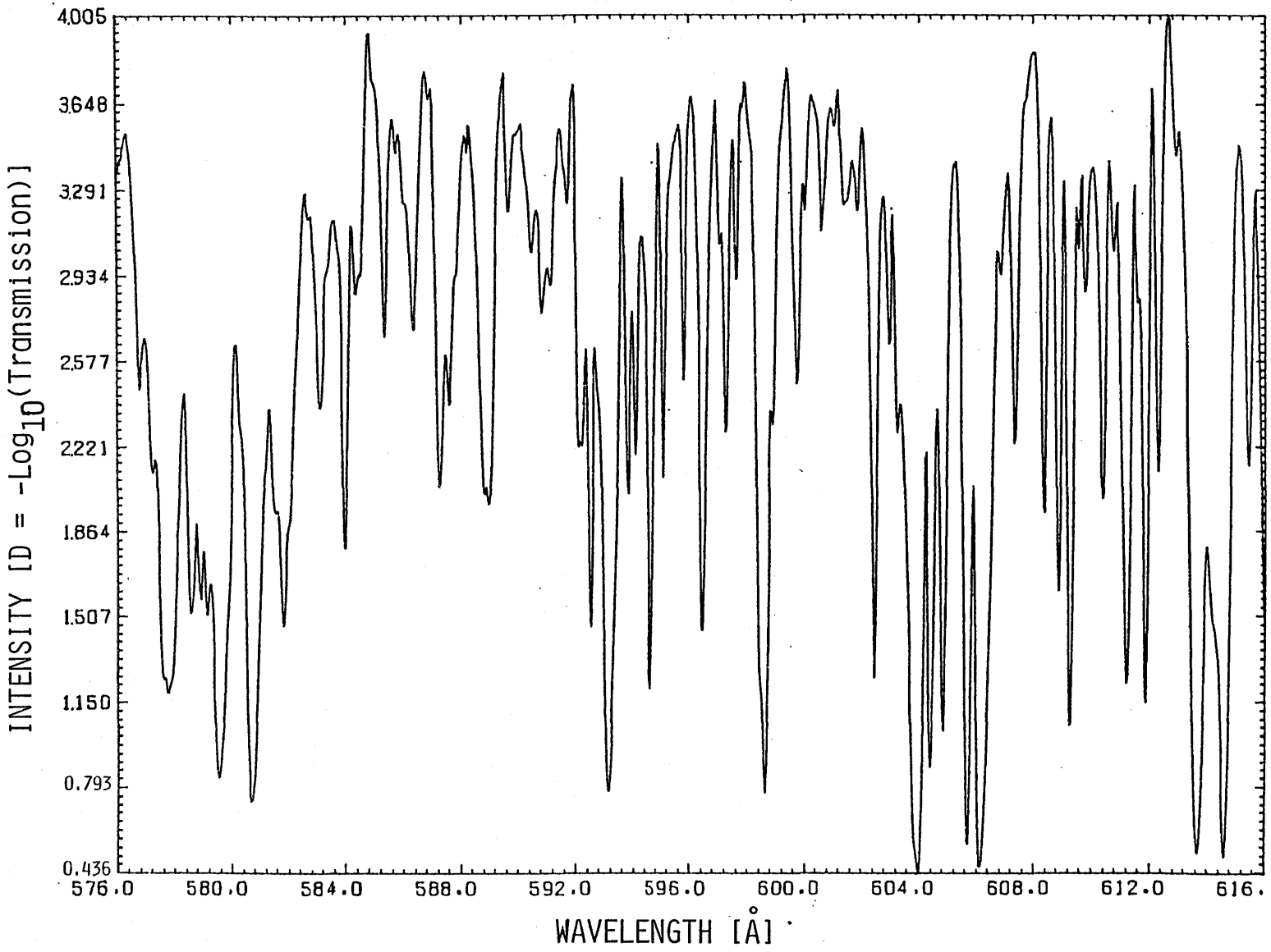


FIGURE 5D2b(iv): PHOTO-ABSORPTION SPECTRUM OF LASER EXCITED BARIUM BETWEEN 576Å AND 616Å

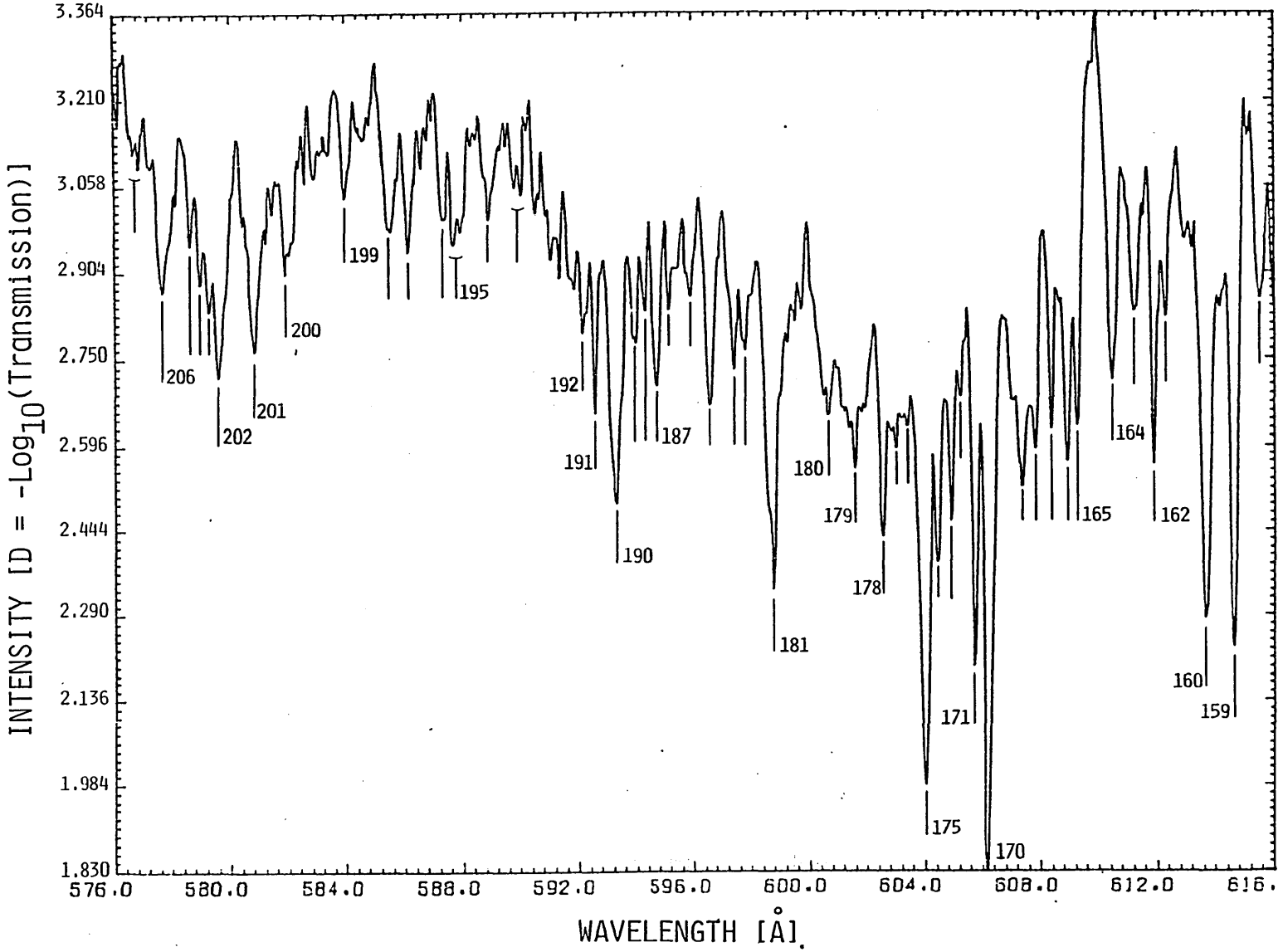


FIGURE 5D2a(v): PHOTO-ABSORBTION SPECTRUM OF UNEXCITED BARIUM BETWEEN 604Å AND 644Å

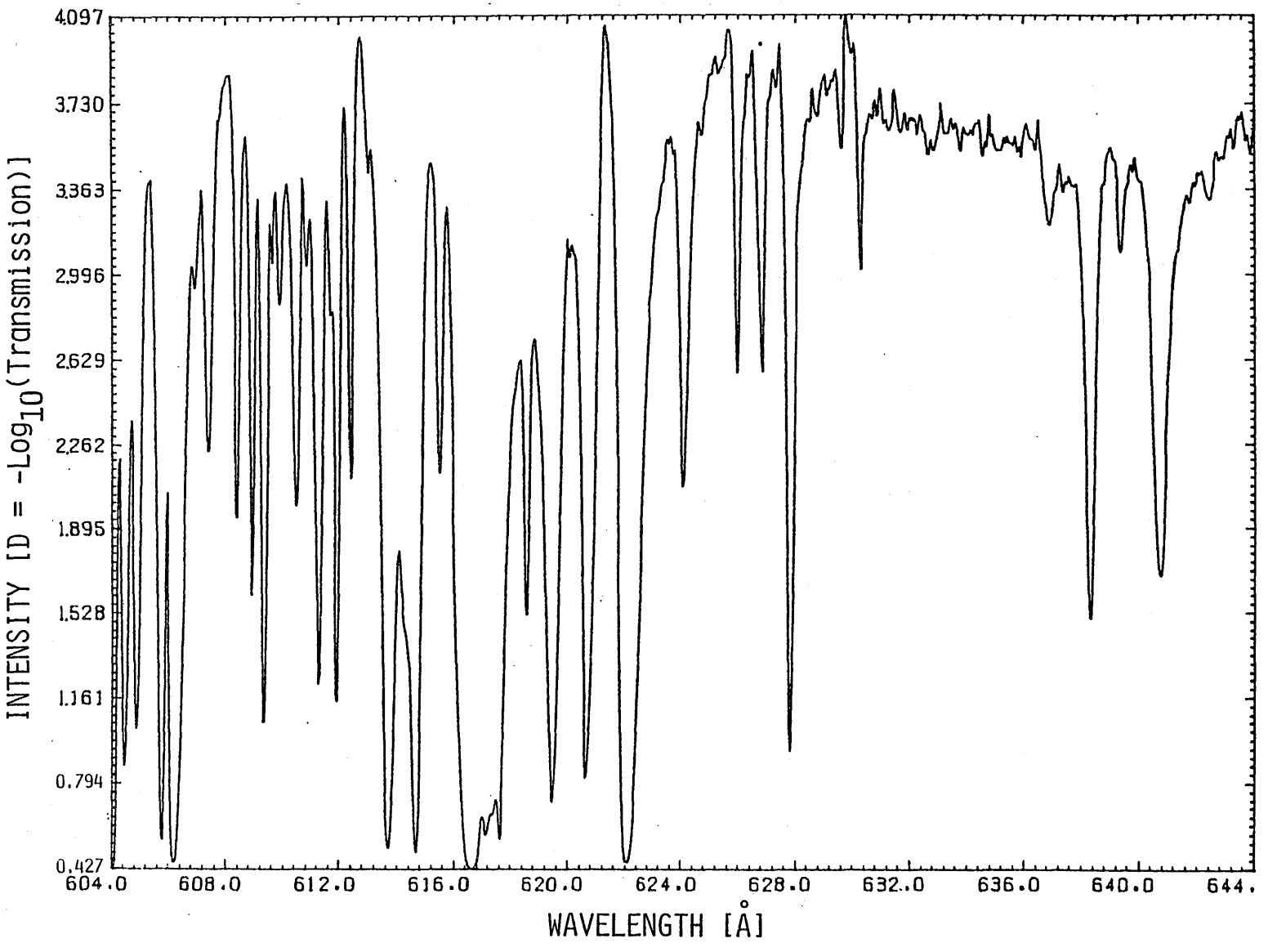


FIGURE 5D2b(v): PHOTO-ABSORPTION SPECTRUM OF LASER EXCITED BARIUM BETWEEN 604Å AND 644Å

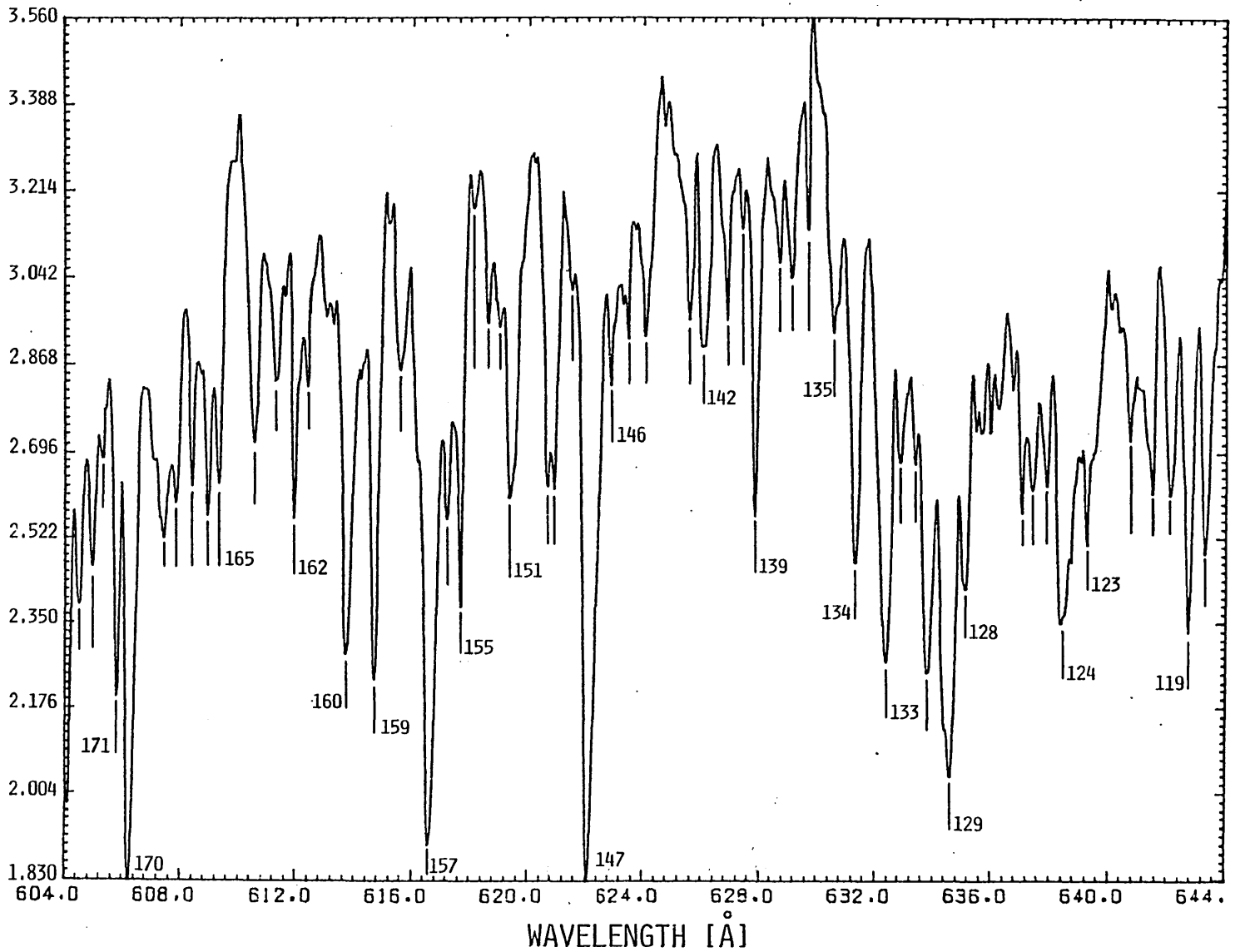


FIGURE 5D2a(vi): PHOTO-ABSORPTION SPECTRUM OF UNEXCITED BARIUM BETWEEN 632Å AND 672Å

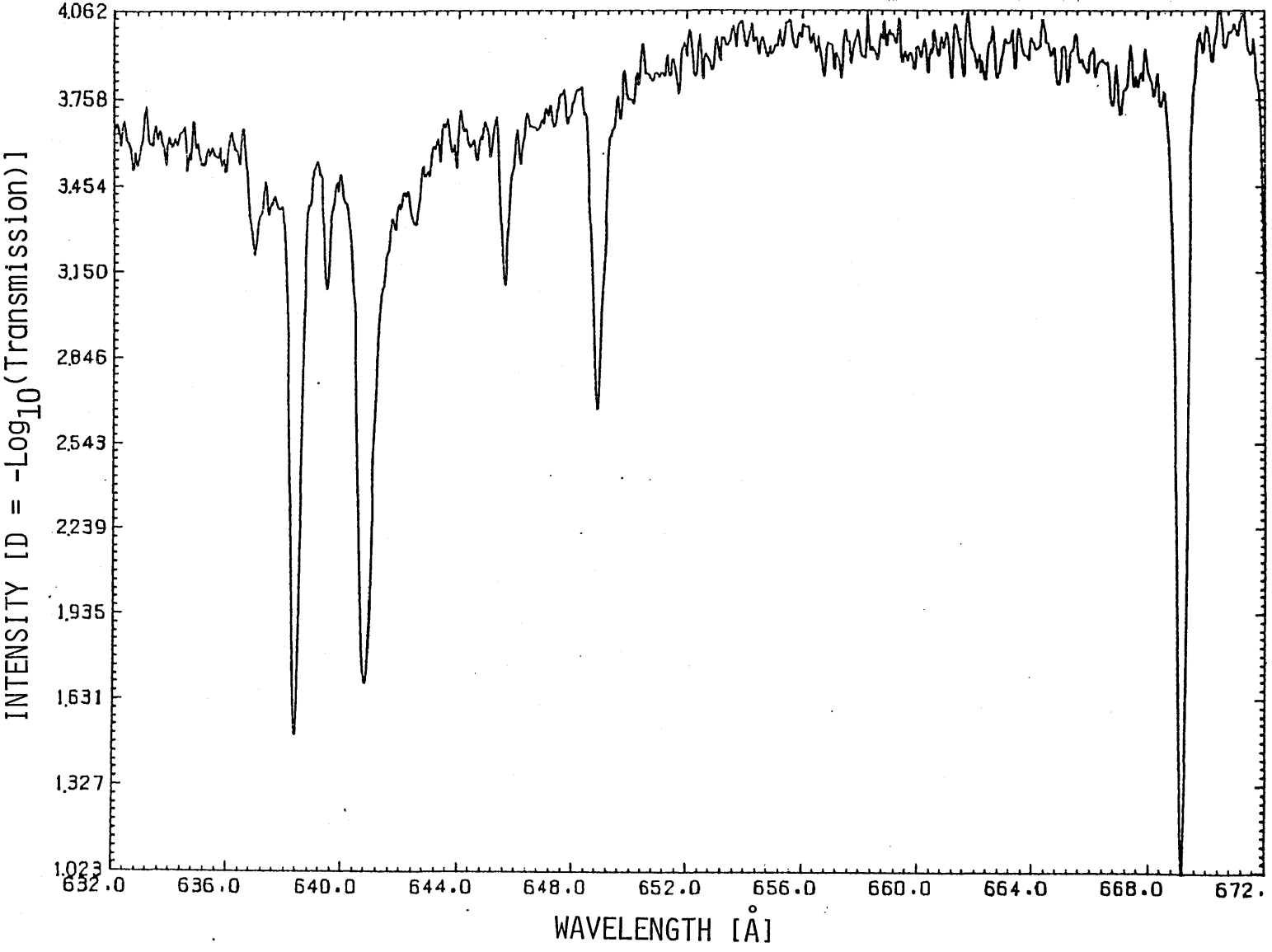


FIGURE 5D2b(vi): PHOTO-ABSORPTION SPECTRUM OF LASER EXCITED BARIUM BETWEEN 632Å AND 672Å

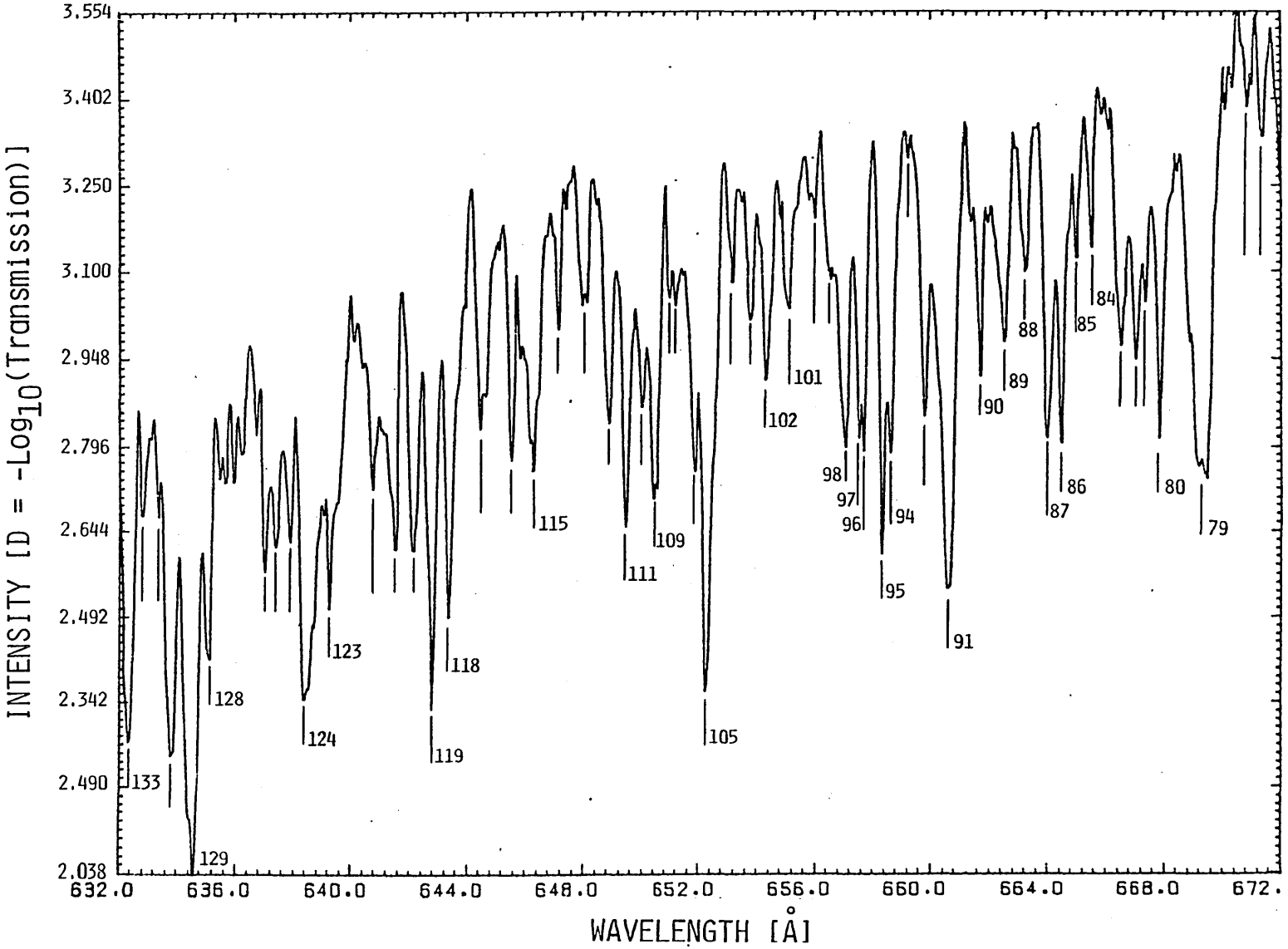


FIGURE 5D2a(vii): PHOTO-ABSORPTION SPECTRUM OF UNEXCITED BARIUM BETWEEN 600Å AND 700Å

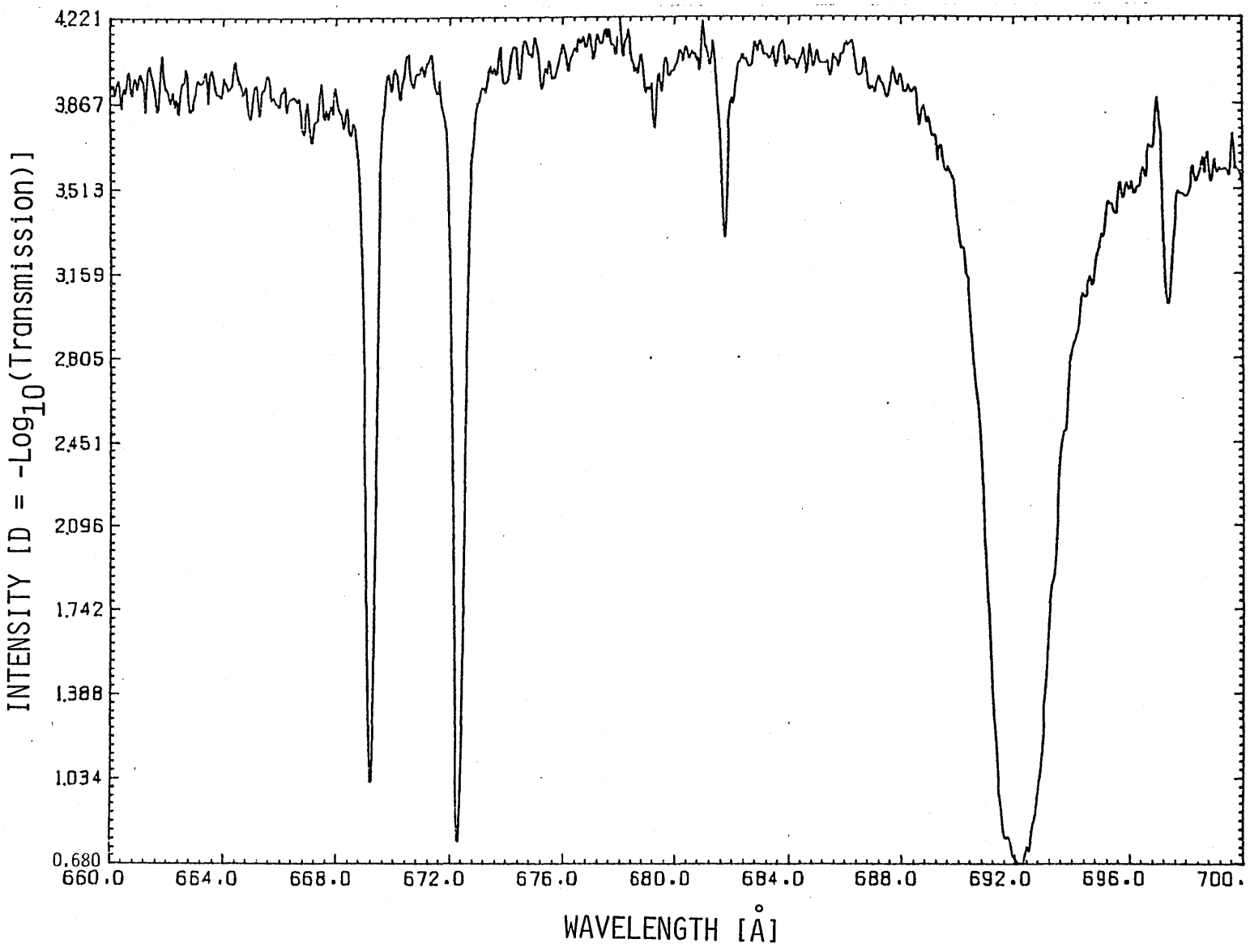


FIGURE 5D2b(vii): PHOTO-ABSORPTION SPECTRUM OF LASER EXCITED BARIUM BETWEEN 660Å AND 700Å

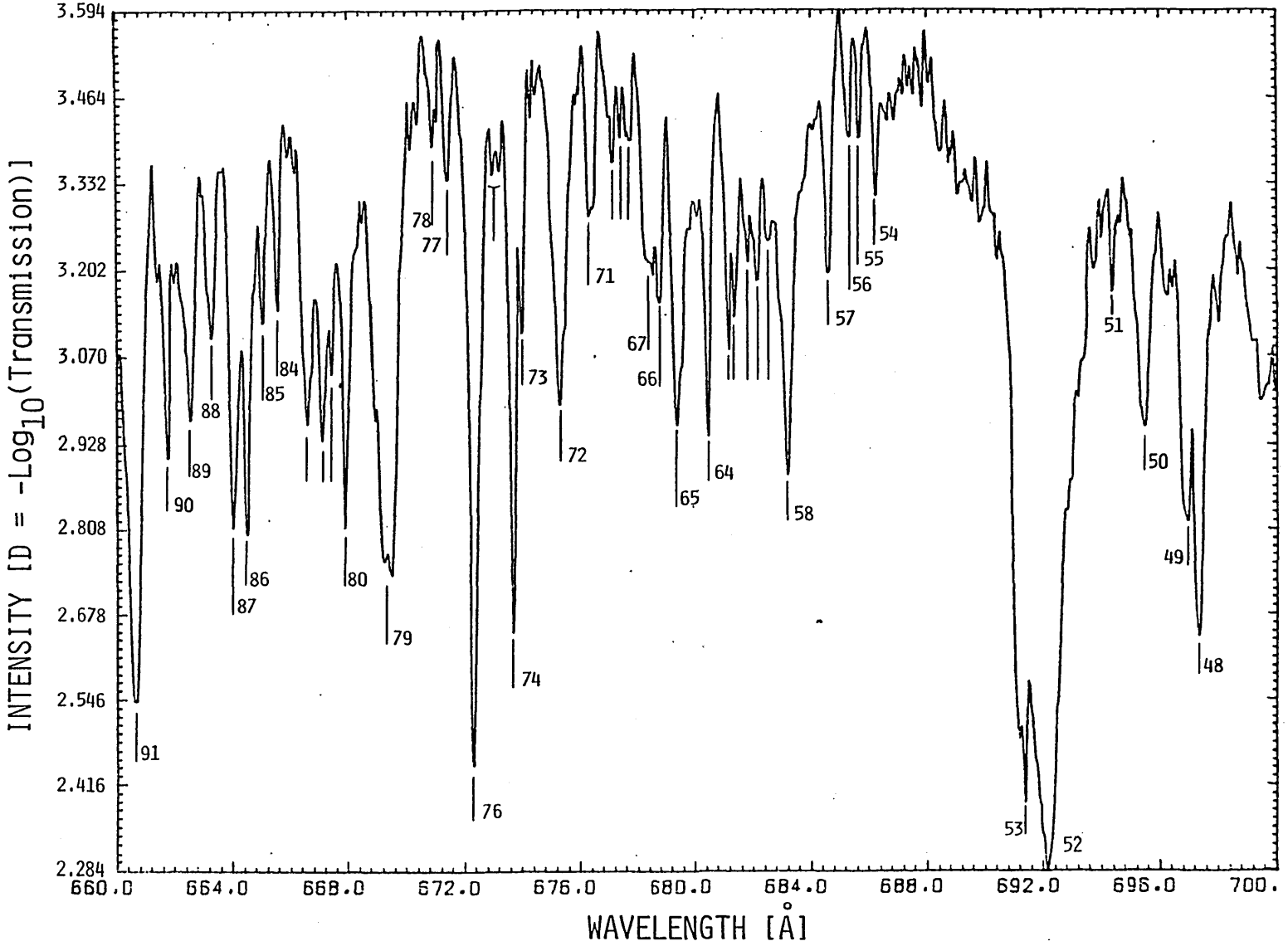


FIGURE 5D2a(viii): PHOTO-ABSORPTION SPECTRUM OF UNEXCITED BARIUM BETWEEN 688Å AND 728Å

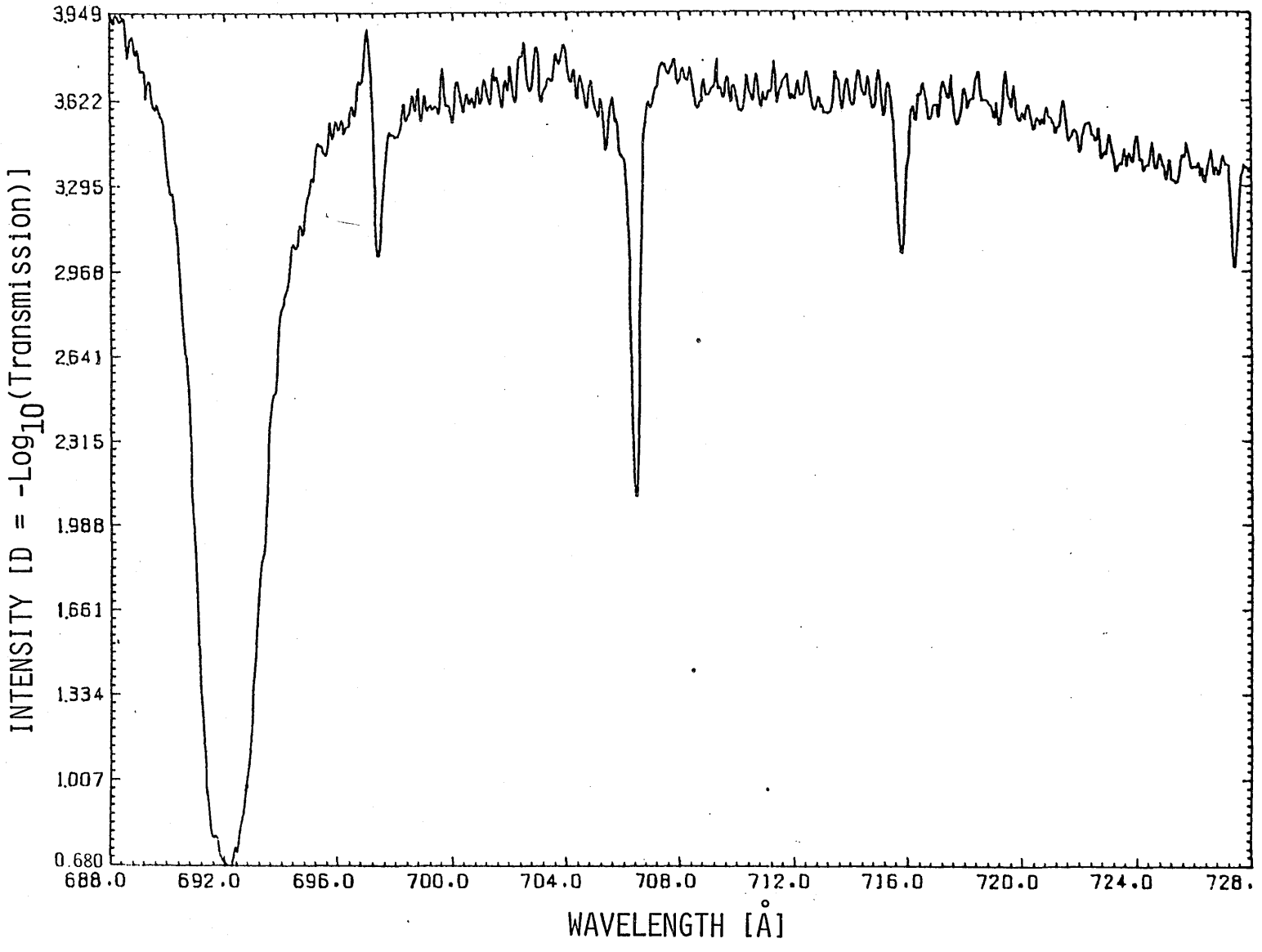


FIGURE 5D2b(viii): PHOTO-ABSORPTION SPECTRUM OF LASER EXCITED BARIUM BETWEEN 688Å AND 728Å

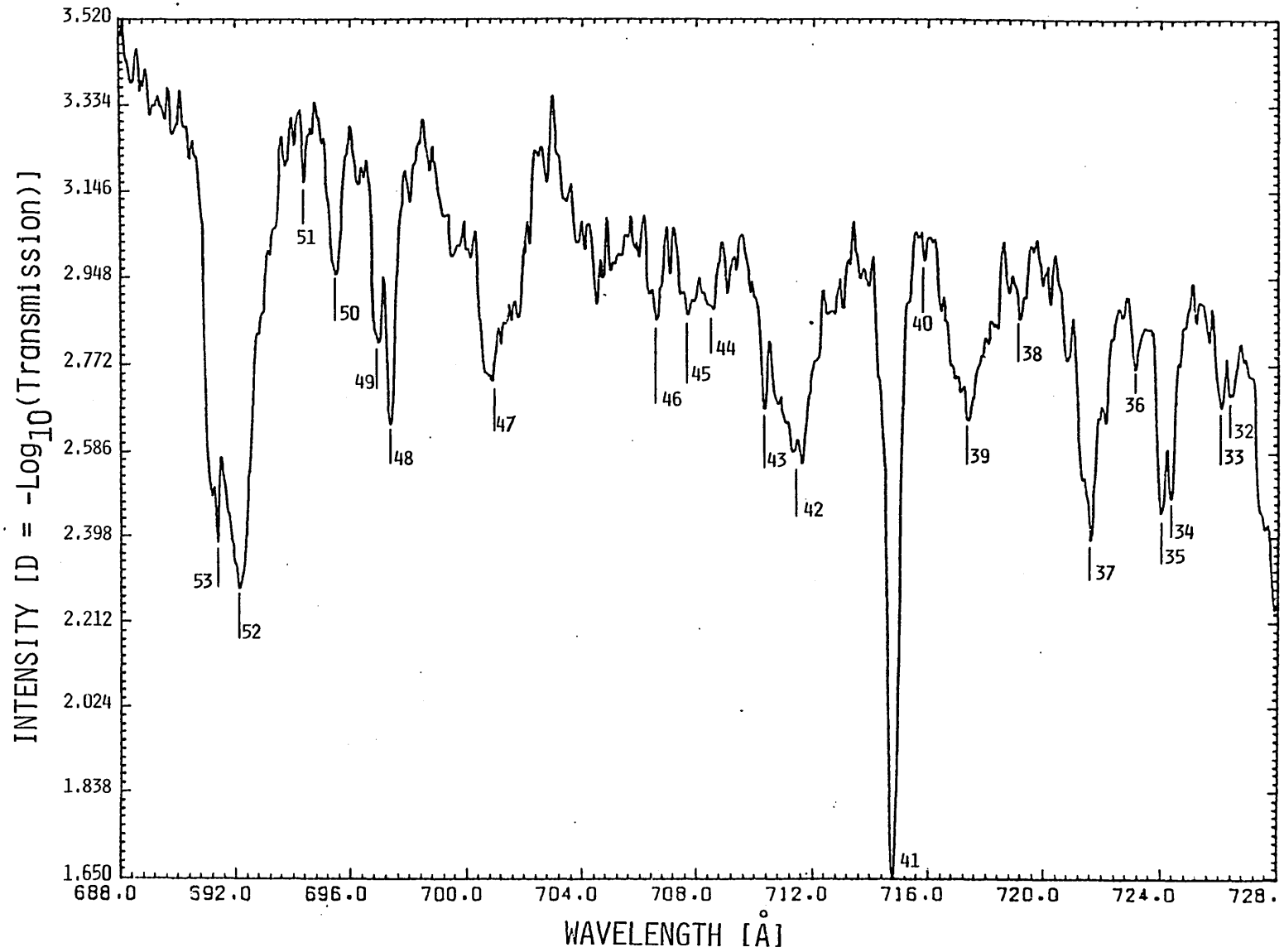


FIGURE 5D2a(ix): PHOTO-ABSORPTION SPECTRUM OF UNEXCITED BARIUM BETWEEN 716Å AND 756Å

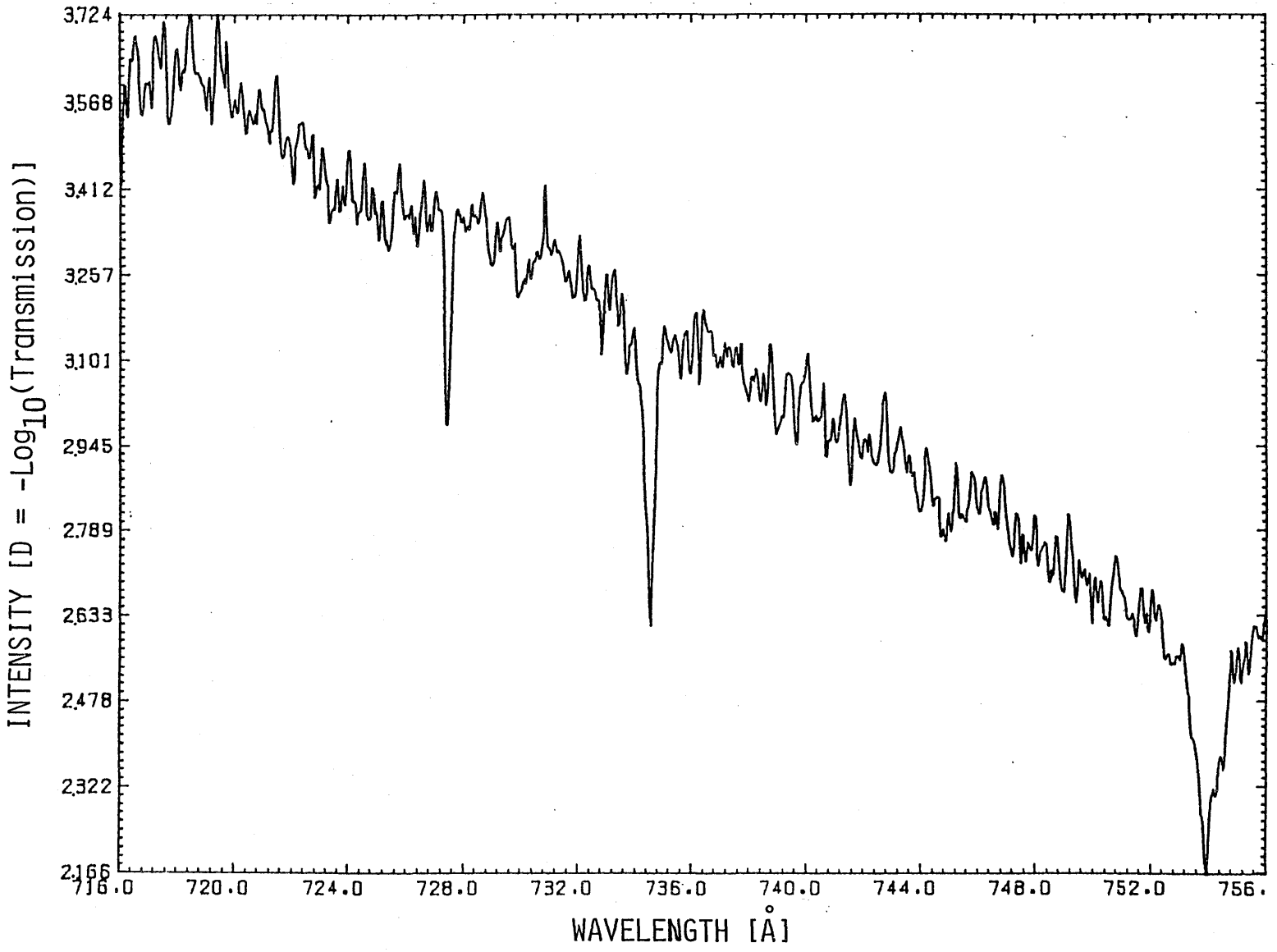


FIGURE 5D2b(ix): PHOTO-ABSORPTION SPECTRUM OF LASER EXCITED BARIUM BETWEEN 716Å AND 756Å

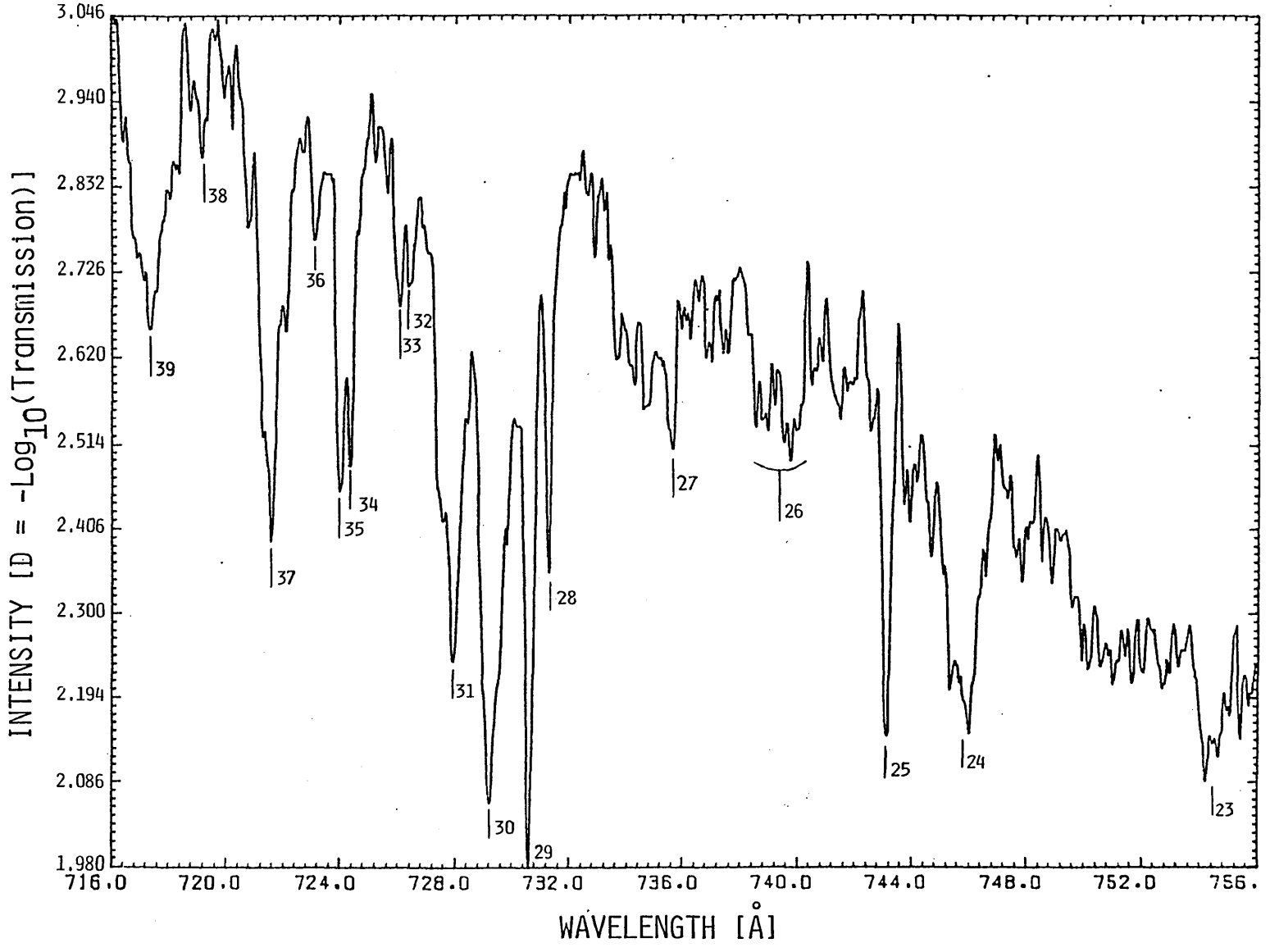


FIGURE 5D2a(x): PHOTO-ABSORPTION SPECTRUM OF UNEXCITED BARIUM BETWEEN 744Å AND 784Å

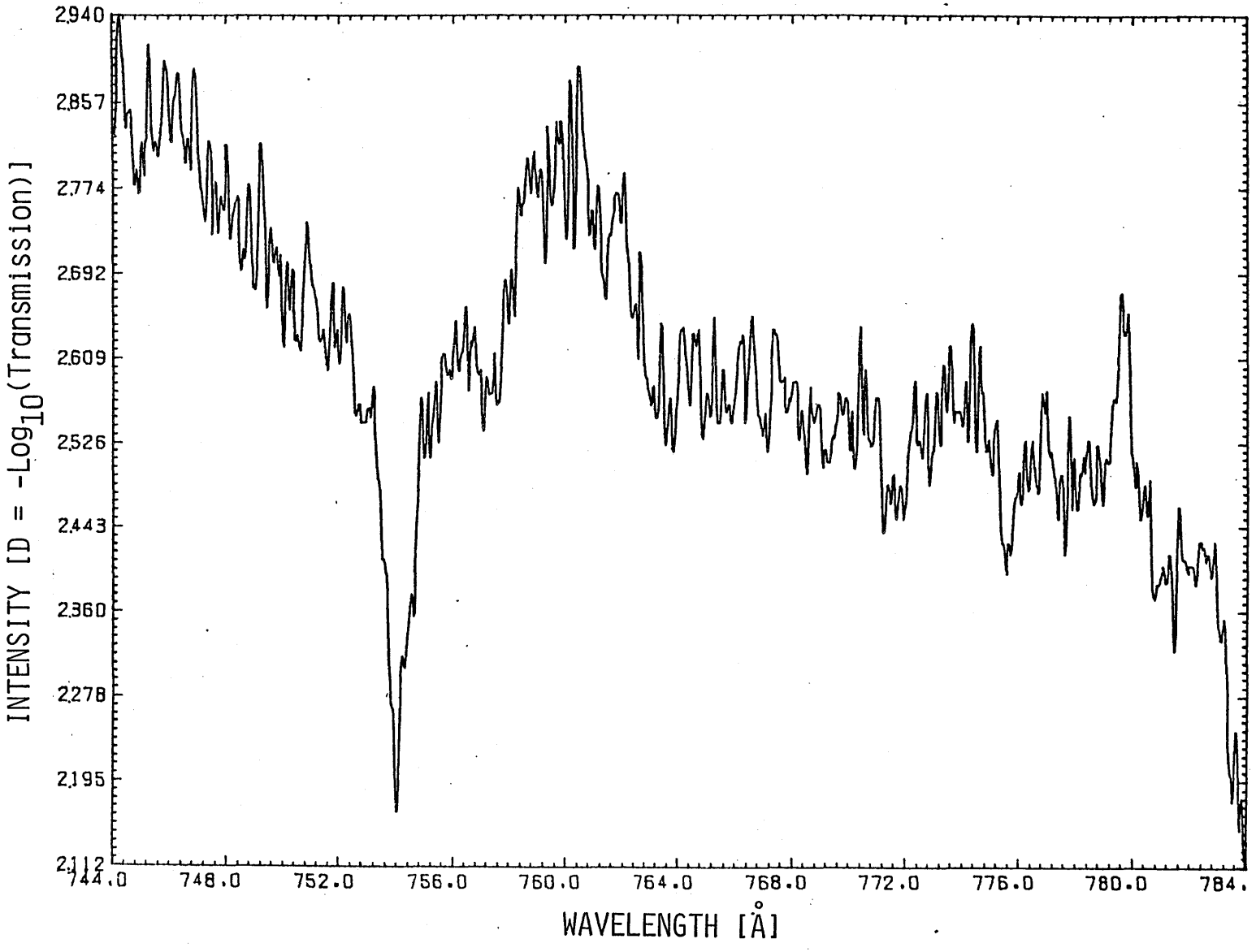


FIGURE 5D2b(x): PHOTO-ABSORPTION SPECTRUM OF LASER EXCITED BARIUM BETWEEN 744Å AND 784Å

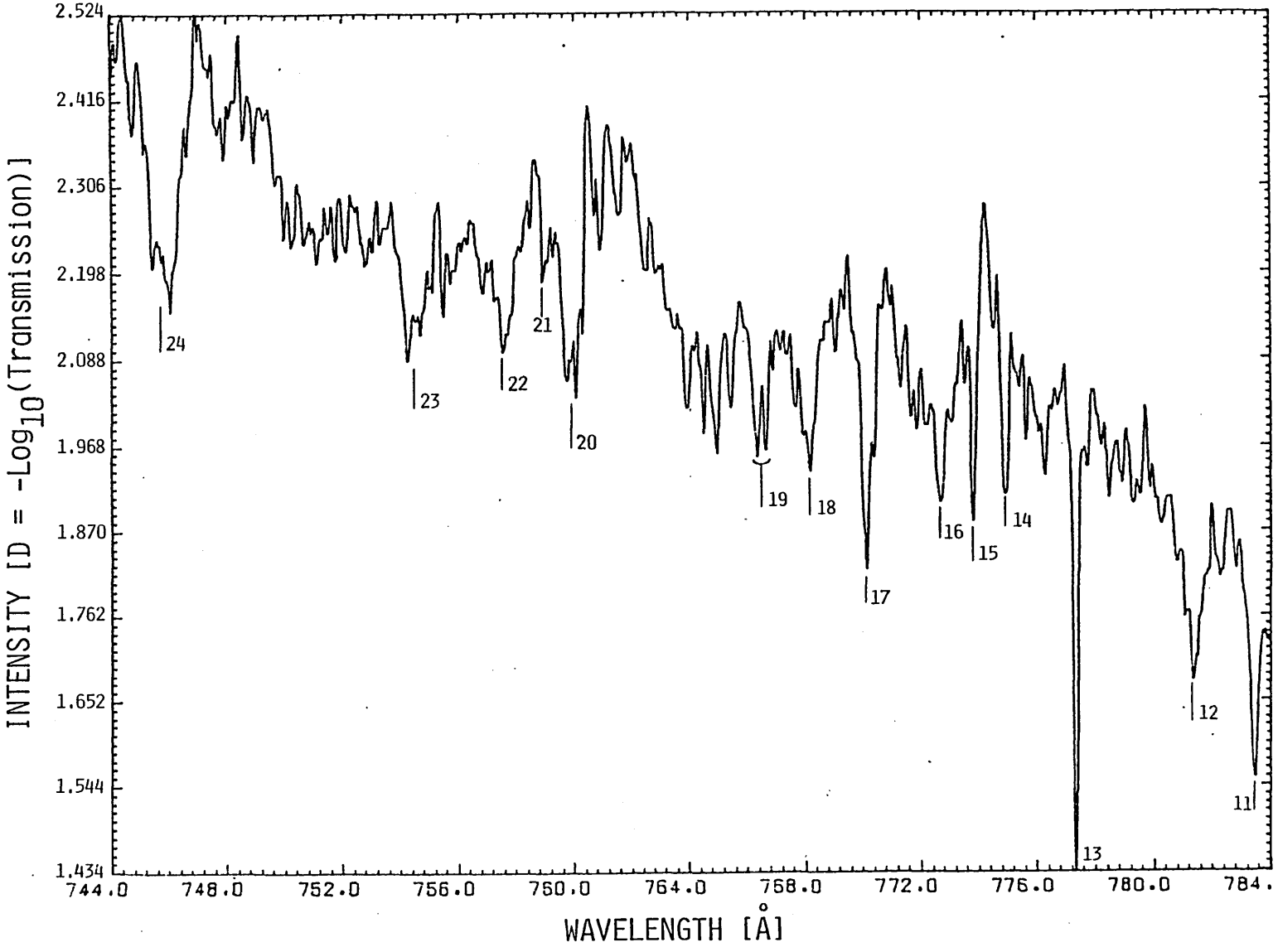


FIGURE 5D2a(xi): PHOTO-ABSORPTION SPECTRUM OF UNEXCITED BARIUM BETWEEN 772Å AND 812Å

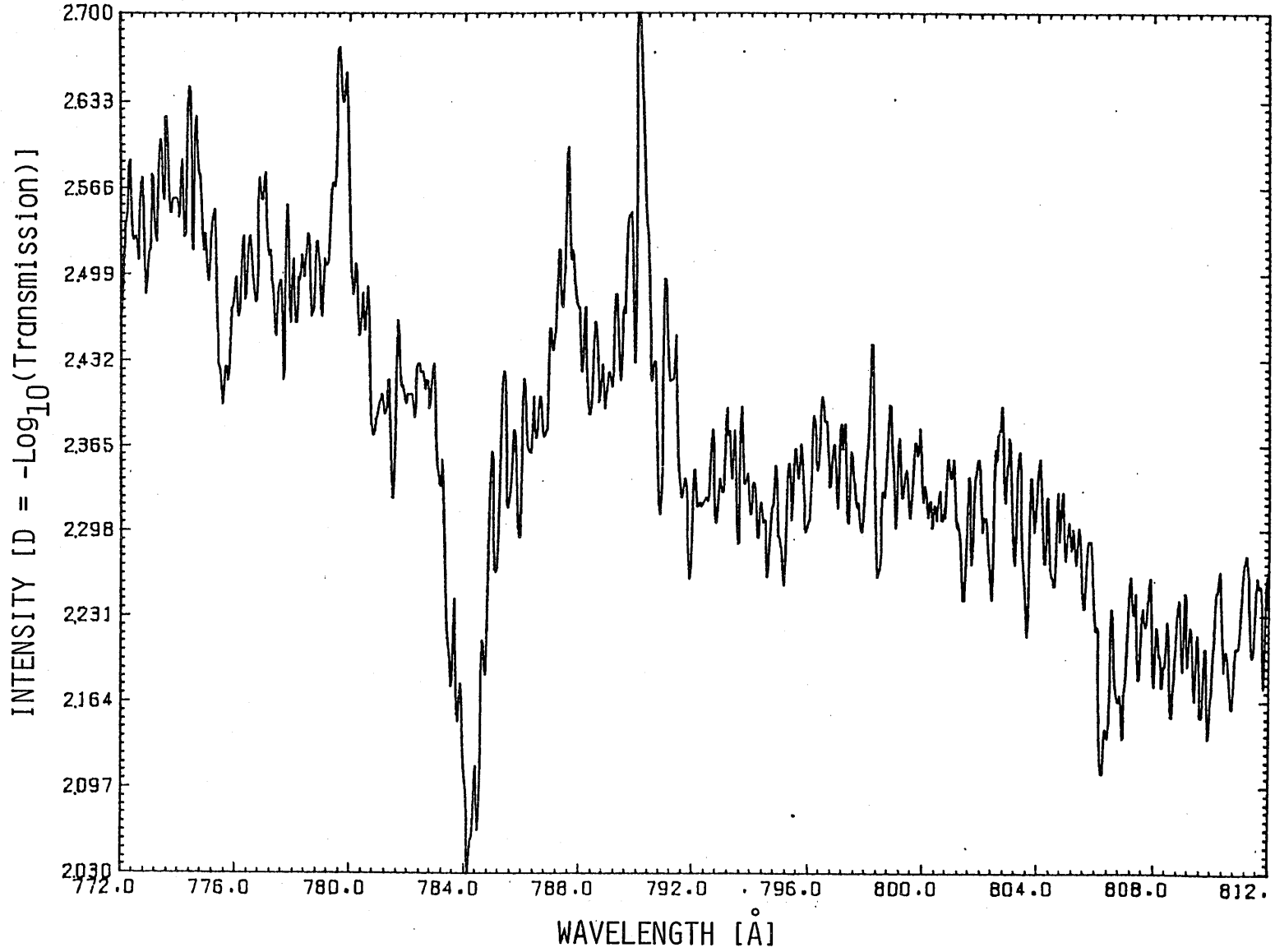


FIGURE 5D2b(xi): PHOTO-ABSORPTION SPECTRUM OF LASER EXCITED BARIUM BETWEEN 772Å AND 812Å

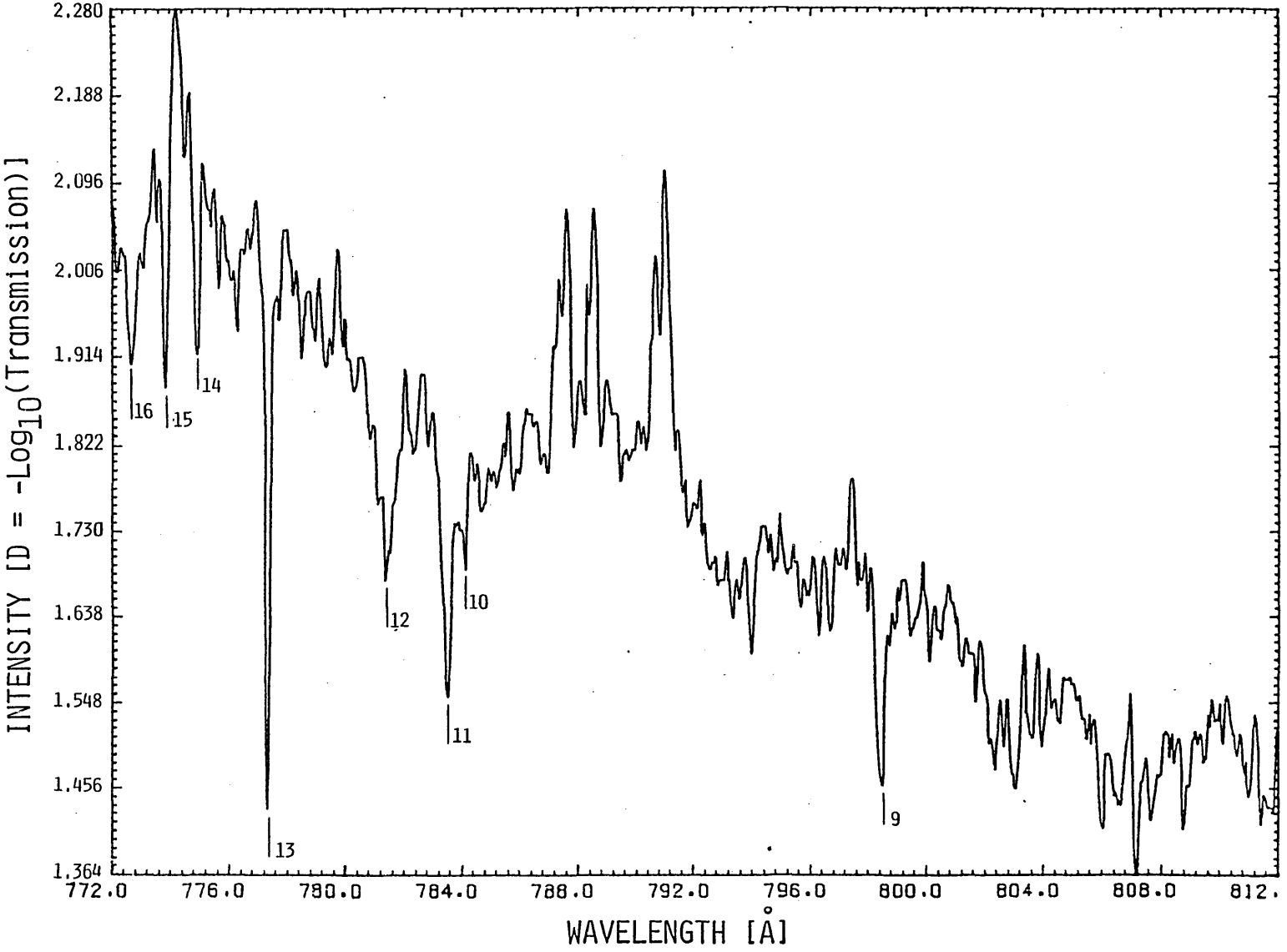


FIGURE 5D2a(x11): PHOTO-ABSORPTION SPECTRUM OF UNEXCITED BARIUM BETWEEN 800Å AND 840Å

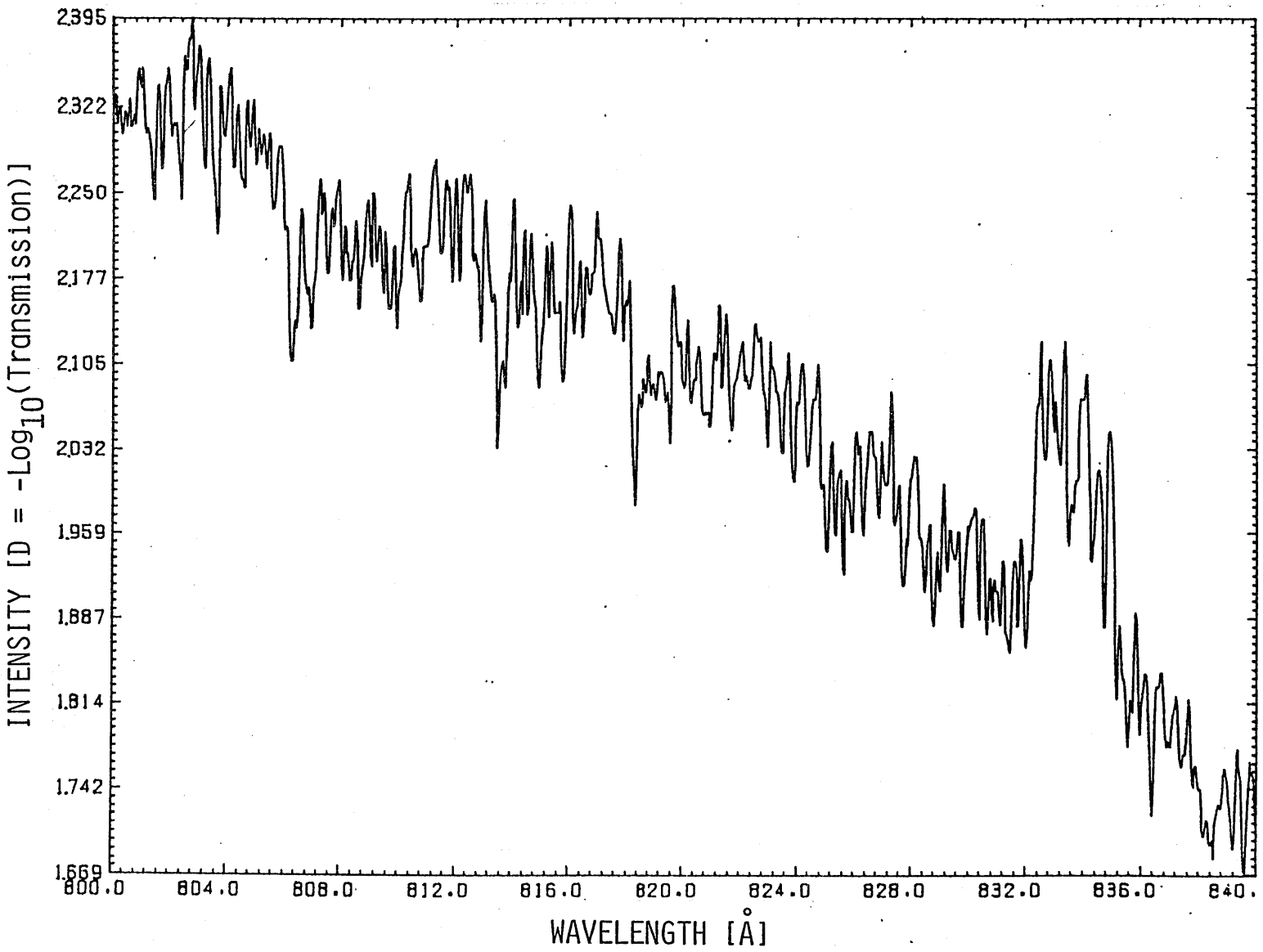


FIGURE 5D2b(xii): PHOTO-ABSORPTION SPECTRUM OF LASER EXCITED BARIUM BETWEEN 800Å AND 840Å

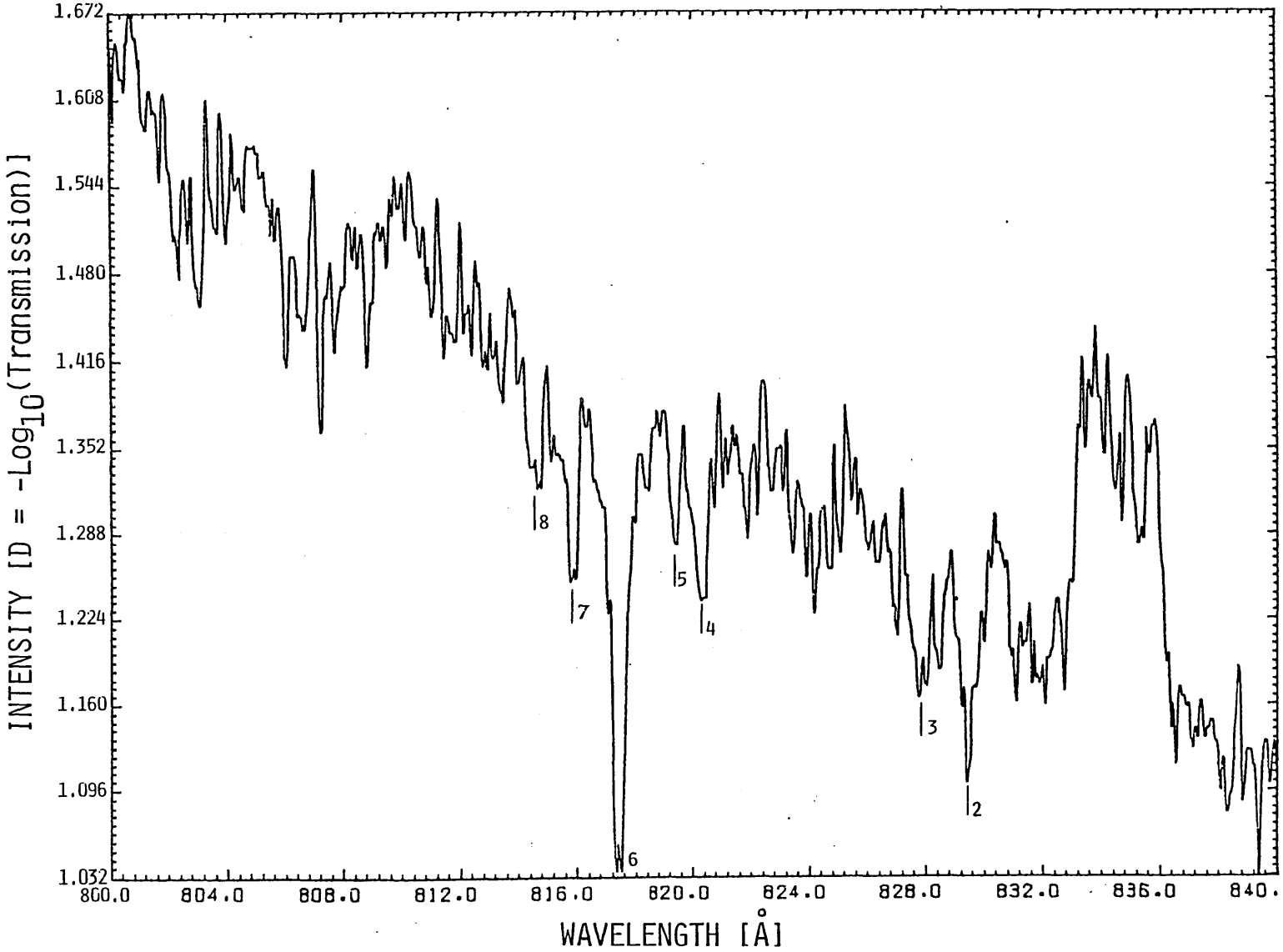


FIGURE 5D2a(xiii): PHOTO-ABSORPTION SPECTRUM OF UNEXCITED BARIUM BETWEEN 819Å AND 859Å

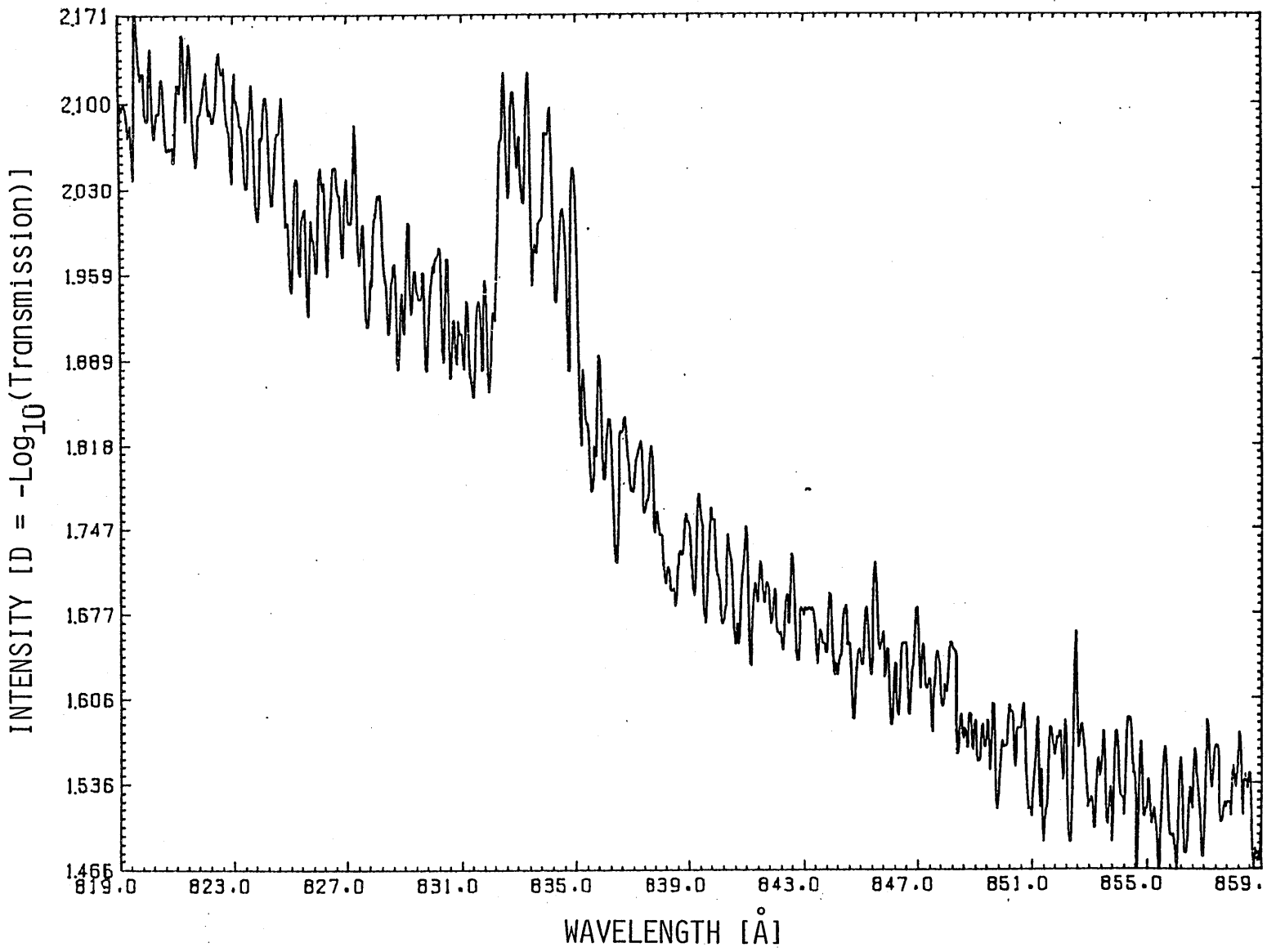


FIGURE 5D2b(xiii): PHOTO-ABSORPTION SPECTRUM OF LASER EXCITED BARIUM BETWEEN 819Å AND 859Å

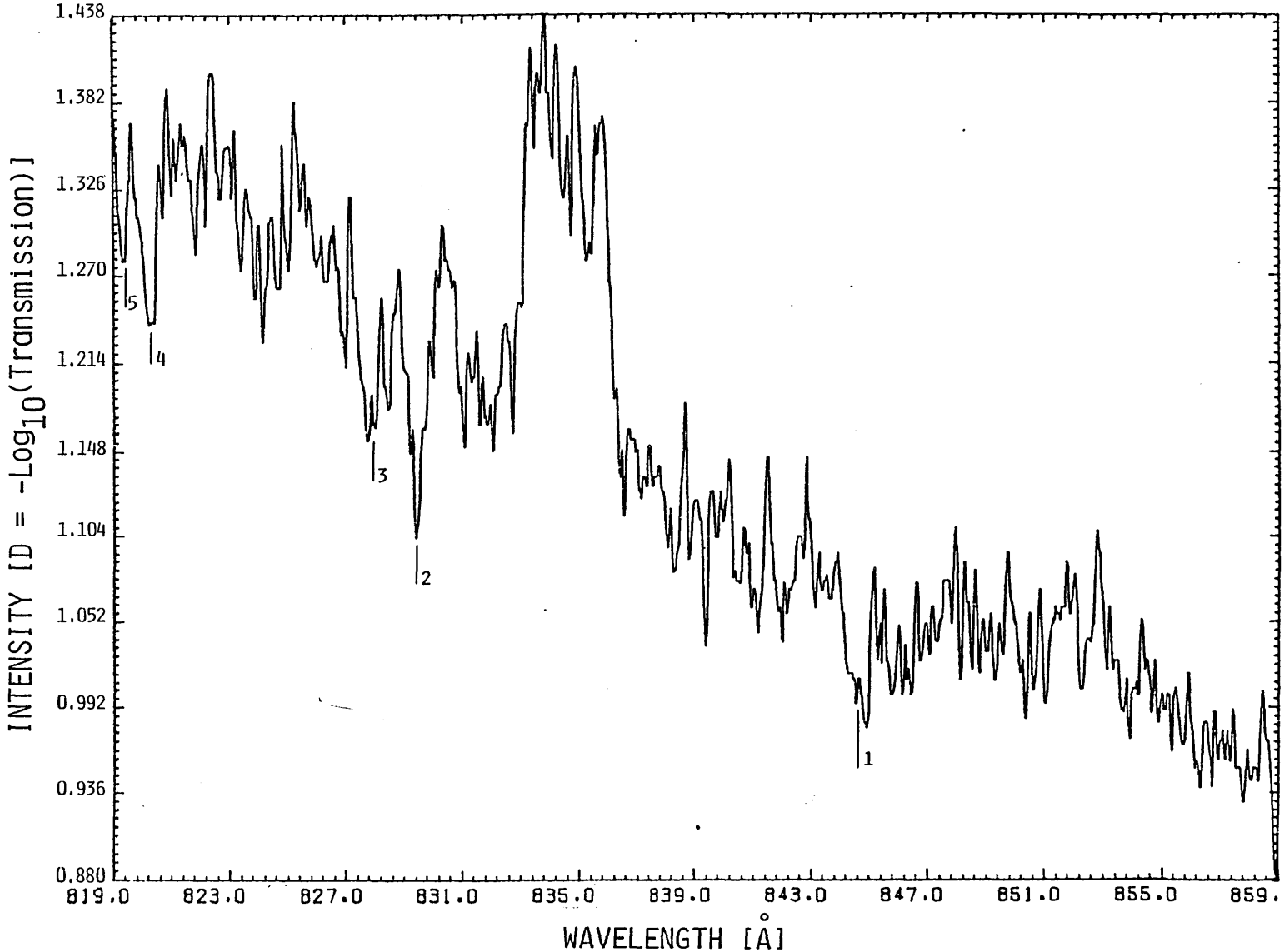


TABLE 2: Line list of resolved VUV features between 844.6Å and 549.9Å of laser excited Barium corresponding to excitations from the levels 6s5d $^1D_2$, $^3D_2$ and $6s^2\ ^1S_0$

Key

Key to symbols in the line number column, see end of table

LINE No.	WAVELENGTH [Å]	ENERGY [cm^{-1}]
1	844.6	118399.
2	829.4	120569.
3	827.8	120802.
4	820.3	121907.
5	819.4	122041.
6	817.4	122339.
7	815.8	122579.
8	814.5	122775.
9	798.4	125251.
10 **	784.1	127535.
11 -	783.5	127632.
12	781.4	127975.
13 -	777.3	128650.
14 -	774.9	129049.
15 -	773.8	129232.
16	772.7	129416.
17 -	770.1	129853.
18	768.1	130191.
19	766.4	130480.
20	759.9	131596.
21	758.9	131770.
22	757.5	132013.

TABLE 2: continued

LINE No.	WAVELENGTH [Å]	ENERGY [cm^{-1}]
23	754.4	132556.
24 -	745.9	134066.
25 -	743.1	134571.
26	739.3	135263.
27 -	735.6	135943.
28 -	731.3	136743.
29 -	730.6	136874.
30 -	729.2	137137.
31 -	727.9	137382.
32 -	726.4	137665.
33 -	726.0	137741.
34 -	724.3	138064.
35 -	724.0	138122.
36	723.1	138293.
37 -	721.6	138581.
38	719.1	139063.
39 -	717.4	139392.
40	715.9	139684.
41 -	714.8	139899.
42 -	711.3	140588.
43	710.3	140786.
44	708.5	141143.
45	707.7	141303.
46 -**	706.6	141523.
47 -	700.8	142694.
48 -	697.4	143390.
49 -	697.0	143472.

TABLE 2: continued

LINE No.	WAVELENGTH [Å]	ENERGY [cm^{-1}]
50 -	695.5	143781.
51	694.4	144009.
52 -*	692.2	144467.
53 -	691.4	144634.
54	686.2	145730.
55	685.7	145836.
56	685.3	145921.
57 -	684.6	146071.
58 -	683.2	146370.
59 -	682.6	146499.
60	682.1	146606.
61 -	681.8	146671.
62 -	681.4	146757.
63 -	681.1	146821.
64 -	680.4	146972.
65 -	679.4	147189.
66 -	678.8	147319.
67	678.4	147406.
68	677.7	147558.
69	677.4	147623.
70	677.1	147689.
71 -	676.3	147863.
72 -	675.2	148104.
73 -	674.0	148368.
74 -	673.6	148456.
75	673.1	148566.
76 -*	672.3	148743.

TABLE 2: continued

LINE No.	WAVELENGTH [Å]	ENERGY [cm^{-1}]
77 -	671.4	148943.
78 -	670.9	149054.
79 -+	669.3	149410.
80 -	667.9	149723.
81	667.4	149835.
82 -	667.0	149925.
83 -	666.5	150038.
84 -	665.5	150263.
85 -	665.0	150376.
86 -	664.5	150489.
87 -	664.0	150602.
88 -	663.2	150784.
89 -	662.5	150943.
90 -	661.7	151126.
91 -	660.6	151378.
92 -	659.8	151561.
93	659.2	151699.
94 -	658.6	151837.
95 -	658.4	151883.
96 -	657.7	152045.
97 -	657.5	152091.
98 -	657.0	152207.
99 -	656.5	152323.
100	656.0	152439.
101 -	655.1	152648.
102 -	654.4	152812.
103 -	653.8	152952.

TABLE 2: continued

LINE No.	WAVELENGTH [Å]	ENERGY [cm^{-1}]
104 -	653.2	153092.
105 -	652.3	153304.
106 -	651.9	153398.
107 -	651.2	153563.
108 -	651.0	153610.
109 -	650.4	153752.
110	650.0	153846.
111 -	649.4	153988.
112 -*	648.9	154107.
113 -	648.0	154321.
114 -	647.1	154536.
115 -	646.3	154727.
116 -	645.5	154919.
117 -	644.5	155159.
118 -	643.4	155424.
119 -	642.8	155569.
120 -	642.1	155739.
121 -	641.5	155885.
122 *	640.7	156079.
123 -	639.2	156446.
124 -+	638.5	156617.
125 -	637.9	156764.
126 -	637.4	156887.
127 -	637.1	156961.
128 -	635.1	157456.
129 -	634.6	157580.
130 -	633.8	157778.

TABLE 2: continued

LINE No.	WAVELENGTH [Å]	ENERGY [cm^{-1}]
131	633.4	157878.
132	632.8	158028.
133 -	632.4	158128.
134 -	631.3	158403.
135 -	630.5	158604.
136 -++	629.6	158831.
137	629.1	158957.
138	628.7	159058.
139 -*	627.8	159286.
140	627.3	159413.
141 -*	626.8	159541.
142 -*	626.0	159744.
143 -	625.5	159872.
144 -*	624.0	160256.
145 -	623.4	160411.
146 -	622.8	160565.
147 -*	622.1	160746.
148 -	621.4	160927.
149 -	620.8	161082.
150 -**	620.6	161134.
151 -*	619.3	161473.
152	618.9	161577.
153 -*	618.5	161681.
154	618.1	161786.
155 -*	617.6	161917.
156 -*	617.1	162048.
157 -*	616.5	162206.

TABLE 2: continued

LINE No.	WAVELENGTH [Å]	ENERGY [cm^{-1}]
158 -*	615.5	162470.
159 -*	614.7	162681.
160 -*	613.7	162946.
161 -*	612.3	163319.
162 -*	611.9	163425.
163 -*	611.3	163586.
164 -*	610.5	163800.
165 -*	609.3	164123.
166 -*	608.9	164231.
167 -*	608.3	164393.
168 -	607.8	164528.
169 -*	607.4	164636.
170 -*	606.2	164962.
171 -*	605.7	165098.
172	605.2	165235.
173 -*	604.9	165317.
174 -*	604.4	165453.
175 -*	604.0	165563.
176	603.4	165728.
177 **	603.0	165837.
178 -*	602.5	165975.
179	601.6	166223.
180	600.6	166500.
181 -*	598.8	167001.
182	597.8	167280.
183	597.4	167392.
184 -*	596.6	167616.

TABLE 2: continued

LINE No.	WAVELENGTH [Å]	ENERGY [cm^{-1}]
185 -**	595.9	167813.
186 **	595.2	168011.
187 -*	594.7	168152.
188 -**	594.3	168265.
189 -**	593.9	168379.
190 -*	593.3	168549.
191 -*	592.6	168748.
192 *	592.2	168862.
193	589.9	169520.
194	588.9	169808.
195 -*	587.8	170126.
196 *	587.3	170271.
197	586.1	170619.
198	585.5	170794.
199 -*	584.0	171233.
200 *	581.9	171851.
201 -*	580.8	172176.
202 -*	579.6	172533.
203 -*	579.2	172652.
204 -*	579.0	172712.
205 *	578.6	172831.
206 *	577.6	173130.
207	576.7	173400.
208	576.1	173581.
209	575.7	173702.
210	575.2	173853.
211 *	574.7	174004.

TABLE 2: continued

LINE No.	WAVELENGTH [Å]	ENERGY [cm^{-1}]
212 *	574.4	174095.
213	573.8	174277.
214	572.5	174672.
215 **	571.6	174948.
216	570.7	175223.
217 *	570.0	175439.
218	568.7	175840.
219	567.3	176274.
220 -*	566.9	176398.
221 -**	566.4	176554.
222	565.7	176772.
223	565.3	176897.
224 **	564.7	177085.
225 **	564.3	177211.
226	563.8	177368.
227	562.6	177746.
228	561.7	178031.
229 *	560.3	178476.
230	559.2	178827.
231	558.4	179083.
232	557.6	179340.
233	557.2	179469.
234 -++	556.6	179662.
235 -++	555.9	179888.
236 -++	555.4	180050.
237	554.5	180343.
238 *	553.7	180603.

TABLE 2: continued

LINE No.	WAVELENGTH [Å]	ENERGY [cm^{-1}]
239	553.2	180766.
240 **	552.7	180930.
241	552.3	181061.
242 *	551.5	181324.
243	550.7	181587.
244	549.9	181851.

Error on the given wavelengths ±0.08A.

Key

Key to the symbols in the line number column are as follows: -

-, lines also listed in a previous, but now superseded, line list prepared from optical comparator measurements.

*, lines corresponding to transitions from the $6s^2$ $^1S_0$ ground state of Barium.

**, lines tentatively identified as corresponding to transitions from the $6s^2$ $^1S_0$ ground state of Barium.

+, features believed to consist of a superposition of a ground state line with an excited state line(s).

++, lines due to absorption in the Samarium source.

5.2.2 Commentary on the Photographic Spectra and Microdensitometer Traces

The photographic spectra of figure 5P1 show quite clearly the difference between the Barium ground state and the laser excited state spectrum. The excited state spectrum is very complex, but the intensities of its absorption lines are in general. much weaker than those found in the ground state spectrum. These absorption lines at wavelengths below 628Å clearly replicate those of the ground state spectrum, but are of course much weaker since the residual population of Barium atoms in the ground state is much smaller. A great majority of the resolvable lines below 628Å can be attributed to absorption lines from the Barium ground state. Only a few are unique to the excited state spectrum which indicates one of two possibilities: either there are few excited state lines in this region, or that their intensity is extremely weak on the whole. Judging from the darker background appearance of the excited state spectra in this region, it would appear possible that these resolved lines are superimposed on an absorption continuum. Such a result would be consistent with the suggestion in Chapter 2 that "only the strongest transitions could be expected to be observed and that the presence of the rest might well be indicated by a quasi

continuum".

The excited state spectrum unlike the ground state spectrum is very complex in the wavelength region between 622Å and 692Å. In general appearance it consists of a complex of many sharp albeit weak absorption lines which almost merge together to form a continuum.

There are far fewer absorption lines in the excited state spectrum at wavelengths greater than 692Å and many of these are quite broad ($\sim$1-2Å). These broad lines have the appearance of molecular features whose width is derived from unresolved rotational structure. For example the "lines" 39, 42 and 47 in figure 5D2b(viii) look plausibly like a vibrational sequence converging to the long wave. However, it will be seen in subsection 5.3.3 that any reasonable value for the Barium dimer's vibrational constant ω_e is far too small for this assertion to be correct. The most clearly observable of these proposed broad structures lie between 692Å and 732Å and their presence is clearly observable in figures 5P2c and 5P2d.

Earlier in this section it was pointed out that the ground state spectrum below 628Å was replicated in the excited state spectrum albeit much more weakly. There are however intensity anomalies in the strength of such replicated lines at wavelengths

above 628Å. For example there are four very strong and sharp lines in the ground state spectrum which correspond to the first four members of the two "k" series at 672.27Å, 669.15Å, 640.46Å and 638.38Å (see figure 1P1 - chapter 1). Of these four lines only the line at 672.27Å shows up clearly in the excited state spectrum. Further confirmation of this result is provided by the microdensitometer traces 5D2a(vi) and (vii). This result is unusual since all of these lines are much stronger than some of the Barium ground state lines below 628Å which are clearly visible in the excited state spectra. The anomaly cannot be explained in terms of non-linearities in the response function of the film and its origin is unclear.

The two sets of microdensitometer traces, 5D2a(i) to (xiii) and 5D2b(i) to (xiii) accurately reproduce most of the features observed in the Barium spectra of figure 5P1. The set of traces 5D2a(i) to (xiii) corresponding to the ground state spectrum compare favourably with those published by Baig et al (1984) achieved at 17 times the authors experimental resolution. Looking in more detail at the Barium ground state absorption traces reveals a number of interesting features which have been picked up. The very asymmetric line profile at 697.3Å in figure 5D2a(viii) is genuine and is an

example of a line which is strongly coupled into the continuum via a broad autoionising resonance, which in this case is the resonance at 692.2Å. It should be noted that the wavelength of this broad resonance ($6s^2\ {}^1S_0 \longrightarrow 5p^5\ 6s^2\ 5d\ {}^3P_1$) is given as 693.66Å by Connerade et al (1979a). This value is clearly incorrect from the trace and a better value for its wavelength would be 692.2Å. Another interesting feature which is picked up in these traces is the change in the symmetry of the line profiles of the "a" series identified originally by Connerade et al (1979a) (see figure 1P1 of Chapter 1). Part of series "a" is clearly discernible in figure 5D2a(i) and the symmetry of the asymmetric profiles seen in the lines at 517.6Å (n=3) and 511.4Å (n=4) change abruptly to the opposite on proceeding to the next member of the series at 508.2Å (n=5). This phenomenon is documented in the literature and is given the name: "q switching" (see Connerade et al, 1985).

The microdensitometer traces of the excited state spectrum recorded ~250 [ns] after the rise time of the dye laser pick up all of the resolved structure between 624Å and 692Å as may be seen by comparing the traces 5D2b(v) to 5D2b(vii) with figure 5P2b. The structure in the broad resonance at ~ 692Å is clearly observable, and probably corresponds to the superposition of a new line at 691.4Å with the line list due to the extremely strong

transition to the $5p^5 6s^2 5d\ ^3P_1$ level from the remaining Barium atoms in the ground state. The lines picked out and numbered 1 to 244 correspond to those listed in the line list of table 2 (see section 5.2.3). Some of the lines which have been picked out may seem "optimistic" but many have been supported by previous measurements by the author using an optical comparator. For example the lines marked 149 and 150 in figure 5D2b(vi) were described in the original line list that was prepared from optical comparator measurements, as a struture consisting of "two closely spaced superimposed lines". One of the interesting features of this spectrum which can be seen in these traces are the broad absorption structures at wavelengths above 692Å. These structures are thought to be molecular in origin and the best examples may be seen in figures 5D2b(viii) to (x)

5.2.3 The Line List

The line list of table 2 gives the wavelengths in angstroms [Å] to one decimal place of the resolved lines/structures between 845Å and 549Å which have been marked out on the microdensitometer traces 5D2b(i) to (xiii). All of these correspond to structures which can be confidently linked to those visible on an enlarged photographic print of the excited state spectrum of Barium recorded 250 [ns] after the rise of the pump dye laser. The lines on the list marked with a hyphen (-) correspond to those also listed in a

previous, but now superseded, line list prepared from optical comparator measurements. Those lines marked with an asterisk (*) or a pair of asterisks (**) correspond to those lines which can either be confidently or tentatively identified as transitions from the Barium ground state. Lines marked with a single addition symbol (+) correspond to those which are believed to be superposition of a ground state line with an excited line(s). Those marked with a pair of addition symbols (++) are identified as absorption lines due to the samarium source.

The error on the given wavelength is ±0.08Å

5.3 Discussion

5.3.1 Barium level populations following laser excitation on the resonance line at 5535.48A

A successful analysis of the Barium excited state absorption spectrum is very dependent on knowing which levels were populated when the continuum source was fired. Absorption spectra were recorded over a range of different delays between the dye laser's rising edge and the peak of the continuum source. These ranged from ∼10 [ns] up to ∼600 [ns] and therefore probed the excited vapour column both during and after the dye laser. The resulting spectra reveal the same basic structure: A

complex of new lines common to all delays superimposed onto a greatly diminished absorption spectrum arising from the residual population of the unexcited Barium atoms.+

Consequently, the 6s6p $^1P_1$ level may be ruled out as a possible starting level for the observed absorption lines since the spontaneous lifetime of this level is only 8.4 [ns]. The levels responsible for the above absorption spectra must be both long lived (>>250 [ns]) and accessible from the laser populated 6s6p $^1P_1$ level. Ba^+ can also be ruled out as a starting level for the observed spectra on two counts: First, laser induced ionisation was not expected to be important in this experiment for the reasons elucidated in chapter 1 and second, there is no correlation between the line list of table 2 with that given by Roig (1976) for Ba^+. The list of plausible starting levels for the observed spectra is thus reduced to the set of

+The two spectra recorded at $\sim$10 [ns] and $\sim$ 600 [ns] delays between the dye laser and the continuum source were not particularly successful. In the case of the former the triggering proved problematic: approximately one third of the continuum shots were before the rise of the dye laser, while in the 600 [ns] delay experiment the Barium number density was much lower than usual for spurious experimental reasons. This last comment is based on the clearly reduced strength of the Barium ground state spectra taken before and after the main excited state spectrum. Consequently the absence of many of the weaker lines seen in the excited state spectra of other runs was not remarkable. Nevertheless the more prominent lines, for example the strong line at 714.8Å, were again seen in both spectra.

metastable states lying below the 6s6p $^1P_1$ level (see figure 1D3 of chapter 1). These are the 6s6p $^3P_{0,1,2}$, the 6s5d $^1D_2$ and the 6s5d $^3D_{1,2,3}$ metastable levels, a total of seven in all.

The 6s6p $^3P_1 \longrightarrow 6s^2\ ^1S_0$ transition is spin forbidden and therefore weak and its A value corresponds to a spontaneous lifetime of $\sim$1.25[μs] (Bowen, 1982). Of course the strengths of the dipole forbidden transitions from any of the other six levels to the ground state are much weaker still. Hence the chief quenching mechanism for these metastable levels is via collisions with other Barium atoms. The resulting collisional lifetimes of these levels may be calculated from their respective quenching crossections due to Barium collisions which are: -

$\sigma_{Ba}(^3P_2) = (2.7\pm2)\times10^{-17}$ [m^2] Bowen et al (1985)

$\sigma_{Ba}(^1D_2) = (6\pm2)\times10^{-18}$ [m^2] Bowen et al (1985)

$\sigma_{Ba}(^3D_J) = (1.3\pm0.1)\times10^{-19}$ [m^2] Whitkop et al (1980)

The corresponding collional lifetimes τ_c of these levels (= $1/[n_{Ba}\langle v_{Ba}\sigma_{Ba}\rangle]$) at a number density of 10^{21} [m^{-3}] would be: -

$\tau_c(^3P_2) = 81 \pm 60$ [ns]

$\tau_c(^1D_2) = 370 \pm 120$ [ns]

$$\tau_c(^3D_J) = 1700 \pm 100 \text{ [ns]}$$

Assuming that the above data on the quenching crossections are correct, it would appear that the metastable 6s5d D levels are sufficiently long lived to account for the observed spectra. The $^3P_{0,1,2}$ levels are a more border line case, bearing in mind the uncertainty in both the Barium number densities and the quenching crossection data, since these levels should have relaxed back to the ground state in the $\sim$ 250 [ns] delay experiment ($\sigma_{Ba}(^3P_{0,1}) \simeq \sigma_{Ba}(^3P_2)$ assumed). Further evidence against the 6s6p ^3P levels being responible for the observed spectra are provided by the $\sim$ 10 [ns] delay experiment which indicated an extreamely fast mechanism ($\lesssim$ 10 [ns]) for the populating of the responsible level(s). Such a rapid risetime would imply a radiative rather than a collisional mechanism and electric dipole transitions from the 6s6p $^1P_1$ level to the 6s6p $^3P_{0,1,2}$ levels are forbidden on parity grounds.

Only the 6s5d $^1D_2$ and 6s5d $^3D_{1,2}$ levels are radiatively connected to the 6s6p $^1P_1$ level. Experimentally deduced A values for the transitions to the two triplet states do not appear to have been published in the literature, except for an indirect reference by Bowen et al (1985) to some work by Niggli and Huber on the 6s5d $^3D_2$ level. Experimentally based A values have on the other hand

been published for the 6s6p $^1P_1$-6s5d $^3D_2$ transition. Miles and Weise (1969) report an A value of 0.049 while the much latter work of Bernhardt et al (1976) gives a value of $\lesssim 0.0017$. Bernhardt et al's result is certainly too large judging from the details given in their paper+. From chapter 1 it would appear that the literature is in some disagreement regarding the relative strengths of the 6s6p $^1P_1$ -6s5d $^3D_2$ and 6s6p $^1P_1$-6s5d $^1D_2$ transitions. However the experimental evidence of Bricks et al (1978) provides convincing evidence (in the author's opinion) that the intercombinational line is in fact stronger than the spin allowed transition; the infra red "discharge heated Barium metal vapour laser" of Bricks et al was found to lase initially on the 6s6p $^1P_1$ - 6s5d $^3D_2$ intercombinational line at 1.13 [μm] during the heating up sequence before eventually lasing on the 6s6p $^1P_1$ - 6s5d $^1D_2$ line at 1.5 [μm]. This conclusion is supported by the A value calculations of Hafner et al (1978) who gives values of 4×10^4 and 1.2×10^5 [s^{-1}] for the singlet and triplet transitions, respectively. As for the 6s6p $^1P_1$ - 6s5d $^3D_1$ intercombinational transition, this is by far and away the weakest of the three dipole allowed

+Bernhardt et al's technique was based on deducing the Branching Ratio of spontaneous emission from the 6s6p $^1P_1$ level to either the 6s^2 $^1S_0$ or 6s5d $^1D_2$ level. They neglected the spontaneous emission to the 6s5d $^3D_2$ level which is comparable to the spontaneous emission to the 6s5d $^1D_2$ level (Hafner et al (1978), Kunnemeyer et al (1983)). So their given A value (1.7×10^5 [s^{-1}]) is in fact equal to the sum of the A values for the 6s6p $^1P_1$-6s5d $^1D_2$ and $^3D_2$ transitions, which compares favourable with the theoretical sum of 1.6×10^5 [s^{-1}] of Hafner et al (1978).

transitions judging from the indirect evidence of Bricks et al.

These A values are far too small to account for the observed rapid build up of the metastable 6s5d $^1D_2$ and 6s5d $^3D_2$ levels ($\lesssim$ 10 [ns]), in terms of just spontaneous emission from the higher 6s6p $^1P_1$ level, which would require time scales of 25 [μs] and 8.3 [μs] for the singlet and triplet transitions, respectively. Some other population mechanism for these levels is therefore necessary if they are to account for the observed absorption spectrum.

This problem has been studied by Bowen and Thorne (1985) and the rapid population of these two levels can be understood in terms of Amplified Spontaneous Emission. Saturation of the $6s^2\ ^1S_0$-6s6p $^1P_1$ transition by the pump laser gives rise to a population inversion between the 6s6p $^1P_1$ level and the lower 6s5d $^1D_2$ and 6s5d $^3D_2$ metastable levels. Hence the spontaneous emission from the 6s6p $^1P_1$ level to those metastable levels can exhibit light amplification by stimulated emission. Of course the importance of such stimulated emission to the population rate of the metastable levels is dependent on the "gain" of the vapour medium; and this gain is determined by the number density of the available excited atoms in the 6s6p $^1P_1$ level as well as the geometry of the vapour column, as was explained by Bowen et al. For

example, the greatest amplification of spontaneous emission will be along the length of the pumped vapour column and most of the resulting infra-red radiation will fall into two narrow cones centred on the pump laser axis[+].

The validity of this A.S.E. model is tested by the requirement that the build up of the metastable populations should be on a time scale of the order of 10 [ns] (to explain the 10 [ns] delay experiment). A similar situation was analysed by Bowen et al (1985), see appendix 5, and their test requirement was that the time t_o taken for the stimulated rate to equal the spontaneous rate should be less than 10 [ns]. This criterion is natural since the stimulated rate is proportional to the infra red photon density ρ, and the increase in ρ is initially exponential in time, leading to their observation that "the system will be driven very rapidly to equilibrium for $t > t_o$".

According to the analysis of Bowen et al (1985), the time t_o is given by the relationship: -

$$t_o = \frac{8\pi \ln(1/\alpha)\, \Gamma}{c\, \lambda^2\, A_{23} \beta\, N_2} \qquad 1$$

[+]Kunnemeyer and Koch (1983) have observed both 1.5 [μm] and 1.13 [μm] radiation in the forward direction after excitation on the Barium resonace line (No. density - 10^{19} - 10^{21} [m^{-3}] for a column length of 20 [cm]).

where α is a geometrical factor giving the fraction of emitted spontaneous photons which travel along the vapour column, Γ is the "rectangular" line width of the 6s6p $^1P_1$ - 6s5d $^{3,1}D_2$ transitions which is governed by the broadening of the 6s6p $^1P_1$ level by the "Autler-Townes" effect+, c is the velocity of light, λ the wavelength of the infra red transition, A_{23} is the spontaneous rate connecting the 6s6p $^1P_1$ - 6s5d D_2 levels and N_2 is the number density of atoms in the 6s6p $^1P_1$ level. β is a factor which accounts for photons escaping along the length of the excited vapour column and is given by:-

$$\beta = 1 - \exp(-k_o l') \qquad 2$$

"where l' is a "typical" length (say half the column length) and (since $N_3 \simeq 0$)": -

$$k_o = \frac{N_2 \lambda^2 A_{23}}{8\pi \Gamma} \qquad 3$$

+The Autler Townes effect is the splitting of the fluorescence from a single upper level "a" to a single lower level "b" into two frequency components as a result of the coupling of a third level "c" to the level "a" by a high power laser. The splitting is a function of the electric field strength E. Thus in an excited vapour column where the laser power is not homogenous over the crossection, but varies from zero power to full power, the Autler Townes effect will give rise to fluorescence which is broadened rather than consisting of two sharp frequency components.

Substituting in the following values for the quantities in equations 1,2 and 3: -

$\lambda(^1D_2) = 1.5$ [μm], $\lambda(^3D_2) = 1.13$ [μm]

$A_{23}(^1D_2) = 4\times10^4$ [s^{-1}], $A_{23}(^3D_2) = 1.2\times10^5$ [s^{-1}]

$\Gamma = 23$ [GHz]$^+$

$l' = 0.105$ [m]
$\alpha = 10^{-4}$
} For the geometry of this experiment

yields over the number density range 10^{20} - 10^{21} [m^{-3}] values t_o which decrease from 2.5 [ns] to 0.19 [ns] for the singlet $^1D_2$ transition and 1.2 [ns] to 0.12 [ns] for the triplet $^3D_2$ transition. Of course these values do not reflect the finite time (∿ 10 [ns]) it takes to initially populate the 6s6p $^1P_1$ level over the length of the vapour column. However

$^+\Gamma$ correponds to the Autler Townes splitting which which is given by: -

$$\Gamma = \sqrt{\Delta^2 + \Omega_o^2}$$

where Δ is the detuning of the laser from the resonace frequency (∿ 0 here) and Ω_o is the Rabi frequency: -

$$\Omega_o = \sqrt{\frac{A_{21}\,\lambda^2\,F}{8\pi^3\,n}}$$

where $A_{21} = (1/8.4)\times10^9$ [s^{-1}], $\lambda = 5535.48$Å, F is the laser flux = 1.1×10^{28} [photons s^{-1} m^{-2}] corresponding to 0.4 [MW cm^{-2}] and n is the number of laser modes = 3.

they do serve to demonstrate that the ASE mechanism for populating the $^1D_2$ and $3D_2$ levels is indeed a viable explanation, provided the A values given by Hafner et al (1978) are correct (or too small).

The above amplified spontaneous emission will eventually lead to the Barium atom population being distributed amongst the four levels in the ratio of their statistical weights. This would lead to 71.4% of the population being shared equally between the $^3D_2$ and $^1D_2$ levels, with the remainder being shared in the ratio of 1:3 between the $^1S_0$ and $^1P_1$ levels. This of course takes no account of collisional redistribution amongst the $^3D_{1,2,3}$ levels resulting in more population being drawn out of the $^1S_0$ and $^1P_1$ levels in order to maintain the statistical equilibrium between the $^1P_1$ and $^3D_2$ levels. It should be noted that the remaining population in the 6s6p $^1P_1$ level will drop back to the ground state after the pump laser terminates. Hence the ground state population, in the absence of such collisional redistribution, should quadruple resulting in more prominent Barium ground state lines in the 250 [ns] delay experiment compared with the 60 [ns] delay experiment. Such an effect is indeed seen when account it taken of the 24 shots in the 60 [ns] delay experiment where the dye laser did not fire before the continuum pulse compared with the corresponding 5 such events in the 250 [ns] delay experiment.

In conclusion, the Barium level populations during the excited state absorption experiments will be distributed predominantly in the 6s5d $^1D_2$ and 6s5d $^3D_2$. This is due to ASE from the 6s6p $^1P_1$ level. The population in the 6s6p $^3P_{0,1,2}$ is not expected to be important. Collisional redistribution amongst the 6s5d $^3D_{1,23}$ states could lead to a significant population in the 6s5d $^3D_{1,3}$ levels which might give rise to some of the observed excited state lines. Finally, the 6s6p $^1P_1$ level does not appear to have contributed to the observed spectra since the spectra taken at delays of 60 [ns] and 250 [ns] reveal the same new structure.

5.3.2 Comparison of experimental spectra with theoretical calculations

Theoretical Calculations on the 5p absorption spectrum of Barium from the $6s^2\ ^1S_0$, 6s5d $^1D_2$ and 6s5d $^3D_{1,2,3}$ levels have been performed by Dr M.W.D. Mansfield,[+] These calculations were performed using the Cowan code which is based on the HXR (Hartree plus exchange with relativistic correction) Model. This code is thus a hybrid in that it is based on the non-relativistic Schrodinger equation but with relativistic corrections added. Such corrections

[+]Present Address: Physics Department, University College, Cork, Ireland.

are important in Barium since the 5d wavefunction is "soft" resulting in small effects being greatly magnified as was described in Chapter 2. The Cowan code is one of the best available ab initio codes, second only to the Multi Configurational Dirac Fock Code of Rose et al (1980) which is based on a full implementation of the Dirac equation rather than the 'hybrid' approach above and therefore yields more reliable results (Connerade 1985, Private Communication).

The most relevant calculations to the present work evaluated the energies and strengths of the 5p absorption transitions from the $5p^6 6s^2\ ^1S_0$, $5p^6 6s5d\ ^3D_2$ and $5p^6 6s5d\ ^1D_2$ levels to a limited number of upper levels. The importance of 6s5d mixing was acknowledged by representing each level by an array of configurations constructed from the manifold ($6s^2 x 6s5d x 5d^2$). On an operational level, the Cowan code uses the same average of configuration 6s or 5d wavefunction for <u>each</u> level of a given system of interacting configurations. However these wavefunctions were constructed to minimise the energy of the manifold of interacting configurations, $6s^2$, 6s5d, $5d^2$, where the weighting factors of these were optimised to minimise the average energy of the system. This approximation is valid provided the one electron wavefunctions are insensitive to small perturbations by a given level to the "average" effective field seen by a

particular electron. The code then proceeds to evaluate the total wavefunction of each desired level built on the above set of interacting configurations, although the weighting factors for each of these would depend on the level. For example, the level normally labelled $6s5d\ ^1D_2$ contains a small $5d^2$ component but no $6s^2$ component, while the nominally $6s^2\ ^1S_0$ level contains small contributions from both 6s5d and $5d^2$ as was calculated by Rose et al (1978).

The 5p transitions calculated by Mansfield were restricted to those terminating on levels built from a mixture of the three configurations $5p^5 5d 6s^2$, $5p^5 5d^2 6s$ and $5p^5 5d^3$. Calculating these levels is an obvious first move in any detailed analysis of the excited state spectrum. The "complex" region of the spectrum below 690Å is characterized by many closely spaced lines, while on the other hand, the "simple" region at higher wavelengths has comparatively few lines and these are separated by relatively large wavelength intervals. It is thus more fruitful to concentrate on this "simple" spectral range where the best hopes lie of linking observed lines to calculated lines. Most of the lines in this simple region will correspond to excitations to the levels where the running electron is either 6s or 5d.

Mansfields calculations were in intermediate

coupling and his communication states that the states parameters were scaled as follows; "F and G down 15%, R down 20%, ζ down 5%." According to Mansfield, "Slater Intergrals of this sort tend to reproduce the gross effects of interaction with further configurations". Configuration mixing was found to be severe in the presence of the 5p core vacancy, in agreement with the discussion of Chapter 2. Single L-S term assignments to given lines had little meaning with the largest L-S components being well below 50% and "j-j coupling was even less appropriate".

An indication of the accuracy of these calculations was provided by those on the transitions arising from the $6s^2\ ^1S_0$ level. However these particular calculations suffered a special problem due to the $5p^5 5d 6s^2\ ^1P_1$ solution being substantially different from the configurational average solution. A similar effect was observed by Connerade et al (1979a) in their Hartree Fock calculations on the same levels. As a result the energies and oscillator strengths of the J=1 levels were "badly described" by these calculations, but the J≠1 levels are not affected by this problem according to Mansfield. A total of thirty nine transitions from the ground state to J=1 levels built on the $5p^5(5d6s^2 x 5d^2 6s x 5d^3)$ manifold of configurations were predicted, with eleven of these in the wavelength range 785Å to 680Å. The

corresponding theoretical oscillator strengths for these eleven lines were found to range from $\sim 1 \times 10^{-11}$ to 0.2433, see table 3. Of these eleven lines , only seven could in fact be related to observed lines. The error between the calculated and observed wavelengths for these seven lines had a standard deviation of only $\sim$ 0.5%. As for the four unobserved lines, three had calculated oscillator strengths much weaker than the weakest observed line (gf (calculated) = 0.0006). So the theoretical calculations of the 5p absorption spectrum from the ground state appear to be in fair agreement with the observed spectrum at wavelengths above 680Å.

Mansfield's calculations predict that the excitation schemes $6s5d\ {}^3D_2 \longrightarrow 5p^5(5d6s^2 x 5d^2 6s x 5d^3)$ and $6s5d\ {}^1D_2 \rightarrow 5p^5(5d6s^2 x 5d^2 6s x 5d^3)$ each give rise to 138 transitions. The wavelength distribution and corresponding oscillator strengths of these two sets of transitions are conveniently summarized by the two "stick diagrams" of figures 5D3 and 5D4. Each vertical line or "stick" corresponds to a predicted line at that wavelength and its height yields the corresponding oscillator strength. From figure 5D3 it can be seen that calculated absorption lines from the $6s5d\ {}^3D_2$ range from $\sim$ 832Å down to $\sim$ 525Å, 50% of them below 676Å. A similar distribution is predicted for the $6s5d\ {}^1D_2$ level, figure 5D4, with lines ranging from $\sim$ 860Å to $\sim$ 536Å of which 50% are located below $\sim$ 695Å.

FIGURE 5D3: STICK DIAGRAM REPRESENTING THE CALCULATED (COWAN CODE) PHOTO-ABSORPTION LINES CORRESPONDING TO THE EXCITATION SCHEME $6s5d\ ^3D_2 \text{—} 5p^5(5d6s^2 x 5d^2 6s x 5d^3)$

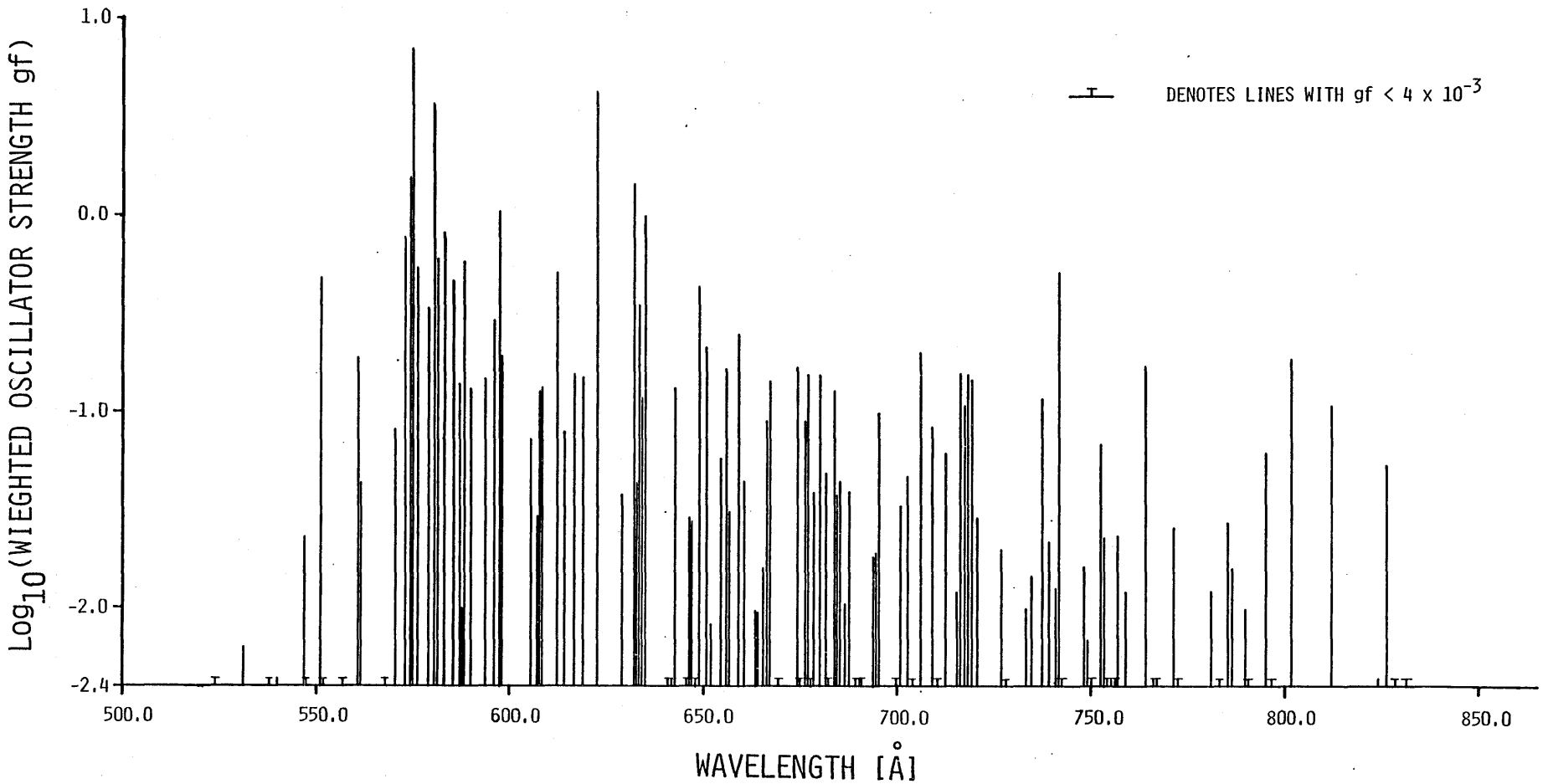


FIGURE 5D4: STICK DIAGRAM REPRESENTING THE CALCULATED (COWAN CODE) PHOTO-ABSORPTION LINES CORRESPONDING TO THE EXCITATION SCHEME $6s5d\ ^1D_2 — 5p^5(5d6s^2 x 5d^2 6s x 5d^3)$

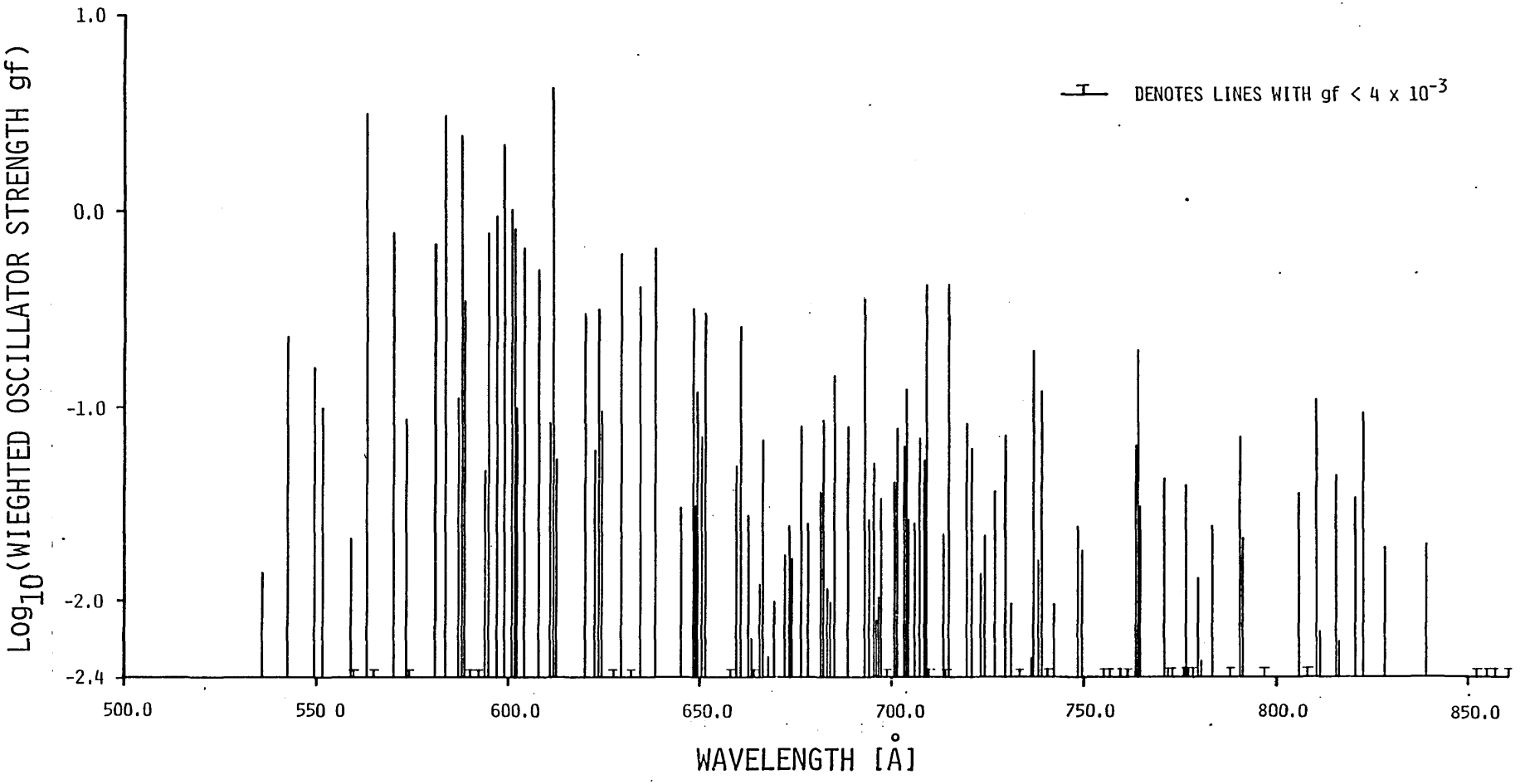


TABLE 3: Theoretical (Cowan Code) 5p transitions above 680Å from the $6s^2\ ^1S_0$ level of Barium to levels built on the mixed manifold $5p^5(5d6s^2 x 5d^2 6s x 5d^3)$ compared with observation

Observed Wavelength [Å]	Calculated Wavelength [Å]	Calculated gf
---	784.94	0.0001
784.31	784.44	0.0047
753.86	748.36	0.0116
734.50	732.02	0.0006
727.40	726.97	0.0025
---	717.62	0.0051
715.69	714.26	0.0068
---	711.86	0.0001
706.43	703.65	0.0199
---	692.01	$1x10^{-11}$
693.66	682.26	0.2433

Data Source

Observed transitions - Connerade et al (1979a)

Calculated transitions - Mansfield, M.W.D.; (1985) Private Communication

Calculations were performed with the Cowan Code. 6s-5d mixing was also incorporated in the initial level by including mixing with the $5p^6 6s5d$ and $5p^6 5d^2$ configurations.

Many of the most intense lines arising from the two metastable levels are predicted to be at wavelengths below $\sim$620Å where in reality very few excited state lines were in fact resolved. Of course the spectrum in this region will be characterized by severe interchanneling coupling of the type discussed in the MQDT discussion of sub-section 2.3.2 (Chapter 2). As a result the levels responsible for these absorption lines will certainly be heavily mixed with other levels where the "running" electron is nominally in ns,n'd (n>6 n'>5). This interchannel coupling will dilute the oscillator strength of these "calculated" lines amongst all the other lines in this region. Such an effect would probably lead to a quasi continuum in the 5p absorption spectrum of the metastable levels at lower wavelengths due to the enormous number of "interacting" levels. The appearance of the excited state spectrum at wavelengths below 620Å would appear to support this assertion. For example, in the ground state spectrum, the spectral region below 620Å is incredibly complex with many very strong lines. Yet there are "clear" segments interspersed between these strong features where the transmission is high. By comparison, the excited state spectrum is not characterized by such clearly defined transmission windows. It instead gives the impression of a fairly uniform attenuation onto which is superimposed features due to the residual

population in the Barium ground state.

A total of 52 absorption lines from the 6s5d $^3D_2$ level and 72 absorption lines from the 6s5d $^1D_2$ level are predicted by Mansfields calculations in the "simple" spectral region at wavelengths above 690A. By comparison, the line list of table 2 lists only 53 lines of which six are probably molecular in origin (see subsection 5.2.3) and another three probably Barium ground state lines. This leaves only 44 "atomic" excited state 5p absorption lines which is a lot less than the 128 predicted by Mansfield. However two factors have not been taken into account. First, many of the predicted lines have such small calculated oscillator strengths that they are unlikely to be seen. Secondly, only $\sim$35% of the initial Barium population will be located in either the 6s5d $^3D_2$ and 6s5d $^1D_2$ levels, assuming that both these levels are saturated by the ASE mechanism of subsection 5.3.1. Now the average calculated gf value for the six <u>weak</u> but "observed" 5p absorption lines above 690Å (Table 3) originating from the $6s^2\ ^1S_0$ level is 0.0077. This result would suggest that an appropriate criterion, for deciding which predicted lines are likely to be resolved from either the 6s5d $^3D_2$ (table 4) or 6s5d $^1D_2$ (table 5) initial levels, would be to ask whether the calculated gf value exceeded 3x0.0077 (only $\sim$1/3 of population in each metastable). Applying this criterion to Mansfields data, leads to the

TABLE 4: Theoretical (Cowan Code) 5p transitions above 690Å from the 6s5d $^3D_2$ level of Barium to levels built on the mixed manifold $5p^5(5d6s^2 x 5d^2 6s x 5d^3)$

Calculated Wavelength [Å]	Calculated gf	Calculated Wavelength [Å]	Calculated gf
831.7	0.0026	748.3	0.0161
828.7	0.0043	741.6	0.0007
826.7	0.0532	741.5	0.4905
824.3	0.0005	741.0	0.0126
812.1	0.1067	739.3	0.0220
802.0	0.1801	737.6	0.1143
796.8	0.0001	737.8	0.0142
794.8	0.0605	733.4	0.0096
790.8	0.0016	728.1	0.0003
789.9	0.0092	727.0	0.0197
786.3	0.0155	720.9	0.0287
785.4	0.0269	719.2	0.1434
783.2	0.0013	718.1	0.1529
781.2	0.0122	717.3	0.1049
772.5	0.0003	715.9	0.1514
771.5	0.0254	715.8	0.0118
766.9	0.0046	712.6	0.0621
766.5	0.0013	710.6	0.0019
764.3	0.1701	709.1	0.0824
759.9	0.0123	706.5	0.2239
757.0	0.0232	704.1	0.0004
756.5	0.0026	702.9	0.0464
755.2	0.0066	700.9	0.0331
753.9	0.0010	699.9	0.0016
752.9	0.0230	695.0	0.0971
752.8	0.0679	694.2	0.0183
750.1	0.0022	693.9	0.0164
749.1	0.0068	690.1	0.0019

Data Source

Mansfield, M.W.D.; (1985) Private Communication. Calculations were performed with the Cowan Code. 6s-5d mixing was also incorporated in the initial level by including mixing with the $5p^6 6s^2$ and $5p^6 6s5d$ configurations when deducing the average of configuration one electron wavefunctions.

TABLE 5: Theoretical (Cowan Code) 5p transitions above 690Å from the 6s5d $^1D_2$ level of Barium to levels built on the mixed manifold $5p^5(5d6s^2 x 5d^2 6s x 5d^3)$

Calculated Wavelength [Å]	Calculated gf	Calculated Wavelength [Å]	Calculated gf
860.1	0.0001	748.7	0.0243
856.9	0.0001	742.1	0.0082
854.7	0.0005	740.4	0.0007
852.2	0.0002	739.1	0.1177
839.2	0.0196	738.4	0.0166
828.4	0.0183	736.9	0.1879
822.8	0.0905	736.8	0.0051
820.8	0.0341	733.3	0.0000
816.4	0.0060	731.2	0.0093
815.5	0.0438	729.6	0.0715
811.7	0.0067	726.9	0.0364
810.7	0.1091	724.4	0.0217
808.4	0.0012	723.1	0.0135
806.3	0.0358	720.9	0.0591
797.0	0.0015	719.9	0.0826
791.0	0.0214	714.7	0.9179
790.6	0.0709	713.9	0.0012
788.2	0.0008	713.5	0.0220
783.6	0.0240	709.5	0.0000
780.5	0.0043	708.9	0.4123
779.9	0.0135	708.7	0.0534
778.5	0.0032	707.1	0.0691
777.2	0.0013	705.9	0.0251
776.1	0.0398	703.6	0.0259
776.0	0.0011	703.4	0.1258
773.2	0.0026	703.2	0.0611
772.1	0.0013	701.1	0.0786
771.3	0.0418	700.9	0.0401
764.1	0.0296	698.9	0.0024
764.0	0.1915	696.5	0.0338
763.5	0.0629	695.7	0.0103
761.6	0.0000	695.4	0.0078
759.9	0.0016	695.2	0.0508
756.9	0.0011	695.0	0.0259
755.4	0.0006	693.1	0.3666
749.8	0.0183		

Data Source

Mansfield, M.W.D.; (1985) Private Communication. Calculations were performed with the Cowan Code. 6s-5d mixing was also incorporated in the initial level by including mixing with the $5p^6 6s^2$ and $5p^6 6s5d$ configurations when deducing the average of configuration one electron wavefunctions.

conclusion that only about 52 lines in the spectral region above 690A would in fact on average be resolved. A result which is reasonably consistent with the observed line list, bearing in mind the crudity of the above criterion.

A more definitive test of the worth of Mansfield's Data, with regard to the excited state spectrum, is whether they correctly predict the wavelength distribution and promimence of the observed spectrum. Careful comparison of the observed excited state spectrum with the stick diagrams of figures 5D3 and 5D4 indicate that Mansfields calculations do not even approximately yield the correct distribution. Neither can any reasonable agreement be achieved by simply translating the entire calculated spectrum up or down in wavelenth to account for any systematic errors in the calculations. Configuration interaction of the upper levels calculated here, with others where the running electron was in a higher n value was of course possible. However, if this was the sole reason for the discrepancy between theory and experiment, then the theoretical distribution would have tended to be good at longer wavelength but get progressively worse at shorter wavelengths. This is not the case either, so it would appear that something more fundamental is occurring (assuming of course that the discussion in subsection 5.3.1 is correct regarding which levels are populated).

A recap of the most important points at this stage is probably worthwhile, before examining the origin of the poor agreement between theory and experiment regarding the distribution of absorption lines in the excited state spectrum. Mansfield's calculations on the ground state spectrum at wavelengths above 690Å appear broadly correct, the accuracy of the theoretical wavelength for each "identified" line being usually within 0.5% of the value deduced from the experimental spectrum. On the other hand, the distribution of structure predicted by his excited state calculations appears to be in disagreement with experiment. Nevertheless it is interesting to note that both theory and experiment are in agreement when it comes to the number of "observable" lines above 690Å (after due account is taken of predicted oscillator strengths). This agreement is interesting for two reasons. First, it implies that the basic premise of incorporating 6s5d mixing in both the initial and final states of the excited state spectrum is valid (correct number of lines predicted). Secondly, it provides tentative evidence that interchannel mixing with higher series members is unimportant in the "simple" region above 690Å. The excited state spectrum would have contained rather more lines in this region if such mixing had been important. These additional lines would have corresponded to the higher series members responsible for the above mixing. Accurate

calculation of the levels in this spectral range would then be difficult. This is because the array of interacting configurations, from which each level is constructed, would require expansion to include the perturbing higher series members.

Barium (z=56) occupies a critical position in the periodic table in that it preceeds the beginning of the filling of the 5d subshell with Lanthanum (z=57) and the filling of the 4f subshell with Cerium (z=58). This critical position is therefore characterized by 4f and 5d effective potentials which are remarkably "soft" in the manner described in Chapter 2. Probably the key to understanding the failure of Mansfield's theoretical calculations, when applied to the 6s5d metastable levels of Barium, lies in the "soft" character of the 5d potential. In Chapter 2 it was pointed out that the presence of the 5p hole resulted in the 5d wavefunction being "pulled in" (the atomic field looks more like lanthanum). The additional excitation of a 6s electron to a 5d orbital via laser excitation and subsequent decay would further increase the effective field seen by the 5d electrons, and give rise to further contraction. So the 5d Barium wavefunction is very sensitive in Barium and this might possibly be amplified in the case where the initial configuration is 6s5d rather than $6s^2$. Consider the consequence of this effect if it is true. The "effective potential" seen by a 5d wavefunction is

determined (i) by the total configuration of the atom and (ii) by centrifugal barrier effects. Nevertheless different levels of a given configuration will possess slightly different effective fields and these very small changes can occasion significant changes in the radial wavefunction. This can cause problems because of the way the Cowan code computes the one electron wavefunctions from which the total wavefunction is constucted.

The "average of configuration" approximation used in the Cowan code may break down for a sufficiently sensitive one electron wavefunction. This would result in an inaccurate wavefunction, i.e. not the best solution, being used in the construction of a given level. Such an effect might lead to the theory predicting the correct number of lines, which tentatively appears to be the case, yet incorrectly predicting the wavelength distribution and oscillator strengths as is in fact found. The solution to this problem, in the event of it occurring, would be to optimise all of the one electron wavefunctions for each calculated level. This is not possible with the Cowan Code and would in any case consume enormous quantities of computer time. An intermediate approximation would be to optimise only the especially sensitive one electron wavefunction(s) and use average of configuration wavefunctions for the rest.

The pronounced sensitivity of the 5d wavefunction discussed above could also result in serious errors being generated by the m. D-F* code used by Rose et al (1980). This code is based on the Multi-Configurational Dirac Fock (MCDF) theory and was successfully used by Rose et al (1980) in their studies on the Barium ground state 5p spectrum. The basic building block of this approach is the "configuration state function" (CSF) which like its counterpart in the Cowan Code, the average of configuration wavefunction, is not optimised for any given level of an array of interacting configurations. To quote Rose et al (1980), "each CSF is constructed from Dirac central field orbitals and has total angular momentum numbers J and M, and parity P". Each of these CSF's are constructed from a given configuration and corresponds to a pure j-j coupled state. Now Mansfield's calculations show that the upper level accessed by the excitation of a 5p electron from either of the 6s5d ^{3,1}D levels exhibits intermediate coupling, and that 6s-5d configuration mixing is important (as expected). So a real level of the Barium excited atom would be represented by an array of different CSF's which have not been optimised for the intermediately coupled level. Thus a sufficiently sensitive wavefunction could likewise lead to serious errors in the predictions of the MCDF based theory.

*m. D-F multiconfigurational Dirac-Fock (acronym used by Rose et al)

5.3.3 Possible molecular features in the excited state spectrum at wavelengths above 690Å

One of the unusual aspects of the excited state spectrum is the presence of a number of weak but very broad (∿1.5-2Å) features at wavelengths above 690Å. Six of these features are listed on the line list of table 2 ("lines" 23,24,26,39,42 and 47), and the profiles of three of these (39,42,47) may be viewed in figure 5D2b(viii). These profiles are quite unlike the great majority of the lines listed in table 2 which in general are "sharp" by comparison. The origin of these lines is most unclear; they have the kind of profile and width (equivalent to 1/2 kT) that might reasonably be expected for a molecular structure at a temperature of 880°C ($kT \simeq 0.1$ [eV]), yet it is not possible to link them to any observed electronic transition of the atom as will be seen in this subsection. It is of course possible to suggest that these broad profiles are simply the envelope of an unknown number of atomic lines which are nearly coincident, but whose individual features were not resolved. However this is an unconvincing answer for the following reasons. First, all of these profiles are roughly similar in width. Second, the region above 690Å is fairly simple with relatively few lines and no such profiles are seen at short wavelengths where the spectrum is complex and coincidences more likely. Thirdly, similar broad but weak and

featureless profiles are not seen in the Barium ground state spectrum.

On the other hand these features may be molecular in origin, arising from excited Barium dimers of the type; $Ba(6s^2)$-$Ba^*(6s5d)$ or $Ba^*(6s5d)$-$Ba^*(6s5d)$. The formation of such dimers is a natural result of the Linear Combination of Atomic Orbitals (LCAO) model of molecular bonding. Each molecular orbital in this model is constructed from a pair of atomic orbitals (Φ_i), one for each atom which are then combined to form either a "bonding" (Ψ_-) or an "anti-bonding" (Ψ_+) molecular orbital: -

$$\Psi_- = N(\Phi_1 + \Phi_2) \qquad 4a$$

$$\Psi_+ = N(\Phi_1 - \Phi_2) \qquad 4b$$

where N is a normalization constant. The bonding orbital gives rise to a build-up of charge between the two atoms resulting in a bound state, while the anti-bonding state gives rise to a charge depletion between the two atoms and thus to a repulsive state. It follows that both the bonding and the anti-bonding molecular orbitals are occupied by the four valence electrons for the $Ba(6s^2)$-$Ba(6s^2)$ dimer, since each molecular orbital may only take two electrons by the Pauli principle. This dimer will be extremely weakly bound and will probably dissociate at temperatures of 880^oC resulting in no observable molecular transitions in the VUV

spectrum of unexcited Barium. The formation of more strongly bound dimers built on excited states of Barium such as $Ba^*(6s5d)$ is much more likely. This is because the four "valence" electrons can now in principle be accommodated in a pair of bonding molecular orbitals. For example, molecular orbitals built from the two combinations 6s-6s and 6s-5d could bind the $Ba(6s^2)$-$Ba^*(6s5d)$ dimer, while the $Ba^*(6s5d)$-$Ba^*(6s5d)$ dimer could be bound by molecular orbitals built from 6s-6s and 6s-5d.

Molecular features in the VUV must involve transitions between different electronic states of the dimer, which in the case of Barium would correspond to the excitation of a 5p electron. On top of this basic electronic transition will be superimposed contributions due to both vibrational and rotational structure. The spacings of the latter levels will determine the kind of spectral features which will be seen in an experimental absorption spectrum. In the absence of centrifugal effects, the vibrational energy levels are given approximately by the relationship: -

$$E_{Vib}(\nu) = \omega_e(\nu + 1/2) - x_e\,\omega_e(\nu + 1/2)^2 \qquad 5$$

where ω_e is the "Vibrational Constant", ν is the Vibrational Quantum Number and x_e is the Anharmonicity Constant which takes account of the departure of the molecular potential from a simple harmonic shape leading to a "closing up" of the

vibrational levels. The energies of the rotational levels are by comparison given approximately by the relationship: -

$$E_{rot}(J) = B_e J(J + 1) \qquad 6$$

where B_e is the "rotational constant" (= $\frac{\hbar^2}{2\mu r_o^2}$, μ = the reduced mass of the dimer system and r_o is the separation of the two atoms) and J is the rotational quantum number.

Unfortunately, neither the vibrational nor the rotational constants for either the $Ba(6s^2)$-$Ba^*(6s5d)$ or the $Ba^*(6s5d)$-$Ba^*(6s5d)$ dimers are available to the author. It is however possible to make some kind of estimate of the vibrational energy level spacings; based on the known vibrational constants of the Cesium dimer ($\sim$40 [cm^{-1}] $^1\Sigma_g^+$ state) and the Iodine molecule ($\sim$214 [cm^{-1}] $^1\Sigma_g^+$ state) (Huber and Hertzberg (1978).

A word of caution needs to be inserted here regarding the effect on a molecule of a high rotational angular momentum quantum number J. The spinning of the molecule adds a repulsive centrifugal term $\frac{J(J + 1)\hbar^2}{2\mu r_o^2}$ (= reduced mass) to the molecular potential. This term reduces the depth of the molecular well and its width (The centrifugal Barrier term dominates at sufficiently

small r_o). In addition, the shape of the molecular potential will no longer be even approximately Simple Harmonic for sufficiently large J, even for small vibrational quantum numbers (equation 5 invalid). Nevertheless the energy spacings of the lowest vibrational levels will tend to be smaller than the values expected from equation 5.

The value of the vibrational constant ω_e for the Cesium (z=55) Dimer will probably be of the same order as the excited state Barium Dimer (similar mass, one 6s valence electron so only a bonding orbital is filled), while that of the strongly bound Iodine (z=53) molecule will act as an upper limit. These values would yield vibrational spacings in the VUV at 700A of 0.2Å and 1Å respectively. Note that the corresponding spacings of the rotational energy levels are much smaller.

These estimates indicate that the proposed molecular features do not belong to vibronic sequences, and each one must correspond to a different electronic transition in the dimer system. It is not possible to calculate the energies of the "parent" electronic transitions in the Barium atom from the known wavelength of these profiles. This would require a knowledge of the molecular potentials of both the upper and lower state of the dimer which are not known in the first phase. Nevertheless it is possible to estimate a plausible

upper bound on the energy separation between electronic 5p transitions in the atom and corresponding 5p transitions in the dimer.

The formation of bound $Ba^*(6s5d) - Ba(6s^2)$ or $Ba^*(6s5d) - Ba^*(6s5d)$ dimers is dependent on the excitation of a 6s electron to a 5d orbital. This allows a pair of bonding orbitals to be formed, one of which utilizes the 5d orbital. Now the 5d wavefunction is known to collapse significantly in the presence of a 5p hole from the calculations of Rose et al (1978) and Rose (1985) (Table 1). If the binding energy of the $Ba^*(6s5d)$ dimers is predominantly due to the molecular orbital built from 6s5d atomic orbitals, then $5p^5 6s5d\ nl - 6s^2$ dimer is likely to be weakly bound, since the collapse of the 5d wavefunction will in turn weaken a molecular bond built form a 5d atomic orbital. In this case the energy shift between an atomic line and the corresponding dimer band is determined by the dimer binding energy of the lower state and cannot exceed the dissociation energy of this state. This criterion would correspond to the molecular potential of the dimer being "flat", with essentially no well, in the presence of a 5p hole. Again, taking the dissociation energy of the Cesium dimer (0.394 [eV]) as being roughly comparable to the Ba^* dimer and the corresponding dissociation energy of the I_2 molecule (1.54 [eV]) as an upper limit, yield <u>maximum</u> wavelength shifts at 700Å of

$\sim$15Å and $\sim$61Å, respectively. (Data source, Huber and Hertzberg (1979). The above assumptions correspond to the atomic lines lying to the long wavelength side of the observed "molecular" profiles. Inspection of the experimental spectra at longer wavelengths than these "molecular" profiles does not reveal six particularly intense atomic (i.e. sharp) lines with which to even tentatively link these features.

So in conclusion the origin of these broad profiles remains unknown. It is unlikely that they are merely the superposition of an unknown number of unresolved atomic lines for the three reasons given at the beginning of this subsection. They have a width of $\sim$ 1/2 kT ($\sim$2Å) which is consistent with a molecular structure, the width being due to unresolved rotational and vibronic structure. Consequently they are very tentatively assigned as being due to electronic transitions in a $Ba^{*}(6s5d)$ dimer system. The different features correspond to different electronic transitions in the dimer system since any reasonable value for the vibrational constant is far too large to account for the spacing of the features.

CHAPTER 6 CONCLUSIONS AND SUGGESTIONS FOR FURTHER WORK

6.1 Conclusions

The present experimental work demonstrates the value of probing inner shell excitations in the presence of a well defined excited spectator electron. The scope for such work is vast especially if one considers the possibility of measuring the inner shell spectra of selectively excited ion stages. The apparatus in this thesis was certainly not ideal for the work and in Appendix 6 its major deficiencies and suggested improvements for future experiments of this type are discussed. Also in Appendix 7, a simple but novel focussing arrangement for improving the "useful" power output of the plasma continuum source is described.

In this thesis are presented the first measurements of the VUV 5p absorption spectrum of selectively excited Barium in the 6s5d $^1D_2$ and $^3D_2$ metastable levels. One hundred and seventy four new features are listed in the line list of table 2. The excited state spectrum is extremely complex as expected, the complexity being due to; (i) severe 6s-5d mixing in the atom core in the presence of a 5p core vacancy, and (ii) the very much greater number of possible excitation schemes (Appendix 1) from initial levels with J=2 compared with the

ground state spectrum (J=0). Many of the new lines are too weak to resolve and/or are so closely spaced as to give the appearance of quasi-continuous absorption. This effect is especially apparent at wavelengths below $\sim$622Å where very few "new" lines are resolved. This result points to the need of further work on this spectrum at the highest possible resolution (Resolution in this work $\pm$0.1A).

At wavelengths above 690Å a number of features whose profiles are of molecular appearance are seen. Six of the most clearly observed features are listed in table 2. These features are believed to be due to Ba_2^* dimers which will be more strongly bound than Ba_2 dimers. The observed profiles do not belong to vibronic sequences and each one must correspond to a different electronic upper level. It has not proved possible to link them with any of the observed atomic features in the excited state spectrum.

No "new" structure was resolved which could be attributed to the 5p absorption from the 6s6p $^1P_1$ level of Barium. This result was a consequence of the rapid depopulation ($\lesssim$10 [ns]) of this level into the lower lying 6s5d $^1D_2$ and $^3D_2$ metastable levels due to Amplified Spontaneous Emission (subsection 5.3.1.).

Comparison of the experimental excited state spectrum with the calculations using the Cowan code reveal a basic disagreement between the two with regard to the distribution of lines and their relative strength. However the importance of 6s5d mixing is very tentatively confirmed by Mansfields calculations, since the number of "observable" lines predicted by the theory is comparable to the number listed in table 2 (after taking account of the calculated oscillator strengths). The disagreement between theory and experiment has been attributed to the 5d wavefunction being especially sensitive to different levels of the Barium electronic configuration incorporating both a 5p core vacancy and an excited valence electron. This level dependence of the 5d wavefunction means that ab initio calculations based on an "average of manifold" approach are unlikely to give good results for the Ba(6s5d) 5p absorption spectrum. It is anticipated that the m. D-F code used by Rose et al (1980) will likewise give poor results for this spectrum. The solution to this difficulty would involve incorporating a routine in the ab intio codes which would optimise the sensitive one electron wavefunction(s) for each level belonging to a given configuration.

6.2 Suggestions for further work

Suggestions for further work are as follows: -

(I) Measurement of the 5p absorption spectrum of Barium while in the excited 6s6p $^1P_1$ level corresponding to the excitation scheme (section 2.4): -

$$5p^6 6s6p\ ^1P_1 + h\nu_{VUV} \longrightarrow \{5p^5(6s6px5d6p)\}ns,nd \quad J=0,1,2$$

This spectrum was not observed in the present experimental work due to the rapid depopulation (<10 [ns]) of the 6s6p $^1P_1$ level into the 6s5d $^{3,1}D_2$ levels by Amplified Spontaneous Emission (A.S.E.). The characteristic time t_o for this stimulated process to become important is given by the formula (subsection 5.3.1): -

$$t_o = \frac{8\pi \ln(1/\alpha)}{c\ \lambda^2\ A_{23}\ \beta\ N_2}$$

Values for t_o in the present experiment varied between 0.12 [ns] ($N_2 \sim 10^{21}$ [m^{-3}]) to 1.2 [ns] ($N_2 \sim 10^{-20}$ [m^{-3}]) for the 6s6p $^1P_1$——6s5d $^3D_2$ transition (the faster of the two). These numbers point to the need to (a) increase t_o, and (b) probe the excited Barium column immediately after optical excitation with a short (∿10 [ns] say) continuum pulse with a synchronisation jitter of say ∿1 [ns].

Increasing the characterisic time t_o can be achieved by (i) using a longer furnace so that N_2

can be reduced while maintaining an adequate Barium column density (ii) increasing the Autler Townes broadening by increasing the laser flux per laser mode and (iii) increasing $\ln(1/\alpha)$ by reducing the ratio of the diameter to length of the laser excited Barium vapour column.

Generating a shorter continuum pulse could be easily achieved by using a Nd:Yag laser. For example the "HY 750" Nd:Yag laser by J.K. Lasers Ltd. (U.K.) produces 0.8 [J] pulses of 8 [ns] FWHM at a repetition rate of 10 [Hz]. Achieving reliable synchronisation between such a laser and another "independent" dye laser of $\sim$ 1 [ns] or better would be problematic. A better solution would be to frequency double the Nd:Yag output and use the doubled radiation (5320Å) to pump a tuned dye laser, and to use the unconverted fundamental (450 [mJ] for the HY 750 laser system) to generate the samarium plasma. Since the pulse lengths are so short, synchronisation between the dye laser and the continuum source could be accurately controlled by adjusting the optical delay of the unconverted infra red beam.

Such an approach has two disadvantages (i) The pulse length of the dye laser ($\sim$5 [ns] typically) will be shorter than the continuum pulse ($\sim$8 [ns]) (ii) The pulse length of the dye laser is so short that the propargation time of the laser beam through the furnace becomes significant. For

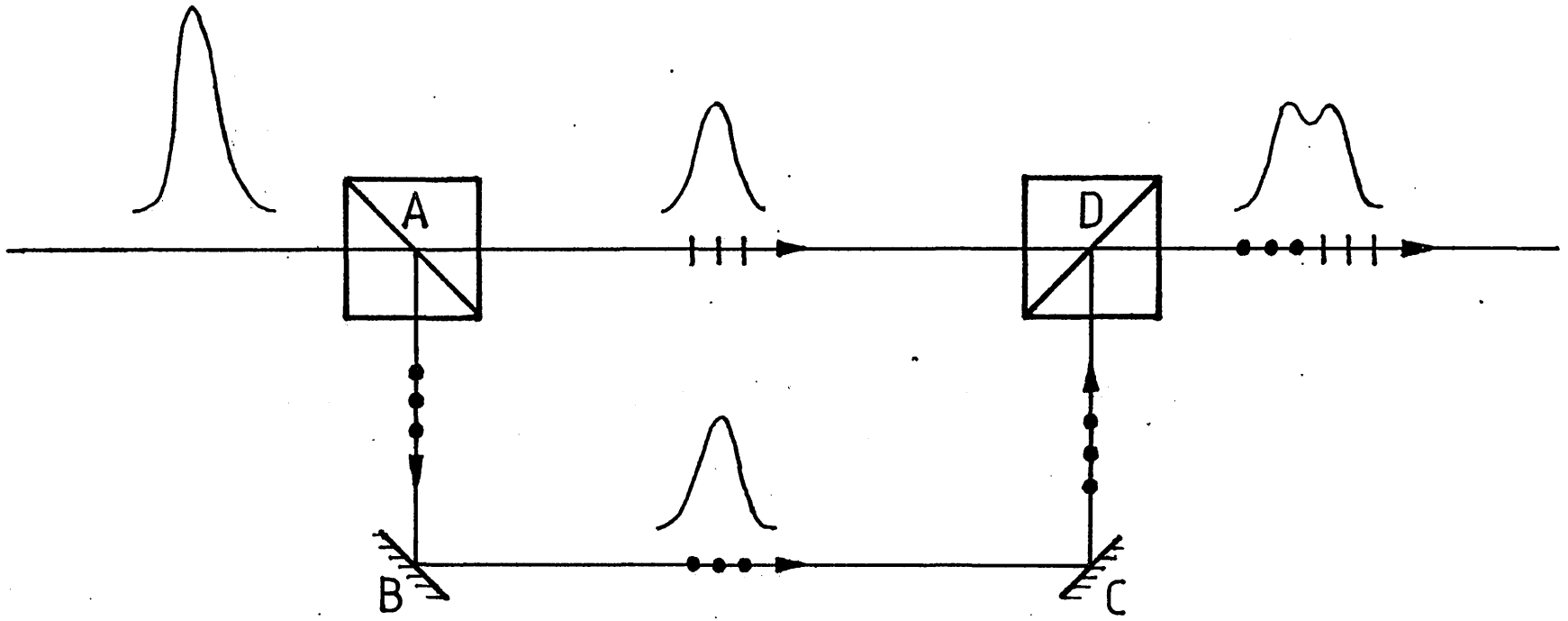
example a laser pulse would take 6.7 [ns] to traverse a 2 [m] long furnace (such a furnace would allow the reduction of N_2 by a factor of 10 on the present work while maintaining the same column density). Both of these factors mean that the Barium vapour would not be excited throughout the continuum pulse.

A partial solution to this difficulty would be to split the dye laser beam into two parts using a Glan Taylor polarizer, optically delay one of the beams by $\sim$ 5 [ns] and then "resplice" the two beams using a second Glan Taylor polarizer to produce a pulse of $\sim$ 10 [ns] length, see figure 6D1. Note that the output from a Littman type oscillator amplifier system is highly polarised.

(II) Investigation of the occurance of Barium dimers after laser excitation on the $6s^2\ {}^1S_0$ —— $6s6p\ {}^1P_1$ transition by absorption spectroscopy. The pulsed background source for such absorption work might for example be a Nitrogen laser pumped broad band dye laser.

The absence of additional absorption features due to the presence of Ba_2^* dimers in the above experiment, would rule out the dimer suggestion for the origin of the broad VUV features observed above 690Å in the authors experiment, while their presence would support it.

FIGURE 6D1: SCHEMATIC ARRANGEMENT FOR LENGTHENING A LINEARLY POLARISED LASER PULSE



Explaination

A 5 [ns] long (say) laser pulse linearly polarised at 45^{o} to the plane ABC is split by the Glan-Taylor Polaiser A into two equal parts. The path ABCD is arranged to be say 1.5 [m] longer than the the path AD (5 [ns] delay) and the two pulses are then "respliced" by the second Glan-Taylor Polariser D to create a 10 [ns] long pulse.

The above experiment would also be of value in cheaking the validity of the corrections proposed by Jahreiss and Huber (1985) to the absolute oscillator strengths of a selected number of Barium transitions. In particular, these workers suggested that the previous f values for transitions from the $6s6p\ ^1P_1$ and $6s5d\ ^{3,1}D_2$ levels should all be scaled by a factor of about 0.49. The experimental method of Jahreiss et al (1985) involved recording the "interferometric anomalous dispersion" (or Hooks method) of Barium vapour at wavelengths close to atomic transitions from populated Barium levels, using a pulsed broad band light source. Their basic assumption when deducing the above scaling factor was that the known column density of Barium atoms before laser excitation on the resonance line at 5535Å, was subsequently shared amongst all the populated <u>atomic</u> levels (number density N_i) so that $N_o l_o = \Sigma N_i l_i$. The formation of Ba_2^* dimers would however remove some of the Barium atomic population and thus give rise to a lower N_i. This would result in the calculated oscilator strengths f_i being too large since $N_i l_i \propto \Delta^2/f_i$ in the Hook formula, relating the separation of the Hooks (Δ) to the column density $N_i l_i$.

(III) Measurement of the 5p absorption spectrum of laser excited $6s6p\ ^1P_1$ and $6s5d\ ^1D_2$ Ytterbium ($z = 70$). Unlike Barium, 6s5d mixing is unimportant in unexcited Ytterbium (Connerade et al, 1979a) and

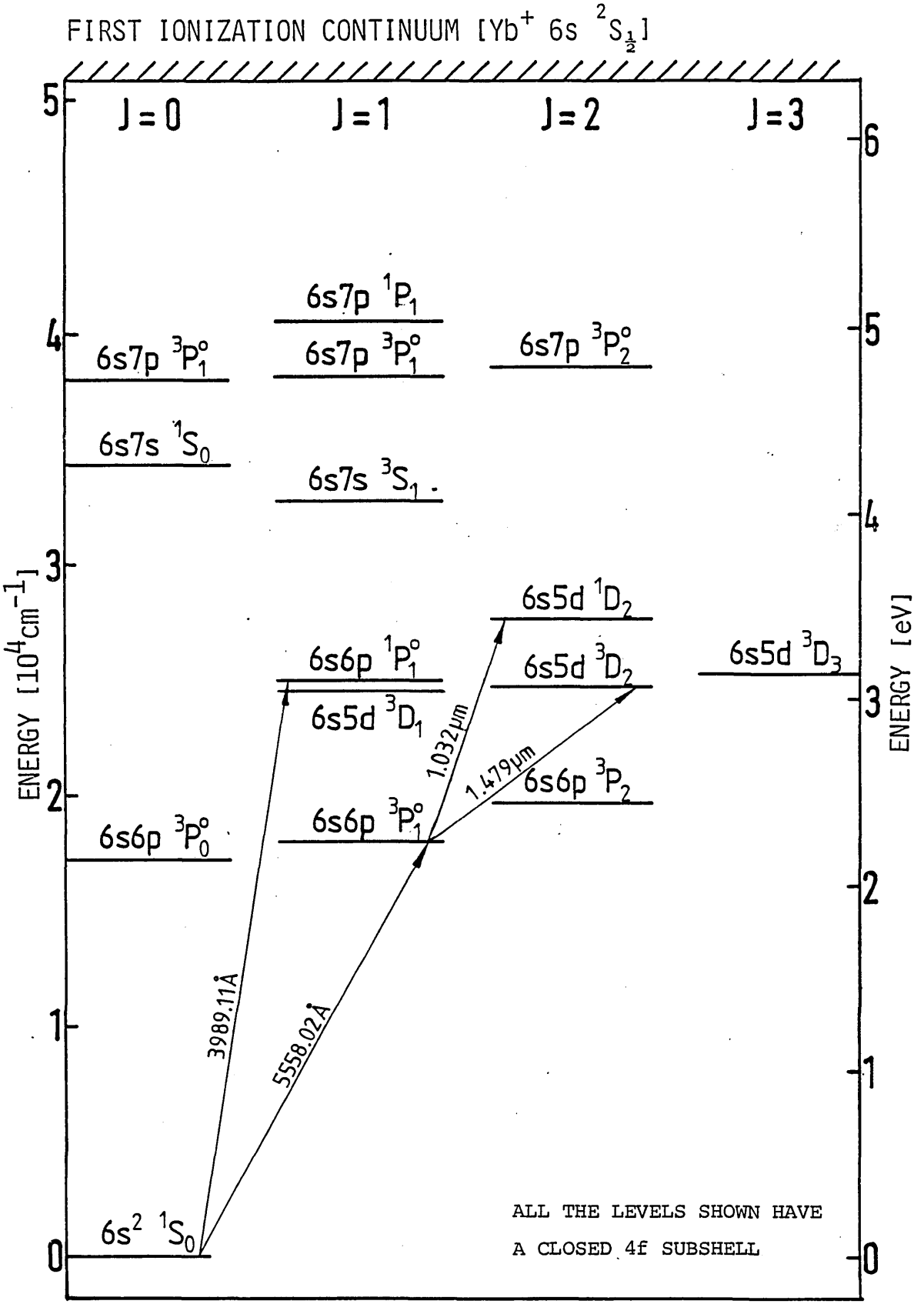
will remain so in any excited state. Consequently the 5p absorption spectrum of Ytterbium is much simplier than that of Barium and may be regarded as the hypothetical form of the Barium 5p spectrum in the absence of 6s-5d mixing (closed 4f subshell screens the nucleus effectively). Hence the Ytterbium spectrum may be used to assist in the unravelling of the more complex Barium spectrum (subsection 2.3.1).

On an practical level, such experiments would be more difficult than the present work as may be deduced from the Ytterbium partial term diagram, figure 6D2. Populating the 6s6p $^1P_1$ Yb I level would require radiation at 3989.11Å. Generating this wavelength with a tuned oscillator amplifier system which was pumped by a broad band coaxial laser would not be a good approach. This is because coaxial lasers are not very efficient at 3700-3800Å. A better approach would be to pump the tuned dye laser with the tripled output from a Nd:Glass laser (∿3550Å). The unconverted fundamental would be used to generate the VUV continuum as in suggestion (I). This approach would have the advantage of good synchronisation between the dye laser and the continuum source. Its disadvantage would be the shorter pulse length of the dye laser output compared with the continuum output. Nd:Glass has the advantage of producing longer pulses than Nd:Yag and so the problems

outlined in suggestion (I) are less severe. A commercial laser suitable for this work might be a Q.S.G. Series Nd:Glass Laser by J.K. Lasers Ltd. (U.K.). This can produce 35 [ns] pulses with energies up to 10 [J].

Populating the 6s5d $^1D_2$ level (or 6s5d $^3D_2$ level) would require two photon excitation and would be even more difficult. Resonant two photon excitation of the 6s5d $^1D_2$ level via either the 6s6p $^1P_1$ or $^3P_1$ levels would require high power radiation in the infra red at 3.832 [μm] or 1.032 [μm], respectively. The generation of tunable high power radiation at these wavelengths would be very difficult (Hutchinson, 1985 Private Communication). However non resonant two photon excitation of the 6s5d $^1D_2$ level via a "virtual state" located close to the 6s6p $^3P_1$ level is a viable alternative. This is because of the fortuitous near coincidence of the 6s6p $^3P_1$——6s5d $^1D_2$ transition wavelength to that of a Nd:Glass laser at either 1.05 [μm] (phosphate glass) or 1.064 [μm] (silca glass). This near coincidence is important since the lifetime of the virtual state (∿18 [fs] with 1.064 [μm] radiation, $\Delta E \Delta t \sim \hbar$) scales with the recipical of the energy detuning from the real level. This in turn decreases the infra red photon flux necessary to depopulate the virtual state, within its lifetime, into the 6s5d $^1D_2$ excited state.

FIGURE 6D2: SIMPLIFIED PARTIAL TERM DIAGRAM FOR YTTERBIUM I



A scheme for doing this experiment would involve frequency doubling the output from a Nd:Glass laser. The doubled output would then be used to pump a dye laser tuned to 5508.74Å (for 1.064 [μm] radiation). The unconverted infra red laser beam would be split into two beams. One beam being used to generate the plasma source, the other arranged to propergate coaxially and synchronously with the dye laser beam. These two beams would then be injected into the furnace containing the Ytterbium vapour.

(IV) Finally on the theoretical side, it would be very fruitful to perform calculations on the transitions from either the $6s5d\ ^1D_2$ and $6s5d\ ^3D_2$ levels to levels built on the mixed manifold $5p^5(5d6s^2 x 5d^2 6s x 5d^3)$ using the m. D-F code of Rose et al (1980). In section 5.3.2 it was suggested that the m. D-F code like the Cowan code would give poor results. This possibility was attributed to the breakdown of the "Configuration State Function" approach in the m. D-F code because of the extreme sensitivity of the 5d wavefunction to individual levels of a given configuration.

Appendix 1. List of Possible Transition Manifolds of the upper states corresponding to the 5p absorption spectrum from the metastable $6s5d^{3,1}D_{1,2,3}$ levels

$5p^6 6s5d\ {}^1D_2 \rightarrow$	$5p^5(6s^2x6s5dx5d^2)[{}^2P_{1/2,3/2}]$ ns,nd	J=1
	$5p^5(6s5dx5d^2)\ [{}^2D_{3/2}]$ ns	J=1
	$5p^5(6s5dx5d^2)\ [{}^2D_{3/2,5/2}]$ nd	J=1
	$5p^5(6s5dx5d^2)\ [{}^2F_{5/2}]$ nd	J=1
$5p^6 6s5d\ {}^1D_2 \rightarrow$	$5p^5(6s^2x6s5dx5d^2)[{}^2P_{3/2}]$ ns	J=2
	$5p^5(6s^2x6s5dx5d^2)[{}^2P_{1/2,3/2}]$ nd	J=2
	$5p^5(6s5dx5d^2)[{}^2D_{3/2,5/2}]$ ns,nd	J=2
	$5p^5(6s5dx5d^2)[{}^2F_{5/2}]$ ns	J=2
	$5p^5(6s5dx5d^2)[{}^2F_{5/2,7/2}]$ nd	J=2
$5p^6 6s5d\ {}^1D_2 \rightarrow$	$5p^5(6s^2x6s5dx5d^2)[{}^2P_{3/2}]$ nd	J=3
	$5p^5(6s5dx5d^2)[{}^2D_{5/2}]$ ns	J=3
	$5p^5(6s5dx5d^2)[{}^2D_{3/2,5/2}]$ nd	J=3
	$5p^5(6s5d5d^2)[{}^2F_{3/2,7/2}]$ ns,nd	J=3
$5p^6 6s5d\ {}^3D_1 \rightarrow$	$5p^5(6s^2x6s5dx5d^2)[{}^2P_{1/2}]$ ns,nd	J=0
	$5p^5(6s^2x6s5dx5d^2)[{}^2P_{3/2}]$ nd	J=0
	$5p^5(6s5dx5d^2)[{}^2D_{3/2}]$ nd	J=0
	$5p^5(6s5d)^*[{}^4P_{1/2}]$ ns	J=0
	$5p^5(6s5d)^*[{}^4P_{3/2}]$ nd	J=0
	$5p^5(6s5d)^*[{}^4D_{1/2}]$ ns	J=0
	$5p^5(6s5d)^*[{}^4D_{3/2}]$ nd	J=0
	$5p^5(6s5d)^*[{}^4F_{3/2}]$ nd	J=0

* erratum - "(6s5d)" should in fact read as "$6s5dx5d^2$)"

$5p^6 6s5d\ {}^3D_1 \longrightarrow$	$5p^5(6s^2 x 6s5d x 5d^2)[{}^2P_{1/2,3/2}]$ ns,nd	J=1
	$5p^5(6s^2 x 6s5d x 5d^2)[{}^2D_{3/2}]$ ns,nd	J=1
	$5p^5(6s5d x 5d^2)[{}^2D_{5/2}]$ nd	J=1
	$5p^5(6s5d x 5d^2)[{}^2F_{3/2}]$ ns,nd	J=1
	$5p^5(6s5d x 5d^2)[{}^2F_{5/2}]$ nd	J=1
	$5p^5(6s5d)^*[{}^4P_{1/2,3/2}]$ ns,nd	J=1
	$5p^5(6s5d)^*[{}^4P_{5/2}]$ nd	J=1
	$5p^5(6s5d)^*[{}^4D_{1/2,3/2}]$ ns,nd	J=1
	$5p^5(6s5d)^*[{}^4D_{5/2}]$ nd	J=1
	$5p^5(6s5d)^*[{}^4F_{3/2,5/2}]$ nd	J=1
$5p^6 6s5d\ {}^3D_1 \longrightarrow$	$5p^5(6s^2 x 6s5d x 5d^2)[{}^2P_{1/2}]$ nd	J=2
	$5p^5(6s^2 x 6s5d x 5d^2)[{}^2P_{3/2,5/2}]$ ns,nd	J=2
	$5p^5(6s5d x 5d^2)[{}^2D_{1/2}]$ nd	J=2
	$5p^5(6s5d x 5d^2)[{}^2D_{3/2,5/2}]$ ns,nd	J=2
	$5p^5(6s5d x 5d^2)[{}^2F_{5/2}]$ ns,nd	J=2
	$5p^5(6s5d x 5d^2)[{}^2F_{7/2}]$ nd	J=2
	$5p^5(6s5d)^*[{}^4P_{1/2}]$ nd	J=2
	$5p^5(6s5d)^*[{}^4P_{3/2,5/2}]$ ns,nd	J=2
	$5p^5(6s5d)^*[{}^4D_{1/2}]$ nd	J=2
	$5p^5(6s5d)^*[{}^4D_{3/2,5/2}]$ ns,nd	J=2
	$5p^5(6s5d)^*[{}^4D_{7/2}]$ nd	J=2
	$5p^5(6s5d)^*[{}^4F_{3/2,5/2}]$ ns,nd	J=2
	$5p^5(6s5d)^*[{}^4F_{7/2}]$ nd	J=2
$5p^6 6s5d\ {}^3D_2 \longrightarrow$	$5p^5(6s^2 x 6s5d x 5d^2)[{}^2P_{1/2,3/2}]$ ns,nd	J=1
	$5p^5(6s^2 x 6s5d x 5d^2)[{}^2D_{3/2}]$ ns,nd	J=1
	$5p^5(6s^2 x 6s5d x 5d^2)[{}^2D_{5/2}]$ nd	J=1
	$5p^5(6s5d x 5d^2)[{}^2F_{3/2}]$ ns,nd	J=1
	$5p^5(6s5d x 5d^2)[{}^2F_{5/2}]$ nd	J=1
	$5p^5(6s5d)^*[{}^4P_{1/2,3/2}]$ ns,nd	J=1
	$5p^5(6s5d)^*[{}^4P_{5/2}]$ nd	J=1
	$5p^5(6s5d)^*[{}^4D_{1/2,3/2}]$ ns,nd	J=1
	$5p^5(6s5d)^*[{}^4D_{5/2}]$ nd	J=1
	$5p^5(6s5d)^*[{}^4F_{3/2,5/2}]$ nd	J=1

$5p^6 6s5d\ {}^3D_2 \longrightarrow$	$5p^5(6s^2x6s5dx5d^2)[{}^2P_{1/2}]$ nd	J=2
	$5p^5(6s^2x6s5dx5d^2)[{}^2P_{3/2,5/2}]$ ns,nd	J=2
	$5p^5(6s5dx5d)[{}^2D_{1/2}]$ nd	J=2
	$5p^5(6s5dx5d^2)[{}^2D_{3/2,5/2}]$ ns,nd	J=2
	$5p^5(6s5dx5d^2)[{}^2F_{5/2}]$ ns,nd	J=2
	$5p^5(6s5dx5d^2)[{}^2F_{7/2}]$ nd	J=2
	$5p^5(6s5d)^*[{}^4P_{1/2}]$ nd	J=2
	$5p^5(6s5d)^*[{}^4P_{3/2,5/2}]$ ns,nd	J=2
	$5p^5(6s5d)^*[{}^4D_{1/2}]$ nd	J=2
	$5p^5(6s5d)^*[{}^4D_{3/2,5/2}]$ ns,nd	J=2
	$5p^5(6s5d)^*[{}^4D_{7/2}]$ nd	J=2
	$5p^5(6s5d)^*[{}^4F_{3/2,5/2}]$ ns,nd	J=2
	$5p^5(6s5d)^*[{}^4F_{7/2}]$ nd	J=2
$5p^6 6s5d\ {}^3D_2 \longrightarrow$	$5p^5(6s^2x6s5dx5d^2)[{}^2P_{3/2}]$ nd	J=3
	$5p^5(6s5dx5d^2)[{}^2D_{5/2}]$ ns	J=3
	$5p^5(6s5dx5d^2)[{}^2D_{3/2,5/2}]$ ns	J=3
	$5p^5(6s5dx5d^2)[{}^2F_{5/2,7/2}]$ ns,nd	J=3
	$5p^5(6s5d)^*[{}^4P_{3/2}]$ nd	J=3
	$5p^5(6s5d)^*[{}^4P_{5/2}]$ ns,nd	J=3
	$5p^5(6s5d)^*[{}^4D_{3/3}]$ nd	J=3
	$5p^5(6s5d)^*[{}^4D_{5/2,7/2}]$ ns,nd	J=3
	$5p^5(6s5d)^*[{}^4F_{3/2}]$ nd	J=3
	$5p^5(6s5d)^*[{}^4F_{5/2,7/2}]$ ns,nd	J=3
	$5p^5(6s5d)^*[{}^4F_{9/2}]$ nd	J=3

* erratum - "(6s5d)" should in fact read as "$6s5dx5d^2$)"

APPENDIX 2 The Optimum Optical Arrangement for the Osmium Coated Condenser Mirror

The optimum condenser mirror configuration corresponded to that which maximized the flux density at the spectrographs film plane subject to certain practical constraints described later. Note that it does not necessarily follow that the configuration satisfying the above requirement simultaneously maximizes the flux density at the slit. This observation will become clearer later on but essentially is a consequence of the astigmatism of the grating.

Two schematic diagrams of the optical arrangement are given below in figure 3D8 (i) and (ii), in which (i) represents a magnification of the source image on the spectrograph slit and (ii) a demagnification. The source of brightness I_o [Wm^{-2} $srad^{-1}$] was assumed to be circular with a radius η_s for the purposes of this analysis. The osmium coated mirror of reflectivity R_{os} subtended a solid angle Ω_s at the source and formed an image at the spectrograph slit plane of width s[m]. Ω_i, the solid angle of the cone of light subtended at the slit, was related to Ω_s by the equation $\Omega_s = M_T^2 \Omega_i$, where M_T is the transverse magnification of the system. The limiting apperture of the system was defined by the diameter of the laser excited column of barium vapour. The Furnace as result of

FIGURES 3D8(i)&(ii): SCHEMATIC DIAGRAMS OF TWO CONFIGUARATIONS FOR FOCUSING THE SOURCE ONTO THE SPECTROGRAPH SLIT VIA THE FURNACE

FIGURE 3D8(i): MAGNIFYING CONFIGURATION

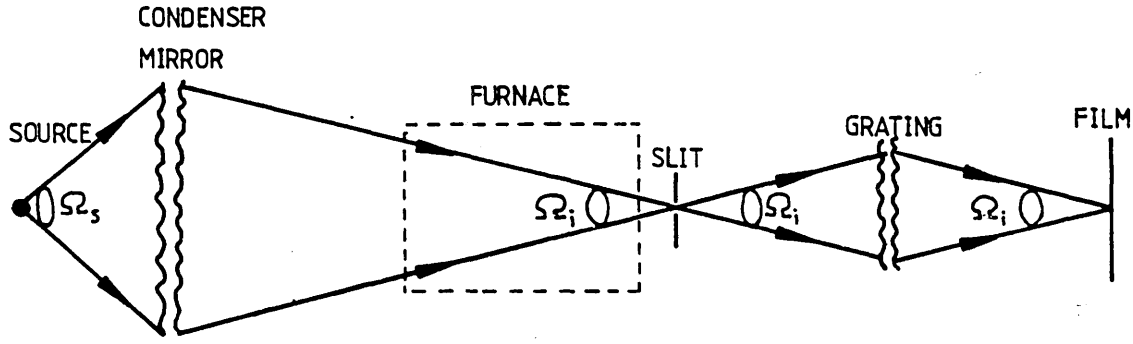
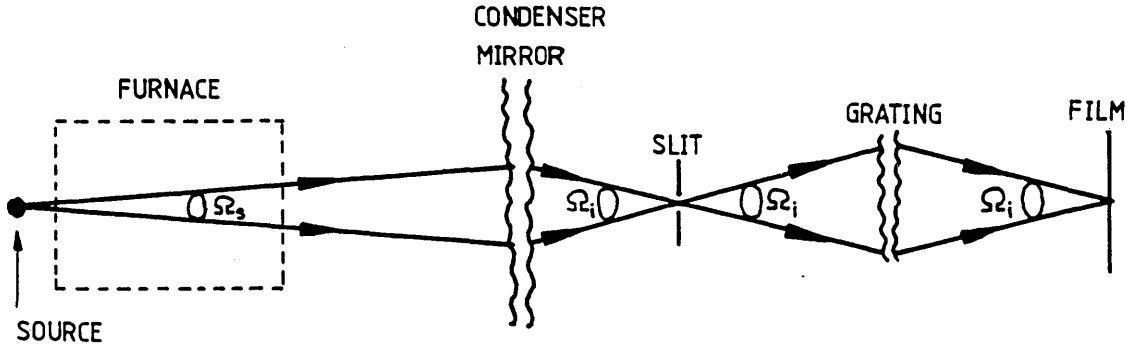


FIGURE 3D8(ii): DEMAGNIFYING CONFIGURATION



the small diameter of this column should always have been located in the longer arm of the optical system which corresponded to the smaller divergence cone of light, as shown in figure 3D8.

Experimental constraints on the condenser mirror magnification

A knowledge of these constraints was important for the assessment of the magnifying or demagnifying arrangements. The maximum useful magnification for the experimental system in a magnifying configuration was x2. This value arose from the need to separate the condenser mirror and the target by at least 2.5 [m] for reasons previously explained in subsection 3.3.1. Lack of laboratory space precluded larger magnifications. If laboratory space had not been important, the ultimate limitation on the magnification would have been $\sim$x12 at which point the diameter of the source's image would have equalled the furnace apperture (3.6 [mm]). The minimum useful magnification for the demagnifying arrangement was $\sim$ x1/5. This represented, for the solid angle of light transmitted by the furnace the point at which light condensed onto the slit started to miss the edge of the grating.

Experimental constraints on the solid angles transmitted by the furnace

In the demagnifying case, the furnace centre was located 750 [mm] away from the source and a solid angle of $\sim 2 \times 10^{-5}$ steradians was transmitted. For the magnifying case, the separation between the furnace centre and the spectrograph slit needed to be 1090 [mm] for a practical arrangement. This distance being set by the necessity of reflecting the dye laser beam off a small mirror located near the spectrograph slit, whilst maintaining an adequate overlap between the laser and the continuum beams in the furnace core. The solid angle which could have been transmitted in this case was smaller at $\sim 1 \times 10^{-5}$ steradians.

The analysis

The flux F falling on the spectrograph slit plane would be given by the equation: -

$$F = I_o \, \pi\eta_s^2 \, \Omega_s \, R_{os} \quad [W] \qquad 1$$

Brightness — I_o

Source area — $\pi\eta_s^2$

Solid angle effectively collected by mirror — Ω_s

Mirror reflectivity — R_{os}

In the absence of any optical abberations this flux would form a circular image of the source of area $\pi\eta_i^2$. Hence the flux density S at the slit would be given by: -

$$S = \frac{I_o \eta_s^2 \Omega_s R_{os}}{\eta_i^2} \quad [W\ m^{-2}] \qquad 2$$

In a situation where $\eta_i > s$, the slit width, the light throughput T into the spectrograph would be: -

$$T \sim 2 S \eta_i s$$
$$\sim 2 I_o R_{os} \Omega_s \frac{\eta_s^2 s}{\eta_i} \quad [W] \qquad 3$$

The light throughput given by equation 3 is still valid even if the condenser mirror exhibits astigmatism, since the ideal image at the slit plane would just be stretched into a vertical elipse of the same width. This light throughput T would then fall onto the spectrographs grating and part of it would be diffracted into first order. The final flux density at the film would be proportional to the light throughput T divided by the spectrum height of the illuminated slit and on the gratings astigmatism.

The image height at the spectrograph's slit was a function of both the magification M_T of the condensing mirror and its astigmatism. The contribution due to astigmatism would give rise to an image height x which could be evaluated from the formula (Samson (1967), p.14): -

$$x = \frac{2 L v}{R} \sin I_{pr} \tan I_{pr} \quad [m] \qquad 4$$

where, L was the height of the mirror which was illuminated, v the separation between the mirror and the slit, R was the radius of curvature of the mirror

mirror and I_{pr} the angle of incidence. This formula may be derived easily form the formulae describing the locations of the mirrors "Saggital" and "Tangential" focii which are given in Longhurst (1968) on page 370.

The height z of the contribution towards the final height h of the spectrum due to the gratings astigmatism is given by the formula (Samson, (1967) page 14).

$$z = \{\sin^2\beta + \sin\alpha \tan\alpha \cos\beta\}\, l \quad [m] \qquad 5$$

where α is the angle of incidence of light onto the grating, β is the angle of diffraction and l is the height of the illuminated grating. Note that this formula is only strictly correct when the image at the slit exhibits no astigmatism. However, this formula would remain approximately correct if the astigmatism of the mirror was small compared with the grating. This assertion was checked in practice using ray tracing programs (see later). At this point the analysis can conveniently be divided into two parts. The first part refers to Figure 3D8 (ii) and the second to Figure 3D8 (i).

Case 1 - A demagnifying arrangement

The Ω_s in equation 3 for T is a constant here and using $\eta_i = M_T \eta_s$ yields the following expression for the

the light transmission: -

$$T(\text{case 1}) = 2 I_o R_{os} \Omega_s \frac{\eta_s s}{M_T} \quad [W] \qquad 6$$

Inspection of equation 6 shows that T is maximized by making M_T (the only variable here) as small as possible, i.e. $M_T = 1/5$. However there is little overall gain in the flux density at the film because the height of the spectrum ($\sim x+z$) also scales with $\sim 1/M_T$. This result follows since z, the dominant contribution to the height of the spectrum as is demonstrated in the numerical example below, scales with the illuminated height of the grating l (equation 5) which in turn scales with $1/M_T$.

Numerical Example

Taking $M_T = 1/5$ (the smallest practical)

let R = 1 [m] - A standard mirror substrate

$I_{pr} = 15^o$ - The angle used in practice

$\Omega_s = 2 \times 10^{-5}$ [srad] - Due to the furnace

and $\alpha = 12^o$ - For the Jobin Yvon spectrograph

$\beta = 20.5^o$ - At 600Å for a 2400 [lines/mm] grating

implies that v = 580 [mm]

L = 14.6 [mm]

l = 25.6 [mm]

It therefore follows that x = 1.2 [mm] due to mirror and that z = 4.2 [mm] due to spectrograph.

In conclusion, the optimum demagnifying arrangement would be that with the highest possible demagnification. This is because although the flux density at the film is insensitive to magnification, the height of the spectrum is maximized. The flux density at the film of the numerical example given would be:-

$$F_{Film}(\text{case 1}) = \frac{KT(\text{case 1})}{(x + y)} = 1.4\text{x}10^{-10} K I_o R_{os} \quad [\text{W m}^{-2}] \qquad 7$$

where K is a constant depending on the dispersion and efficiency of the grating and is therefore constant for all configurations. Also the slit width has been taken as 25 [μm] which was the experimental value, and the source radius η_s has been taken as $\sim 1.5 \times 10^{-4}$ [m].

Case 2 - A magnifying arrangement

Here the Ω_s in equation 3 for the light throughput is no longer a constant. It depends on both M_T and Ω_F where Ω_F represents the solid angle of light which can fall on the slit via the furnace. Ω_F is equal to $\sim 1 \times 10^{-5}$ [srad] and the relationship between Ω_F and Ω_s is summarized by $\Omega_s = M_T^2 \Omega_F$. Again $\eta_i = M_T \eta_s$ and equation 3 for the light transmission past the

slit reduces to: -

$$T(\text{case 1}) = 2I_o R_{os} \Omega_F \eta_s s\, M_T \quad [W] \qquad 8$$

This time T is maximized by making M_T as large as possible (i.e. $M_T = 2$). The spectrum height is now given by $\sim (x + Z + 2\eta_i)$. $2\eta_i$, which scales as M_T, is now included because the image height at the slit (excluding astigmatism) is no longer negligible. z is now independent of M_T since the illuminated height of the grating is now fixed by the solid angle Ω_F subtended by the furnace aperture. It can be shown that:-

$$x = L(M_T + 1)\text{Sin}^2 I_{pr} \quad [m] \qquad 9a$$

$$\propto M_T(M_T + 1)\text{Sin}^2 I_{pr} \quad [m] \qquad 9b$$

L scales as M_T because the source-mirror distance should not be reduced below 2.5 [m]. Hence for non zero I_{pr}, th flux density F_{Film} scales as $1/M_T$ (for large values of M_T) and is therefore maximized by taking M_T as small as possible (i.e. $M_T = 1$).

It is possible with a magnifying arrangement to "fold" the source-condenser mirror axis almost on top of the condenser mirror-spectrograph slit axis such that $I_{pr} \simeq 0^\circ$. This is because the furnace is no longer in the way for sufficiently large magnification. Therefore x (equation 9a) will no longer be significant and can be ignored. So that the flux density F_{Film} is relatively insensitive to M_T, but is nevertheless maximized by taking M_T as large as possible (i.e. $M_T = x2$).

Numerical Example

Taking M_T = x2 (the largest practical)

Let R = 3.33 [m] -Gives x2 magnification 2.5 [m] and 5[m] conjucates

$I_{pr} \simeq 0^{o}$

$\Omega_F = 1 \times 10^{-5}$ [srad] -Due to the furnace

and $\alpha = 12^{o}$ -For the Jobin Yvon spectrograph

$\beta = 20.5^{o}$ -At 600A for a 2400 [lines/mm] grating

which implies that: -

v = 5000 [mm]

L = 17.8 [mm]

l = 3.5 [mm]

It therefore follows from equations 4 and 5 that

$x \simeq 0$ [mm]

z = 0.6 [mm]

and $2\eta_i = 0.6$ [mm]

The flux density at the film is given by:-

$$F_{Film}(\text{case 2}) = \frac{KT(\text{case 2})}{(x+z+2\eta_i)} = 1.25 \times 10^{-10} K I_o R_{os} \ [W\ m^{-2}] \qquad 10$$

Conclusions

The results summarized in equations 7 and 10 indicate that the best practical demagnifying arrangement is marginally better ($\sim$1.12 times) than the corresponding magnifying arrangement, with regard to flux densities at the film. This demagnifying arrangement also yields a much larger spectrum height ($x + z + 2\eta_i$) compared with the "best" practical magnifying arrangement.

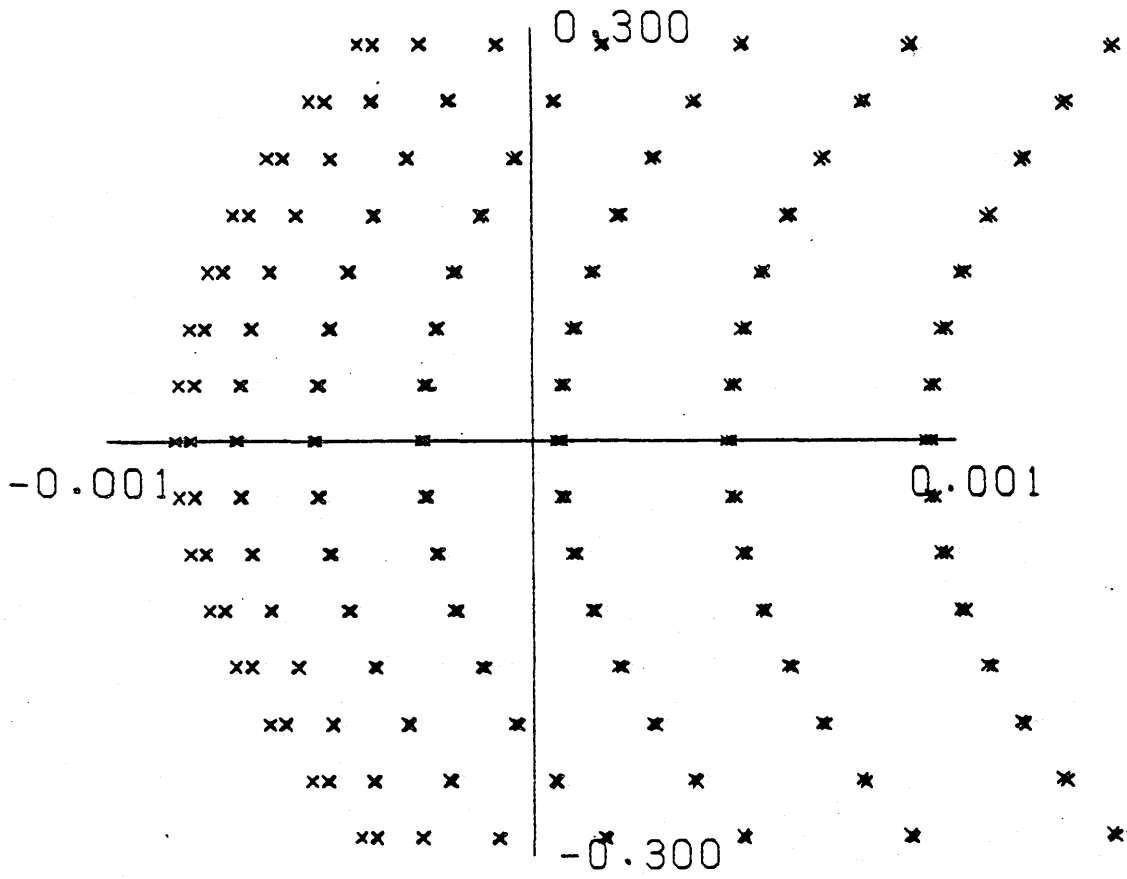
In practice, a demagnification of x 0.317 (1/3.15) was used for reasons given in subsection 3.3.1. No significant increase in the exposure time would have resulted however since the flux density at the film was relatively insensitive to demagnification. Also this lower demagnification reduced the angular precision to which the condenser mirror needed to be aligned to just $\sim$ 10 seconds of arc (image diameter of source $\sim$95 [μm]). The manufacturers quoted values for the ultimate angular resolution and angular setability for the mirror gimbol mount were 1 second of arc and 30 seconds of arc respectively using manual micrometer screws. It was anticipated that the resolution of the mount with electrically driven micrometer screws would not be so good. This was because these motors have a minimum turning speed before they stall. In the actual experiment it was found that these screws were <u>just</u> capable of aligning the condenser mirror

to the required 10 seconds of arc.

Ray tracing in this work

Extensive use was made of a ray tracing programme written by Dr. M.Crisp, formally of this laboratory, during the early design work on the optical system. This programme, called "PROCRT" was written by Crisp as part of his postgraduate research programme on the design of spectrograph optics. As such, the programme turned out to be nearly ideal for generating ray traces of given optical layouts of the type discussed in this text. These ray traces were used first, as a check to see if other optical aberrations such as coma besides astigmatism were significant or not. Second, they were used as independent checks on the analysis presented above with regard to the height of the images to be expected at the slit and the film plane. It was found that only astigmatism was important in this work and that the heights of the images due to astigmatism, as predicted by the preceding analysis were approximately correct. Figures 3D9, 3D10 and 3D11 shows a typical output for a x1/3 demagnifying arrangement using a 1.5 [m] radius of curvature mirror at 15^{o} angle of incidence, the experimental spectrograph and a solid angle of only 3.8×10^{-6} [srad] transmitted by a square apperture in the furnace. Figure 3D9 shows the image at the slit due to the mirrors

FIGURE 3D9: IMAGE ABBERATIONS AT THE SPECTROGRAPH SLIT DUE TO THE CONDENSER MIRROR

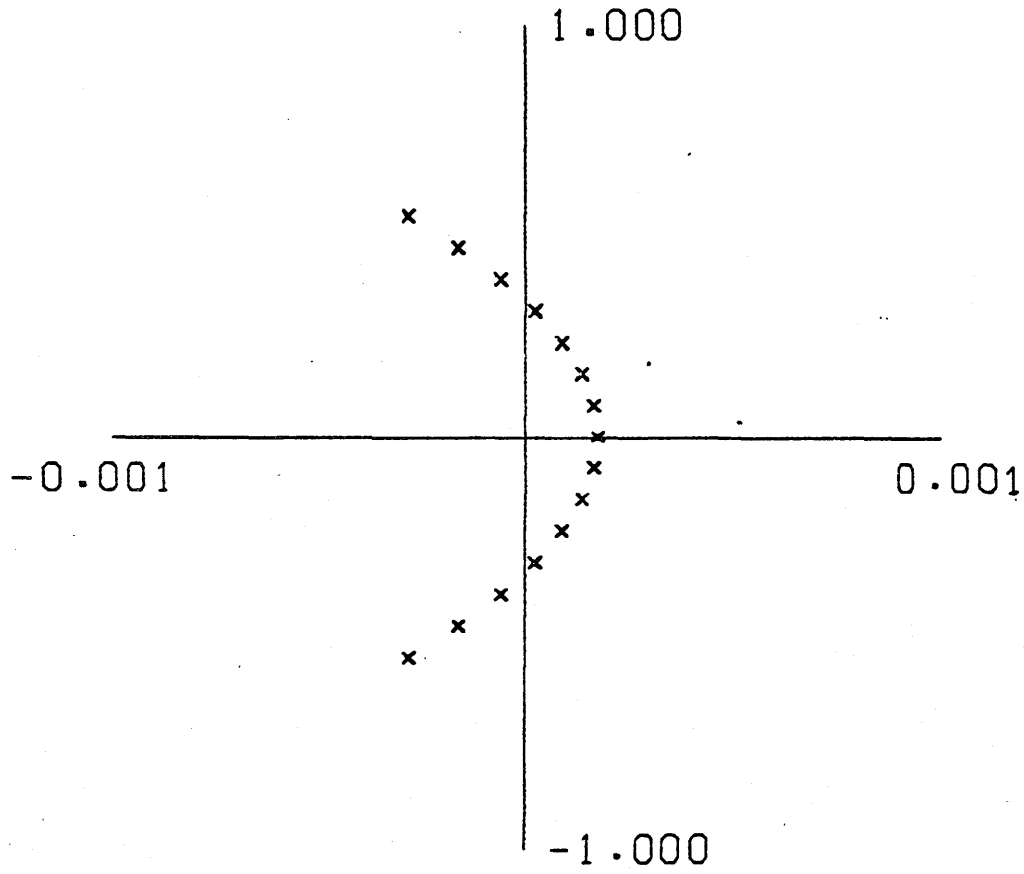


SCALE IN M.M.

Calculated abberations for a x 1/3 demagnifying arrangement using a 1.5 [m] radius of curvature mirror at 15° angle of incidence and a 3.8×10^{-6} [srad] solid angle (square apperture) pencil of rays.

astigmatism. Figure 3D10 shows the image at the film plane for 600Å rays due to the gratings astigmatism alone. Lastly, figure 3D11 shows the image at the film plane for 600Å rays due to the combined astigmatism of both the mirror and the grating. The values of x, z and x+z as deduced from formulae 7 and 9 were 0.6 mm, 1.12 mm and of course 1.72 respectively. These values are in good agreement with the ray traces for x and z, but the real x+z is in fact $\sim$ 13% larger than the height of image at the film as predicted by the ray trace programme.

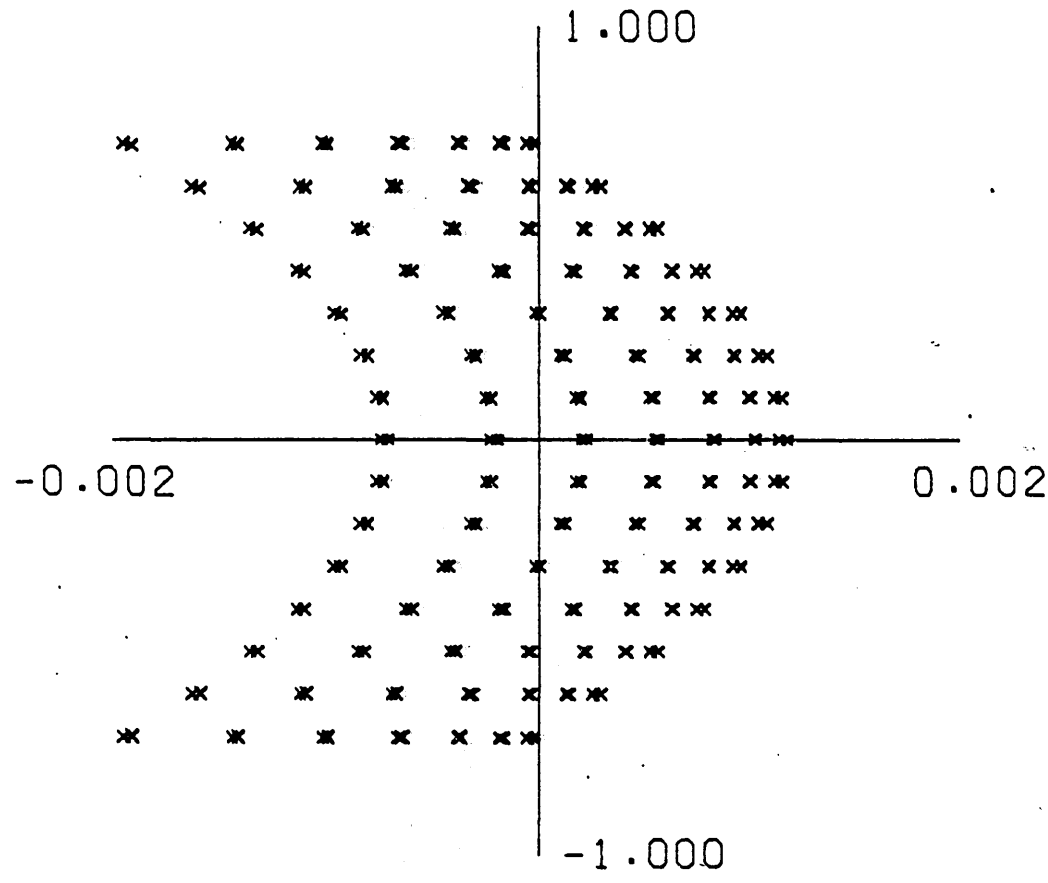
FIGURE 3D10: IMAGE ABBERATIONS AT THE SPECTROGRAPH FILM PLANE (600Å) DUE TO THE GRATING ONLY



SCALE IN M.M.

Calculated abberations at the film plane of the experimental spectrograph (Chapter 3) arising from its grating only for a pencil of radiation (at 600Å) of 3.42×10^{-5} [srad] ($=(1/3)^2\ 3.8 \times 10^{-6}$ [srad]) solid angle.

FIGURE 3D11: IMAGE ABBERATIONS AT THE SPECTROGRAPH FILM PLANE (600Å) DUE TO BOTH THE CONDENSER MIRROR AND THE GRATING



SCALE IN M.M.

Calculated Image abberations at the film plane arising from both the condenser mirror (1/3 demagnified image, 1.5 [m] radius of curvature, 15° angle of incidence) and the grating of the experimental spectrograph (Chapter 3). The spot diagram corresponds to the point spread function for a 3.8×10^{-6} [srad] (square apperture) solid angle pencil of rays (600Å) collected by the condenser mirror.

APPENDIX 3 Summary of Pipe Conductances in the Molecular Regieme

The following information was obtained from the reference by Turnbull et al (1962). The original formulae were published with lengths measured in imperial inches. Those quoted below have been converted to metric.

Nomenclature

D = Pipe diameter [cm]

L = Duct length [cm]

A = Crossectional area [cm^2]

Conductance in parallel $C_T = C_1 + C_2$ [L/s]

Conductance in series $1/C_T = 1/C_1 + 1/C_2$ [L/s]

Long circular pipe $C = 12.25\ D^3/L$ [L/s]

Short circular pipe (approx) $C = 12.25\ D^3/(L + 1.33D)$ [L/s]

Orifice of Area A $C = 11.63A$ [L/s]

Orifice of Area A in plate blocking the end of a pipe of area A_o $C = 11.63\ A\ A_o/(A_o + A)$ [L/s]

Bend or elbow - The conductance of a bend of circular crossection is the same as that of a short circular pipe of equal diameter and of length equal to the length of the bend measured along its centre line.

Appendix 4 Preparation of a line list from optical comparator measurements

Preparation of a line list from these measurements involved three basic operations similar to those discussed in Chapter 4: First, the positions of lines observed in the excited state spectrum were measured and absorption/emission lines from the continuum source were identified. Second, a set of wavelength standards were selected from the source lines together with a few ground state Barium absorption lines. The wavelengths of these lines were known from the work of Connerade et al (1979a). From these lines a dispersion curve could be generated in the manner described later in this appendix. Thirdly, the measured positions of the lines on the photographic plate were converted into wavelengths.

A Carl Zeiss Jena (East Germany) Optical Comparator with a resolution of 1 [μm] was used to measure the positions of the spectral lines. The instrument as fitted with a pair of microscopes, one to look at the spectrum and the other at a millimeter scale. Setting up the instrument involved first adjusting the microscope looking at the film until the image generated by its objective lens lay in the plane of the microscope's "crosshair" graticule. This focussing condition was confirmed by the lack of parallax between the image

of the film and the graticule as observed through the microscope eye piece. The photographic film was then rotated until the "crosshair" of the graticule ran perpendicular to the spectral lines as the plate was scanned in wavelength.

It was found that weak spectral lines in the spectrum could not be resolved with a high magnification eye piece (x6.3) due to the lack of contrast in the magnified images. The best results were achieved with a low magnifying eye piece (~x3) with which the "crosshair" could be set onto the centre of a typical spectral line with an accuracy of ~10 [μm]. This value was however dependent on the contrast of the line with respect to the background and was therefore dependent on both the intensity and width of the line. A figure for the accuracy to which lines were measured was gained by measuring the spectrum twice, first going from long wavelength to short and then vice versa. Enlarged photographic prints of the three spectra recorded on a single film during an experimental run were used to tentatively identify spectral lines arising from a residual Barium ground state population in the excited state spectrum. They were used as an aid for picking out the two sharp impurity lines in the continuum source at 555.9Å and 554.4Å. These two lines as well as the two emission lines at 790.0Å and 787.6Å were vital for accurately generating the wavelength dispersion curve of the excited state

spectrum and thus calibrating the spectrum in wavelengths as will be now seen.

To avoid any inaccuracies arising from chance co-incidences between ground state and excited state absorption lines, the dispersion curve was constructed purely from the ground state spectrum on the same plate and was applied to the excited state spectrum by using the above four source absorption/emission lines as transfer standards. It should be noted that these lines lay in regions where there are very few (or no) 5p absorption lines due to the Barium metastable D states. This technique of course assumes that any irregularities along the film will be the same for both spectra.

The dispersion curve representing the functional relationship between the line positions on the film and their corresponding wavelength was generated using a Chebyshev Polynomial fit routine (Connerade and Baig, 1984, Private Communication), with the coefficients being chosen by the method of least squares using the calibraton lines decribed above. The errors between the fitted curve and the calibration lines used to generate it were outputted by Connerade's program permitting the identification of any incorrect calibration lines. The fitting routine was then re-run using only the "correct" calibration lines and the wavelengths for all the other observed lines were outputted by merely

entering their spatial positions on the "plate". Wavelength errors arose from inaccuracies in the measured positions of the lines (approximately deduced by measuring each line twice). Thus a knowledge of the recipical linear dispersion (3.95 [Å/mm]) permitted an assessment of the wavelength error on each line.

Appendix 5 Derivation of the time t_o taken for the stimulated rate to equal the spontaneous rate for the transitions 6s6p $^1P_1$ - 6s5d $^3D_2$ and $^1D_2$

Saturation of the $6s^2\ ^1S_0$ - 6s6p $^1P_1$ transitions by a high power dye laser gives rise to a population inversion between the 6s6p $^1P_1$ and the 6s5d $^3D_2$ or $^1D_2$ levels. This gives rise to the possibility of stimulated emission, the importance of which may be assessed by deducing the time t_o for the stimulated rate to equal the spontaneous rate. The following derivation follows that given by Bowen and Thorne (1985).

Let 1 and 2 be the $^1S_0$ and $^1P_1$ levels, locked in equilibrium by the laser, while level 3 designates either $^1D_2$ or $^3D_2$. The ^3P levels can be ignored because they are populated collisionally, much more slowly. The spontaneous emission rate for the transition 2→3 is N_2A_{23} [photons s^{-1} cm^{-3}], of which a fraction α travel along the vapour column while the remainder were lost. Like Carlsten, we assume a rectangular line shape of width Γ (Hz) for this transition. Then if ρ is the photon density, the stimulated emission rate is: -

$$(N_2B_{23} - N_3B_{32})\rho h\nu/\Gamma \ [s^{-1}\ cm^{-3}]$$

where the Einstein coefficients are defined for energy density per Hz. Initially $N_3=0$ and N_2 is maintained at a constant value $g_2/(g_1+g_2)N$ by the laser. The early stages of the process are therefore described by the equation: -

$$\frac{d\rho}{dt} = \beta\left(\frac{N_2 c\, \lambda^2 A_{23}\, \rho}{8\,\pi\,\Gamma} + \alpha N_2\, A_{23}\right) \qquad 2$$

where we have used the Einstein relation between B_{23} and A_{23} and introduced the factor β to allow for photons escaping along the length of the column. In terms of the absorption coefficient k_o over the rectangular line: -

$$\beta = 1 - \exp(-k_o l') \qquad 3$$

where l' is a 'typical' length (say half the column length) and (since $N_3 \simeq 0$)

$$k_o \Gamma = N_2\, B_{23}\, h\nu\, /c = N_2\, \lambda^2 A_{23}/8\pi \qquad 4$$

The solution to equation (2) is

$$\rho = \frac{8\pi\,\Gamma\alpha}{c\,\lambda^2}\,(\exp(K\beta\, N_2 t) - 1) \qquad 5$$

where

$$K = \frac{c\,\lambda^2 A_{23}}{8\pi\,\Gamma} \qquad 6$$

The time t_o taken for the stimulated rate to equal

the spontaneous rate will determine whether stimulated emission is significant. For equal rates

$$t_o = \frac{\ln(1/\alpha)}{K\beta N_2} = \frac{8\pi \ln(1/\alpha)\Gamma}{c\lambda^2 A_{23}\beta N_2} \qquad 7$$

using equation (5), $\exp(K\beta N_2 t_o) = 1/\alpha + 1 \simeq 1/\alpha$ since $\alpha \ll 1$, therefore

Appendix 6 Identification of the main limitations of the apparatus and suggested improvements

The experimental technique of probing inner shell excitations with a VUV continuum source after prior excitation of a valence electron to a selectively excited state is an important new development. Its value lies in the ability to probe different excitation channels of the atomic inner shells not normally accessible from the ground state. The results of these studies may then be compared with theory and thus assist in the refinement of the latter. Consequently it is likely that such work will be done again in the future. It is therefore useful to identify the weaknesses of the present apparatus and to suggest improvements in anticipation of such future work.

The spectral resolution achieved in this experiment was not particularly high at 0.1Å, but higher resolution work would have been impractical with the present apparatus due to the limitations of the pump dye laser as will be seen later. Nevertheless, this experiment demonstrates the need for higher resolution work since only the most prominent features of the complex spectrum were resolved. The suggested improvements to be incorporated in any future work, are made with a view to matching the resolution of 0.005Å achieved by Baig et al (1984) on the Barium ground state spectrum.

The Dye Laser

(i) Limitations

Without any doubt the weakest link in the apparatus was the dye laser system. The chief problem being the extremely poor repetition rate of 2 [shots/minute]. This was governed by the relaxation time of the thermal turbulence generated in the oscillator and amplifier dye cells by the pump laser. The obvious answer would have been to flow dye in both of these cells using a pair of circulation units. However each unit would have required about a quarter of a litre of dye solution which would have cost £100 a refill at 1984 prices (For Coumarin 540A). This was prohibitively expensive bearing in mind the very limited resources available for this work. Nevertheless, from an experimental point of view it was the only viable solution. Had the dye been flowed, the repetition rate of the dye laser system would have been limited by the repetition rate of the coaxial laser to about 6 [shots/minute]. Keeping in mind time wasting factors succh as for example, the time taken to record the delay between the dye and ruby laser, two or three spectra could have been recorded in the time taken for just one in practice.

The other major limitation of the dye laser system was the relatively low output power of only

70 [kW]. This restricted the column density and area of the Barium vapour column which could be optically excited to the values given in section 3.4. Higher column densities would have been desirable in order to bring out the weak features of the Ba(6s5d) 5p absorption, while pumping a larger area of the vapour column would have cut the number of shots required for a spectrum. Achieving these two aims would have required a more powerful pump source for the oscillator-amplifier. The peak power from the experimental Co-axial laser was about 1 [MW] but it was a very inefficient pump with a pulse length (FWHM) of over five times that of the tuned output (section 3.4). Particularly bad was the fact that the tuned output envelope fell within the rising edge of the pump laser.

(ii) Suggested improvements

For this experiment a more powerful (MW) but shorter pulse length pump source would have been more appropriate. The "SLL 500M" Co-axial flashlamp dye laser marketed by Candela Corporation (US) fits both of these requirements. This system produces 15 [MW] (3.8 [J] in 250 [ns] FWHM) of broad band emission centered at 4900Å. Other characteristics of the system are synchronisation reproducibility of up to ±5 [ns] and its maximum repetition rate of 0.5 [Hz] at 3.8 [J]. An additional pair of amplifying cells for the tuned laser would have been

necessary to efficiently utilize the additional power available from this source. Tuned outputs in excess of 140 [mJ] for the same pulse length of $\sim$100 [ns] FWHM ($\gtrsim$1.4 [MW]) would have been expected compared with the present 7 [mJ] maximum.*

The cost of the Candela SLL 500M system is not cheap at £26,400 (1985 prices). Nevertheless the twenty lines (plus) improvement in tuned output would have been invaluable for work at higher column densities and/or higher spectral resolution. Consider for example the recent experimental work of Baig et al (1984) mentioned earlier. They used a 3 [m] vacuum spectrograph with a recipical dispersion of 0.27 [Å/mm] at a slit width of 10 [μm] to give them a resolution of 0.005Å.+ A spectrum at their resolution would have required around 6000 shots for the same optical arrangement, spectrum height, grating efficiency and furnace conditions of this work. (They don't quantify either the astigmatism or grating efficiency of their spectrograph.) This is clearly out of the question for the laser used in this work. However this enormous figure could have been cut by a factor of twenty (plus) to a more manageable 300 shots or less by pumping a larger diameter of Barium vapour using the laser specified above.

*The figure of 140 [mJ] is based on the additional amplifiers having the same efficiency as the experimental amplifier. As such the figure is probably very conservative since in practice passive amplifiers tend to be more efficient as the number of stages increase (Loth and Meyer (1976)).

+Resolution was limited by number of illuminated gratings.

The Furnace

(i) Limitations

In section 3.7 a method for maintaining high column densities of Barium vapour in the furnace optical axis without using a buffer gas was described. However the furnace was not at all suitable for the installation of such a "dynamic containment system" because of the ovens side ports. The necessary isolation between the interior of the containment system and these side ports was achieved by a pair of concentric rolled sheets of stainless steel. This approach was obviously unsatisfactory but was used because of the urgent need to quickly fabricate a workable system in the shortest possible time (i.e. days). The urgency arose from the lack of remaining time for further experiment work. In the event successful spectra were recorded but the vapour containment of the device was inefficient. As a result, a great deal of time was wasted stripping the furnace and reloading with fresh Barium between experimental runs. Another consequence of the inefficiency of the experimental containment system was that higher column densities could not be maintained for sufficient lengths of time to record a spectrum.

(ii) Suggested Improvements

Future work should be done using a furnace consisting of a simple tubular jacket with no side ports. The central region of the heated section would be enclosed by a pair of tight fitting stops. A long tube of inner diameter equal to the excitation laser beam would confine the escaping vapour to the laser axis as usual. The tight fitting stops would be made out of thin metal sheet to enable the core to be knocked out after use as recommended by Tracy (1975).

A dynamic containment system of the type described by Tracy (1975) is recommended whenever VUV absorption work is being performed on metal vapours, since they require no buffer gas. Hence the entire vacuum system may be pumped continuously without the difficulties of maintaining a static column of buffer gas within the furnace using a differential pumping system.

Appendix 7 Novel focussing arrangement for improving the "useful" power output of the plasma continuum source

In this appendix a novel focussing arrangement which could be used to decrease the number of shots required for recording a photographic spectrum will be described.

The intensity of the continuum emitted by the laser generated plasma has been found to be weakly dependent on laser energies above about one Joule (O'Sullivan, 1982). O'Sullivan does not advance any specific opinion on the reason for this results, but it must be connected to the reflection of incoming radiation by the plasma's free electrons. This occurs when the plasma and laser frequencies become equal, and further energy is only absorbed to maintain the electron density of the expanding plasma such that the plasma frequency remains unchanged. The net result is that further increases in the laser energy above one Joule are not very effective if a spherical lens is used for focussing the laser beam onto the metal target.

This is no longer the case if a cylindrical lens is used to produce a line image on the metal target. The ideal would be to exploit the basic astigmatism of the spectrograph. That is the property where every point on the slit is focussed onto a line

image of height equal to the "point spread function" of the grating. The height of the point spread function will approximately equal the height of the spectrum provided the illuminated length of the slit is small by comparison. It therefore follows that the flux density at the film will scale with the length of the "plasma line" in this case, since the brightness of the plasma is restricted by the plasma frequency.

The approach for setting up such a focussing arrangement for best results might be as follows. The output of say a 10 Joule Q switched laser would be focussed onto the target using a cylindrical and spherical lens to produce a line image. The laser output would then be increased until the "turnover energy" was reached where the continuum intensity becomes weakly dependent on laser energy. The length of the "plasma line" would then be changed by moving the cylindrical lens with respect to the spherical lens until the turnover energy occurred at 10 Joules.

The maximum useful height of the plasma line, with regard to minimizing the number of shots required for a spectrum, would be determined by equating the height of the continuum image at the spectrograph slit to that of the spectrographs point spread function. Consider for example the instrumentation used for this experiment. The

height of the spectrum due to the astigmatism was about 5.4 [mm] (For completly filled grating corresponding to 1/5 demagnifying arrangement). Thus the maximum-useful plasma length would have been 13 [mm] bearing in mind the demagnification of 2.4 of the osmium coated mirror. Note that in practice the diameter of the optically pumped column of Barium at 3.6 [mm] would have been the true limiting value on the useful height of the plasma.

REFERENCES

1. Amusia, M. Ya; (1974) "Vacuum Ultra-Violet Radiation Physics" (Pergamon View eg) p. 205.

2. Arfken, G; (1970) "Mathematical Methods for Physicists" Second Edition, International Edition (Academic Press, New York, San Francisco and London) p. 624.

3. Armstrong, J.A; Esherick, P. and Wynne, J.J; (1977) Phys.Rev. A15, 180.

4. Bachor, H.A. and Kock, M; (1981) J.Phys.B.At.Mol.Phys. 14, 2793.

5. Baig, M.A.; Connerade, J.P. and Newsom, G.H; (1979), Proc.Roy.Soc.Lond.A. 367, 381.

6. Baig, M.A.; Connerade, J.P.; Mayhew, C. and Sommer, K; (1984) J.Phys.B., At.Mol.Phys. 17, 371.

7. Balloffet, G; Romand, J. and Vodar, B; (1961) C.R. Acad.Sci.Paris 252, 4139.

8. Bernhardt, A.F; Duerre, D.E; Simpson, J.R. and Wood L.L; (1976) J.Opt.Soc.Am. 66 416

9. Bowen, J.L; (1982) Ph.D Thesis, Univ. of London.

10. Bowen, J.L. and Thorne, A.P; (1985) J.Phys.B. At.Mol.Phys. 18, 35.

11. Brehm, B. and Bucher, A; (1974), Int.J.Mass.Spectrom.Phys. 15, 463.

12. Brehm, B. and Hofler, K; (1975) Int.J.Mass.Spectrom.Phys. 17, 371.

13. Bricks, B.G; Karras, T.W. and Anderson, R.S; (1978) J.Appl.Phys. 49, 38.

14. Burton, W.M; Hatter, A.T. and Ridgeley, A; (1973) Appl.Opt. 12, 1851.

15. Carroll, P.K; Kennedy, E.T. and O'Sullivan, G; (1978) Opt.Lett. 2, 72.

16. Carroll, P.K; Kennedy, E.T. and O'Sullivan, G; (1980) App.Opt. 19, 1454.

17. Carroll, P.K; Kennedy, E.T. and O'Sullivan, G; (1983) I.E.E.E. J.Quant.Electro. 12, 1807.

18. Codling, K; (1973) Rep.Prog.Phys. 36, 541.

19. Condon, E.U. and Shortley, G.H; (1935) "The Theory of Atomic Structure" Reprinted 1963 (University Press, Cambridge) p.366.

20. Connerade, J.P; (1977) J.Phys.B. At.Mol.Phys. 16, L239.

21. Connerade, J.P; (1978a) Contemp.Phys. 19, 415.

22. Connerade, J.P; (1978b) Nucl.Instrum. & Methods (Netherlands) 152, 271.

23. Connerade, J.P; (1984) J.Phys.B. At.Mol.Phys. 17, L165.

24. Connerade, J.P; Tracy, D.H; Mansfield, M.W.D. and Thimm, K; (1974) "Vacuum Ultra-Violent Radiation Physics" (Pergammon Vieweg) p. 243.

25. Connerade, J.P. and Tracy, D.H; (1977) J.Phys.B., At.Mol.Phys. 10 L235.

26. Connerade, J.P; Rose, S.J. and Grant, I.P; (1978) J.Phys.B.At.Mol.Phys. 12, L53.

27. Connerade, J.P.; Mansfield, M.W.D.; Newsom, G.H.; Tracy, D.H.; Baig, M.A. and Thimm, K; (1979a) Phil.Trans.Soc.Lond.A. 290, 327.

28. Connerade, J.P. and Martin, M.A.P; (1980) J.Phys.B. At.Mol.Phys. 13, 373.

29. Connerade, J.P.; Baig, M.A. and Newsom, G.H; (1981) Proc.Roy.Soc.Lond.A. 378, 445.

30. Connerade, J.P. and Martin M.A.P; (1983) J.Phys.B. At.Mol.Phys. 16 L577.

31. Connerade, J.P.; Lane, A.M. and Baig, M.A; (1985) J.Phys.B. At.Mol.Phys. 18 3507.

32. Cox, J.T; Mass, G; Remany, T.B. and Hunter, W.R; (1973) J.Opt.Soc.Am. 63, 435.

33. Ederer, D.L.; Lucatorto, T.B. and Saloman, E.B; (1974) "Vacuum Ultra-Violet Radiation Physics", (Pergamon Vieweg) p. 245.

34. Ehler, A.W; (1966) J.Appl.Phys. 37, 4962.

35. Exciton Chemical Company, Inc., (1983)

36. Fano, U; (1970) Phys.Rev.A. 2, 353.

37. Fox, J.N. and Wheaton, J.E.G. (1973) J.Phys.E. Scient.Instrm., 6, 655.

38. Hafner, P. and Schwarz, W.H.E; (1978) J.Phys.B. At.Mol.Phys. 11, 2975.

39. Hansch, T.W; (1972) Appl.Opt. 11, 895.

40. Hansen, J; (1975) J.Phys.B. At.Mol.Phys. 8, L403.

41. Holland, D.M.P. and Codling, K; (1980) J.Phys.B.At.Mol.Phys. 13, L293.

42. Hotop, H. and Mahr, D; (1975) J.Phys.B.At.Mol.Phys. 8, L301.

43. Huffman, R.E; Tanaka, Y. and Larrabee, J.C; (1963) J.Chem.Phys. (U.S.A.) 39 910.

44. Huffman, R.E; Larrabee, J.C. and Tanaka, Y; (1964) J.Chem.Phys. (U.S.A.) 40, 356.

45. Jahreiss, L. and Huber, M.C.E; (1983) Phys.Rev.A. 28, 3382.

46. Jahreiss, L. and Huber, M.C.E; (1985) Phys.Rev.A. 31, 692.

47. Kelly, H.P; (1975) "Photoionization and Other Probes of Many Electron Interactions"; Nato Advanced Study Institute Series, (Plenum Press, New York and London,) p.83.

48. Kompaneyets, A.S; (1961) "Theoretical Physics" (Foreign Languages Publishing House, Moscow) p. 258.

49. Kuhne, M; (1982) Appl.Opt. 21, 2124.

50. Kuhne, M. and Kohl, J.L; (1977) Appl.Opt. 16, 1786.

51. Kunnemeyer, R. and Kock, M; (1983) J.Phys.B. At.Mol.Phys. 16, L607.

52. Kunz, C; (1974) "Vacuum Ultra Violet Radiation Physics" (Pergamon View eg) p. 753.

53. Lee, S.T; Suzer, S; Matthias, E; Rosenberg, R.A. and Shirley, D.A; (1977) J.Chem.Phys. 66, 2496.

54. Lewandowski, B; Ganz, J; Hotop, H. and Ruf, M.W; (1981) J.Phys.B.At.Mol.Phys. 14, L803.

55. Littman, M.G. and Metcalf, H.J; (1976) Appl.Opt. 17, 2224.

56. Longhurst, R.S; (1968) "Geometrical and Physical Optics", Second Edition Second Impression, (Longman, Green and Co Ltd, London) p. 406.

57. Loth, C; Meyer, Y.H; (1976) Opt.Comm. 16 312.

58. Lu, K.T. and Fano, Uu; (1970) Phys.Rev.A. 2, 81.

59. Lucatorto, T.B. and McIlrath, T.J; (1976) Phys.Rev.Lett. 37, 428.

60. Lucatorto, T.B. and McIlrath, T.J; (1980) Appl.Opt. 19, 3948.

Mahajan, C.G; Baker, E.A.M. and Burgess, D.D. (1979) Opt.Lett., 4, 283.

61. Measures, R.M; (1977) J.Appl.Phys. 48, 2673.

62. Miles, B.M and Wiese, W.L; (1969) At.Data. 1 1.

63. Moore, C.E; (1958) "Atomic Energy Levels N.B.S. Circular" No 467 Vol 3 (Washington D.C. U.S. Govt. Printing Office).

64. O'Sullivan, G; (1983) J.Phys.B.At.Mol.Phys. 16, 3291.

65. O'Sullivan, G; Roberts, J.R; Ott, W.R; Bridges, J.M; Pittman, T.L; Ginter, M; (1982) Opt.Lett. 7, 31.

66. Roig, R.A; (1976) J.Opt.Soc.Am. 66, 1400.

67. Rose, S.J; Pyper, N.C. and Grant, I.P; (1978) J.Phys.B.At.Mol.Phys. 11, 755

68. Rose, S.J; Grant, I.P. and Connerade, J.P; (1980), Phil.Trans.Roy.Soc.Lond. 296, 527.

69. Rosenberg, R.A; Lee, S.T. and Shirley, O.A; (1980) Phys.Rev.A. 21, 132.

70. Salter, J.M; (1979) Ph.D Thesis, Univ. of London.

71. Samson, J.A.R; (1967) "Techniques of Vacuum Ultra Violet Spectroscopy" (John Wiley and Sons Inc) p. 98.

72. Seaton, M.J. (1966) Proc.Phys.Soc. 88, 801.

73. Skinner C.H; (1974) Ph.D Thesis, Univ. of London.

74. Skinner, C.H; (1980) J.Phys.B. At.Mol.Phys. 13, 55.

75. Stacewicz, T. and Krasinski, J; (1981) Opt.Commun. 39, 35.

76. Starace, A.F; (1976) "Photoionization and other Probes of Many-ElectronInteractions"; Nato Advanced Study Institute Series, (Plenum Press, New York and London) p. 395.

77. Tracy, D.H; (1975) Proc.Roy.Soc.Lond.A. 344, 563.

78. Tracy, D.H; (1977) Proc.Roy.Soc.Lond.A., 357, 485.

79. Turnbull, A.H; Burton, R.S. and Riviere, J.C; (1962) "An introduction to Vacuum Technique" (George Newness Ltd, London)

80. Wendin, G; (1973) Phys.Lett. 46A, 119.

81. Wendin, G; (1974) "Vacuum Ultra Violet Radiation Physics" (Pergamon Vieweg) p. 225.

82. Wendin, G; (1978) Daresbury Laboratory Report DL/SCl/R11 p. 1.

83. Whitkop, P.G. and Wiesenfield, J.R; (1980) J.Chem.Phys. 72, 1297.

84. Woodgate, G.K; (1980) "Elementary Atomic Structure" Second Edition (Clarendon Press, Oxford) p. 92.

85. Wynne, J.J. and Armstrong, J.A; (1979) Comments.At.Mol.Phys. 8, 155.